High Accuracy Attitude Control of a Micro-Satellite

Byung Jin KIM

Submitted to the University of London
for the degree of Doctor of Philosophy

May, 2002

Mullard Space Science Laboratory
Department of Space and Climatic Physics
University College London
Holmbury St. Mary
Dorking, Surrey

Abstract

There have been great efforts in the field of space technology to make space programmes more affordable ones. Smaller size design of spacecraft becomes a common goal for the mission planners and manufactures around the world. Currently developing technologies enable us to achieve a level of performance that was only feasible with large scale missions in the past.

Attitude determination and control system(ADCS) is in the heart of the technical challenges for miniaturisation of a satellite. It is generally believed that higher accuracy control system requires massive and expensive sensing and actuating devices. This paper is focused on how a budget mission can overcome the limitation. The hardware and software designs involved in a micro-satellite programme, KITSAT-3, were explained to support this topic.

The mission objectives of the satellite were overviewed including a brief introduction to the pushbroom type electro-optical camera and the space science experiment package. ADCS related requirements were analysed for payload operations. Derived requirements were examined with the performance analysis results considering design margins. Spacecraft attitude dynamics and description methods were presented for the control theory developments.

The system design and test results of the attitude hardwares are the main part of this thesis. System architecture of a three-axis attitude control system was proposed. The design process of the magnetorquer system was described in detail. Test results of the reaction wheels and fibre optic gyros were provided and analysed. Based upon the actual experimental results, dynamic models of the hardwares were constructed. Command and data handling protocols of the ADCS were also established for proper data management.

Environmental disturbance sources were modelled. The effects of micro vibrations induced by mechanically moving parts were assessed to verify the attitude stability requirements. Three-axis magnetorquering algorithm was suggested based on the actual implementation result. Initial detumbling and momentum dumping laws were proposed to increase the control efficiency.

Large angle manoeuvring scheme using error quaternion feedback control was modified for small satellite application where torque and momentum capacities were severely limited. Kalman filtering technique was applied for gyro bias estimation and compensation. Actual in-flight attitude telemetry data were analysed to verify the control performance.

To my beloved
wife Seonhee
and
daughter Jiyun

There are a small number of errors which can now be rectified by the insertion of a short note into the thesis:

1) On p83 the text should read " increasing the value of the 10k resistor to 100k in the first stage will diminish this effect",
2) On p123 the title of Fig 4-48 appears to be in error.
3) On p 169 the ordinate should be labelled Nm , not Nmsecs.

Table of Contents

List of Figures

Chapter 1

Chapter 2

Chapter 3

Chapter 4

Chapter 5

Chapter 6

Chapter 7

Chapter 8

List of Tables

Chapter 1

Chapter 2

Chapter 4

Chapter 5

Chapter 6

Chapter 7

Chapter 8

Chapter 1. Introduction

1.1 Backgrounds

Recently there has been a large increase in the demands on applications of small satellites. Rapidly developing technology, especially in electronics, has had a huge influence on space engineering, which is traditionally one of the most conservative areas in science and engineering. Large scale integration technologies in semiconductor device manufacturing have made dramatic changes during the last decade. The use of powerful microprocessors in space platforms has enabled us to greatly reduce what was previously bulky electronics. Moreover, the processing power enhancements of computers have made it possible to use more sophisticated control algorithms that were formerly only discussed in theoretical domains.

Currently flourishing micro-machining technology certainly has immense potential in space applications. Extremely small sensors, such as a gyro the size of a small coin, will dramatically change the concept of satellite engineering in the next few years (Barbour *et al.*, 1996). Micro-satellites are already being used in practical areas (Sweeting, 1994). Nano-satellites or even pico-satellites, which weigh less than 10 kg, will be challenging issues in the near future.

The Satellite Technology Research Centre (SaTReC) in Korea started research in the field of micro-satellites in 1989 in collaboration with the United Kingdom. After the successful launches and operations of KITSATs 1 and 2, SaTReC has gained considerable expertise in space technology. Based upon these experiences, the KITSAT-3 programme was proposed in 1994 to develop and demonstrate advanced space technology. Compared to its two predecessors, KITSAT-3 has more sophisticated requirements, especially in the area of attitude control and the remote sensing payload. There has been a great leap in technological achievement between these programmes. High accuracy three-axis attitude stabilisation is one of the most demanding requirements among them. Figure 1-1 shows the outlines of the KITSAT series satellites.

SaTReC has sponsored a number of students via international corporations with overseas educational institutes since the start of its activities in space. A group of students who studied at University College London played a key role in the KITSAT-3 programme. These scientists and engineers are now actively engaged in the Korean domestic space programme. The currently booming space industry in Korea will benefit from the results attained during the KITSAT-3 programme.

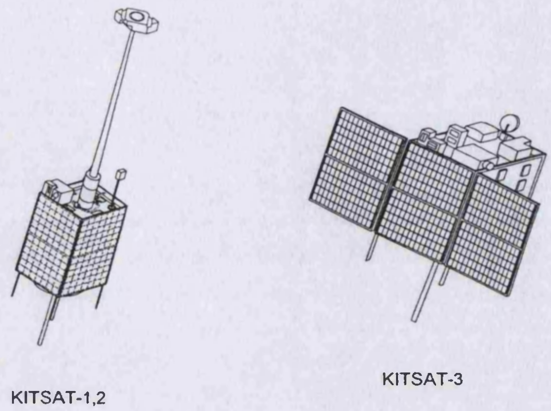

Figure 1-1 The KITSAT series satellites

1.2 Mission Objectives of KITSAT-3

The primary objective of the mission is to develop satellite bus technology. The remote sensing and space science payloads have been proposed as secondary objectives (Park *et al.*, 1995). Some of the mission aims are very challenging, especially, in the area of attitude determination and control. The required level of performance is high considering the small size of the satellite and budgetary constraints. The mission objectives are defined so as to achieve improvements in both bus and remote sensing technology. They can be summarised as follows.

1.2.1 Objectives in Bus System Development

- Design of a unique satellite bus system
- Development of a high accuracy 3-axis attitude control system
- Realisation of high data rate transmission system
- Design and evaluation of the solar panel deployment mechanism
- Implementation of modular command & data handling network

1.2.2 Objectives in Payload System Development

- Design and deployment of an electro-optic camera with multi-spectral capability
- Design and development of space science payloads for *in-situ* measurements (4 space science payloads as a package)

1.3 Mission Overview of KITSAT-3

The KITSAT-3 programme is briefly overviewed in this section in order to introduce the mission and the objectives. System configurations and the specifications are outlined in general to a level appropriate for understanding of the attitude determination and control system design and analysis throughout this paper.

1.3.1 Payload System

1.3.1.1 Multi-spectral Earth Imaging System (MEIS)

Panchromatic area type Charge Coupled Device (CCD) cameras have been tested during operations of KITSAT-1 and 2, which have 400 m and 200 m of Ground Sampling Distance (GSD) respectively. An objective on KITSAT-3 has been to achieve higher resolution with multi-spectral capability. The proposed pushbroom type camera is lightweight and small. The development of this electro-optical instrument is carried out as an international co-operation with the University of Stellenbosch of South Africa.

The camera has 3-band linear CCDs with 3456 pixels on its focal plane. It has 13.8m GSD and 47.7 km swath width at the 720 km nominal operation altitude. The satellite image contains information comparable to 1:25,000 scale maps. The camera is not designed and manufactured for commercial services. However, it can be used, in a limited way, for map-making, urban planning, environmental and disaster monitoring, agricultural and geological applications.

A particularly challenging aspect of the project was development of a mass memory module. The multi-spectral nature of the camera results in high data rate. The image has to be stored on board when a real time transmission is not allowed. With the in-kind support from the Samsung electronics company, solid-state recorders of 2 Gbits of Static Random Access Memory (SRAM) and 8 Gbits of flash RAM were developed.

Table 1-1 The spectral bands of the camera

Spectral band	Wave length (nm)
Green	520~620
Red	620~690
Near IR	730~900

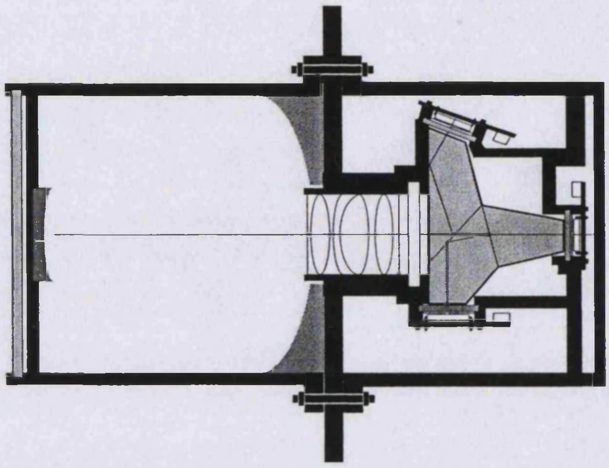

Figure 1-2 KITSAT-3's electro-optic camera

Table 1-2 Specifications of the camera

CCD type	Linear, TC104 (Texas Instrument)
Number of Pixels in CCD	3456
Size of a CCD Pixel	$10.7\,\mu m \times 10.7\,\mu m$
Focal Length	557.7 mm
F Number	5.6
MTF	>13% at Nyquist frequency
Mass	6.5 kg
Power Consumption	17 W (Nominal)
Swath Width at 720 km Altitude	47.9 km

1.3.1.2 Space Environment Science Experiments (SENSE)

The following space science experiments were proposed for *in-situ* measurements of the space environment.

- High Energy Particle Telescope (HEPT)
- Radiation Effect on Micro-Electronics (REME)
- Scientific Magnetometer (SMAG)
- Electron Temperature Probe (ETP)

HEPT is an improved version of KITSAT-1's Cosmic Ray Experiment (CRE). It measures the energy of electrons, protons, and alpha particles in the energy range 0.25 MeV to 60 MeV. It can also determine the incident angle of incoming particles with four detectors within the telescopic structure. The following research topics were proposed for the HEPT experiment.

- Effects of solar activities on particle distribution and energy variations in the Van Allen Belts
- Dynamic processes of particles
- Verification of the third radiation belt due to anomalous cosmic rays

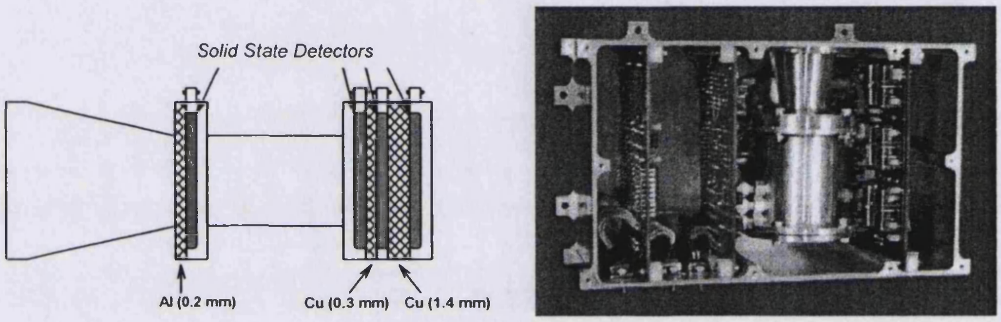

Figure 1-3 Mechanical structure and photograph of HEPT

Four Surface-barrier Silicon Detectors (SSD) in HEPT generate signals for charge sensitive amplifiers and counters. Three layers of blocking materials are used to enhance the discriminating capability as shown in Figure 1-3 and Table 1-3. The particle identification block in HEPT classifies the incident energy into 7 channels.

Table 1-3 Particle types and energy in the channels of HEPT

Channel	Particle type	Energy (MeV)
pE1	Proton	30 – 38
pE2	Proton	15 – 30
pE3	Proton	6.4 – 15
eE1	Electron	> 2.0
eE2	Electron	0.72 - 2.0
eE3	Electron	0.25 - 0.7
AA	Alpha particle	15 – 60

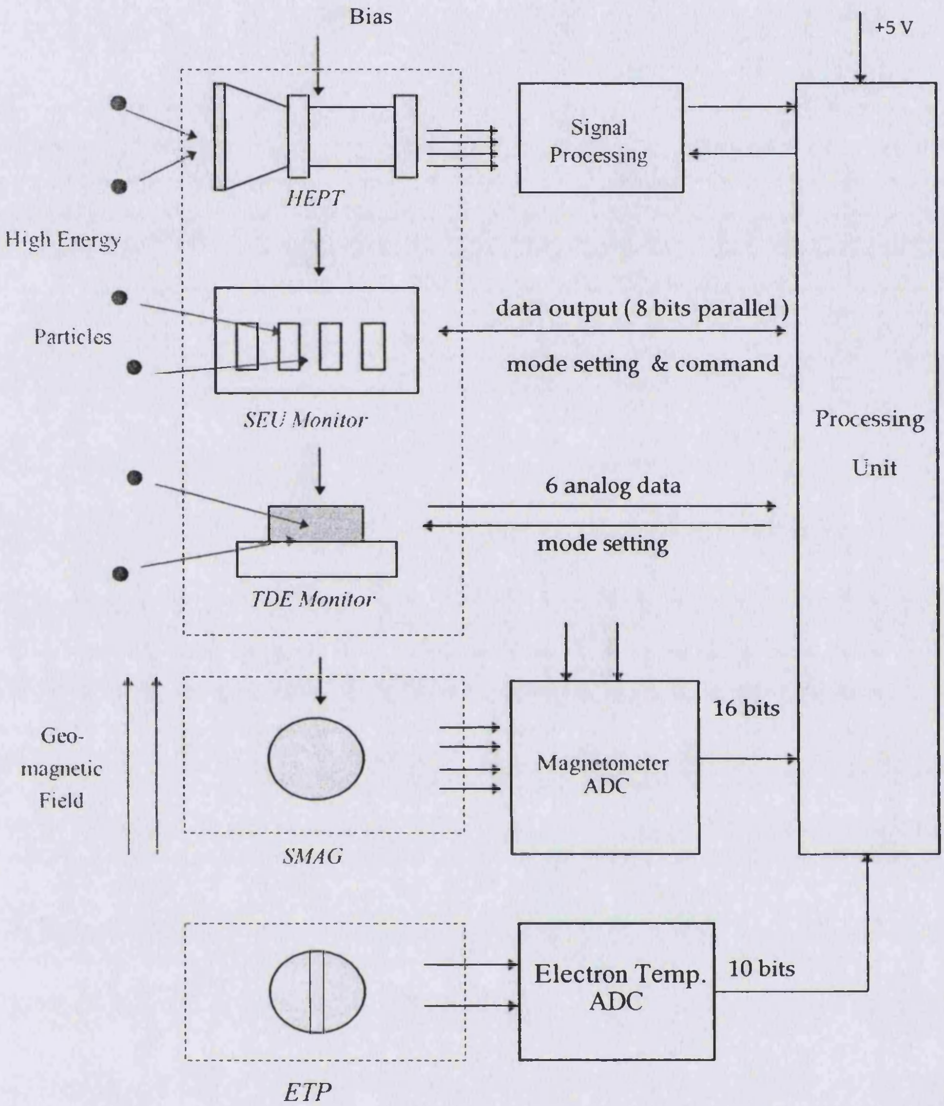

Figure 1-4 SENSE module block diagram

REME is an experiment aimed at the understanding of the degradation processes of commercial electronic components in space environments. Conventionally used memory devices were mainly used as the test samples. Single Event Upsets (SEUs) will be detected and investigated with the test samples manufactured by different integration technologies. To support the analysis for REME, Total Dose Experiment (TDE) is to be performed simultaneously by using Radiation Sensitive Field Effect Transistor (RADFET) devices.

SMAG is an improved version of the navigational magnetometer (NMAG) used for attitude determination. The resolution is improved from 30 nT to 5 nT. The sensor part is positioned far from the main satellite body, on the edge of the solar panel, to reduce the magnetic field disturbance from the main satellite body. It is to be used as a back-up sensor of the navigational magnetometer.

ETP is designed to measure low energy electrons of 1 eV level. The density of these particles is so high that measuring individual characteristics is impossible. Detecting the kinetic energy, or the electron temperature, can be an alternative statistical method. The data will be used to aid understanding of the interaction between the ionosphere and the magnetosphere.

1.3.2 Bus System

1.3.2.1 Attitude Determination and Control System (ADCS)

The ADCS should meet the attitude pointing accuracy and stability requirement imposed by the remote sensing camera. It also has to be capable of providing proper attitude requirements during the science payload operation mode.

A magnetometer and a sun sensor are used as the fundamental ADCS sensors; each has well proven heritage in KITSAT-1 and 2 missions. A low power analogue sun sensor is used to provide 2-axis attitude information. In this configuration, the spacecraft should be operated within 8° of pointing error during the coarse Sun tracking mode. A combination of three-axis reaction wheels and fibre optic gyros are used for fast large angle attitude manoeuvring and stabilisation. Star sensors and an infrared Earth horizon sensor are used as high accuracy attitude sensing devices during the fine control mode.

The remote sensing camera imposes the most stringent requirements in the mission operation. At the proposed 720 km nominal altitude, it has 13.8 m GSD in nadir direction. The ADCS has to provide 0.5° pointing accuracy with 0.016 deg/sec platform stability for imaging. It is also proposed to rotate the pitch axis with a period of 1~3 minutes for the operation of the high energy particle telescope. The ADCS will support the telecommunications and the power subsystem requirements for Earth pointing and Sun tracking.

1.3.2.2 Power System

The power system converts solar energy into electrical power. It also stores energy in the rechargeable battery units during the sunlit periods. It provides the 25~29V satellite bus voltage. Two battery packs are connected in parallel, each pack comprising 20 D-size NiCd cells in series. The Power Conditioning Module (PCU) regulates the unconditioned bus voltage. The Power Distribution Module (PDM) supplies +5V, +12V and -12V as the standard voltages to other subsystems.

1.3.2.3 Communication System

The multi-spectral linear CCD camera in KITSAT-3 has an output data rate of 40.4 Mbps. An X-band transmitter is required to handle this high-speed image data rate even though the on-board mass memory system is used as a buffering device. Satellite telemetry is to be sent by an S-band transmitter. A frequency Shift Keying (FSK) modulated Ultra High Frequency (UHF) transmitter is assigned for an extra telemetry down-link. A super heterodyne type Very High Frequency (VHF) receiver has two fold redundancy to improve reliability of the up link.

1.3.2.4 Solar Panel Deployment Mechanism

The remote sensing payload requires high power. It also causes the data transmission system to dissipate high power. Body mounted type solar panel systems used in the previous KITSAT series are not suitable for supplying the required amount of power. We need to expand the solar power capacity by deploying panels. The solar panel release and deployment mechanism consists of pyros, active and passive hinges, and shear cons and cups. Three accelerometers were proposed to monitor the deployment shock characteristics on-board.

1.3.2.5 Modular Command & Data Handling (MCDH) Network

The subsystems of KITSAT-3 are connected to the Modular Telemetry and Command (MTC) system to share the communications, telemetry & telecommand information with each other. The shared bus structure is a modification of the MIL-STD-1553B bus. Expanding the structure of MTC is relatively simple. Therefore it could easily accommodate subsystem design changes during the development phase. Due to its versatile nature, it will be used for the future KITSAT series missions. Since the entire satellite system is relying on the MCDH network, it has to be designed to have high reliability. An emergency data path is reserved in case of primary link failure.

1.4 System Overview of KITSAT-3

The system architecture of KITSAT-3 is designed with a modular bus structure concept as defined in the mission objectives. It has two payload systems, MEIS and SENSE. The bus system is composed of 5 subsystems; attitude determination & control, power, communication, mechanical structure & thermal control and command & data handling.

Each subsystem is connected to one of the four network controllers, MTC, as shown in the system block diagram in Figure 1-5. Not only the telecommand and telemetry data are shared through these controllers, but also the communication links between subsystems are established via this network. This decentralises the data handling system and improves the reliability of the whole satellite system. The power distribution module is located in the MTC as well to provide power lines to the subsystems.

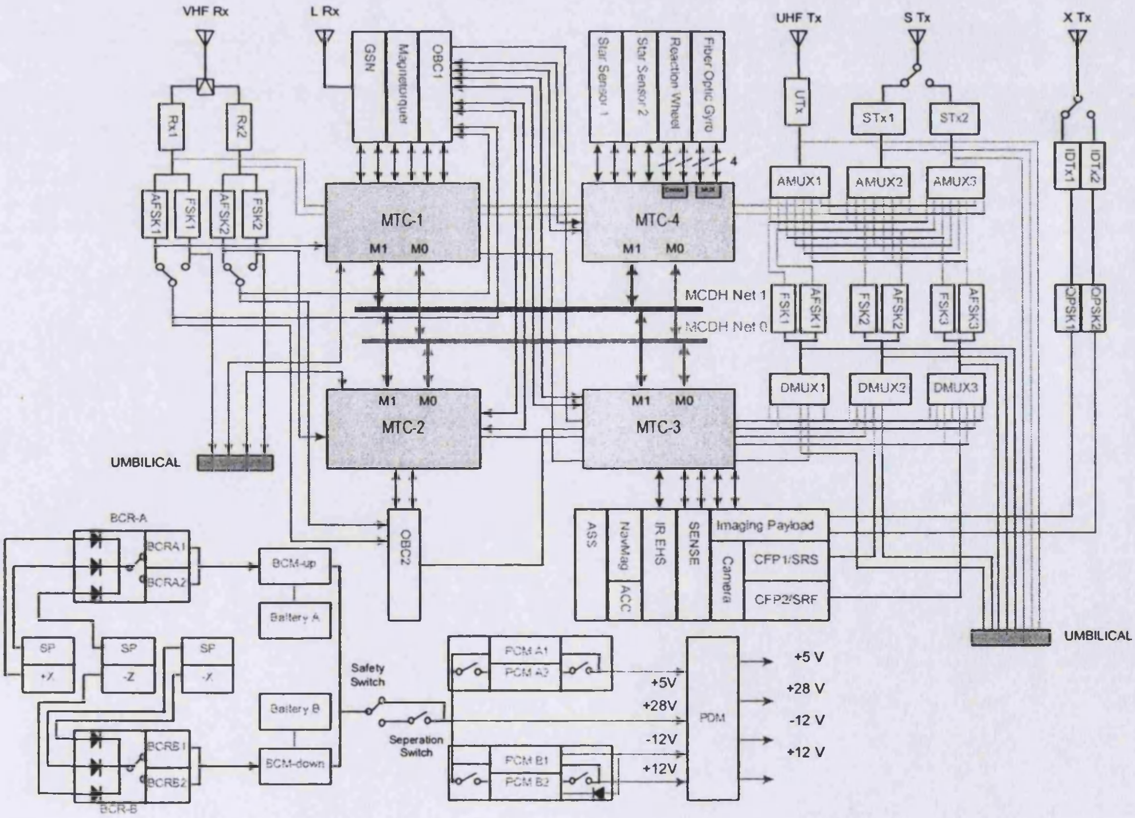

Figure 1-5 System block diagram of KITSAT-3

MTC has 2-fold redundant structure to avoid single point failure. The common bus architecture gives a certain degree of flexibility. Modification of the satellite system is relatively easy since the standardised MTC offers easy plug-and-play adaptations for new designs. The role of each MTC is demonstrated in Figure 1-5. MTC 1 and 2 are mainly used for the bus systems. MTC3 is concerned with the payload systems and attitude sensors. MTC4 is totally dedicated for the attitude determination and control system.

Figure 1-6 is an exploded view of the KITSAT-3 mechanical structure. The satellite interfaces with the launcher with the adapter located on $+y$ direction. The UHF and VHF antennae are positioned on the bottom corners.

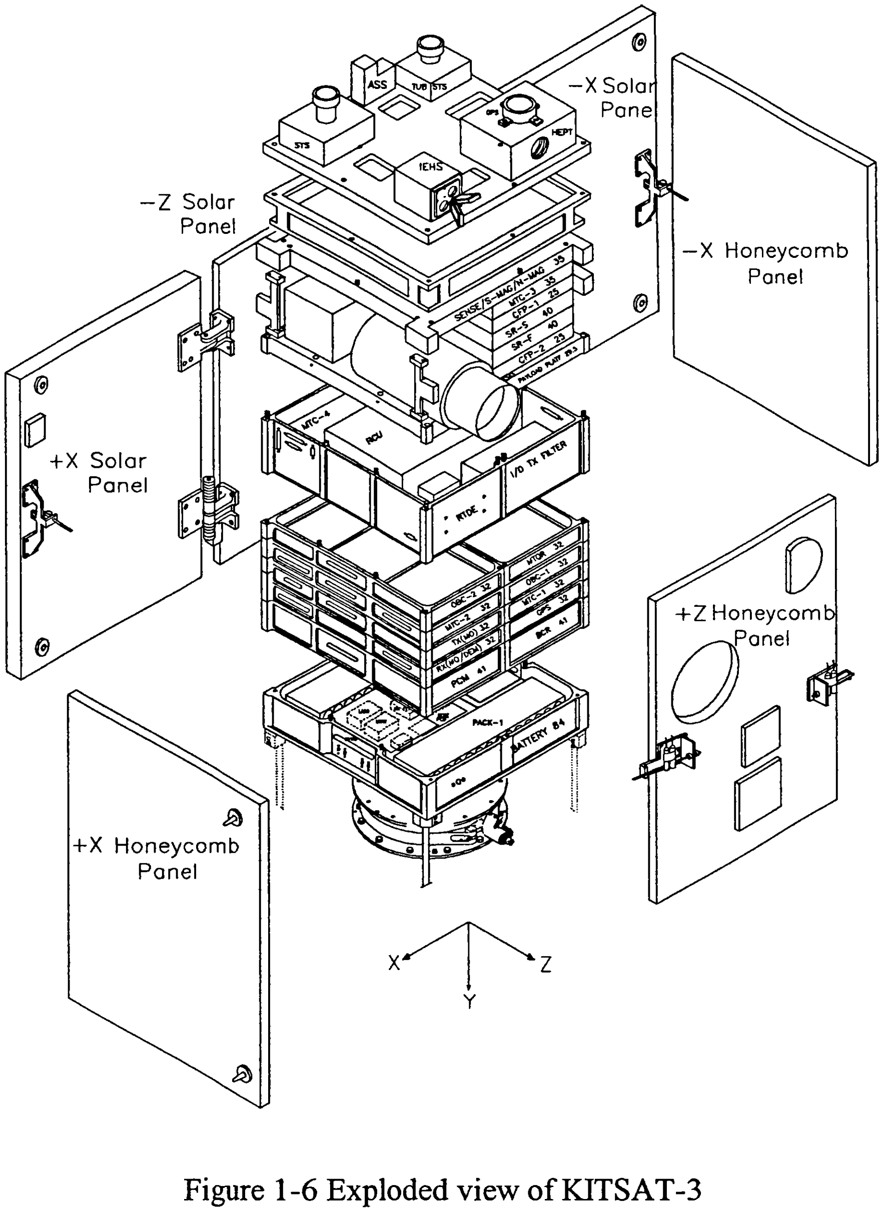

Figure 1-6 Exploded view of KITSAT-3

The satellite stabilises the attitude in such a way that the y axis is normal to the orbital plane and the z axis toward the Earth for imaging. The y axis attitude control will provide maximum solar power since the nominal orbit is a sun-synchronous one with 12:00 a.m. local Sun time. This simplifies the Sun tracking mode operation. As a matter of fact, the pitch control can provide all the required mission operations including Sun tracking, Earth imaging and spinning for HEPT experiment.

The mechanical structure of the KITSAT-3 in Figure 1-6 can be divided into four major sections. The bus part has a tray type structure, which is at the bottom half of the main structure. The payload system is placed on the bus system and can be separated from the rest of the structure as a distinct module. Attitude sensors and space science payloads are located on the top of the sensor platform. The honeycomb and solar panels are placed around the main satellite structure.

Figure 1-7 is a photograph of KITSAT-3 Flight Model (FM) in a clean room. The picture was taken with the solar panels folded. The pyro devices and solar panel release mechanism can be seen at the front of the satellite. The baffle of MEIS and the ETP sensor are also clearly visible.

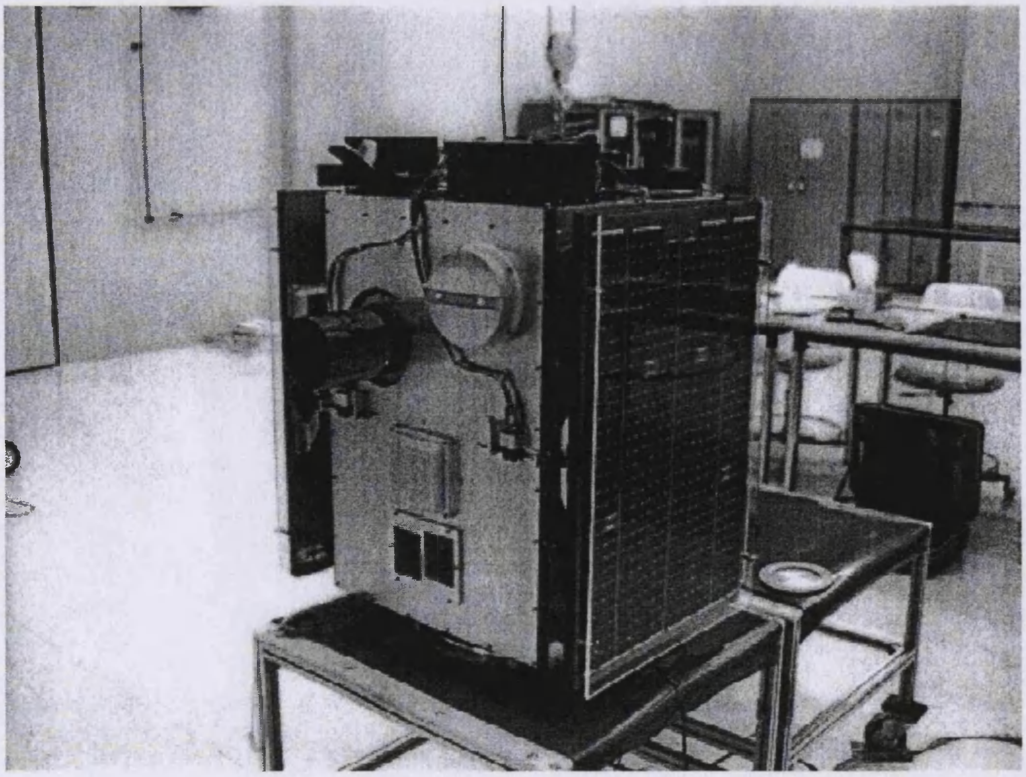

Figure 1-7 Photograph of KITSAT-3 flight model

Table 1-4 summarises the specifications of the KITSAT series satellites in comparison with the well-known French remote sensing satellite SPOT-3. It indicates the technological leap and the level of performance that a low cost micro-satellite mission can achieve.

Table 1-4 System specifications

	KITSAT-1/2	KITSAT-3	SPOT-3
Weight	~ 50 kg	~ 110 kg	1830 kg
Power	30 Watt	150 Watt	1 kWatt
Solar panels	Body fixed	2 Deployable, 1 Fixed	15.6 m of solar array span
Data transmission Scheme	UHF : 9.6 kbps	X-band : 3.3 Mbps	X-band : 50 Mbps
Attitude control	Gravity gradient	3-axis stabilised	3-axis stabilised
Attitude control Accuracy	$< 5^{\circ}$	$< 0.5^{\circ}$	$< 0.1^{\circ}$
Attitude control Actuator	Gravity gradient boom Magnetorquers	Reaction wheels Magnetorquers	Reaction wheels Magnetorquers Propulsion
Remote sensing payload	Area CCD (pan & Colour)	Linear CCD (multi-spectral)	Linear CCD (pan/multi-spectral)
Spatial resolution	400/200 m	13.8 m	10/20 m

1.5 Attitude Determination and Control System of KITSAT-3

The system architecture of the ADCS of KITSAT-3 is summarised in Figure 1-8. This demonstrates how the system interfaces with the MCDH network, which has two separate data paths, M0 and M1. It also should be noted that the MTC4 is totally dedicated to the ADCS. It interfaces with subsystems that require only digital telemetries and telecommands. Therefore, analogue to digital conversion capability is not required; this simplifies the hardware design of MTC4. Since it has the highest data communications load, a direct data path has been provided with the main on-board computer. The OBC1 has a 32 bit Reduced Instruction Set Computer (RISC)-type microprocessor, i80960, with the processing capability of 1.8 MIPS.

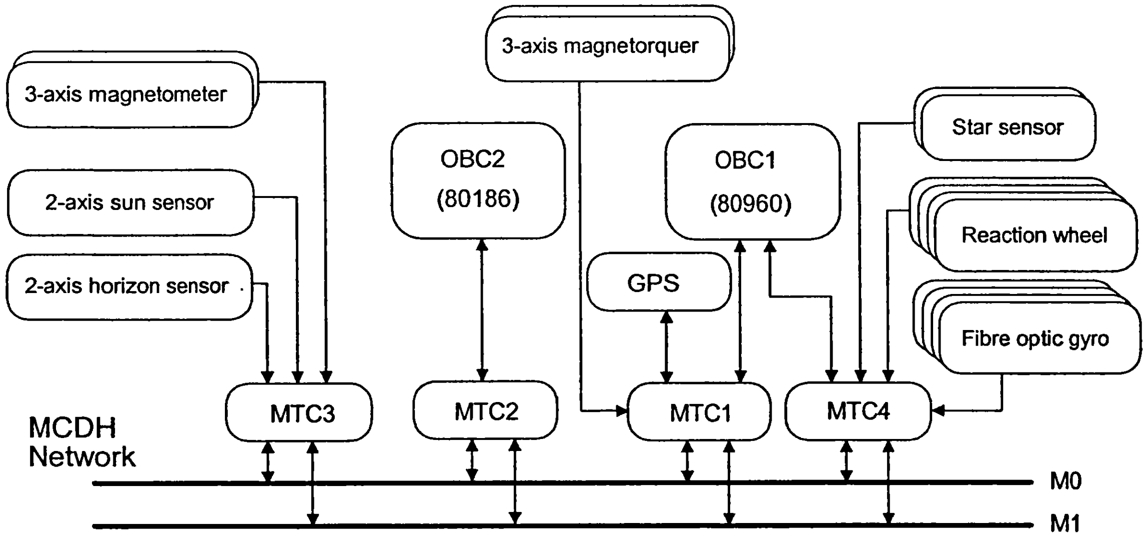

Figure 1-8 ADCS architecture

The ADCS has a sun sensor and two flux gate type magnetometers as its fundamental attitude sensors. They have high reliability and have flight heritages in KITSAT-1 and 2. The infrared horizon sensor is, however, developed for an engineering test purpose.

During the initial operation phase after the launch, the satellite uses magnetometer and magnetorquer to reduce the injection spin rate. The sun sensor will be adopted for Sun acquisition. The star sensor is for the fine control mode for imaging mission. The inertial navigation system constructed with fibre optic gyros and reaction wheels are at the heart of the attitude control system.

1.6 Scope of Work

This paper is focused on the attitude determination and control system design of the KITSAT-3 micro-satellite. Since the mission analysis is very closely related with the ADCS design, it will be handled rigorously. The system designs and tests results of the attitude hardware will be the major part of this paper. Modelling of attitude hardware and disturbance sources will be emphasised. Attitude control theory and simulation results will also be provided to validate the system performance. In-flight attitude data will be presented to support the proposed design and analyses results. Design margins of attitude control system performance will also be assessed and scrutinised.

Chapter 2. Mission Analysis

2.1 Mission Requirements

The mission success of the KITSAT-3 largely depends on the performance of the ADCS. The MEIS and HEPT operations require special consideration of the ADCS. Other factors, such as power, mass and link budget requirements should be taken into account for the mission analysis. However, only the ADCS related topics, including orbit analysis, will be discussed in this paper.

2.1.1 General Requirements

Due to the constraints of a budget mission, a launch opportunity as a piggyback payload is an essential requirement. Designing a satellite that can only be compatible with one launcher may be too risky, especially, when we are looking for a piggyback opportunity. At the early stage of the programme, two launch possibilities, ARIANE-4 and Long March-4, were under consideration. KITSAT-3 design started out aiming to meet all the launch vehicle environments required for these two preliminary launch vehicles. In fact, the launcher was selected at the later on in the programme, which is not unusual in the micro-satellite community. The Indian Polar Satellite Launch Vehicle (PSLV) was finally selected as its launcher. Table 2-1 lists general orbit characteristics of KITSAT-3.

Table 2-1 Orbit characteristics

Parameters	Preliminary	Final (pre-launch)
Orbit type	Circular Sun-synchronous	Circular Sun-synchronous
Altitude	600 ~ 1000 km	720 km (Nominal)
Period	96.69 ~ 105.12 mins	99.19 mins
Inclination	97.79 ~ 99.48 deg	98.27 deg
Local sun time	~ 10:30	12:00
Mission life	2 years	2 years
Designed life time	3 years	3 years
Launcher	ARIANE-4 or Long March-4	PSLV

Since the electro-optic remote sensing payload requires uniform Sun illumination, a circular sun-synchronous orbit is advantageous. An orbit with 10:30 a.m. local sun time is widely used to efficiently minimise the possibilities of optical path blocking by fogs and clouds (Joseph, 1996). An altitude of 800 km was set as a baseline design requirement during the preliminary mission analysis. The spacecraft is designed to satisfy 600 ~ 1000 km operational orbit requirements in order to be compatible with as wide a range as possible of launch opportunities. The finalised pre-launch orbit parameters are in Table 2-1.

The ground station, which will be located in Korea, needs to be completed prior to the launch of the KITSAT-3. Years of operational experience of receiving SPOT and JERS satellite data have been accumulated prior to the launch. A 13 m diameter parabolic satellite tracking antenna system has been built for this purpose.

2.1.2 Remote Sensing Payload Requirements Analysis

Attitude pointing accuracy capability of the spacecraft is a major issue. KITSAT-3 does not have a propulsion system. Generally, pointing accuracy of an on-off type thruster is limited to 0.1 ~ 1.0 degrees by the amplitude of limit cycles. If more accuracy is required reaction wheels should be used (Bryson, 1994).

The pointing accuracy is largely dependent on the attitude sensors. Alignments and calibration errors directly contribute to the system accuracy. The star sensors and the IR Earth horizon sensor for fine attitude determination of the KITSAT-3 were newly developed items. Fortunately the wide filed of view of MEIS allows a less stringent pointing requirement. 0.5° was determined as the pointing accuracy requirement.

The pointing error will turn out as a misallocation of a target from the desired position in the acquired image. The objective of KITSAT-3 mission is not military surveillance. In environmental monitoring applications, large scale targets are less susceptible for pointing error. We need to establish the Earth and satellite geometric relations to assess the pointing and ground positioning errors.

The angular radius of the Earth, ρ, can be defined first in Figure 2-1 as

$$\sin\rho = \cos\lambda_{o} = \frac{R_e}{R_e + h} \tag{2-1}$$

, where R_e is the Earth equatorial radius and h is the nominal orbit altitude 720 km.

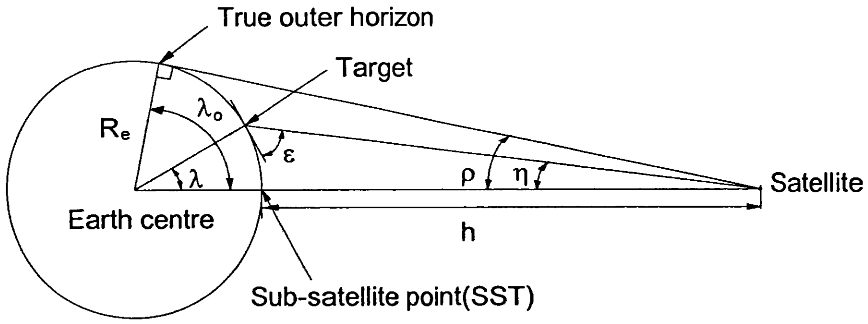

Figure 2-1 Earth-Satellite Geometry

If the Earth central angle λ is known, we can find the satellite nadir angle η (Larson & Wertz, 1992)

$$\tan\eta = \frac{\sin\rho\sin\lambda}{1-\sin\rho\cos\lambda} \tag{2-2}$$

The elevation angle, ε, measured from the horizon to the satellite is also given as

$$\cos\varepsilon = \frac{\sin\eta}{\sin\rho} \tag{2-3}$$

Another important property in the satellite-Earth geometry is readily available from the triangle in Figure 2-1.

$$\lambda + \varepsilon + \eta = 90^\circ \tag{2-4}$$

These results are very useful in planning and analysing satellite orbit characteristics. We can obtain the pointing offset distance on the ground, D, due to the attitude error η from Equation (2-5). Therefore, 0.5° of pointing error at 720 km altitude implies 6.3 km error on the ground in nadir direction.

$$D = \lambda R_e \tag{2-5}$$

The Ground sampling Distance (GSD) of the remote sensing camera, Δ, the projected size of a CCD cell on the ground, can be determined by the geometric relation between the focal length F of the optics and the CCD cell size d.

$$\Delta = \frac{dh}{F} \cong \frac{1.07 \times 10^{-5}\ \text{m} \times 7.2 \times 10^{5}\ \text{m}}{0.56\ \text{m}} = 13.8\ \text{m} \tag{2-6}$$

Substituting the camera parameters given in Chapter 1 to Equation (2-6), we can obtain the GSD of 13.8 m. Therefore, the swath width of MEIS, W, is given as

$$W = n\Delta = 3456 \times 13.8\ \text{m} = 47.9\ \text{km} \tag{2-7}$$

, where n is the number of pixels in a CCD line.

Hence, considering a cross track error of 0.5°, approximately 86.8 % of the desired area will be covered within the captured image. The along track error is neglected since scanning motion compensates it. Table 2-2 shows cross track error versus percentage of target area that can be covered assuming vertical pointing on a flat surface. The *useful swath* means the guaranteed swath width regardless of the assigned pointing error.

Table 2-2 Cross track pointing error versus area covered

Cross Track Error (deg)	Percents of Area Covered (%)	Useful Swath (km)
1.0	73.7	35.2
0.5	86.8	41.5
0.3	92.1	44.0
0.1	97.4	46.5

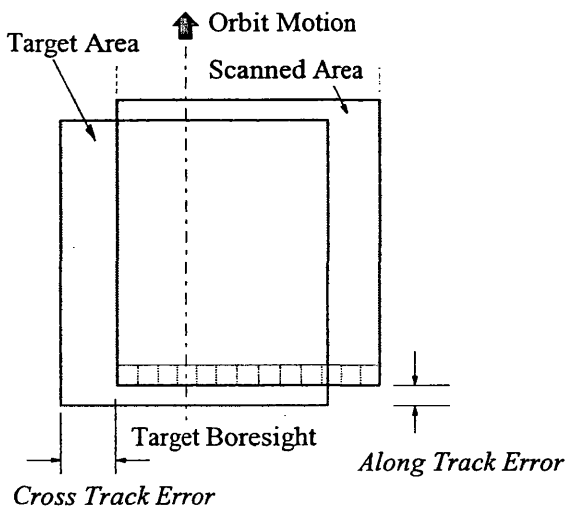

Figure 2-2 Scanned area offset due to attitude error

The error budgets can be analysed by breaking down possible error sources in detail. Table 2-3 shows the pointing error sources with respect to the spacecraft axes defined in Figure 2-7. The attitude control errors are the major contributor to the total system error when calculated by Root Sum Square (RSS) manner. Since MEIS is fabricated with a single-body-structured fused silica, the effects of thermal distortion are relatively small compared to other errors. The thermal effect has been neglected for the yaw axis, which is parallel to the optical axis. The attitude control parts include both attitude determination and control errors.

Table 2-3 Pointing error allocation

Axis	Error Source	Error (deg)	RSS Angular Error (deg)
Roll	Mounting knowledge	0.2	0.49
	Attitude control	0.45	
	Others	0.02	
Pitch	P/L to bus alignment knowledge	0.2	0.49
	Attitude control	0.45	
	Others	0.02	
Yaw	P/L to bus alignment knowledge	0.2	1.03
	Attitude control	1.0	
	Others	0.1	

The satellite pointing errors for the roll and pitch axes correspond to the cross and along track positioning errors respectively, as depicted in Figure 2-2. The cross track error is more important than the along track error. Considering other error sources such as GPS ephemeris error, the cross-track error is calculated in Table 2-4.

Table 2-4 Cross track error allocation

Cross track swath positioning error (km)	6.22
Cross track GPS ephemeris allocation (km)	0.5
Allowed cross track pointing offset (km)	7.16
Useful swath width (km)	35.5
System margin (km)	3.55

The swath positioning error is the RSS of all the roll error sources shown in Table 2-3. The GPS ephemeris allocation represents the orbital position error. Fifteen percent of target miss positioning with respect to the total swath width allows a cross track offset of 7.16 km. Comparing the allowed and allocated offset errors gives rise to the system margin of 3.55 km. This corresponds to 0.28° pointing error for the satellite. Therefore, the attitude control accuracy has enough system margin for 15 % of image positioning offset.

Unlike a staring or an area type CCD system, a linear pushbroom type remote sensing camera utilises the orbital motion of a platform for scanning. This has advantages in sensor uniformity and allows development of a wide swath system. However, it is more complicated than other types and it imposes harsh requirements on the attitude determination and control system. The analysis of the attitude stability is more complex than the pointing requirement case. Since it involves image quality assessment, the analysis can be characterised as a combination of an analytical and partly subjective reasoning process.

The stability requirement should be considered in a temporal sense. The oscillation or vibration effects on the platform can be subdivided into three different groups according to their nature. Low frequency vibration acts like a drift of the pointing accuracy and it corresponds to large-scale image distortion and localisation error. On the contrary, high frequency attitude movement causes image smearing. The limit of vibration frequency needs to be defined according to the exposure time of single CCD line. The mid-frequency vibration results in internal distortions of medium sized objects. The image distortion effects caused by the attitude instability during an imaging period are visualised in Figure 2-3. The actual effects are a combination of all the frequency components. We need to characterise and define requirements for each frequency band separately.

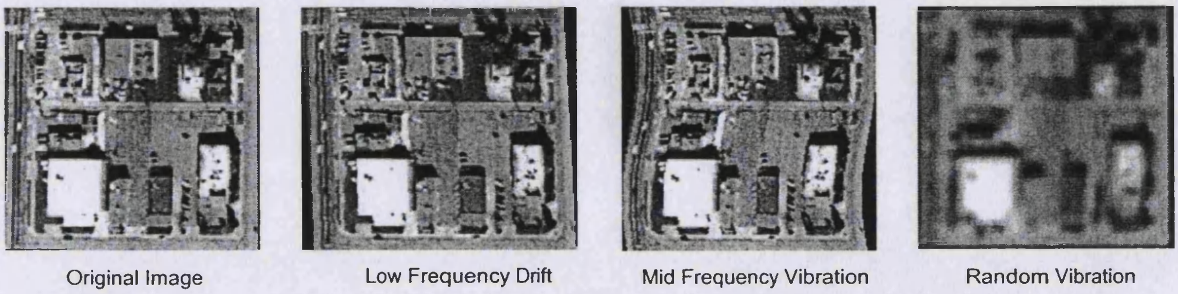

Figure 2-3 Effects of platform instability on linearly scanned images

For the analysis, we first need to derive some basic camera and orbit related parameters first. The circular orbital period P at altitude h can be found from a well known astrodynamic equation (Chetty, 1991). (The orbit parameters will be discussed in more detail in Section 2.3.1.)

$$P = 2\pi\sqrt{\frac{(R_e + h)^3}{\mu}} = 99.19 \text{ min} \tag{2-8}$$

, where μ is the Earth's gravitational constant, $3.986005 \times 10^{14}\ \text{m}^3/\text{sec}^2$.

The orbital velocity of a satellite V_o and the ground track velocity V_g, can both be obtained from the following relation:

$$V = \frac{2\pi r}{P} \tag{2-9}$$

, where r is $R_e + h$ for V_o and r is R_e for V_g, respectively. Therefore, the KITSAT-3 spacecraft will orbit the Earth with the velocity of $7.49\ \text{km/sec}$ and it sweeps the surface of the Earth at the rate of $6.73\ \text{km/sec}$.

A CCD pixel is allowed to integrate the signal and transfer the data to storage devices within a limited time $t_s = 2.05\ \text{msec}$.

$$t_s = \Delta / V_g \tag{2-10}$$

The boundary of the low frequency can be defined as 0.5 Hz, a quarter of the attitude sensor sampling rate 2 Hz, to account for recoverable image distortion only. Ground image processing can compensate slowly varying attitude errors based on the interpolation of the sensor measurements. Attitude movements faster than this frequency cannot be identified nor properly processed. The low frequency image deformation is not necessarily translated into the ADCS requirement. It is only related to the measurement system capability considering image reconstruction in ground processing. It implies that it is desirable but not mandatory.

We assumed that 5% of pixel-to-pixel error in the cross track direction is acceptable considering the proposed sensor capability and human perception of unprocessed raw image in this context. The error corresponds to a cross track error of 0.67 km for 13.5 km of along track scan. If it is converted into satellite pointing using an approximated form of Equations (2-1) ~ (2-5), the required attitude rate sensing capability is:

$$\tan^{-1}(0.67\ \text{km}/h)\ \text{rad}/2\ \text{sec} = 5.3\times10^{-2}\ \text{deg}/2\ \text{sec} \tag{2-11}$$

Mid-frequency vibrations are associated with internal deformations of small objects. We have assigned more stringent requirement than the low frequency case since they are irrecoverable. The effects of mid-frequency noise on the image quality are largely dependent on the texture of an image. The image quality is also a function of the vibration noise frequency. Precise analysis requires allocation of different requirements for each frequency in the spectrum. However, we can recognise, from the discussions in Chapter 6, that the sinusoidal vibration in the 20 ~ 80 Hz range is dominant. This originates from mechanically moving parts in the satellite such as the reaction wheels and the vibrating chopper in the Earth horizon sensor.

A ratio of 3% of along track versus cross track migration has been allocated as the requirement over 20 Hz range. It corresponds to the maximum bias of 0.75 pixels on 25 pixels length, which is equal to 10.1 m error on the ground. Therefore, the required attitude stability of the platform can be calculated from Equation (2-12).

$$\frac{\tan^{-1}(10.1\,\text{m}/h)}{t_s\times 25}\,\text{rad} = 8.0\times10^{-4}\ \text{deg}/0.05\,\text{sec} \tag{2-12}$$

So far we have only discussed the attitude stability requirements for low frequency attitude drift. However, high frequency attitude movements may also cause image smearing. Due to the loss of high frequency image information, the quality of an image degrades in terms of the contrast. The limit of vibration frequency needs to be defined according to the exposure time of single CCD line. The result in Equation (2-10) suggests that the scanning frequency is 487 Hz. Following the same argument as in the previous case, at the quarter of this frequency, ~120 Hz, smearing effect begins to emerge.

The effects of this kind of vibration can be assessed analytically in terms of the Modulation Transfer Function (MTF). It is a widely used concept to interpret image degradation in optical engineering with the following definition (Campana, 1993):

$$OTF(f) = \frac{\Im\{O(x)\}}{\Im\{\delta(x)\}} = \Im\{O(x)\} = MTF(f)e^{iPTF(f)} \tag{2-13}$$

, where Optical Transfer Function (OTF) is the impulse response of an optical system and MTF is the magnitude of OTF and Phase Transfer Function (PTF) is its phase.

$O(x)$ is the probability density function(PDF) of the output and $\delta(x)$ is an impulse function. $\Im\{\cdot\}$ is the Fourier transform operator for spatial frequency f, defined in a one dimensional case as

$$\Im\{O(x)\} = \int_{-\infty}^{\infty} O(x)e^{-2\pi ixf}dx \equiv \boldsymbol{O}(f) \tag{2-14}$$

A random vibration with a standard deviation σ, for example, has the following PDF

$$O_{rand}(x) = \frac{1}{\sigma\sqrt{2\pi}}e^{-x^2/2\sigma^2} \tag{2-15}$$

Therefore, the MTF reduction by a random vibration can be obtained by substituting Equation (2-15) into (2-14) and integrating it over the interval $[-\infty,+\infty]$.

$$MTF_{rand}(f) = e^{-2\pi^2\sigma^2 f^2} \tag{2-16}$$

However, a sinusoidal vibration with amplitude of A has the PDF as defined in Equation (2-17) over $[-A,+A]$

$$O_{sine}(x) = \frac{1}{\pi\sqrt{A^2 - x^2}} \tag{2-17}$$

MTF reductions by sinusoidal vibration with peak-to-peak deviation A is, therefore,

$$MTF_{sine} = \frac{1}{\pi}\int_0^{\pi}\cos(\pi Af\sin\theta)d\theta = J_o(\pi Af) \tag{2-18}$$

,where $J_o(x)$ is the Bessel function of the first kind of order zero.

The stability requirement in Equation (2-12) is for the roll rate. A pushbroom scanner is less sensitive to pitch rate error compared to a Time Delay Integration (TDI) type scanner (Holst, 1996). In this sense, the pitch and the yaw rate requirements are set to the same level for simplicity. The mean and peak-to-peak displacements due to random and sinusoidal vibrations are allocated as 4.5 % and 12.6% of the pixel's Instantaneous Field of View (IFOV) to meet the stability requirements. Table 2-5 is the stability error allocation for MEIS. The requirements are applicable for roll and pitch axes. Yaw axis requirement is much less stringent since yaw movement has compatibly small effects.

Table 2-5 High frequency rate stability requirement allocation (roll-pitch)

Mean : Random vibration (deg)	9.7×10^{-5} (>120Hz)
Peak-peak : Sinusoidal vibration (deg)	2.7×10^{-4} (>120Hz)
Require system MTF	0.10
Camera MTF	0.13
Attitude control requirement MTF	0.77
MTF reduction due to random vibration	0.92
MTF reduction due to sine vibration	0.92
MTF reduction due S/C motion	0.85
MTF system margin	0.90

The stability requirements for a remote sensing camera have been divided into three different cases: low frequency length alteration, mid-frequency distortion and high frequency smearing. The first category is the easiest part to eliminate by means of ground image processing with the attitude ancillary telemetry data from the sensors. The higher frequency part is difficult to estimate or reduce. Any attempt is very costly and this becomes an important restriction in designing a satellite for commercial or military quality remote sensing imaging. The uncontrollable frequency parts will be considered only for the error budgeting purpose.

During the Earth imaging mode, the pitch rate y'_o of the platform has to be synchronised with the orbital rate around the Earth. It can be directly obtained from the orbit period in Equation (2-8) as

$$-y'_o = 360° \,/\, P = 0.06 \text{ deg/sec} \tag{2-19}$$

KITSAT-3 is to be operated with a biased pitch rate of - 0.06 deg / sec while taking images, where the platform stability deviation has to be maintained within the previously specified error boundaries. As an example, Figure 2-4 shows typical attitude rate characteristics during the Earth imaging mode.

The pitch rate should be controlled to keep its mean value about - 0.06 deg / sec . The roll/yaw motions are mutually coupled with each other for a small angle model (Kim, 1991). The biased pitch rate error is assigned as the same level as the mid-frequency rate error requirement. The deviation is defined in 2σ uncertainty level. The probability or confidence level of the rate control is, therefore, 0.7385 for 3-axis (Wertz, 1978).

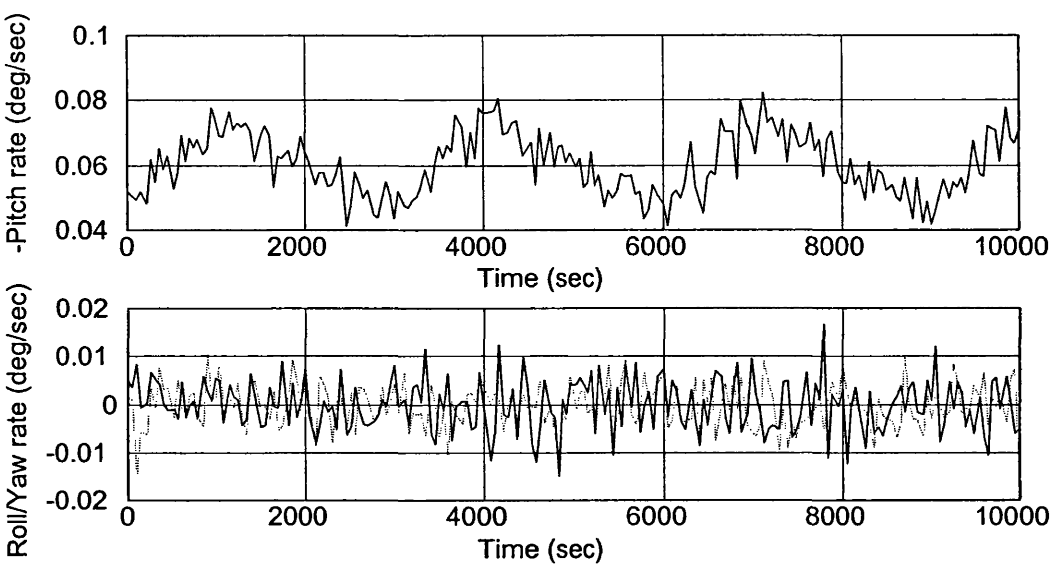

Figure 2-4 Attitude rate profile trends during the imaging mode

We can summarise the attitude stability requirements discussed so far as Table 2-6. Only the long term biased rate is controllable. The boundaries of the biased rate error are indicated. The low frequency noise requirement is reflected in determining the gyro performance. Mechanically induced noise in KITSAT-3 are modelled and analysed to verify the compliance of the requirements. Higher frequency noise will not be discussed since it is out of the capability of the attitude control system. We should note that the analyses have been performed for roll. The pitch and the yaw requirements are assumed as the same level as that of the roll. We have, in fact, large margins for the yaw pointing and stability.

Table 2-6 Camera platform stability requirements

Description	Frequency (Hz)	Requirement
Biased rate (Controllable)	~ 0	
Pitch		-0.06 ±0.016 deg/sec
Roll / Yaw		±0.016 deg/sec
Low frequency (Measurable)	$0 \sim 0.5$	5.3×10^{-2} deg/ 2 sec
Mid frequency sinusoidal vibration	$0.5 \sim 120$	8.0×10^{-4} deg/ 0.05 sec
High frequency		
Mean : Random vibration	>120	9.7×10^{-5} deg
Peak-peak : Sinusoidal vibration	>120	2.7×10^{-4} deg

2.1.3 Science Payload Requirements

The HEPT instrument requested a special operation scheme. We need to measure the pitch angle α of the incident particles. The definition of α is different from the pitch axis defined in Figure 2-7. Takaki (1994) defined α as the angle between the magnetic field vector and the velocity vector of the incoming particles. Figure 2-5 depicts the particle-magnetic field relation in the satellite body fixed frame *xyz*.

The pitch angle α can be obtained from the right spherical triangle formed by ϕ, $\pi/2-\theta$, and α. From spherical trigonometric relation (Larson, 1992),

$$\cos\alpha = \cos(\pi/2-\theta)\cos\phi = \sin\theta\cos\phi \tag{2-20}$$

The components of the magnetic field can be found from Figure 2-5 as

$$\begin{aligned} B_x &= B\sin\theta\sin\varphi \\ B_y &= B\cos\theta \\ B_z &= B\sin\theta\cos\varphi \end{aligned} \tag{2-21}$$

,where B is the magnitude of the magnetic field vector $\vec{B}$.

The angles, θ and φ, can be calculated from observed magnetic field vector in the satellite body frame.

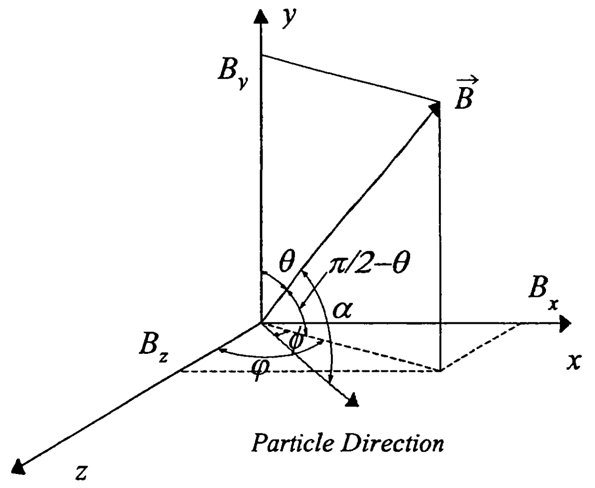

Figure 2-5 Definition of pitch angle α

$$\theta = \cos^{-1}\left(\frac{B_y}{B}\right)$$
$$\varphi = \cos^{-1}\left(\frac{B_z}{B\sin\theta}\right) \tag{2-22}$$

Since the particle telescope is mechanically fixed along the +*z* axis, we can only observe particles from that direction. Thus, it simplifies the angular relation as

$$\phi = \varphi \tag{2-23}$$

Therefore, the pitch angle α is from Equation (2-20) and (2-22).

$$\cos\alpha = \sin\theta\cos\varphi$$
$$\alpha = \cos^{-1}(\sin\theta\cos\varphi) \tag{2-24}$$

Charged particles are trapped by the Earth's magnetic field. Their basic motion is circular, with a superimposed longitudinal drift around the Earth, and a latitudinal reflection or bounce between mirror points (Tascione, 1988). As the particles move closer to the mirror points, the gyrating motion becomes perpendicular to the field line. Then we can assume that it is confined to the geomagnetic field. By measuring the pitch angle and the energy band of the incoming particles, we can obtain further information concerning their dynamic processes.

The pitch angle distribution measurement results from the OHZORA satellite showed that most of the trapped particle population was near 90° of pitch angle (Kohno *et al.*, 1990). This suggests that the mirror points are closely located around the operating orbit region, a perigee of 350 km and an apogee of 850 km with an inclination of 75°. Miah, (1991 and 1992) suggests that we maximise the observation opportunity of the highly confined particles by providing attitude rotation.

We can simulate the pitch angle distribution with various spin rates. Figure 2-6 shows typical distribution characteristics of the observed particles if the particles are uniformly distributed. The *y* axis is rotated with the period of 300 and 0 seconds whilst it is fixed to the orbit normal inertial direction in the simulation. Highly confined particles have more opportunities to be observed by rotating the satellite around the *y*-axis. However, the advantage is relatively small than because the rotation axis is almost perpendicular to the magnetic field vector. The geomagnetic field is modelled as a dipole system in this simulation (Refer 3.3).

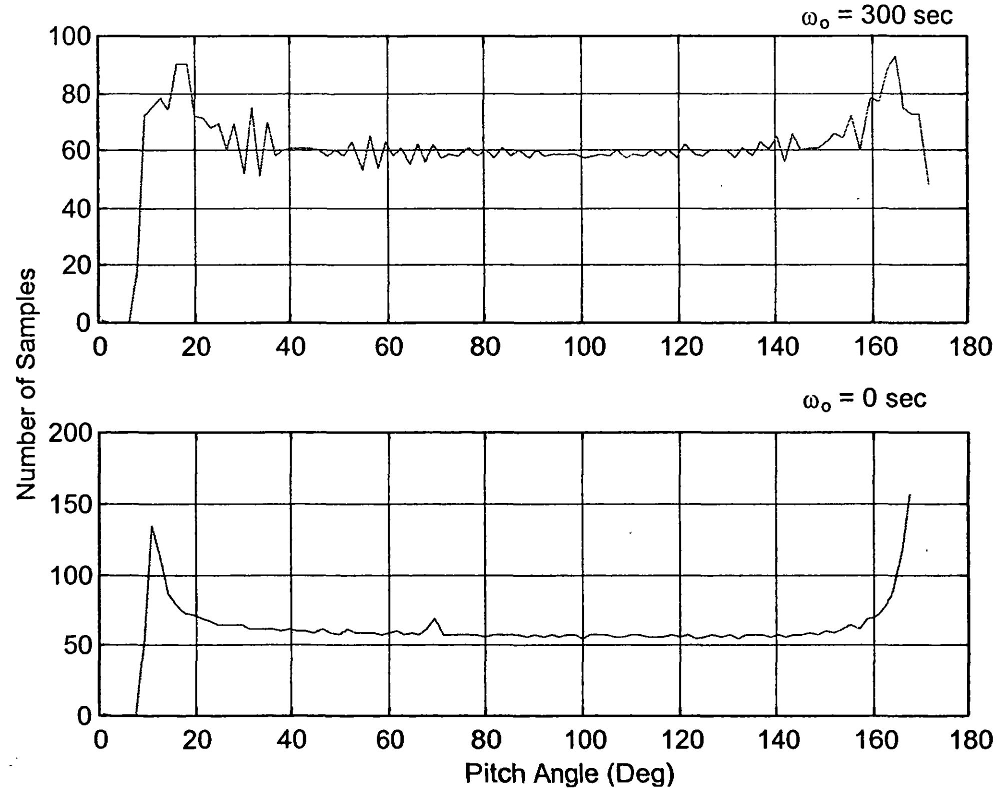

Figure 2-6 Pitch angle distributions

HEPT has the best performance if the rotation axis is parallel to the magnetic field line in terms of the number of chances to detect highly confined particles. Due to the limitation of the ADCS, only the pitch axis manoeuvre is considered even though it has less efficiency for the HEPT experiment. The guaranteed minimum rate that the attitude control system can provide is 1 revolution /300 sec.

While the satellite is in this operation mode the absolute accuracy of the pitch rate is not important. The nutation effect is also negligible. However, the SMAG data must be precisely measured for ground data processing. Accurate attitude analysis will be performed in Chapter 7.

Table 2-7 Rotation control requirements for HEPT

Pitch rotation period (sec/revolution)	~ 300
Direction of rotation	Orbit normal
Pitch rate accuracy	N/A
Roll, yaw angle error	N/A

2.2 Operational Modes

2.2.1 Overview

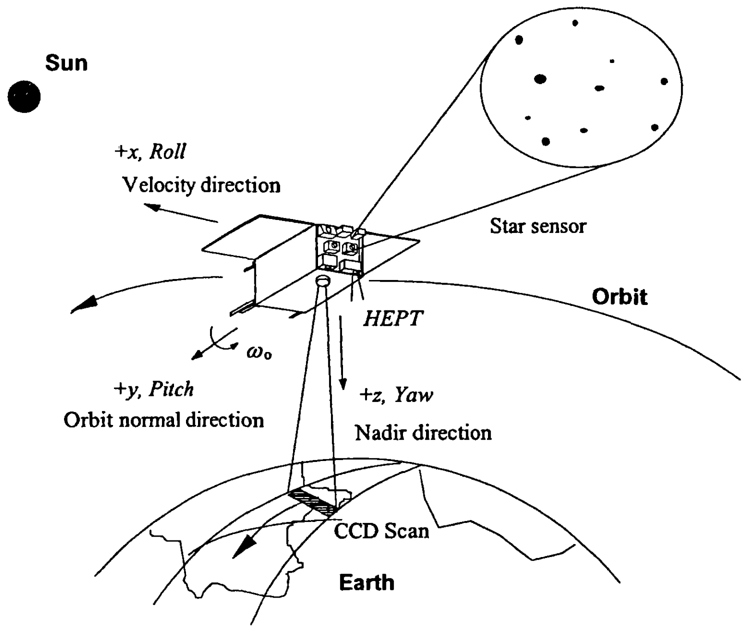

Figure 2-7 KITSAT-3 orbit operation

Figure 2-7 illustrates the operation of KITSAT-3. The body-referenced coordinate system, *xyz,* is shown with the orbital coordinate roll, pitch and yaw system. The roll axis is defined as the orbit velocity direction. The yaw axis is to the nadir direction. The pitch axis is defined to be normal to the orbit direction to complete a right hand rectangular coordinate system. The two coordinate systems in Figure 2-7 are perfectly matched when the satellite is ideally controlled during nadir pointing mode. It should be noted that the pitch rate is $y' = -\omega_o$, where ω_o is the mean motion of the satellite orbit. Equation (2-19) can be rewritten according to the definition in Figure 2-7.

$$y_o' = -360^\circ / P = -\omega_o = -0.06 \text{ deg/sec} \tag{2-25}$$

The other two axes should remain quiescent while the pitch rate is synchronised with the orbital rate given in Equation (2-25). Therefore, it is true, as far as nadir pointing is concerned, a single biased momentum wheel system can support the mission. This fact is considered in the reaction wheel configuration in Chapter 4.

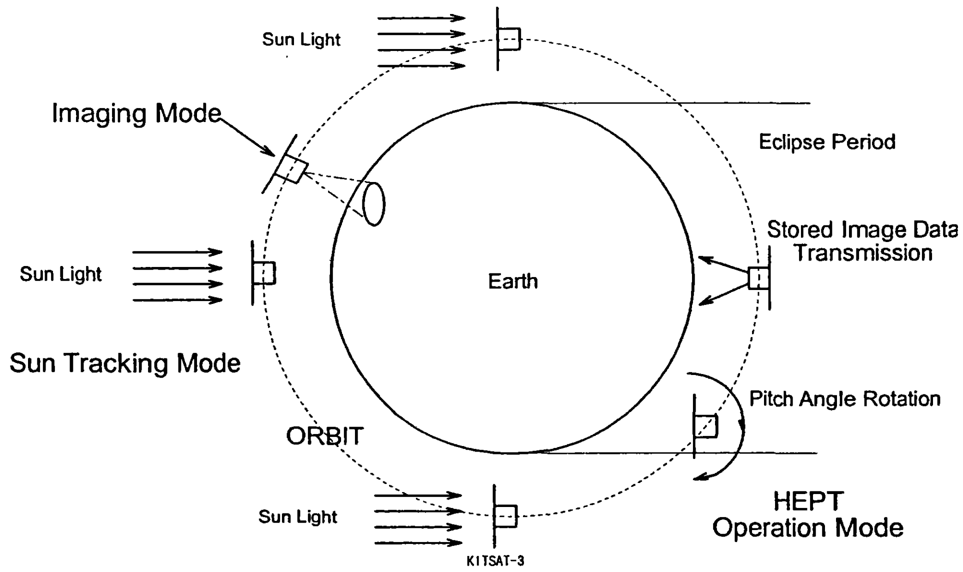

Figure 2-8 Operational modes

2.2.2 Sun Tracking Mode

The Sun tracking mode is the fundamental operational mode and, as such, should be designed with high reliability. The deployed solar panel configuration is vulnerable to attitude loss in terms of power generation. While the satellite is in idle operation, it should point toward the Sun as default. The battery units need to be charged during that time. At the beginning of the mission analysis, the design baseline was having roll tilting of 22.5° based for an orbit of 10:30 am local Sun time. If the satellite tilts γ about the x axis to get the best sun incident angle, then:

$$\gamma = \frac{360^\circ}{24\ \text{hr}} \times 1.5\ \text{hr} = 22.5^\circ \tag{2-26}$$

, where 1.5 hr comes from the local Sun time.

For instance, zero γ angle implies 22.5° sun incident angle, which results in solar power loss of

$$\text{Power Loss} = 1 - \cos\gamma = 8\ \% \tag{2-27}$$

To minimise this loss the satellite should have a constant roll angle offset $\gamma = 22.5^\circ$. Otherwise, 8% loss of solar power is inevitable.

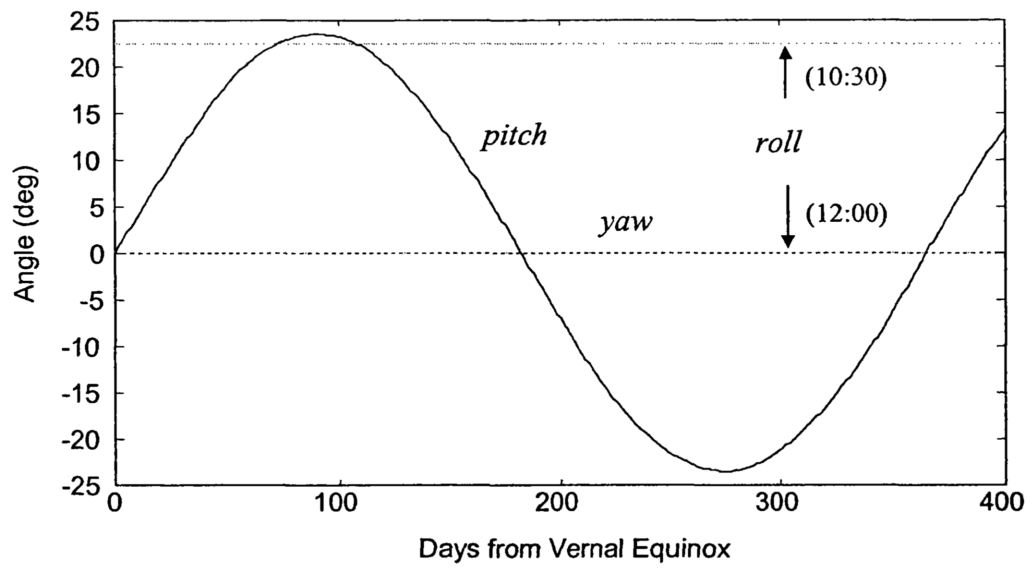

Figure 2-9 Optimised Sun tracking angle

The Earth rotation axis tilt $\tau = 23.5^{\circ}$ with respect to the normal vector of the ecliptic plane causes a seasonal change in the Sun angle. The pitch axis also has to be controlled to track this motion. The pitch angle offset is zero when it passes over the equator at the equinoxes. To get the maximum Sun power, the attitude needs to be stabilised according to the change of the Sun angle. Only the pitch angle shows an annual cycle as depicted in Figure 2-9.

The starting day in Figure 2-9 is referred to the vernal equinox. The pitch angle follows a sinusoidal curve, increasing as the summer solstice approaches. The spacecraft will keep the attitude described in the figure for most of the time. When an imaging mode is required, a relatively short excursion will be made from the curve. We should note that without the roll control capability, solar power loss is 8% as shown in Equation (2-27). However, the loss of seasonal pitch control will cause maximum 15.3 % power reduction at the solstices if the roll axis is uncontrolled at the same time.

$$\text{Power Loss} = 1 - \cos\gamma \times \cos\tau = 15.3\ \% \tag{2-28}$$

Fortunately, the proposed PSLV orbit is 12:00 a.m. as shown in Table 2-1. Therefore, the roll control is not required to maximise the solar power, which simplifies the attitude control requirement of the Sun tracking mode. The coarse Sun tracking mode allows $\pm$ 8° of pointing error, which corresponds to just 1% of solar power loss.

2.2.3 Earth Imaging Mode

As defined in Section 2.1.2, KITSAT-3 is to operate with a constant pitch rate of $-0.06\ \mathrm{deg/sec}$ during the Earth imaging mode, where the platform stability deviation has to be maintained within $0.016\ \mathrm{deg/sec}$ from the nominal pitch rate in the mid-frequency case. Star sensor information provides accuracy of 1 arc minute for this mode. Gyros are be used as inertial sensors to detect the angular rate for manoeuvring and stabilisation. In case of gyro failure, it is possible to utilise star sensor data to calculate the angular velocity (Renner *et al.*, 1993).

It is a challenging requirement for the ADCS system to quickly change the operational mode from the Sun tracking to Earth imaging mode. Large angle manoeuvring is necessary, which requires non-linear system modelling and control. The size of angle depends on the location of ground targets and the seasonal change of the pitch attitude shown in Figure 2-9. Rotation of 22.5° about the roll axis is also required simultaneously with the pitch manoeuvre for the initial orbit parameters in Table 2-1. However, the final orbit parameters require only the pitch control.

2.2.4 Science Payload Operational Mode

The HEPT requires a rotation about the pitch axis with a period of ~ 300 seconds as discussed in Section 2.1.3. Neither the absolute rotation period nor the rotation axis requirements are specifically imposed since only the magnetometer information is critical for the experiment. The maximum rotation rate is dependent on the initial speed of the pitch axis reaction wheel. By using two pitch wheels at the same time, we can increase the rotation speed of the satellite body. Assuming that the nominal rotation speed of the pitch wheel is 2000 rpm and 4000 rpm is the maximum wheel rotation speed allowance, we can always obtain the spacecraft rotation period of ~300 sec.

The analysis results in Figure 2-6 and Chapter 7 conclude that the pitch spinning control is not as effective as expected at the early mission planning stage. Power loss is critical for this operational mode. Instead of the pitch rotation, normal Sun tracking attitude will be maintained in this reason.

2.2.5 Safe-Hold Mode

Safe-hold mode is defined as an emergency operational mode. Not only the payload operation is prohibited during this mode but also a minimum set of satellite bus systems will be turned on. The reaction wheel system will control the satellite with the use of the sun sensor and magnetometer only. The satellite will be rotated about its y-axis in the originally planed science payload operational mode. Occasional monitoring of the Sun vector will be performed automatically on-board to avoid zero solar energy incidents. Internal or external OBC reset will trigger this operational mode for safety management. Analysis in Chapter 7 showed that there is no significant distinction between the safe-hold and HEPT operational mode as far as the control dynamics is concerned.

2.2.6 *Initial Operational Mode*

The fourth stage of the launch vehicle provides adequate separation sequences for its payload satellites, IRS-P4, KITSAT-3 and DRL-TUBSAT. The analysis results for the orbit injection give 2 ~ 7 °/sec of lateral rotation rate (Antrix, 1998). Even the best estimate does not guarantee us immediate stabilisation of the attitude by using the reaction wheels since the angular momentum storage capacity of the wheels is less than the injection angular momentum.

Magnetorquers will be used together with the magnetometer to generate torque for the reduction of satellite angular momentum. When the rotation rate is less than 0.5 °/sec in all axes, the satellite will operate the reaction wheels to capture its attitude by ground command. Detailed discussions on this subject are presented in Chapter 7. The ground operator will send the solar panel deployment command if it is judged safe. This operational mode is for one time use only.

2.3 Orbit Analysis

2.3.1 *Orbital Parameters*

We need at least 6 orbital parameters to specifically define a position of an Earth-orbiting-satellite with a given epoch time as shown in Figure 2-10 (Wertz, 1978 and Sidi, 1997). Two parameters can specify the shape of the ellipse; semi-major axis and eccentricity are commonly used. A time of flight related parameter is required to define the position of the satellite on the circumference of the ellipse. We also need 3 parameters to describe the orientation of the orbital plane with respect to the Vernal equinox and the ascending node of the orbit defined on the Earth's equatorial plane. These 3 parameters are inclination, argument of perigee and the right ascension of the ascending node.

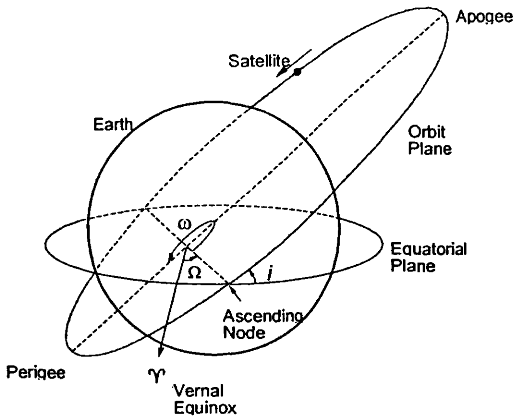

Figure 2-10 Orbit parameter definitions

The proposed orbit related parameters by the PSLV are summarised in Table 2-8 and Table 2-9. The numbers are only tentative and should be revised after launch.

Table 2-8 Orbital parameters

Semi-major axis	7099.809 km
Eccentricity	0.000143
Inclination	98.374 deg
Argument of perigee	10.097 deg
Right ascension of ascending node	184.655 deg
Mean Anomaly	200.723 deg

Table 2-9 Injection parameters

Time	1081.8 sec
Altitude	728.179 km
Velocity	7.49224 km/s
Inclination	98.374 deg
Flight path angle	0.0001 deg
Velocity azimuth	189.74 deg
Latitude	-30.744 deg
Longitude	75.387 deg

2.3.2 Orbit Characteristics

The altitude and inclination values in Table 2-1 suggest that the orbit is a sun-synchronous one, where the satellite orbit plane remains approximately fixed with respect to the Sun vector. The property comes mainly from the oblate shape of the Earth. The nodal regression phenomenon known as the J_2 effect is given in Equation (2-29) (Wertz, 1978)

$$\dot{\Omega}_{J_2} = -2.06474 \times 10^{14} a^{-3.5} \cos i (1 - e^2)^{-2} \tag{2-29}$$

For the given nominal altitude and inclination, the nodal regression rate is $\dot{\Omega}_{J_2} = 0.9856 \text{ deg/day}$, which corresponds to 360 deg / 365 days. However, the orbit injection errors of the PSLV, in worst case, are expected to be ±35 km in altitude and ±0.2 degree in inclination according to the contract specifications. Table 2-10 sums up the analysis results of the local Sun angle drift that may be caused by the obit injection error over the 3 years of designed lifetime.

Since KITSAT-3 doesn't have a propulsion system for orbit maintenance, the error will eventually affect the attitude control system. The results show that the error boundaries of ±20 km in altitude and ±0.1 degree in inclination are acceptable in view of the previous mission analysis results. In fact, the error boundary is expected to be less than the worst case values in fact. If the actual injection error is larger than the launch specifications, two-axis control is required to fulfil the operational modes as depicted in Figure 2-8.

Table 2-10 Sun angle drift due to orbit injection error

	Deviation angle from Sun-synchronous in 3 years (deg)				
Altitude (km)	Inclination (deg)				
	98.08	98.18	98.28	98.38	98.48
685	-6.91	6.28	19.47	32.65	45.83
700	-14.85	-1.76	11.33	24.42	37.50
720	-25.32	-12.35	0.61	13.57	26.52
740	-35.65	-22.82	-9.98	2.85	15.68
755	-43.32	-30.58	-17.84	-5.10	7.64

2.3.3 Ground Tracks & Attitude Repositioning

Satellite ground track is defined as the trace of the sub-satellite points defined in Figure 2-1. The analysis of this pattern is highly sensitive to the exact orbit parameters (Light, 1990). At the proposed nominal altitude and inclination, it is likely that the number of orbits per day is close to 14.5. Since the orbit parameter errors are too large to execute a precise orbit analysis, it is more reasonable to focus on potential problems that may arise from the proposed orbit injection error.

If the ground track pattern repeats after an integer number of days, it is called a Repeating Ground Trace (RGT). This type of orbit is widely used for remote sensing satellites where regular service is an important issue. It has both pros and cons at the same time in terms of KITSAT-3 operation. Depending on the initial orbit parameters, the remote sensing opportunity for the Korean peninsular widely varies. The situation is illustrated well in the simulated ground tracks in Figure 2-11.

It is simulated for 18 days with 720 km altitude and 98.28° inclination. The adjacent group of paths N_{th} and $N+1_{st}$, are intersected by $N+15_{th}$ path group with one day gap. If the number of orbits per day approaches 14.5, the closeness between the minor patterns gets smaller. If there is a large gap between the major patterns, a continuous coverage over a specific region is guaranteed over a long period.

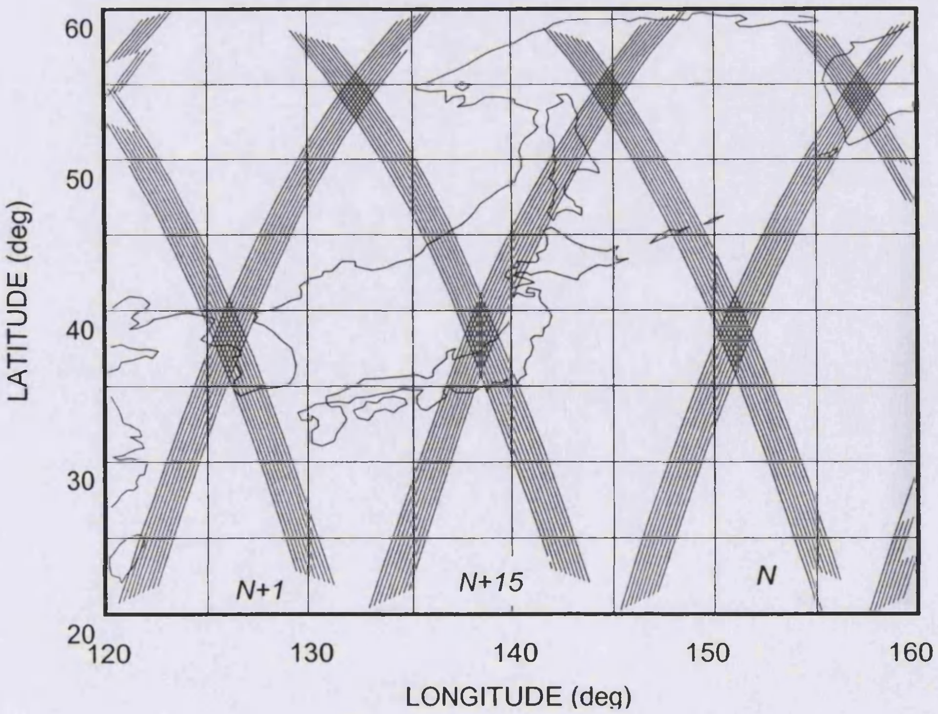

Figure 2-11 Ground tracks over 18 days

The analysis related with the revisiting time gap is extremely sensitive to the orbital parameters. The actual orbit elements have significant impact on the operational aspects. It also should be noted that the ascending paths are not useful since they are on the night side.

An exact RGT orbit is troublesome in the ADCS point of view. If the initial injection places the satellite to produce an exact RGT pattern, we have to provide a roll tilting mechanism for off-nadir pointing. The average longitudinal distance between the N_{th} and the $N+15_{th}$ path groups is approximately 16° near the regions of the latitude 40N. The corresponding angular distance measured at the centre of the Earth is, therefore

$$\lambda = 16^\circ \cos 40^\circ = 12.26^\circ \tag{2-30}$$

The required roll angle for full coverage of the Earth is obtained from Figure 2-1 and Equation (2-2). Considering the FOV of MEIS, 3.8°, effective Earth central angle λ becomes (12.26-3.8)/2=8.46°. Thus, the required roll angle η can be calculated using the angular radius of the Earth in Equation (2-1).

$$\eta = \tan^{-1}\left(\frac{\sin\rho\sin\lambda}{1-\sin\rho\cos\lambda}\right) = 49.9^\circ \tag{2-31}$$

Star sensors on the top of the platform cannot be used in this situation due to the lights from the Sun and the Earth. The result implies that roll manoeuvres are not recommended in this situation. Coarse control scheme using gyro system only is possible if the final orbit is too close to an RGT.

2.4 Mechanical Properties

The mechanical properties of a satellite summarised in Table 2-11 are important not only for launch constraints but also for designing and analysis of the ADCS. The table is based on a finite element model (FEM) of approximately 7000 nodes. The total mass excludes the launch adapter supplied by PSLV. The reference coordinate for the Centre of Gravity (CG) offsets is located on the geometrical centre of the bottom plane of the battery box.

Table 2-11 Mechanical properties of the satellite

	Solar panel stowed	Solar panel deployed
Mass (kg)	104.67	104.67
Size (mm)	623.6×818.5×495	1496.9×818.5×474
CG point offsets (mm)	0.04×-300.4×-0.02	0.1×-300.4×-13.1
Inertia tensor (kg·m^2)	$\begin{bmatrix} 6.78 & -0.035 & 0.014 \\ -0.035 & 4.68 & 0.027 \\ 0.014 & 0.027 & 6.91 \end{bmatrix}$	$\begin{bmatrix} 7.10 & -0.043 & -0.017 \\ -0.043 & 5.84 & 0.017 \\ -0.017 & 0.017 & 8.16 \end{bmatrix}$

The inertia tensor is from the moments and the products of inertia (MoI) of the satellite, which will be discussed in Chapter 3.1. The locations of the CG points are supposed to be within ±1 mm to meet the launch requirement. The MoI estimation or even a direct measurement will contain ±5% of error.

Chapter 3. Attitude Control Theory

3.1 Spacecraft Attitude Dynamics

3.1.1 Angular Momentum of a Rigid Body

The attitude motion of a rigid body spacecraft can be regarded as the motions of a group of infinitesimal masses that are bounded as one body. Generally, flexibility modelling is required when the size of a spacecraft gets large or long appendages are attached. Since KITSAT-3 is small sized and has relatively stiff solar panel deployment mechanism, the attitude motion can be modelled based on a rigid body assumption.

If we begin with a point mass m in Figure 3-1, the linear momentum $\vec{p}$ of m is given in Equation (3-1).

$$\vec{p} = m\dot{\vec{R}} \tag{3-1}$$

The angular momentum $\vec{h}_o$ about an arbitrary reference point O is

$$\vec{h}_o = \vec{r} \times m\dot{\vec{R}} \tag{3-2}$$

$\vec{R}$ and $\vec{r}$ are defined as the vector distance to m from the inertial reference point O' and an arbitrary reference point O, respectively.

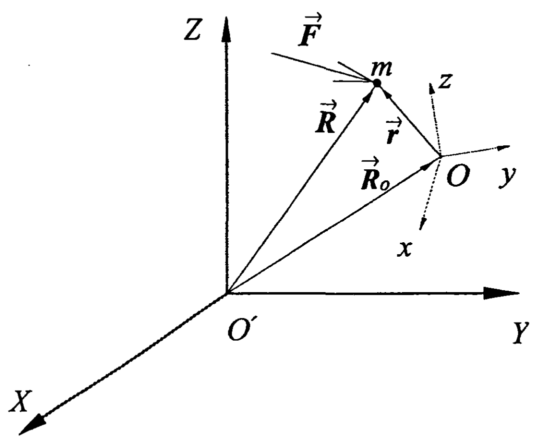

Figure 3-1 The motion of a point mass

Equation (3-2) becomes Equation (3-3), considering $\vec{R} = \vec{r} + \vec{R}_o$.

$$\vec{h}_o = \vec{r} \times m\dot{\vec{r}} + \vec{r} \times m\dot{\vec{R}}_o \tag{3-3}$$

The moment of a force $\vec{F}$ about the origin *O*, i.e. the torque $\vec{T}_o$, acting on the mass *m* can be expressed as

$$\vec{T}_o = \vec{r} \times \vec{F} = \vec{r} \times m\ddot{\vec{R}} = \vec{r} \times m(\ddot{\vec{R}}_o + \ddot{\vec{r}}) \tag{3-4}$$

Equation (3-4) can further be developed in derivative form if we recall that the cross product of two identical vectors is $\vec{0}$.

$$\vec{T}_o = \frac{d}{dt}(\vec{r} \times m\dot{\vec{r}}) - \ddot{\vec{R}}_o \times m\vec{r} \tag{3-5}$$

If we take the time derivative of Equation (3-3), the rate of change of $\vec{h}_o$ is

$$\dot{\vec{h}}_o = \frac{d}{dt}(\vec{r} \times m\dot{\vec{r}}) - \ddot{\vec{R}}_o \times m\vec{r} - \dot{\vec{R}}_o \times m\dot{\vec{r}} \tag{3-6}$$

Comparing Equation (3-5) and (3-6) gives

$$\vec{T}_o = \dot{\vec{h}}_o + \dot{\vec{R}}_o \times m\dot{\vec{r}} \tag{3-7}$$

If *m* is a part of a rigid body, $\vec{r}$ is a constant referring to an arbitrary origin *O*. Therefore, Equation (3-7) can be simplified as

$$\vec{T}_o = \dot{\vec{h}}_o \tag{3-8}$$

Equation (3-8) will be used to derive the attitude dynamics of a rigid body spacecraft. It should be noted that with the absence of external torque $\vec{T}_o$, the angular momentum $\vec{h}_o$ is conserved. The time derivative of an arbitrary position vector $\vec{r}$ in a rotating frame is given in terms of the angular velocity $\vec{\omega}$ of the rotating frame *xyz* and the relative velocity vector $\vec{v}_{rel}$ of $\vec{r}$ with respect to the origin (Riley & Sturges, 1993).

$$\dot{\vec{r}} = \vec{v}_{rel} + \vec{\omega} \times \vec{r} \tag{3-9}$$

$\vec{v}_{rel}$ is $\vec{0}$ under the rigid body assumption since a point in a rigid body does not have relative motion about the body fixed coordinate. Therefore, the absolute velocity of m with respect to the inertial frame XYZ is

$$\dot{\vec{R}} = \dot{\vec{R}}_o + \dot{\vec{r}} = \dot{\vec{R}}_o + \vec{\omega} \times \vec{r} \tag{3-10}$$

We can extend the above study where only one point mass is considered to a group of small masses m_i. Equation (3-2) can directly be applied to obtain the angular momentum of m_i about O, where O is chosen as the centre of mass of a rigid body.

$$\vec{h}_{oi} = \vec{r}_i \times m_i \dot{\vec{R}}_i = \vec{r}_i \times m_i (\dot{\vec{R}}_o + \vec{\omega} \times \vec{r}_i) \tag{3-11}$$

To get the total angular momentum about the centre of mass O, Equation (3-11) has to be summed up as

$$\vec{h}_o = \sum_i \vec{h}_{oi} = \sum_i \vec{r}_i \times m_i (\dot{\vec{R}}_o + \vec{\omega} \times \vec{r}_i) = \sum_i m_i \vec{r}_i \times (\vec{\omega} \times \vec{r}_i) - \dot{\vec{R}}_o \times \sum_i m_i \vec{r}_i \tag{3-12}$$

The last term in Equation (3-12) is 0 since O is taken as the centre of mass of a rigid body B. We can rewrite Equation (3-12) by assuming infinitesimal mass elements dm.

$$\vec{h}_o = \int_B \vec{r} \times (\vec{\omega} \times \vec{r}) dm \tag{3-13}$$

We need to express $\vec{r}$ and $\vec{\omega}$ in terms of the xyz coordinate.

$$\begin{aligned} \vec{r} &= x\vec{i} + y\vec{j} + z\vec{k} \\ \vec{\omega} &= \omega_x \vec{i} + \omega_y \vec{j} + \omega_z \vec{k} \end{aligned} \tag{3-14}$$

, where $\vec{i}$, $\vec{j}$, and $\vec{k}$ are the unit vectors along the x, y, and z axes, respectively.

The integrand of Equation (3-13) can be written using Equation (3-14) as

$$\begin{aligned} \vec{r} \times (\vec{\omega} \times \vec{r}) = & [\omega_x (y^2 + z^2) - \omega_y (xy) - \omega_z (xz)]\vec{i} \\ & + [-\omega_x (xy) + \omega_y (x^2 + z^2) - \omega_z (yz)]\vec{j} \\ & + [-\omega_x (xz) - \omega_y (yz) + \omega_z (x^2 + y^2)]\vec{k} \end{aligned} \tag{3-15}$$

The integration of Equation (3-15) can be obtained using the definition of *moments of inertia* in classical mechanics.

$$
\begin{aligned}
I_x &= \int_B (y^2 + z^2) dm, \quad & I_y &= \int_B (x^2 + z^2) dm, \quad & I_y &= \int_B (x^2 + y^2) dm \\
I_{xy} &= \int_B (xy) dm, & I_{xz} &= \int_B (xz) dm, & I_{yz} &= \int_B (yz) dm
\end{aligned}
\tag{3-16}
$$

Utilising Equation (3-16), we can simplify the angular momentum equation in terms of inertia tensor $\boldsymbol{I}$. (Vector and matrix expressions are mixed for convenience.)

$$
\vec{\boldsymbol{h}}_o = \vec{\boldsymbol{h}} = \begin{bmatrix} h_x \\ h_y \\ h_z \end{bmatrix} = \begin{bmatrix} I_x & -I_{xy} & -I_{xz} \\ -I_{xy} & I_y & -I_{yz} \\ -I_{xz} & -I_{yz} & I_z \end{bmatrix} \begin{bmatrix} \omega_x \\ \omega_y \\ \omega_z \end{bmatrix} = \boldsymbol{I\omega} \tag{3-17}
$$

Equation (3-8) and (3-17) can be combined with a torque $\vec{\boldsymbol{T}}$ applied about the centre of mass. Equation (3-9) is also applicable in calculating the absolute rate of $\vec{\boldsymbol{h}}$.

$$
\vec{\boldsymbol{T}} = \frac{d\vec{\boldsymbol{h}}}{dt} = \dot{\vec{\boldsymbol{h}}}_{rel} + \vec{\omega} \times \vec{\boldsymbol{h}} \tag{3-18}
$$

The torque components of $\vec{\boldsymbol{T}}$ can be expressed by expanding Equation (3-18).

$$
\begin{aligned}
T_x &= \dot{h}_x + \omega_y h_z - \omega_z h_y \\
T_y &= \dot{h}_y + \omega_z h_x - \omega_x h_z \\
T_z &= \dot{h}_z + \omega_x h_y - \omega_y h_x
\end{aligned}
\tag{3-19}
$$

Equation (3-19) is known as *Euler's equation*. It will be used as the fundamental equation describing the attitude motion of a spacecraft throughout this paper.

3.1.2 KITSAT-3 Attitude Dynamics

Equation (3-19) has been derived for a rigid body satellite. Mechanically moving parts were not considered in the dynamic equation. We need to consider the angular momentum originated from the reaction wheel system for the complete attitude dynamic equation. When the reaction wheels are stationary the attitude motion of a rigid body satellite can be described by Euler's equation. If it is written about the principal axes x, y and z, Equation (3-19) becomes more comprehensible.

$$\begin{aligned} I_x\omega_x' + \omega_y\omega_z(I_z - I_y) &= T_x \\ I_y\omega_y' + \omega_x\omega_z(I_x - I_z) &= T_y \\ I_z\omega_z' + \omega_x\omega_y(I_y - I_x) &= T_z \end{aligned} \tag{3-20}$$

Three identical reaction wheels located along the principle axes affect the attitude motion. Each wheel has a moment of inertia of $I_w = 2.39 \times 10^{-4}\ \mathrm{kg \cdot m^2}$. If we let the angular speeds of the wheels be Ω_x, Ω_y, and Ω_z along the x, y, and z axes respectively, the effect of the angular momentum vector derivative in Equation (3-18) by the reaction wheel system is

$$\begin{aligned} \vec{h}_w' &= I_w(\Omega_x\vec{i} + \Omega_y\vec{j} + \Omega_z\vec{k})' \\ &= I_w\left[\Omega_x(-\omega_y\vec{k} + \omega_z\vec{j}) + \Omega_y(\omega_x\vec{k} - \omega_z\vec{i}) + \Omega_z(-\omega_x\vec{j} + \omega_y\vec{i}) + \Omega_x'\vec{i} + \Omega_y'\vec{j} + \Omega_z'\vec{k}\right] \end{aligned} \tag{3-21}$$

The complete attitude motion equation is obtained by expanding Equation (3-21) using the vector relation in (3-9) then substitute it into (3-18).

$$\begin{aligned} I_x\omega_x' + \omega_y\omega_z(I_z - I_y) + I_w(\Omega_z\omega_y - \Omega_y\omega_z + \Omega_x') &= T_x \\ I_y\omega_y' + \omega_x\omega_z(I_x - I_z) + I_w(\Omega_x\omega_z - \Omega_z\omega_x + \Omega_y') &= T_y \\ I_z\omega_z' + \omega_x\omega_y(I_y - I_x) + I_w(\Omega_y\omega_x - \Omega_x\omega_y + \Omega_z') &= T_z \end{aligned} \tag{3-22}$$

The dynamic equation can also be expressed in terms of the angular momentum vector, which is more convenient for simulation. We need to separate the angular momentum components of the reaction wheel, $\vec{h}_w$, and the satellite body, $\vec{h}_s$. Equation (3-18) can be transformed as

$$\vec{T} = \dot{\vec{h}}_s + \dot{\vec{h}}_w + \vec{\omega} \times (\vec{h}_s + \vec{h}_w) \tag{3-23}$$

, where $\dot{\vec{h}}_w$ implies the reaction wheel torque, $\vec{\omega}$ is the satellite body rate about its body axes. $\vec{\omega}$ can be simply calculated from $\omega = I^{-1}h_s$. Figure 3-2 is the basic structure of the dynamic simulation using Matlab Simulink®. Angular velocity comes directly from angular momentum and the angle calculation is discussed in Section 3.2

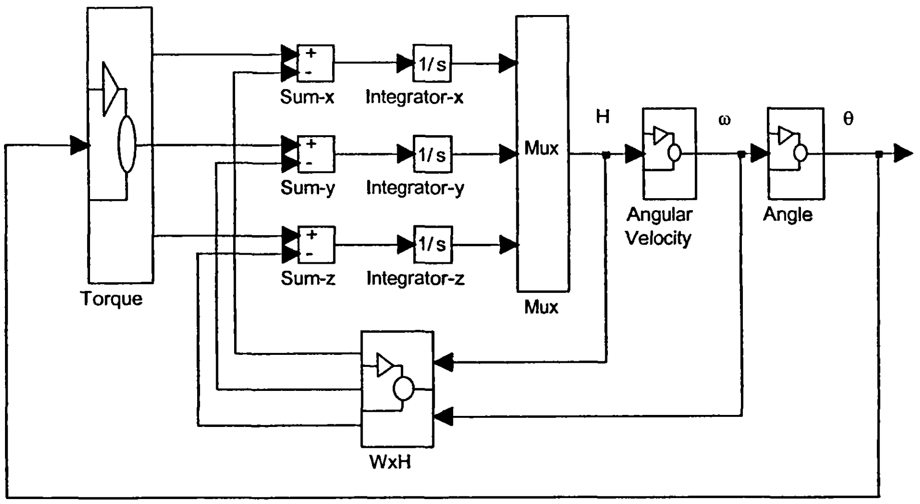

Figure 3-2 The structure of spacecraft dynamic simulator

The torque block consists of the disturbance and control torque terms. Reaction wheel and magnetorquer control algorithms are to be implemented in this block. The angle and angular velocity vectors are measured by attitude sensing hardware and are used for the control law.

We should note that the dynamic equation is based on a satellite body frame. Since most of the satellite operations are referred to a reference direction, we need a description method for the orientation of frames. The subject is discussed in the following section.

As a matter of fact, the spacecraft body axes do not coincident with the principal axes. Figure 3-2 includes the offset angle by applying the inertia tensor in angular velocity block. We need to transform the $\vec{h}_w$ properly to obtain an accurate model.

3.2 Attitude Description

3.2.1 Coordinate Systems

The attitude of a satellite can be understood as the relative orientation of a satellite body referred to an inertial coordinate. The inertial frame can be selected based on the celestial coordinate system that is defined relative to the rotation axis of the Earth and a fixed star. We have other choices such as geocentric or heliocentric coordinates (Wertz, 1978).

Sometimes it is practically convenient to have an orbit-defined coordinate, which is not an inertial coordinate in strict sense. An *l, b, n* system is an orbit-defined coordinate system for which the plane of the spacecraft orbit is in the equatorial plane of the coordinate system. The *l* axis is parallel to the line from the centre of the Earth to the ascending node of the spacecraft orbit, the *n* axis is parallel to the orbit normal and the *b* axis completing the right hand coordinate system satisfies $\vec{b} = \vec{n} \times \vec{l}$. This coordinate is particularly useful when modelling the geomagnetic field for satellite magnetometer applications as discussed in Section 3.3.

Another orbit-defined system is *roll, pitch,* and *yaw* or *RPY,* system, which maintains its orientation relative to the Earth. The yaw axis is directed toward the nadir, the pitch axis is directed toward negative orbit normal and the roll axis is perpendicular to the other two such that unit vectors along the three axes have the relation $\vec{R} = \vec{P} \times \vec{Y}$. For a circular orbit, the roll axis is parallel to the spacecraft velocity vector. The *RPY* coordinate system is useful when a spacecraft's main operation is defined in Earth pointing mode. This coordinate will be used in analysing the attitude control of KITSAT-3 during the Earth imaging mode.

3.2.2 Coordinate Transforms

We need to describe an orientation of a coordinate relative to a reference. The reference frame can be an inertial one or other coordinate such as the *RPY* system. The relative orientations between two coordinate systems can be defined by means of coordinate transformations. We can start with two-dimensional transform and extend the study into three-dimensional case.

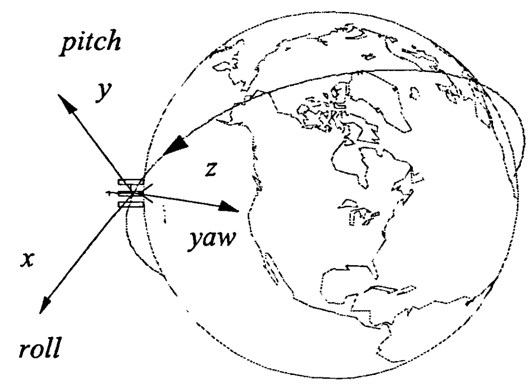

Figure 3-3 Roll, pitch, and yaw coordinate

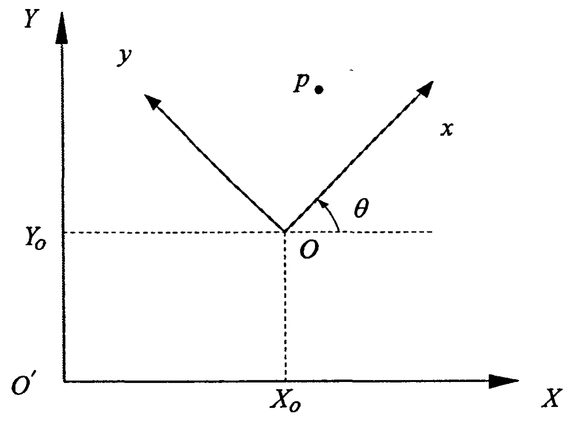

Figure 3-4 Two-dimensional coordinate transformation

The xy coordinate in Figure 3-4 is obtained after a rotation with an angle θ about the axis perpendicular to the XY plane and a translational motion of X_o and Y_o along the X and Y axes, respectively. The point p in the xy coordinate can be related with the XY coordinate in terms of the rotation angle θ and the position in the XY frame.

$$\begin{aligned} X - X_o &= x\cos\theta - y\sin\theta \\ Y - Y_o &= x\sin\theta + y\cos\theta \end{aligned} \tag{3-24}$$

When describing the relative orientation of one coordinate system to another, the translational motion has no effect at all. Therefore, we can ignore X_o and Y_o terms in Equation (3-24). Rearranging the expression for xy coordinate using θ and XY, we can obtain

$$\begin{bmatrix} x \\ y \end{bmatrix} = \begin{bmatrix} \cos\theta & \sin\theta \\ -\sin\theta & \cos\theta \end{bmatrix} \begin{bmatrix} X \\ Y \end{bmatrix} \tag{3-25}$$

We can extend the above equation to a three-dimensional coordinate transformation using the fact that a three dimensional rotation about a coordinate axis is equivalent to a two-dimensional rotation. Equation (3-25) can be expressed in three-dimensional sense as

$$\begin{bmatrix} x \\ y \\ z \end{bmatrix} = \begin{bmatrix} \cos\theta & \sin\theta & 0 \\ -\sin\theta & \cos\theta & 0 \\ 0 & 0 & 1 \end{bmatrix} \begin{bmatrix} X \\ Y \\ Z \end{bmatrix} = \boldsymbol{C}_3 \begin{bmatrix} X \\ Y \\ Z \end{bmatrix} \tag{3-26}$$

,where C_3 is a rotation matrix for an angular displacement θ_3 about the z axis. Other two axes also have similar forms of rotation matrices;

$$C_1 = \begin{bmatrix} 1 & 0 & 0 \\ 0 & \cos\theta & \sin\theta \\ 0 & -\sin\theta & \cos\theta \end{bmatrix}, \quad C_2 = \begin{bmatrix} \cos\theta & 0 & -\sin\theta \\ 0 & 1 & 0 \\ \sin\theta & 0 & \cos\theta \end{bmatrix} \tag{3-27}$$

where C_1 and C_2 are the rotation matrices about x and y axes, respectively. The rotation matrices in Equation (3-26) and (3-27) are called principal rotation matrices since they are defined from rotations about the principal axes, x, y, and z.

The product of any number of rotation matrices is itself a rotation matrix (Hughes, 1986). Therefore, any products of the principal rotation matrices are also rotation matrices. Since a general three-dimensional angular displacement is known to have three degrees of freedom and since each principal rotation matrix has but one degree of freedom, a minimum of three principal rotations must be combined to represent a general rotation. The associated rotations are called *Euler angles* and they uniquely determine the orientation of the body (Kaplan, 1976).

In general, there are 12 possible ways of defining the Euler angles according to the rotation sequence, each resulting in a different form for the rotation matrix. The sequence of multiplying the rotation matrices is very important in this context. Selection of the rotation sequence has to be carefully made at the starting point of attitude dynamics analysis. The 3-2-1 set and 3-1-3 set of Euler angles are commonly used in describing spacecraft attitude motion in direction cosine matrix form.

$$C_1(\theta_1)C_2(\theta_2)C_3(\theta_3) = \begin{bmatrix} C_2C_3 & C_2S_3 & -S_2 \\ -C_1S_3 + S_1S_2C_3 & C_1C_3 + S_1S_2S_3 & S_1C_2 \\ S_1S_3 + C_1S_2C_3 & -S_1C_3 + C_1S_2S_3 & C_1C_2 \end{bmatrix} \tag{3-28}$$

$$C_3(\theta_1)C_1(\theta_2)C_3(\theta_3) = \begin{bmatrix} C_1C_3 - S_1C_2S_3 & C_1S_3 + S_1C_2C_3 & S_1S_2 \\ -S_1C_3 - C_1C_2S_3 & -S_1S_3 + C_1C_2C_3 & C_1S_2 \\ S_2S_3 & -S_2C_3 & C_2 \end{bmatrix} \tag{3-29}$$

, where S and C are abbreviations of the sine and cosine functions.

Equation (3-28) and (3-29) are basically similar except the fact that the axes where singularities exist are different. We need to calculate the Euler angles from the rotation matrix obtained by the measurements of attitude sensors and the target inertial attitude. Unfortunately, this is not always possible since any rotation matrix has a singular problem. Scrutinising Equation (3-28) and (3-29) shows that the 3-2-1 and 3-1-3 sequences have singularities at $\theta_2 = \pi / 2$ and $\theta_2 = 0$. For example, when $\theta_2 = 0$ the {3,3} element of the 3-1-3 rotation matrix is 1. Thus, $\sin\theta_2 = 0$, which results in trivial solutions when calculating θ_1 and θ_3. Although we cannot avoid the singular situation completely, we can choose the angle where it occurs. Apparently the singularity at the reference, $\theta_2 = 0$, is more troublesome. Therefore, the 3-2-1 sequence is more favourable in this sense.

We should note that all the latent problems are not completely removed. The 3-2-1 sequence has twofold solutions when calculating the actual angle at $\sin\theta_2 = 0$, since $\theta_2 = 0$ and $\theta_2 = \pi$ satisfy the condition. Considering Figure 3-3 and relating the rotation axes 1, 2 and 3 to *x*, *y* and *z* reveals that the *y* axis encounters such an ambiguous solution set. Moreover, the *y* axis has to be freely rotated in 2π range during the HEPT operation mode. This is a major drawback of the 3-2-1 sequence. It can be resolved in the sense that an abrupt change never takes place since attitude motion is a continuous one. However, it should be especially considered in implementing ADCS software. There is a need to develop a mathematical method that can circumvent the situation systematically. The concept of *quaternions* described in the following section is an extremely useful tool in interpreting attitude motion.

3.2.3 Quaternions

A proper real orthogonal 3×3 matrix, *C*, has at least one eigen vector, $\vec{e}$, with a unit eigen value (Hughes, 1986). Expressing the members of $\vec{e}$ in a matrix form as $\boldsymbol{e}$ gives

$$\boldsymbol{Ce} = \boldsymbol{e} \tag{3-30}$$

Any rotation matrix, *C*, is a proper real orthogonal matrix, since $\boldsymbol{CC}^T = \boldsymbol{1}$ and $\det \boldsymbol{C} = 1$ (Wertz, 1978). It can be interpreted that there exists a unit vector, $\vec{e}$, that is unchanged by *C*. Therefore, *Euler's Theorem*: the rotation of a rigid body with one point fixed is a rotation about some axis.

Let the components of $\vec{e}$ along the reference axes be e_1, e_2 and e_3, and ϕ is the rotation angle about the eigen axis, *i.e.* Euler axis. Then we are able to express the orientation of an arbitrary coordinate system with respect to a reference frame using four parameters called quaternions. They are defined as

$$q = \begin{bmatrix} q_1 \\ q_2 \\ q_3 \\ q_4 \end{bmatrix} = \begin{bmatrix} e_1 \sin\frac{\phi}{2} \\ e_2 \sin\frac{\phi}{2} \\ e_3 \sin\frac{\phi}{2} \\ \cos\frac{\phi}{2} \end{bmatrix} \tag{3-31}$$

By sacrificing the compactness of the three-parameter system, we can avoid the singularity problem discussed in the previous section. Expressing the orientation using four parameters has an interesting property. Only three of them are independent and they are related with the following equation.

$$q_1^2 + q_2^2 + q_3^2 + q_4^2 = 1 \tag{3-32}$$

Equation (3-32) can be used as an accuracy index when the calculation error becomes non-negligible during computer simulation. The validity should be checked regularly and normalisation is required to compensate numerical errors.

Apart from the attitude representation, we are also interested in describing the attitude propagation using quaternions. The time derivatives of the Euler angles have large errors when the pitch angle approaches π/2. Angular motion interpretation in terms of quaternions also resolves this problem. The time dependency of the quaternions are given as (Sidi, 1997)

$$\frac{dq}{dt} = \frac{1}{2}\Omega q \tag{3-33}$$

, where Ω is a skew-symmetric matrix composed of the satellite body angular velocity components.

$$\Omega = \begin{bmatrix} 0 & \omega_z & -\omega_y & \omega_x \\ -\omega_z & 0 & \omega_x & \omega_y \\ \omega_y & -\omega_x & 0 & \omega_z \\ -\omega_x & -\omega_y & -\omega_z & 0 \end{bmatrix} \tag{3-34}$$

Equation (3-33) and (3-34) suggest that by measuring the initial angle we can calculate the evolution of the attitude using the rate data from gyro measurements. The quaternions can be related with a direction cosine matrix as

$$A(q)=\begin{bmatrix} q_1^2-q_2^2-q_3^2+q_4^2 & 2(q_1q_2+q_3q_4) & 2(q_1q_3-q_2q_4) \\ 2(q_1q_2-q_3q_4) & -q_1^2+q_2^2-q_3^2+q_4^2 & 2(q_2q_3+q_1q_4) \\ 2(q_1q_3+q_2q_4) & 2(q_2q_3-q_1q_4) & -q_1^2-q_2^2+q_3^2+q_4^2 \end{bmatrix} \tag{3-35}$$

Using Equation (3-35) we can transform a vector in an inertial frame, *XYZ*, into satellite body frame, *xyz* easily. The function of $A(q)$ corresponds to C_3 in Equation (3-26).

The Euler angles can be obtained by comparing Equation (3-35) and (3-28) or (3-29). The roll, pitch and yaw angles for a 3-2-1 sequence are given in terms of the elements of $A(q)$, $a_{low-column}$.

$$\phi=\tan^{-1}\frac{a_{23}}{a_{33}},\theta=\tan^{-1}\frac{-a_{13}}{\sqrt{1-a_{13}^2}},\varphi=\tan^{-1}\frac{a_{23}}{a_{33}} \tag{3-36}$$

Although quaternions are rather awkward for human interpretation in a physical sense, they are very convenient for mathematical description. We should note that there is an ambiguity in transforming the direction cosine matrix into Euler angles. If we use the quaternions directly as the attitude reference, we can eliminate this problem. Post performance analysis aided by human insight can prevent incorrect evaluation.

We need to develop a group of mathematical properties of quaternions for the control law design process described in Chapter 7. If q and q' correspond to the rotation matrices A and A', then the rotation described by the product $A'A$ is equivalent to the rotation described by qq'. (Note that the order is inverted.)

$$\begin{aligned} A(q'') &= A(q')A(q) \\ q'' &= qq' \end{aligned} \tag{3-37}$$

The quaternion product can be written in matrix form as follows (Wertz, 1978)

$$\begin{bmatrix} q_1'' \\ q_2'' \\ q_3'' \\ q_4'' \end{bmatrix}=\begin{bmatrix} q_4' & q_3' & -q_2' & q_1' \\ -q_3' & q_4' & q_1' & q_2' \\ q_2' & -q_1' & q_4' & q_3' \\ -q_1' & -q_2' & -q_3' & q_4' \end{bmatrix}\begin{bmatrix} q_1 \\ q_2 \\ q_3 \\ q_4 \end{bmatrix} \tag{3-38}$$

The inverse or a conjugate of q is given from the definition in Equation (3-31).

$$q^{-1} = [-q_1 \quad -q_2 \quad -q_3 \quad q_4]^T \tag{3-39}$$

The inverse of the quaternion product is directly obtainable from Equation (3-37).

$$(q'')^{-1} = (qq')^{-1} = q'^{-1}q^{-1} \tag{3-40}$$

The mathematical properties in Equation (3-37) to (3-40) will be used for defining error quaternions in Chapter 7.

3.3 Geomagnetic Field Model

Magnetometers require a geomagnetic field model to utilise their measurements for attitude determination. IGRF (International Geomagnetic Reference Field) model 2000 is used on-board for accurate calculations. The temporal variation of the geomagnetic field is taken into account to get the local magnetic field in inertial coordinates. Comparing the measured data to the reference gives two-axis information of the attitude.

A dipole model is suitable enough for attitude control system sizing and simulation purposes. It can explain the changes of the magnetic field according to the orbital position of a low Earth orbiting satellites. The simplicity makes it attractive for design purposes.

The magnetic field $\vec{B}$ at a distance R from the Earth centre with a unit position vector $\vec{R}$ is given (Wertz, 1978)

$$\vec{B}(\vec{R}) = \frac{a^3 H_o}{R^3}\left[3(\vec{m}\cdot\vec{R})\vec{R} - \vec{m}\right] \tag{3-41}$$

, where $a^3 H_o = 7.943 \times 10^{15}$ Wb$\cdot$m (T$\cdot$m^3), $\vec{m}$ is the unit direction vector of the Earth's magnetic dipole in the *XYZ* Cartesian coordinate as given Equation (3-42).

$$\vec{m} = \begin{bmatrix} \sin\theta_m \cos\alpha_m \\ \sin\theta_m \sin\alpha_m \\ \cos\theta_m \end{bmatrix} \tag{3-42}$$

$\theta_m = 168.6°$ is the coelevation of the dipole, and the right ascension of the dipole in inertial frame is $\alpha_m = \alpha_{Go} + \frac{d\alpha_{Go}}{dt} + \phi$, where α_{Go} is the Greenwich meridian at the reference time (98.8279° at 0hr UT, December 1979), $\frac{d\alpha_{Go}}{dt}$ is the Earth rotation rate, (360.9856469 deg/day), t is the time since the reference, and ϕ is the longitude of the dipole at that time (109.3 °). For a circular orbit the unit position vector in l, b, n coordinate system can be easily explained as

$$\begin{aligned} R_l &= \cos \text{v} \\ R_b &= \sin \text{v} \\ R_n &= 0 \end{aligned} \tag{3-43}$$

, where v is the true anomaly of the orbit; the satellite position angle measured from the perigee. It can be obtained with a function of time t and the orbit period P as $v = \frac{2\pi}{P} t$.

The magnetic dipole vector in Equation (3-42) can be rewritten in *lbn* coordinate system by multiplying the following rotation matrix.

$$\boldsymbol{C}_{x-l} = \boldsymbol{C}_i \boldsymbol{C}_\Omega = \begin{bmatrix} \cos\Omega & \sin\Omega & 0 \\ -\cos i \sin\Omega & \cos i \cos\Omega & \sin i \\ \sin i \sin\Omega & -\sin i \cos\Omega & \cos i \end{bmatrix} \tag{3-44}$$

, where $\boldsymbol{C}_\Omega$ is for a rotation of Ω about the Z axis and $\boldsymbol{C}_i$ is for a rotation of i about the new X axis (See Equation (3-26) and (3-27)).

Thus, the magnetic dipole components are

$$\begin{aligned} m_l &= \sin\theta_m \cos(\Omega - \alpha_m) \\ m_b &= -\sin\theta_m \cos i \sin(\Omega - \alpha_m) + \cos\theta_m \sin i \\ m_n &= \sin\theta_m \sin i \sin(\Omega - \alpha_m) + \cos\theta_m \cos i \end{aligned} \tag{3-45}$$

, where Ω is the right ascension of the ascending node, and i is the orbit inclination. Substituting Equation (3-43) and (3-45) into (3-41) gives the complete Earth dipole model in *lbn* coordinate.

We can define the attitude of the spacecraft in the reference *xyz* frame when it passes over the equator in the descending path as depicted in Figure 3-3. If the satellite is stabilised with respect to this inertial coordinate, it will have a constant Sun angle. To obtain the maximum solar power, we need to rotate the pitch axis according to the seasonal variation as discussed in Chapter 2. Roll tilting requirement is dependent on the local Sun time of the orbit. The magnetic field vector in the stabilised satellite body frame can be obtained from (Kim *et al.*, 1995)

$$\begin{bmatrix} -B_z \\ B_x \\ -B_y \end{bmatrix} = C_r C_p \begin{bmatrix} B_l \\ B_b \\ B_n \end{bmatrix} = \begin{bmatrix} \cos r(\cos pB_l + \sin pB_n) - \sin rB_n \\ -\sin pB_l + \cos pB_b \\ \sin r(\cos pB_l + \sin pB_b) + \cos rB_n \end{bmatrix} \tag{3-46}$$

, where r is the roll tilting angle and p is the pitch tilting angle.

Figure 3-5 is a simulation result of the geomagnetic fields in its body frame, *xyz*, for a satellite when the attitude is fixed with respect to an inertial coordinate at the proposed orbit of KITSAT-3. The starting point is assumed at the true anomaly of 135°. We should note that the temporal frequencies of x and z fields are twice that of the orbital period. On the contrary, the y field component changes once a day with relatively smaller magnitude. This simulation result will be used to assess the effect of satellite residual dipole moment and to develop a magnetorquering algorithm in Chapter 6 and 7.

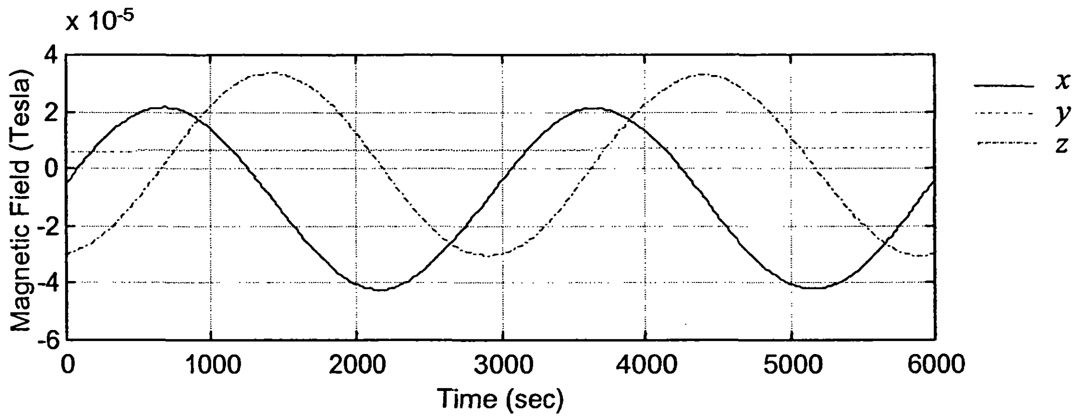

Figure 3-5 Magnetic fields for inertial pointing mode

Equation (3-46) can also be expressed in terms of the quaternions. The discrepancy can be represented by a rotation matrix, C_{lb}, as

$$\begin{bmatrix} x \\ y \\ z \end{bmatrix} = \boldsymbol{C}_{lb} \begin{bmatrix} l \\ b \\ n \end{bmatrix} = \begin{bmatrix} 0 & 1 & 0 \\ 0 & 0 & -1 \\ -1 & 0 & 0 \end{bmatrix} \begin{bmatrix} l \\ b \\ n \end{bmatrix} \tag{3-47}$$

The total rotation, then, can be attained by multiplying Equation (3-35) to $\boldsymbol{C}_{lb}$.

$$\boldsymbol{R} = A(\boldsymbol{q})\boldsymbol{C}_{lb} = \begin{bmatrix} -2(q_1q_3 - q_2q_4) & q_1^2 - q_2^2 - q_3^2 + q_4^2 & -2(q_1q_2 + q_3q_4) \\ -2(q_2q_3 + q_1q_4) & 2(q_1q_2 - q_3q_4) & q_1^2 - q_2^2 + q_3^2 - q_4^2 \\ q_1^2 + q_2^2 - q_3^2 - q_4^2 & 2(q_1q_3 + q_2q_4) & -2(q_2q_3 - q_1q_4) \end{bmatrix} \tag{3-48}$$

Equation (3-48) directly transforms a vector in *lbn* system into stabilised satellite body frame using the integrated quaternions from Equation (3-33).

Chapter 4. Attitude Control System I : Actuators

4.1 Magnetorquer(MTQR)

4.1.1 Principles

A *magnetorquer* or a magnetic torquer is an electromagnet that generates a magnetic moment to make an interaction with the environmental magnetic field. The result of the interaction is an active torque to be used for the spin up / down of the satellite motion and momentum unloading for the reaction / momentum wheels.

The current loop shown in Figure 4-1 generates a magnetic moment, $\vec{m}$, proportional to the area of the loop, A, and the current, I. The magnetic moment is parallel to the loop plane normal vector, $\vec{n}$. It can also be written as Equation (4-1) when the loop has N turns.

$$\vec{m} = NIA\vec{n} \tag{4-1}$$

The magnetic dipole moment depends on the material enclosed by the current-carrying coil and is given as

$$\vec{d} = \mu\vec{m} \tag{4-2}$$

, where μ is the permeability of the core material.

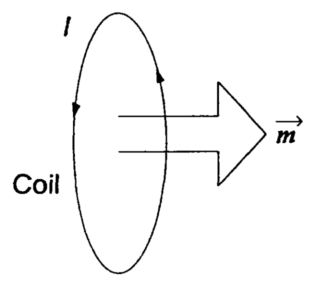

Figure 4-1 Magnetic moment by a current loop

4.1.2 Trade-off Study

The characteristic of the core material determines the overall performance of the electromagnet. Ferromagnetic materials are more efficient in terms of the input power to output dipole moment ratio when they are used as the core of an electromagnet. However, ferromagnetic materials have hysteresis characteristics. Therefore, non-linear characteristics and residual magnetic dipole moment exist. They are critical issues in designing and controlling a ferromagnetic core type torquer.

Micro-satellites that have relatively small moments of inertia are more susceptible to residual magnetic dipole moment. The torque generated by the result of the interaction with the geomagnetic field, $\vec{\boldsymbol{B}}$, is given in Equation (4-3).

$$\vec{\boldsymbol{T}}_m = \vec{\boldsymbol{m}} \times \vec{\boldsymbol{B}} \qquad (4\text{-}3)$$

It is apparent that the magnetic torque, $\vec{\boldsymbol{T}}_m$, has larger effect on a small body if we consider Newton's law of motion; the rate of change of angular momentum of a body is equal to the torque applied. During the mission analysis period, a trade-off study between the efficiency and magnetic cleanness has been performed. Table 4-1 shows typical characteristics of conventional magnetorquers. Ferrite core type magnetorquers are commercially available from Ithaco Inc. To minimise the residual dipole moment effect, a coreless type torquer (*air core*) has been selected as the KITSAT-3 magnetorquer.

Table 4-1 Typical characteristics of magnetorquers

Type	Magnetic Moments (Am^2)		Saturation Voltage (V)	Power at Saturation (W)
	Saturation	Residual		
TR10CFN	15	0.1	13.9	1.3
TR100UPR	130	1.0	20.0	2.4
TR810UPR	810	4.0	27.5	9.2
KITSAT-1, 2	10	0	14.0	7.8
KITSAT-3	10	0	28.0	7.8

4.1.3 System Configurations

The magnetorquer electronics module is located in the satellite bus stack as indicated in Figure 4-2.

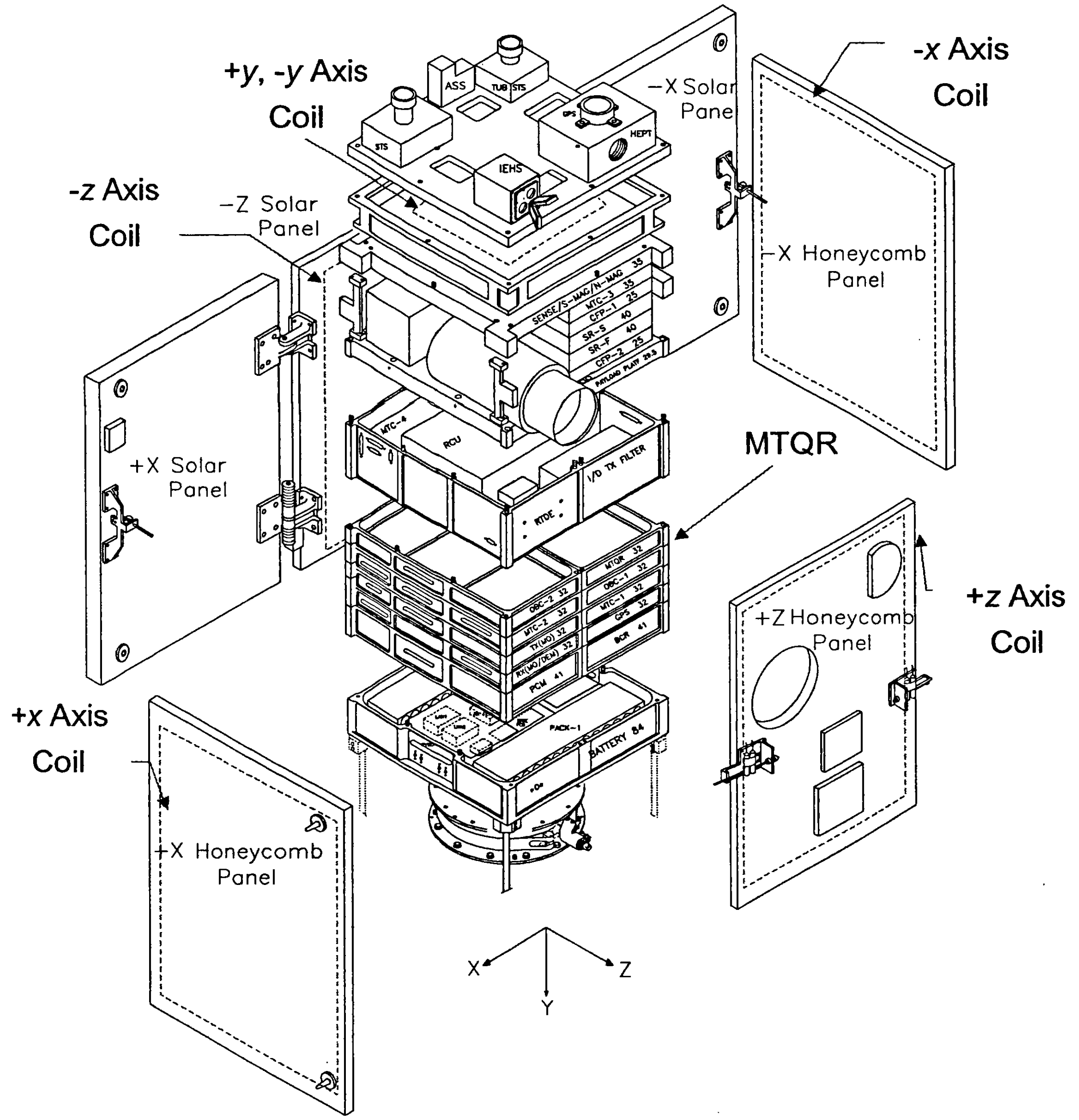

Figure 4-2 The position of the magnetorquer in KITSAT-3

The Magnetorquer system has twofold redundancy. Therefore, it has two completely independent electrical driving units, MTQR1 and MTQR2. The electronics module box in Figure 4-2 has an internal configuration as shown in Figure 4-3. Each unit occupies half of the module box and has a 25 pin D-type male connector interface. The connectors are labelled as Left and Right according to their positions viewed from outside of the box (-*x* direction in Figure 4-2). It should be noted that the harness definitions of these two connectors are not identical. Therefore, extra care should be taken during testing of the module.

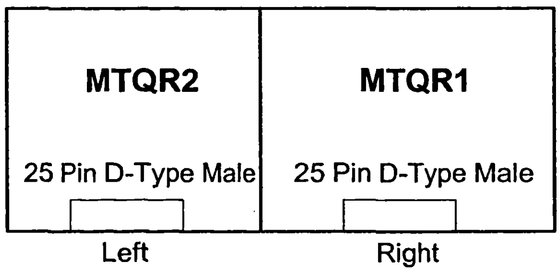

Figure 4-3 MTQR module box configuration

There are six independent magnetorquer coils. The configuration of these coils is shown in Figure 4-4.

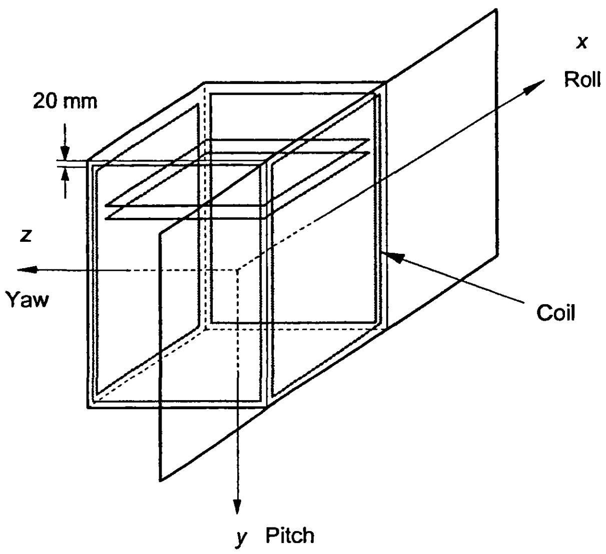

Figure 4-4 Magnetorquer coil configurations

Each axis has positive and negative direction coils. The $+z$ and $\pm x$ coils are identical in their physical structures. Three are wound along the honeycomb panels with 20mm clearance from the panel edges. However, the $-z$ coil has a slightly larger area compared with the previous 3 windings due to the difference in physical size of the $-z$ solar panel. Due to the fundamental structural difference of the y axis, the winding method is quite different from the other axes. The $\pm y$ coils are wound around a specially designed bracket as shown in Figure 4-2 and Figure 4-4. All coils are essentially rectangular in shape.

4.1.4 Operation Concept

Each MTQR unit is responsible for controlling a specific polarity, positive or negative. MTQR 1 is designated to the positive axis coils, x, y, and z, and MQTR2 controls the negative axis coils, $-x$, $-y$, and $-z$. Unless there is failure, each module only has to manage its originally designated axes. Both units operate simultaneously for this reason. However, failure in control of a certain axis due to a hardware malfunction prompts a current polarity changing function using switching relays in the electronics. MTQR1 is connected to the m0 link of MTC1 and MTQR2 is attached to m1. They have identification address as 13H and 1BH, respectively.

MTQR will be used as the main actuator during the initial attitude acquisition mode for de-tumbling control. It will be adapted as a momentum dumping device during the normal operation mode as discussed in Chapter 7.

4.1.5 System Design

It is very important to select the correct resistive component of the coil, *i.e.* power load. The power consumption of the whole system is largely determined according to the resistance of the load. The resistance of a coil was 25 Ω in KITSAT-1 and 2. Since the main bus voltage was +14V, 0.56A of current was designed to flow along a coil in the steady state condition.

The power versus torque conversion efficiency of an air core type magnetorquer is very low, as shown in Table 4-1. It is desirable to keep the power consumption as small as possible if the performance satisfies the control requirements. It is also advantageous to use the unregulated satellite power to minimise voltage conversion loss. The main bus voltage of KITSAT-3 has been increased to +28V. Therefore, similar values of coil resistance will cause an extremely high rate of power consumption.

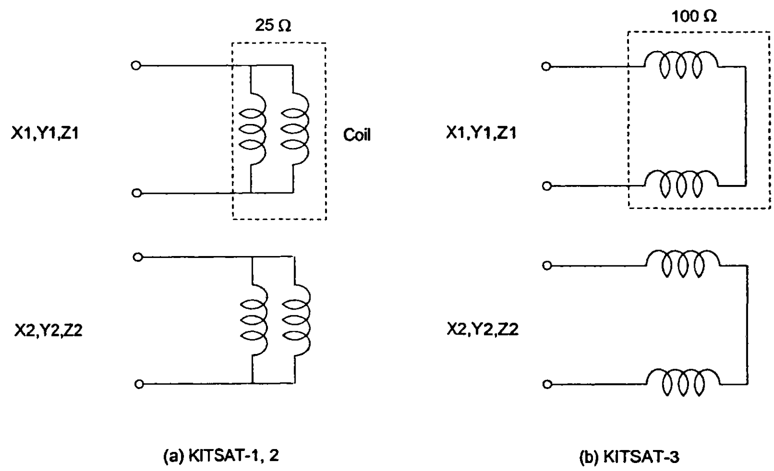

Figure 4-5 The coil connections of the MTQR

The original design baseline of the KITSAT-3 in terms of physical size was close to that of its two predecessors. However, the proportions of the satellite have been increased appreciably in the course of the development. Table 4-2 lists the finalised characteristics of the magnetorquer coils.

Table 4-2 KITSAT-3 magnetorquer coil specifications

	Yaw, Roll Axis (±x, +z)	-Yaw Axis (-z)	Pitch Axis (±y)
Height (mm)	637.5	637.5	307
Length (mm)	410	544	307
Circumstance (m)	2.1	2.4	1.2
Area of the Coil (m^2)	0.26	0.35	0.09
Number of Turns	138	123	236
Coil Resistance (Ω)	100	100.5	100.2
Main Voltage (V)	28	28	28
Maximum Current (A)	0.28	0.28	0.28
Peak Power (W)	7.84	7.80	7.82
Magnetic Moment (Am^2)	10.10	11.88	6.21

The coil connections of KITSAT-1, 2 were made in parallel. Two windings of coils of 50 Ω were coupled at the magnetorquer driving electronics module (Double winding system). This provided redundancy concept in the event of a solder failure due to launch vibration. A simplified single winding method was proposed to limit the power consumption in KITSAT-3. Reduction of power is an important factor in the system design since simultaneous driving of three-axis requires 3 times more power than the previous single axis driving system. Figure 4-5 shows differences in the connection methods.

During the development and operation of the KITSAT-1 and 2 satellites, the magnetorquers had serious limitations and problems. Due to the small capacity of the power systems (about 30 W), only one axis could be operated at any one time. The main purposes of magnetorquering were spin down control during the initial acquisition before the boom deployment and active nutation damping control during normal operation.

The satellite operators experienced a number of abnormally large spinning rates after on-board computer crashes. The cause was interpreted as faulty operation due to the sustained power-on status as a result of the crashed computer being unable to turn it off. Therefore, a safety measure has been proposed to prevent this problem on KITSAT-3. A hardware watchdog timer has been implemented to supervise the operation status.

Figure 4-6 is the block diagram of the magnetorquer of KITSAT-3. The previous magnetorquer models were built with a group of switches and a command decoder. Six bit commands are connected to a decoder, which generates the 32 necessary control signals for switching. They are responsible for toggling on/off status and current polarity. After all the relays are properly set as required, a fire command turns on the power switch, which eventually provides a current path to the coil. The redundant coils were designed to be able to operate either independently or simultaneously. Since it was only possible to turn on one axis at a time, a single analogue telemetry line was sufficient for monitoring the current through both redundant coils. The protection logic inhibits switching commands if a certain switching action is already in progress.

Decoders were used in the previous models, since this provides a simple solution for one-axis on-off control. However, the electrical interface was complicated due to 6 command lines. Moreover, when variable torque control is required it becomes more complex. Therefore, a micro-controller-based system was proposed to overcome these problems. The size of the control processor, Intel 8751, is comparable to a single decoder chip. Utilising a CMOS technology can save a considerable amount of power.

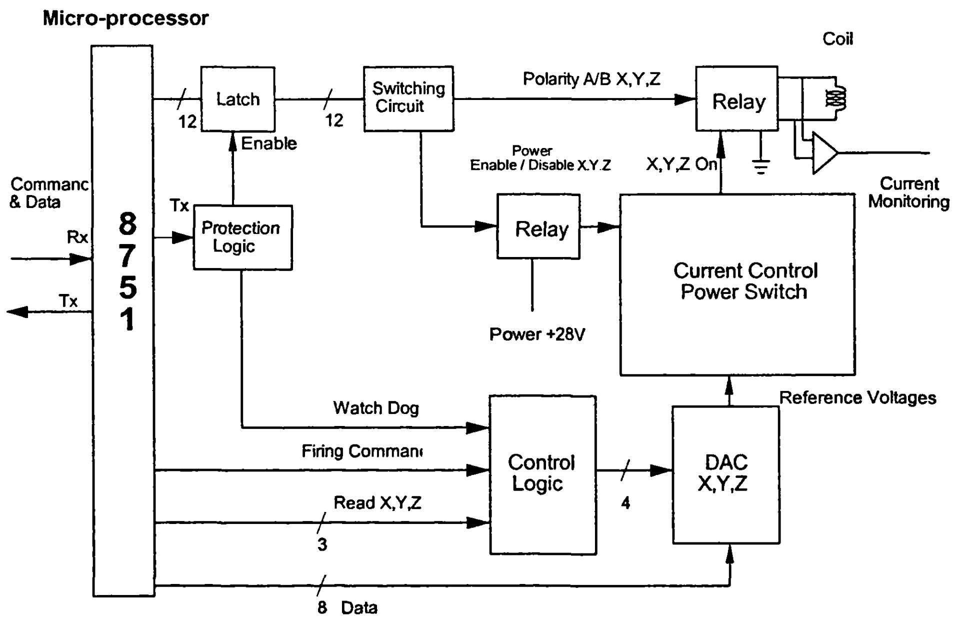

Figure 4-6 Magnetorquer block diagram of KITSAT-3

The power lines are supplied from the power-conditioning module by commands from the on-board computer. These powers are protected by the current limiting switches located on the MTC1. Any unusually high current triggers an automatic shut down mechanism in the switch circuit in order to isolate other systems from a malfunction in the magnetorquer module. The centralised power-conditioning scheme of KITSAT-3 resulted in complex power interface. It has been pointed out that a separate DC-DC converter in the magnetorquer unit may be more efficient. As explained previously, unregulated +28V bus power is used as the main power supply. Other power lines are all regulated. The redundant magnetorquer module shares only the ground plane on the PCB. The electrical interface of the magnetorquer is shown in Figure 4-7.

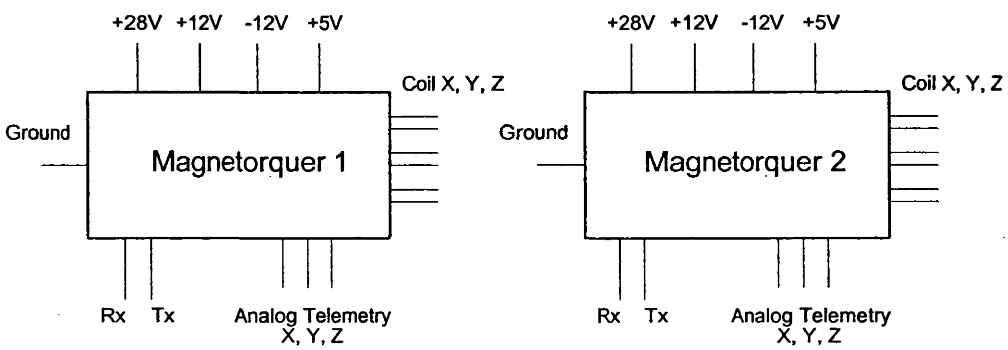

Figure 4-7 Electrical Interface of the magnetorquer

The communication handling hardware can be easily implemented using a built-in serial port in a micro-controller. The received data are analysed and decoded. The 8751 processor has 24 bits of control ports. These ports are used for generating pulses to switch the bi-stable relays. The power enable / disable and polarity switching functions are performed by direct commands from the on-board computer.

4.1.6 Hardware Design

A major change occurs at the power driving circuit compared to the previous KITSAT designs. The 2-stage power driving switch was a simple on-off style that exploits the saturation mode of a transistor. The first stage transistor provides sufficient current that the main power transistor can operate in the saturation mode.

One of the requirements of the KITSAT-3 magnetorquer is to control the three-axis magnetic moment with 8 bit digitising levels. Digital to Analogue Converters (DACs) are used for this multi-level controlling. Another important modification is the concept of feedback control. The amplification coefficient of a transistor is very susceptible to temperature variation. Therefore, the circuit design should not rely on this value. The circuit in Figure 4-8 shows a current sampling small resistor, which is 1000 times smaller than the load. The control reference voltage from the DAC output is compared to this feedback signal by an OP amp.

Neglecting the voltage drop across C-E of the power transistor, the feedback voltage, V_f, indicated in Figure 4-8 ranges between 0~28mV (In fact, the C-E voltage drop is about 2V at saturation). Therefore, the potentiometer should properly divide the DAC output voltage. Since, the DAC uses +7V as a reference voltage, the unipolar mode output V_o has its maximum at +7V. Linearly scaling down the DAC output voltage at a small cost in power at the voltage divider can be implemented with relatively large values of resistance of R_a and R_b. The values of R_a and R_b can be easily determined from the following equation.

$$V_{in} = R_b /(R_a + R_b)V_o \tag{4-4}$$

If we fix R_b as 100 KΩ and R_a as 374Ω then V_{in} becomes 26.1 mV. This is close to the maximum V_f taking into account the saturated C-E voltage drop. The value of R_b is also determined on the basis of commercial availability. In the event of the main satellite voltage +28V dropping, the controlled current reaches saturation.

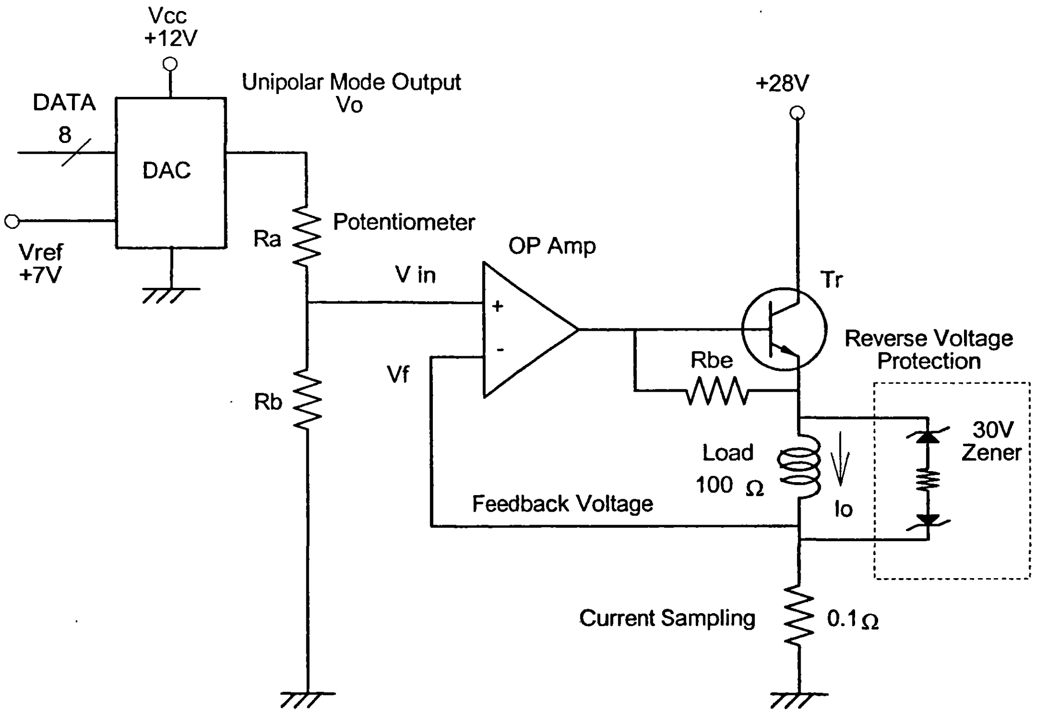

Figure 4-8 Operation of the current control loop

Table 4-3 Characteristics of feedback current control circuit

Advantages	Disadvantages
- Robust to individual transistor device characteristics varieties - Simple circuit design	- Power loss at the potentiometer and C-E of the power transistor. - Calibration required

The power transistor has an amplification coefficient of 80 at -55°C when the collector current is 280mA. Thus, the OP amp should be capable of providing 3.5mA to the base of the power transistor. However, it should also be accurate enough to supply 4.38μA for the smallest control level, 1/255, at 150°C when the current amplification coefficient increases to 250. The selection of the OP amp has to be determined according to these requirements. A general-purpose device, OP 90, is suitable for this application where rapid switching is not necessary. The circuit in Figure 4-8 has the following characteristics.

Special attention should be taken to the power loss at the C-E of the power transistor. This power loss turns out to be heat dissipation at the transistor. During the prototype development, 30 days of continuous burn-in test had been performed at the maximum power loss level without a heat sink. The transistor is thermally coupled to the aluminium module box of the magnetorquer to provide conduction link in FM.

The Zener-to-Zener protection circuit provides a current path when the power transistor is switched off or the main power is shut down by the relay's power disabling action. Essentially, the load has inductive as well as resistive characteristics. A sudden change of the load current is not allowed in inductive circuit. It might be turned out to be a high reverse voltage across the transistor C-E. A pair of the Zener diodes provides bi-directional current paths. It should be noted that a polarity reversing relay circuit is omitted in Figure 4-8.

To convert 8-bit digitised control data to analogue signals, DACs should be used. A latch circuit must temporarily memorise the control data from the main controller, 8751 microprocessor. The controller outputs the data using an 8-bit data bus. The latches store the data by appropriately generated control signals from the control logic. Fortunately, a single DAC chip can perform the latching function. The PM-7224 DAC chip is an attractive candidate for this application. In fact, in order to simplify the hardware circuit, the DAC control logic is implemented within the microprocessor by means of software.

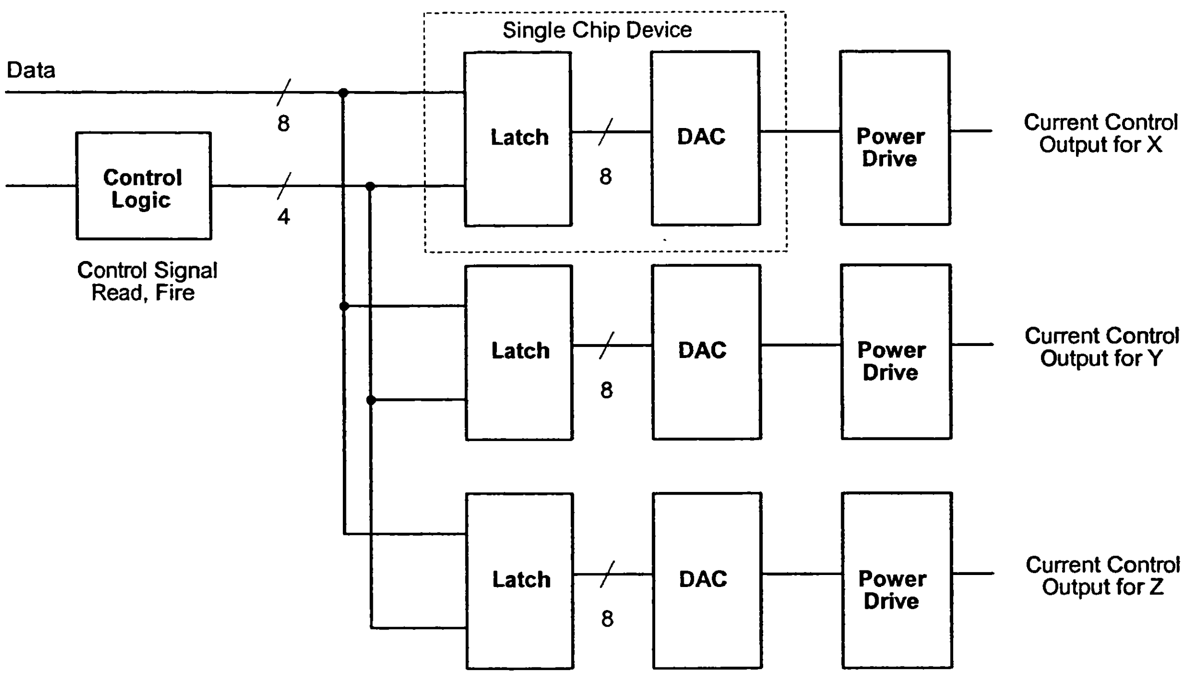

Figure 4-9 DAC Control block diagram

The selection of the DAC chip has been made following consideration of the following aspects. Some chips are highly integrated to accommodate up to 8 independent DAC units. However, separate chip architecture is preferred since a single point failure should be avoided. A voltage output type DAC is favoured over current output devices, which require additional OP amps.

The RESET pin of the DAC is exploited for the watchdog controller. As mentioned previously, the supervisory watchdog timer should be able to shut down the outputs automatically. Supervision is done by a periodic check of communication between magnetorquer and the OBC. The watchdog timer starts a new count whenever it monitors data flow out of 8751. If the timer reaches a predefined counting status it gives a watchdog output signal. The serial Tx line of the 8751 microprocessor is tapped for the life indication signal. The 4536 timer chip is an excellent candidate for this purpose.

The current telemetry circuit takes advantage of the existing sampling resistors for the current feedback. The first OP amp stage in Figure 4-10 is a bi-polar amp with amplification factor of 10. The second stage has the same amplification factor as the first. It also adds the output of the first stage to the reference voltage, 2.5V. The second stage amp is an inverter. Thus, an inverting amp is required at the third stage in order to meet the telemetry requirement of a 0~5V analogue signal. The Zener diode at the output terminal protects the analogue to digital converter (ADC) from over-voltage. All of the OP amps in Figure 4-10 are designed for a single chip OP400, a quadratic OP amp. The bias voltages are ±12V; this ensures bipolar amplification near zero inputs. The coil current and the telemetry output voltage have the following relation.

$$V_o = 10(V/A)I_L + 2.5V \tag{4-5}$$

, where I_L is in Ampere and V_o is in Volt.

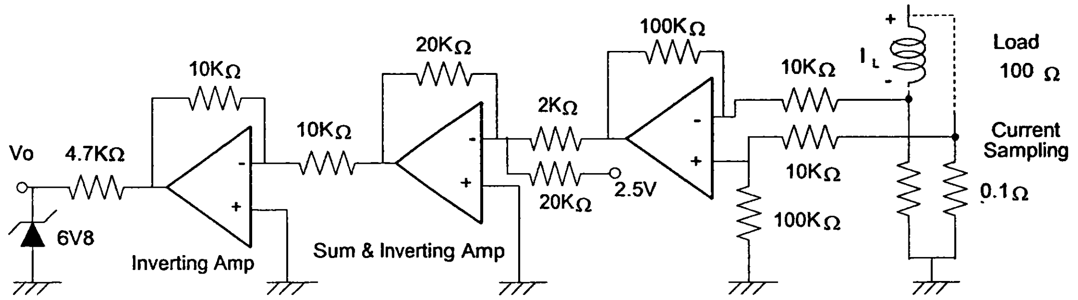

Figure 4-10 Telemetry circuit

The telemetry circuit in Figure 4-10 has non-linearity at zero. Positive and negative gains are slightly different. Since the telemetry is not so critical, the circuit has not been modified during the FM manufacturing stage. Reducing the value of the 10KΩ serial to 100 KΩ in the first stage will diminish this effect.

The magnetorquer uses TO5 size can-type dual relays. There are two control terminals, A and B, in a single component. Each control terminal has an electromagnet with opposite polarity that makes electrical contact by means of mechanical switching. A control signal at one terminal allows both switches to rest in their specific position. A signal at the other terminal toggles their positions. Therefore, the relay is called a bipolar one, which has a mechanical memory.

Driving the relay can be achieved by simple switching circuits. The driving coil in the relay has a small resistance of 61Ω for a 5V application. Thus, it consumes a considerable amount of power, even if it is a short duration (2msec maximum). The TTL devices are not able to drive this amount of power directly. Buffering and current driving devices are required for this reason.

The built-in diode in the relay protects against a high reverse voltage just after the switch off. The resistor between the B-E of the transistor improves the switching speed and also prevents unintentional turn-on due to noise. A general-purpose transistor, 2N2222, is suitable since high speed switching is not required in this circuit. A HC244 is a good candidate as the buffering device. The enable terminal of the buffer is connected to the watchdog protection logic. The serial resistor 1KΩ limits the current to the base of the driving transistor to 5mA. This is sufficiently high to operate the transistor in its saturation mode.

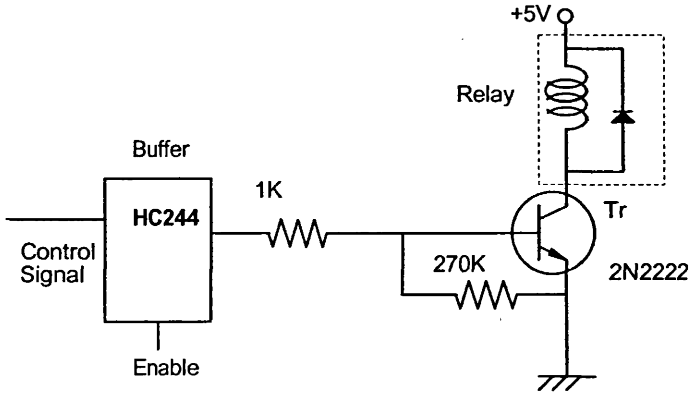

Figure 4-11 Relay driving circuit

The 8751 micro controller is the key component in the magnetorquer circuitry. It receives and transmits serial data with the OBC using MTC packet communication protocol. It also validates the received data and decodes them. The decoded data are used for the DAC control and relay switching. The microprocessor reduces considerably the amount of electronic circuits and harness wires. It utilises its versatility in communications and control function of the microprocessor.

Table 4-4 shows the functions of the micro controller. The 8751 has 24-bit ports after dedicating port 3 for the data link. These ports are used for generating pulses to control the relays. The power enable / disable and polarity changing functions (00~0Bh) are performed by direct commands from the on-board computer. As described previously, the relay driving circuit consumes high power. A pulse-type driving command is preferred to reduce power and enhance the lifetime of the relays. The bi-stable nature of the relays enables us to use such a pulse-type control. The bi-level DAC data reading and firing functions (0C~0Fh) are internally generated by the micro controller. Port 2 is wholly dedicated for DAC data lines. Port 0 controls power enables / disables and polarities of the X and Y-axes. The LSBs (Least Significant Bits) of port 1 are used for relay controls for the Z-axis.

Table 4-4 Decoding functions of 8751 microprocessor

Inputs (Binary, Hex)	Functions	Outputs (Binary, Hex, Port #, Pulse)
0000, 00h	X Power Enable	00000001, 01h, Port 0, ⎍
0001, 01h	X Power Disable	00000010, 02h, Port 0, ⎍
0010, 02h	X Polarity A	00000100, 04h, Port 0, ⎍
0011, 03h	X Polarity B	00001000, 08h, Port 0, ⎍
0100, 04h	Y Power Enable	00010000, 10h, Port 0, ⎍
0101, 05h	Y Power Disable	00100000, 20h, Port 0, ⎍
0110, 06h	Y Polarity A	01000000, 40h, Port 0, ⎍
0111, 07h	Y Polarity B	10000000, 80h, Port 0, ⎍
1000, 08h	Z Power Enable	11110001, F1h, Port 1, ⎍
1001, 09h	Z Power Disable	11110010, F2h, Port 1, ⎍
1010, 0Ah	Z Polarity A	11110100, F4h, Port 1, ⎍
1011, 0Bh	Z Polarity B	11111000, F8h, Port 1, ⎍
1100, 0Ch	Fire	11100000, E0h, Port 1
1101, 0Dh	Read X Data	11010000, D0h, Port 1
1110, 0Eh	Read Y Data	10110000, B0h, Port 1
1111, 0Fh	Read Z Data	01110000, 70h, Port 1
DAC Data	DAC Input Data	8 bit data to Port 2

4.1.7 Software Design

The power and polarity control commands in Table 4-4 are not used frequently in normal operation when all the axes are functioning. Therefore, relay control functions are grouped separately. The rest of the functions in Table 4-4 make up a second group. The first byte of the data field in Table 4-5 indicates the type of the group that the packet is in. CCh and DDh are used to distinguish relay control and DAC data packets, respectively. Three-axis power or polarity changing commands require 3 bytes in the standard MTC communication protocol as show in Table 4-5.

ST	DL	DA	SA	Data			
5Ah	06h	13h or 1Bh	×	CCh	00h(01h) or 02h(03h)	04h(05h) or 06h(07h)	08h(09h) or 0Ah(0Bh)

Table 4-5 MTC → MTQR power & polarity changing packet format

The form of a data packet from MTC is shown in Table 4-6. It has fixed data length. 5Ah can only occur as the starting byte, ST. Thus, the data length byte, DL, can be fixed to 06h. The 8751 microprocessor uses the last 3 bytes of data in the packet sequentially and generates outputs according to Table 4-4. (See 5.2 for more about the MTC format)

ST	DL	DA	SA	Data			
5Ah	06h	13h or 1Bh	×	DDh	X Data	Y Data	Z Data

Table 4-6 MTC → MTQR DAC Data packet format

The micro controller checks the fifth byte of the received packet and performs decoding. It takes appropriate action according to the result. A series of internal commands are generated as the following sequence. The currents of all the axes are maintained as these DAC values until a new data packet is received.

X Data Out → Read X Data (0Dh) → Y Data Out → Read Y Data (0Eh) → Z Data Out → Read Z Data (0Fh) → Fire (0Ch)

The micro controller logically checks the validity of the received packet. When an error is encountered during the validity check process, it returns 0Fh to the original source address. If the checking and control process finish without trouble, 77h is returned. The category of invalidity includes ST or DL error, 5th byte is neither CCh nor DDh, data are greater than 0Bh in case of relay control. The acknowledgement is also made according to the standard MTC protocol as shown in Table 4-7. The DA and SA are, in fact, swapped compared with those in Table 4-5 and Table 4-6.

ST	DL	DA	SA	Data
5Ah	03h	×	13h or 1Bh	77h (Success) or 0Fh (Fail)

Table 4-7 MTQR → MTC acknowledge data packet format

The micro controller should be capable of handling the MTC packet communication protocol. Managing the 5Ah data byte and stuffing are the key factors in writing the code. The 8751 checks the data in the receiving buffer whenever the Receive Interrupt (RI) flag is on. If the newest byte is 5Ah, the 5Ah received flag (01h) is set. In case the next byte is 5Ah and it is not followed by 00h (stuffing byte), previously received data are to be neglected and we consider it as the start of a new packet. If it is followed by a stuffing byte, we should eliminate 00h, and the latest 5Ah is considered as pure data.

The received packet should be always 8 bytes as defined in Table 4-6. If 8 bytes are received, the decoding process begins. Sequentially transmitted data from MTC can be lost during this decoding process. A ring buffer is proposed to temporally store up to 4 packets in the internal memory.

Figure 4-12 shows the structure of the ring buffer as well as the functions of registers.

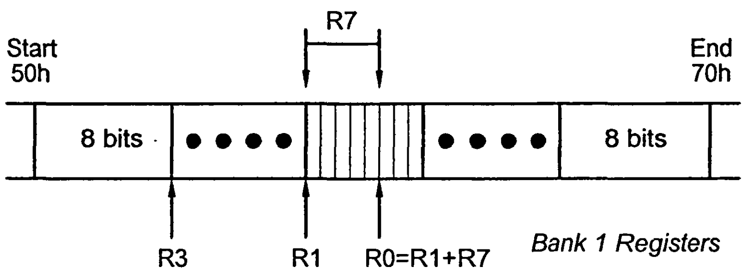

Figure 4-12 Structure of the ring buffer

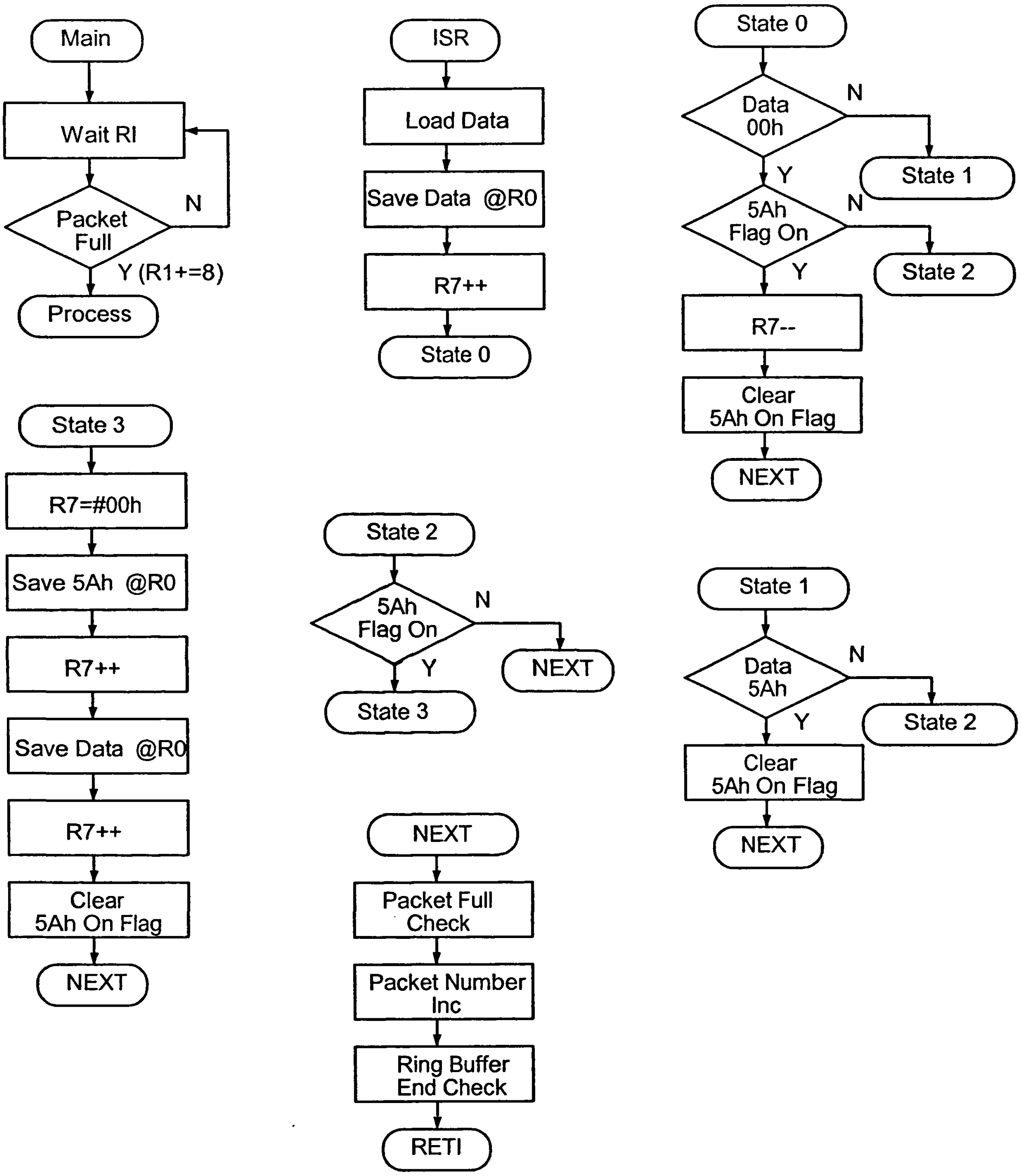

Figure 4-13 Packet receive flow chart

Figure 4-13 is a flow chart of the data receiving part of the assembler program. The main routine waits until the RI is on. A receive interrupt invokes ISR (Interrupt Service Routine). A byte in the receiving buffer is moved to the Ring Buffer where the current address pointer, R0, indicates. R0 is R1+R7 and R7 is incremented by one for receiving the next data. The bit address, 02h, is used as a full packet flag.

The 'Process' routine in Figure 4-14 executes the data validation process and gives an acknowledgement packet according to the format in Table 4-7. The decoding actions of the data field can be performed by taking the data in the accumulator as the input and converting it as the output, according to Table 4-4. The data processing routine ends by decreasing R2, the number of packets remaining in the ring buffer. If this is not zero, the data process routine is called again by the main routine immediately after the return. If R2 is zero. This signifies that there is nothing to do. Therefore, the magnetorquer is in an idle state until the next packet arrives or the watchdog stops the latest current control action.

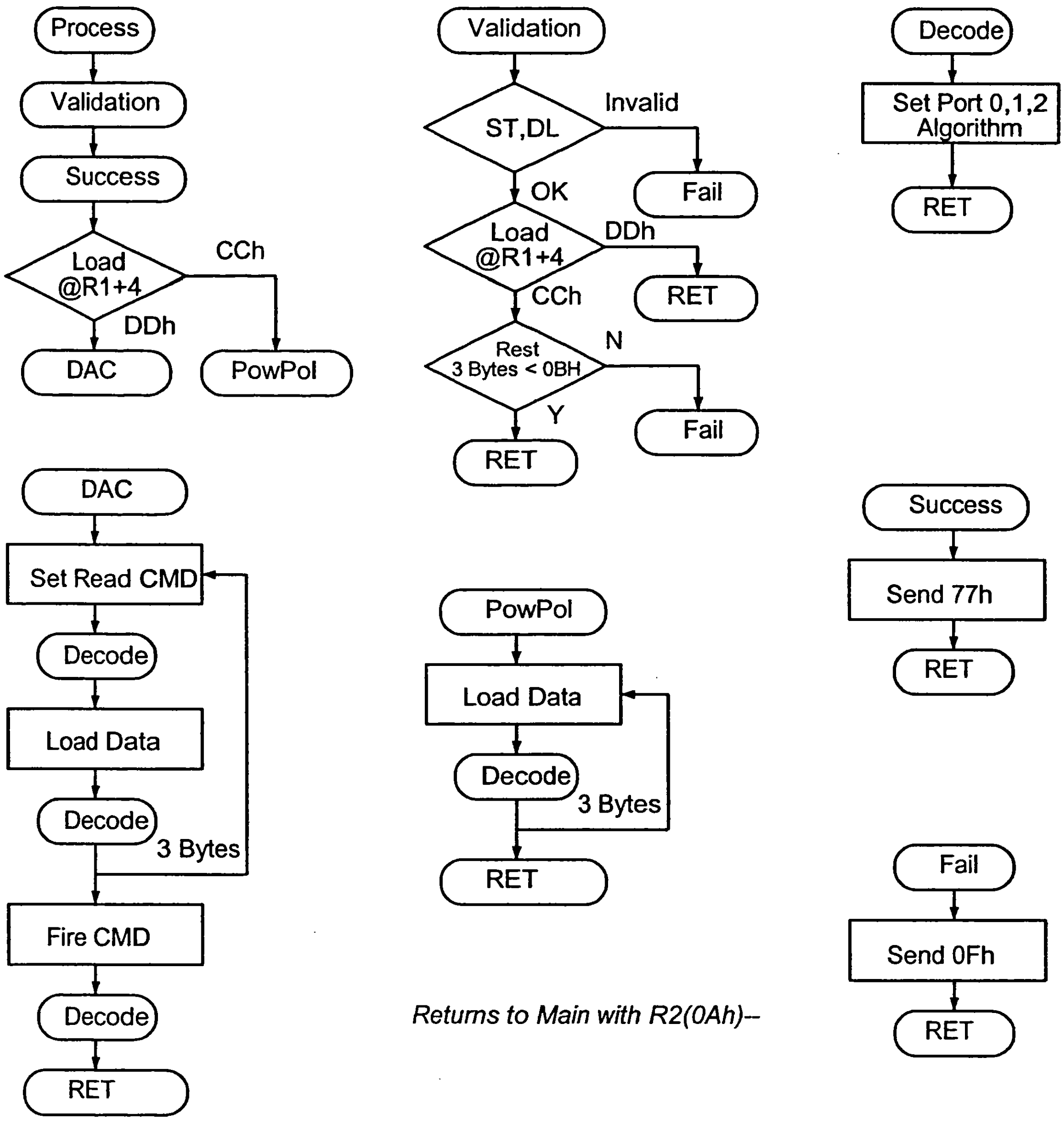

Figure 4-14 Data process flow chart

Table 4-8 Magnetorquer serial communications scheme

Start Bit	1
Stop Bit	1
Data Bit	8
Data Rate	9600

The communications interface scheme of the magnetorquer is presented in Table 4-8. The required data rate is relatively high compared to the attitude control frequency of the magnetorquer. However, slowing down the data rate may increase compatibility of the data handling network since other serial communications lines use 9600 bps as a standard.

4.1.8 Implementation Results

The mechanical dimension of the magnetorquer follow the standard sized KITSAT-3 bus module box. Table 4-9 is the physical size summarises the MTQR module.

Table 4-9 Mechanical size of MTQR

Length	450 mm
Width	225 mm
Height	32 mm

Table 4-10 Mass measurement

	Mass	Description
Module	1471 g	Entire module weight including coating
Wire	220 g / axis	(wire + connector) × 6 axes in total = 1320g
Total	2791 g	

Table 4-11 is the actual measurement results of the magnetorquer coils after integration. (Refer to Table 4-2 for comparison with theoretical estimations)

Table 4-11 Physical characteristics of magnetorquer coils

Coils	Inductance (mH)	Resistance (Ω)
$+x$	13.10	101.0
$-x$	13.25	101.4
$+y$	15.92	99.1
$-y$	17.10	99.5
$+z$	13.09	99.7
$-z$	12.72	100.1

The magnetorquer is implemented within a standard size KITSAT-3 module box. There are a few important factors worth noting in building the hardware module. The power transistor in Figure 4-8 consumes significant amount of power since it is not operated in a saturation mode. In the worst case, approximately, 125mA flows to the load, which is a half of the maximum current. The amount of heat dissipated at the collect-emitter of the transistor is a maximum in this situation. Hence, a proper heat-sinking mechanism should be adapted in order to prevent a burn-out. An 840-hour period of continuous experiment has been performed without a heat sink in order to examine the survivability. Thermal problems are treated analytically in Section 4.1.9. The aluminium module box is thermally connected to the transistors. The contacting side is toward the dark space direction in normal attitude operation. It will improve the thermal environment of the whole satellite by this counter-action. Figure 4-15 is a photograph of the actual magnetorquer module.

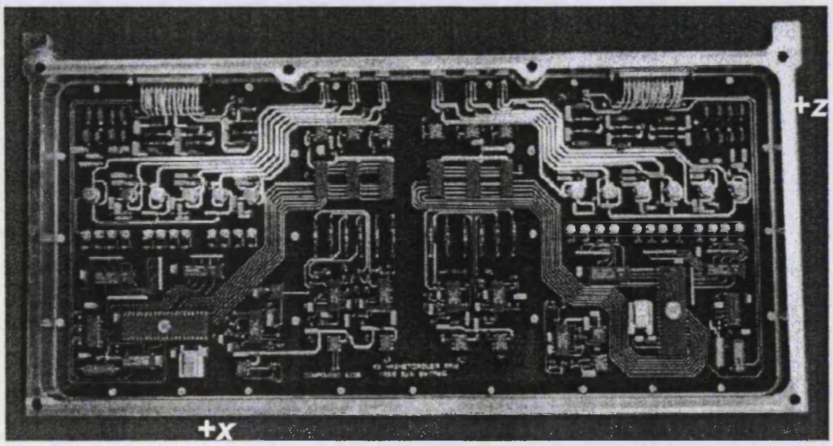

Figure 4-15 Photograph of magnetorquer module

The electrical characteristics of the magnetorquer module are listed in Table 4-12 and Table 4-13. The former lists the power consumption statistics. In stand-by mode, where the main power driving is not applied, one magnetorquer module consumes only 0.45W. When the +28V main power is driven at its maximum, the module uses almost 7W per axis, which in fact dissipates a large amount of heat. A considerable amount of design effort has been expended in dealing with this problem. The $-x$ facet in Figure 4-15 shows that 6 power transistors are mechanically and thermally connected to the module box frame. When the satellite is in normal operation, the frame behaves as a heat sink. Since the $-x$ facet faces towards dark space, it provides good thermal dissipation

Table 4-13 shows the result of in-rush current measurements of the magnetorquer modules when the power supply is turned on. The in-rush current characteristics are important since the solid-state power supply switches located in MTC1 have automatic power shutdown functions to protect over-current in its subsystems. Figure 4-16 shows positive and negative voltage switch circuits. The voltage drop over the resistor R_1 in both switches limits the maximum allowed output current, which generally occurs immediately after the power on.

Table 4-12 Measured power consumption (steady state at maximum drive)

	MTQR1 (mA, W)		MTQR2 (mA, W)	
+5V	22	0.11	23	0.12
+12V	15	0.18	16	0.19
-12V	12	0.14	11	0.13
+28V	247	6.9	247	6.9

Table 4-13 In-rush current measurement

Power	MTQR1		MTQR2	
	Max current (mA)	Duration (msec)	Max current (mA)	Duration (msec)
+5V	160	2	130	2
+12V	20	N/A	N/A	N/A
-12V	40	0.4	30	2
+28V	N/A	N/A	N/A	N/A

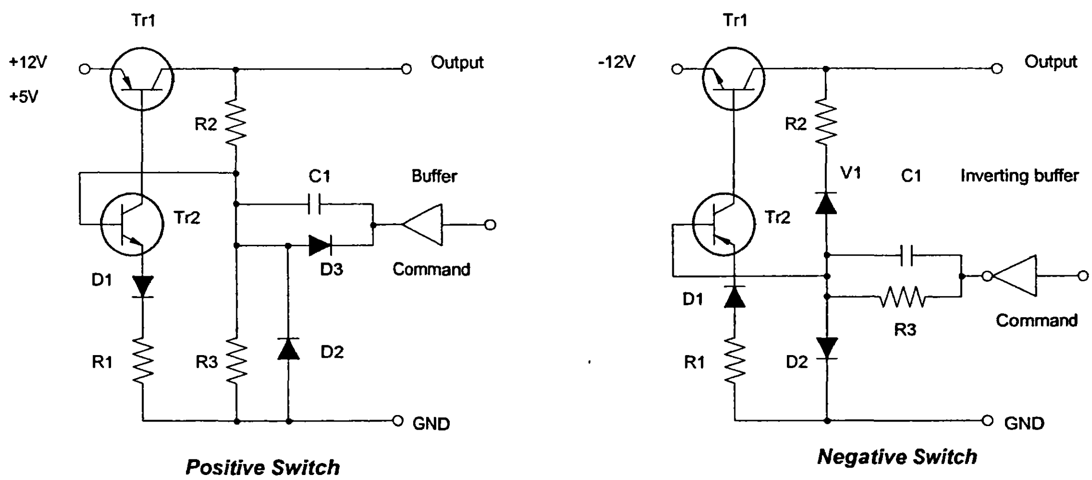

Figure 4-16 Power switches for magnetorquer

The in-rush current measurements were performed with an oscilloscope and current probe. It is considered that the initial spikes originate from the power supply. Thus, the actual peak values are believed to be less than the following measurement plots. The ripples in the +5V power line are the result of digital switching noise from the microprocessor and the crystal oscillator. The measurements indicate that the in-rush characteristics are not so severe as to cause power trip-off.

The duration of the peak current is also an important factor. The *RC* circuit next to the command buffer has a time constant that should be longer than the peak current duration in order to ensure proper switching. Figure 4-20 is not a result from an in-rush current measurement but is a relay driving current for polarity and power on-off switching. Three consecutive switchings were commanded in the experiment. Two short negative peaks indicate the decoding time of the received data required in the micro-controller. Figure 4-20 shows that the +5V line current is approximately 200mA, which is larger than the power on in-rush current of 150mA. Therefore, we should take 200mA as the peak current.

Figure 4-21 is the test result of the current control of the magnetorquer. It is for single axis test. The figure shows the relationship of the output current according to the control input. It has very good linearity except for high control input cases. The output saturates at the input level of 240 (F0h). The saturation point depends on the resistive component in the coil, component preparation during the magnetorquer circuit implementation, and the stability of the +28V power.

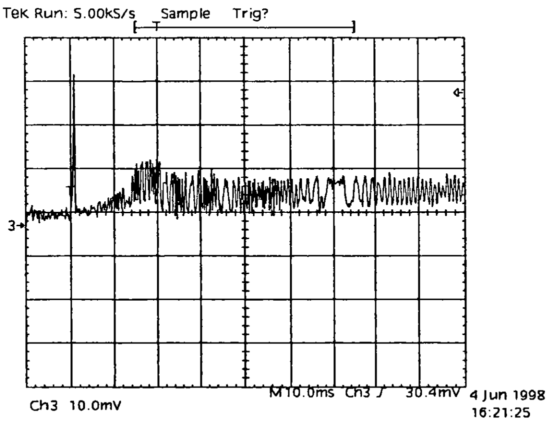

Figure 4-17 +5V in-rush current
(50 mA/div)

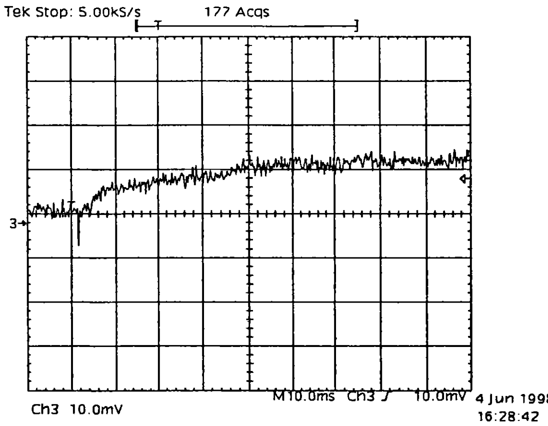

Figure 4-18 +12V in-rush current
(20 mA/div)

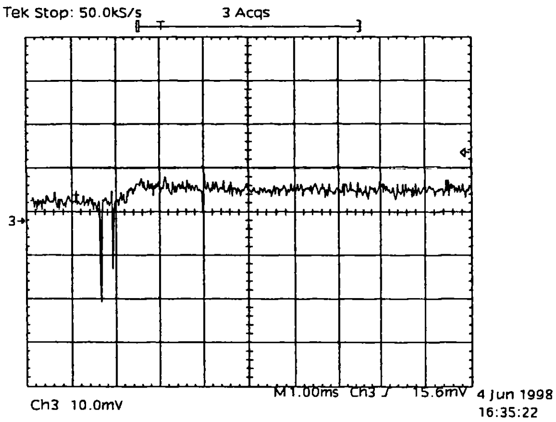

Figure 4-19 MTQR1 -12V in-rush current
(20 mA/div)

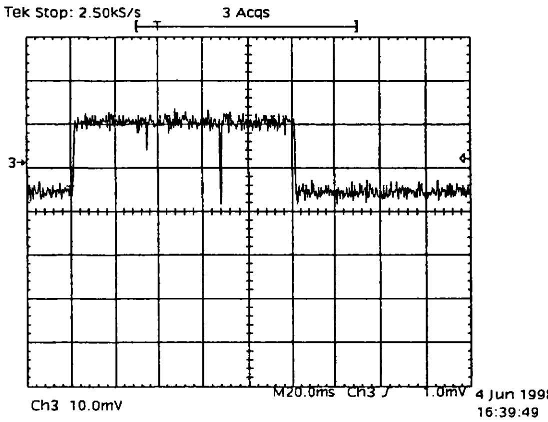

Figure 4-20 +5V Relay driving current
(100 mA/div)

It is safe to design the magnetorquering algorithm considering the saturation point at 232 (E8h). Thus, we can guarantee the linearity of the magnetorquer control output by paying off a fraction of power. The slope of Figure 4-21 indicates the efficiency of the module. What we are actually interested in is the amount of torque the satellite generates, which is linearly proportional to the current flow in the coil, as given in Equation (4-3). A change of the slope tends to occur simultaneously in all axes if the resistances of the control circuit change. This means that the magnitude of the control torque can be slightly different from the desired output. However, the direction of the control vector can be maintained reasonably well.

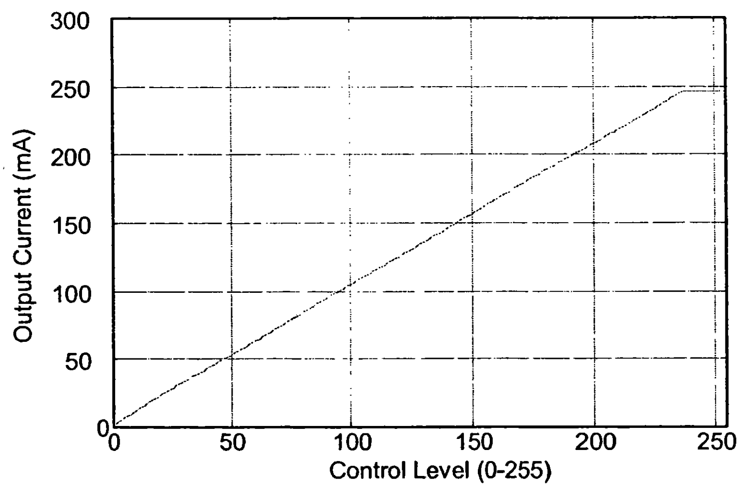

Figure 4-21 Current control result

4.1.9 System Analysis

The magnetorquer coil in KITSAT-3 can be modelled as a rectangular loop located in the x-y plane, as depicted in Figure 4-22. It induces magnetic field when current flows around the coil. The coil consists of four sides that can be considered as a group of infinitesimally small conductive lines dl.

Biot-Savart's law, Equation (4-6), from electromagnetic theory has to be adopted to calculate the magnetic flux density at $P(X,Y,Z)$ (Cheng, 1989),

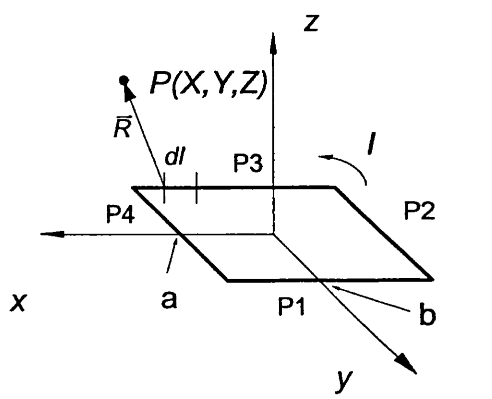

Figure 4-22 Rectangular coil configuration

$$\vec{B} = \frac{I\mu_o}{4\pi} \oint_C \frac{dl \times \vec{R}}{R^3} \tag{4-6}$$

where $\mu_o = 4\pi 10^{-6}$ H / m is the permeability of free space, I is the current, $\vec{R}$ is the position vector of P measured from dl, and the contour integral is to be carried out along the coil.

Figure 4-22 shows a rectangular coil of segment size, $2a$ and $2b$, with respect to the x and y axes. The magnetic field induced by each conductor can be easily obtained. Expressing the terms in Equation (4-6) according to the four-part configuration shown in Figure 4-22 results in

$$\text{Part 1 :} \quad \begin{aligned} dl &= -\boldsymbol{a}_x dx \\ \vec{R} &= \boldsymbol{a}_x(X - x) + \boldsymbol{a}_y(Y - b) + \boldsymbol{a}_z Z \\ dl \times \vec{R} &= \boldsymbol{a}_y Z dx - \boldsymbol{a}_z (Y - b) dx \end{aligned} \tag{4-7}$$

$$\text{Part 2 :} \quad \begin{aligned} dl &= -\boldsymbol{a}_y dy \\ \vec{R} &= \boldsymbol{a}_x(X + a) + \boldsymbol{a}_y(Y - y) + \boldsymbol{a}_z Z \\ dl \times \vec{R} &= -\boldsymbol{a}_x Z dy + \boldsymbol{a}_z (X + a) dy \end{aligned} \tag{4-8}$$

$$\text{Part 3 :} \quad \begin{aligned} dl &= \boldsymbol{a}_x dx \\ \vec{R} &= \boldsymbol{a}_x(X - x) + \boldsymbol{a}_y(Y + b) + \boldsymbol{a}_z Z \\ dl \times \vec{R} &= -\boldsymbol{a}_y Z dx + \boldsymbol{a}_z (Y + b) dx \end{aligned} \tag{4-9}$$

$$\text{Part 4 :} \quad \begin{aligned} dl &= \boldsymbol{a}_y dy \\ \vec{R} &= \boldsymbol{a}_x(X - a) + \boldsymbol{a}_y(Y - y) + \boldsymbol{a}_z Z \\ dl \times \vec{R} &= \boldsymbol{a}_x Z dy - \boldsymbol{a}_z (X - a) dy \end{aligned} \tag{4-10}$$

, where $\boldsymbol{a}_x, \boldsymbol{a}_y,$ and $\boldsymbol{a}_z$ are the orthonormal vectors of the coordinate, xyz, defined in Figure 4-22.

By substituting the Equation (4-7) ~ (4-10) into (4-6) gives rise to the magnetic field equations formed by the rectangular coil.

$$\vec{B}_1 = \frac{-I\mu_o}{4\pi}\int_{+a}^{-a}\frac{\boldsymbol{a}_y Z - \boldsymbol{a}_z (Y-b)}{\left[(X-x)^2 + (Y-b)^2 + Z^2\right]^{3/2}}dx$$

$$\vec{B}_2 = \frac{-I\mu_o}{4\pi}\int_{+b}^{-b}\frac{-\boldsymbol{a}_x Z + \boldsymbol{a}_z (X+a)}{\left[(X+a)^2 + (Y-y)^2 + Z^2\right]^{3/2}}dy$$

$$\vec{B}_3 = \frac{I\mu_o}{4\pi}\int_{-a}^{+a}\frac{-\boldsymbol{a}_y Z + \boldsymbol{a}_z (Y+b)}{\left[(X-x)^2 + (Y+b)^2 + Z^2\right]^{3/2}}dx \tag{4-11}$$

$$\vec{B}_4 = \frac{I\mu_o}{4\pi}\int_{-b}^{+b}\frac{\boldsymbol{a}_x Z - \boldsymbol{a}_z (X-a)}{\left[(X-a)^2 + (Y-y)^2 + Z^2\right]^{3/2}}dy$$

Equation (4-11) can be solved in closed form utilising the following indefinite integral formula.

$$\int\frac{dx}{(x^2+k)^{3/2}} = \frac{1}{k}\frac{x}{\sqrt{x^2+k}} + C \tag{4-12}$$

If we define the constant terms in Equation (4-11) as in Equation (4-13), and make proper modifications of the integration intervals, we can obtain the results in Equation (4-14).

$$\begin{aligned} k_1 &= (Y-b)^2 + Z^2 \\ k_2 &= (X+a)^2 + Z^2 \\ k_3 &= (Y+b)^2 + Z^2 \\ k_4 &= (X-a)^2 + Z^2 \end{aligned} \tag{4-13}$$

$$\vec{B}_1 = \frac{I\mu_o}{4\pi}\left[\boldsymbol{a}_y Z - \boldsymbol{a}_z (Y-b)\right]\frac{1}{k_1}\left[\frac{X+a}{\sqrt{(X+a)^2+k_1}} - \frac{X-a}{\sqrt{(X-a)^2+k_1}}\right]$$

$$\vec{B}_2 = \frac{I\mu_o}{4\pi}\left[-\boldsymbol{a}_x Z + \boldsymbol{a}_z (X+a)\right]\frac{1}{k_2}\left[\frac{Y+b}{\sqrt{(Y+b)^2+k_2}} - \frac{Y-b}{\sqrt{(Y-b)^2+k_2}}\right]$$

$$\vec{B}_3 = \frac{I\mu_o}{4\pi}\left[-\boldsymbol{a}_y Z + \boldsymbol{a}_z (Y+b)\right]\frac{1}{k_3}\left[\frac{X+a}{\sqrt{(X+a)^2+k3}} - \frac{X-a}{\sqrt{(X-a)^2+k_3}}\right] \tag{4-14}$$

$$\vec{B}_4 = \frac{I\mu_o}{4\pi}\left[\boldsymbol{a}_x Z - \boldsymbol{a}_z (X-a)\right]\frac{1}{k_4}\left[\frac{Y+b}{\sqrt{(Y+b)^2+k_4}} - \frac{Y-b}{\sqrt{(Y-b)^2+k_4}}\right]$$

Therefore, the total magnetic flux density induced by the entire loop is the vector sum of the four components in Equation (4-14). It can be simplified if we define the terms in Equation (4-14) as follows

$$M_1 = \frac{1}{k_1}\left[\frac{X+a}{\sqrt{(X+a)^2+k_1}} - \frac{X-a}{\sqrt{(X-a)^2+k_1}}\right]$$

$$M_2 = \frac{1}{k_2}\left[\frac{Y+b}{\sqrt{(Y+b)^2+k_2}} - \frac{Y-b}{\sqrt{(Y-b)^2+k_2}}\right]$$

$$M_3 = \frac{1}{k_3}\left[\frac{X+a}{\sqrt{(X+a)^2+k3}} - \frac{X-a}{\sqrt{(X-a)^2+k_3}}\right] \tag{4-15}$$

$$M_4 = \frac{1}{k_4}\left[\frac{Y+b}{\sqrt{(Y+b)^2+k_4}} - \frac{Y-b}{\sqrt{(Y-b)^2+k_4}}\right]$$

Hence, the total sum becomes

$$\begin{aligned}\vec{B}_{total} &= \vec{B}_1 + \vec{B}_2 + \vec{B}_3 + \vec{B}_4 \\ &= \frac{\mu_o I}{4\pi}\{\boldsymbol{a}_x Z(M_4 - M_2) + \boldsymbol{a}_y Z(M_1 - M_3) \\ &+ \boldsymbol{a}_z[(X+a)M_2 - (X-a)M_4 + (Y+b)M_3 - (Y-b)M_1]\}\end{aligned} \tag{4-16}$$

The magnetic field flux density near the loop can be calculated according to the equation (4-16). Figure 4-23 shows the result when B_z is plotted for the plane 10 cm above the x-y plane. The values of 2a and 2b are assigned as 64 cm and 41 cm according to Table 4-2. The current, I, and the number of turns of the coil, N, are assumed as 250 mA and 140 turns, respectively.

Other magnetic field components, B_x and B_y, with the same configuration as Figure 4-23, are shown in Figure 4-24 and Figure 4-25. The results show that the magnetic field along the z axis has a rectangular shape similar to that of the coil and it is also the major component. B_x and B_y have interesting characteristics along the boundaries of the coil. It helps to figure out the dipole nature of the loop.

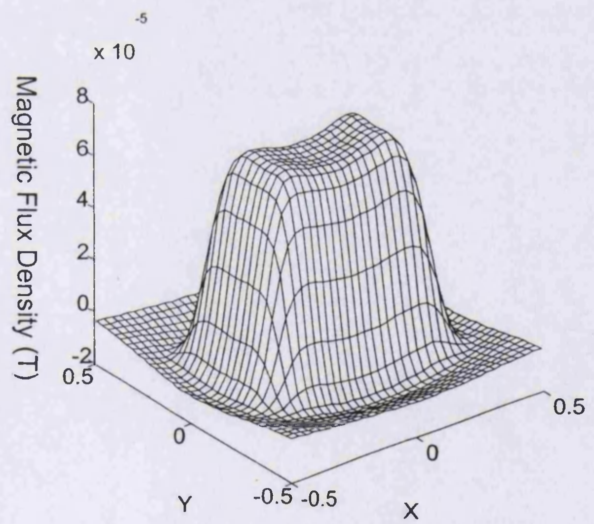

Figure 4-23 Magnetic flux density of B_z at the plane z=0.1

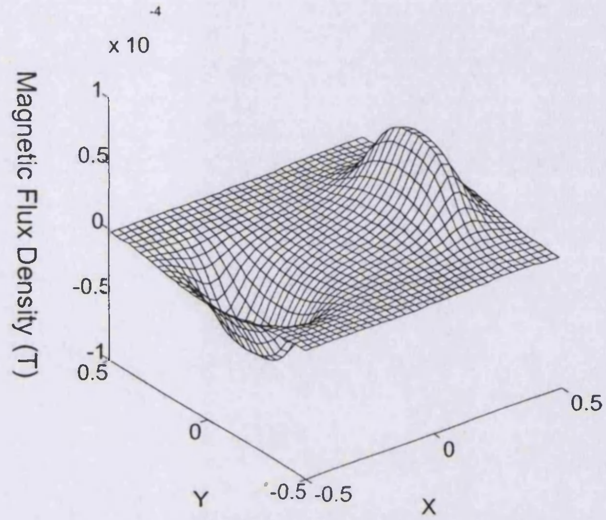

Figure 4-24 Magnetic flux density of B_x at the plane z=0.1

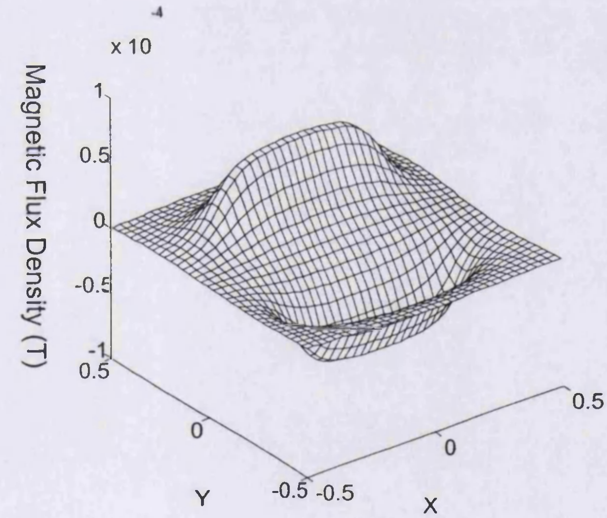

Figure 4-25 Magnetic flux density of B_y at the plane z=0.1

The results of magnetic flux density analysis imply that there are magnetic dipole characteristics and the geometric shape of the coil is directly coupled with the flux density profile. However, we are more concerned in showing the relation between the torque generated by the coil in conjunction with the geomagnetic field. This can be discussed in the following way.

The magnetic force on a differential element of conductor is given as

$$d\vec{F}_m = Idl \times \vec{B} \tag{4-17}$$

Therefore, the magnetic force on a complete (closed) circuit of contour C that carries a current I in a magnetic field $\vec{B}$ is then,

$$\vec{F}_m = I\oint_C dl \times \vec{B} \tag{4-18}$$

If there is a uniform magnetic field, *i.e.* geomagnetic field at a specific position, we can resolve it in a vector form as

$$\vec{B} = \boldsymbol{a}_x B_x + \boldsymbol{a}_y B_y + \boldsymbol{a}_z B_z \tag{4-19}$$

Assuming that we have the same coil configuration as Figure 4-22, the perpendicular magnetic field component is $\boldsymbol{a}_z B_z$. It results in forces $2IbB_z$ on segments 1 and 3 and forces $2IaB_z$ on segments 2 and 4. All the forces are directed outward from the centre of the loop. The vector sum of these four forces is zero, and no torque is produced.

The parallel component of the magnetic flux density, $\boldsymbol{a}_y B_y + \boldsymbol{a}_z B_z$, produces the following forces on the four segments.

$$\begin{aligned} \vec{F}_1 &= -2bI\boldsymbol{a}_z B_y = -\vec{F}_3 \\ \vec{F}_2 &= 2aI\boldsymbol{a}_z B_x = -\vec{F}_4 \end{aligned} \tag{4-20}$$

Again, the net force on the loop is zero. Therefore, there is no force induced by the coil when it is placed in uniform magnetic field perpendicular to the loop plane.

The magnetic torque is caused from the coplanar components of the uniform magnetic field. Although the net force is zero as derived in Equation (4-20), the force pairs 1, 3 and 2, 4 result in a net torque, $\vec{T}_{13} = -4abIB_y\boldsymbol{a}_z$ and $\vec{T}_{24} = 4abIB_x\boldsymbol{a}_y$. The total torque on the rectangular loop is then

$$\vec{T} = \vec{T}_{13} + \vec{T}_{24} = -4Iab(B_y\boldsymbol{a}_x - B_x\boldsymbol{a}_y) \tag{4-21}$$

Since the magnetic moment of the loop is defined as $\vec{m} = 4abI\boldsymbol{a}_z$, Equation (4-21) becomes

$$\vec{T} = \vec{m} \times (B_y \boldsymbol{a}_x - B_x \boldsymbol{a}_y) = \vec{m} \times \vec{B} \tag{4-22}$$

Therefore, Equation (4-3) is verified. It should be noted that the torque formula could be interpreted as the vector product of the unit normal vector of the planar loop to the magnetic field that is proportional to the area of the loop. In fact, this notion holds for any planar loop in a uniform magnetic field.

The above equation is derived for a single planar loop. The motivation of developing a 3-axis torque driving scheme was utilisation of a multiple number of coils simultaneously. Therefore, we have to make sure that reciprocal interaction between individual coils does not generate unwanted disturbance torque. Although they affect each other, the net effect is zero, since the interaction torques are opposite. Therefore, we can use the magnetorquer based on the principle of superposition.

$$\vec{T} = \sum \vec{m} \times \vec{B} = \sum (\vec{m} \times \vec{B}) \tag{4-23}$$

The magnetorquer wires have resistive and inductive properties as shown in Table 4-11. Figure 4-26 is an equivalent electrical circuit for the coil. The loop current I can be expressed with a differential equation as

$$V(t) = i(t)R + L\frac{di(t)}{dt} \tag{4-24}$$

Therefore, the turn-on characteristic can be evaluated based on this equation. A simulated step input of 25V is applied at 0.2 msec in Figure 4-27, where the inductance and the resistance are assumed as 14 mH and 100 Ω, respectively. It takes 0.64 msec to reach 99% of the steady state value. Considering that the transistor switch in Figure 4-8 has fast switching speed, better than 1 μsec, and the maximum control bandwidth of the ADCS is 2 Hz, we can neglect the inductive property in practice.

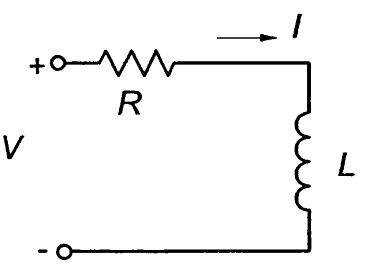

Figure 4-26 Magnetorquer equivalent circuit

The magnetic moment equation in (4-1) can be rewritten as

$$\vec{m} \approx \frac{NA}{R} Q(V)\vec{n} \tag{4-25}$$

, where $Q(V)$ is a quantisation function of the control input.

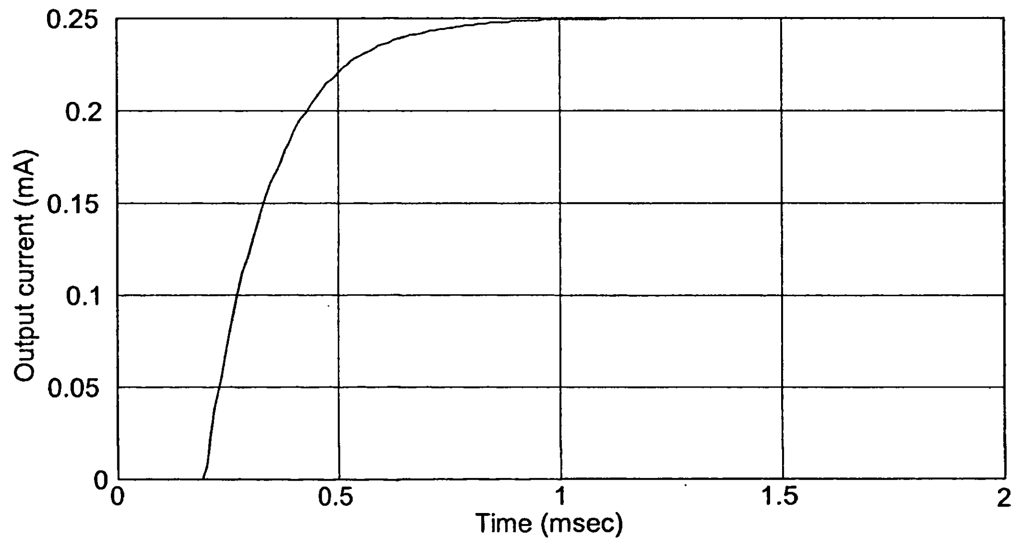

Figure 4-27 Magnetorquer turn-on characteristic

The thermal issue raised in 4.1.8 needs a further analysis. The maximum power handled by the transistor and the temperature of the device junctions are related since the power dissipated by the device causes an increase in temperature at the junction of the device. The power dissipation, however, is only allowed up to some limit temperature. Above this temperature the power dissipation and handling capacity of the device are reduced.

The limiting factor in power handling capacity of a particular transistor is in the temperature of the collector junction. Power transistors are mounted in large metal cases to provide large areas from which the heat generated by the device may radiate. If the device is mounted on some form of heat sink, its power-handling capacity can approach the rated maximum value more closely. In another word, it is necessary to derate the amount of maximum power allowed for a particular transistor as a function of increased case temperature. The power-derating characteristic of the power transistor BD785 given by the manufacture is in Figure 4-28.

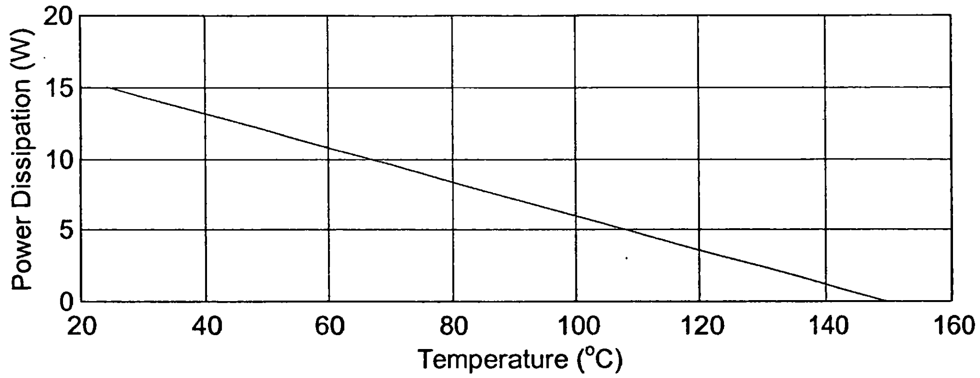

Figure 4-28 Power derating curve for the transistor

The curve shows that linear derating take place after 25°C. The maximum power-handling capacity reaches 0W at 150°C. The linear part can be expressed in mathematical form as

$$P = P_o - D(T - T_o) \tag{4-26}$$

, where T_o is the temperature at which derating begins, T is the particular temperature of interest, P is the maximum power dissipation over T_o, D is the derating factor.

The power transistor dissipates approximately 3.5W in worst case. It allows 120 °C as the maximum operation temperature.

The thermal resistance between the junction and the case of the power transistor, $R_{\theta jc}$, is given as 8.34 °C/W from manufacturer's data. The thermal resistance of the insulator positioned between the transistor case and the module box, $R_{\theta cm}$, is also given as 0.8 °C/W. The summation of these resistance values, $R_{\theta jm}$, gives rise to the system characteristic. Applying the Kirchhoff's law results in the junction temperature floats on the ambient temperature T_a (Boylestad & Nashelsky, 1987).

$$T_j = PR_{\theta jm} + T_a \tag{4-27}$$

If we add some margin to the thermal resistance value, then we can assume $R_{\theta jm} = 10°\text{C/W}$. The ambient temperature is practically quite close to that of the aluminium module box. The pre-launch thermal analysis and in-orbit telemetry data results showed that the temperature is almost stable around 25 °C. Inserting these boundary values, the worst case junction temperature becomes 60 °C, which is far below the design requirement, 120 °C. If we consider that the operation duty cycle is 10%, the junction temperature will be maintained less than 28.5 °C in normal operation. The worst case analysis can be applied for the case when the OBC crashes before the watchdog is triggered.

Figure 4-29 is the plot of the in-flight telemetry of the temperature of OBC and RCU module boxes for one day. Since, temperature sensor is not mounted on the MTQR box, the nearest temperature sensor readouts were used. The position of the RCU box temperature sensor is closer to the actual magnetorquer box. 25 °C is used as the nominal temperature of the MTQR box based on this result.

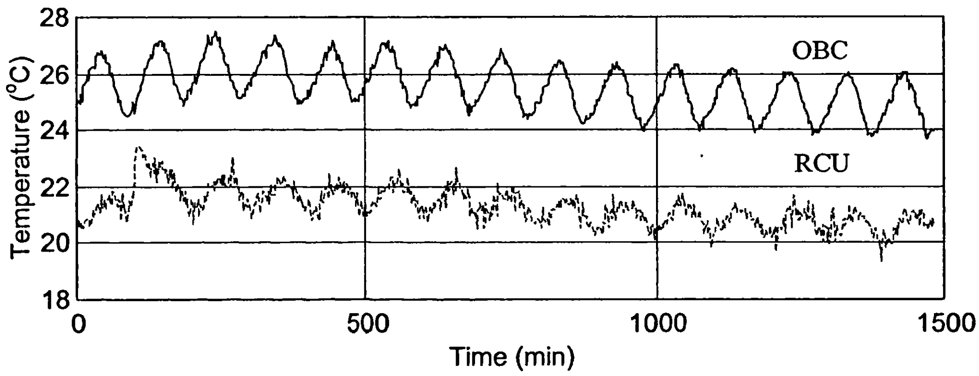

Figure 4-29 Flight telemetry of the temperature

4.2 Reaction Wheel

4.2.1 Introduction

As mentioned in Chapter 2, originally a single momentum wheel system was proposed for the attitude control actuator configuration. This was because attitude control about the pitch axis was mostly required for a successful mission. However, the restriction in the orbit selection for a piggybacked spacecraft and the engineering test nature of the mission objectives made us take a different approach for the ADCS configuration design.

Momentum wheels may be operated at either a constant or a variable speed and are used to control the spin rate and attitude about the wheel axis (Wertz, 1978). Therefore, the alignment of the principal axis of the satellite body and the wheel axis is a very important element in fabricating the mechanical system for single momentum wheel configuration. Moreover, the controllability of the satellite is confined to the axis parallel to the wheel axis. A large number of geostationary communication satellites adopt biased momentum wheel systems, where attitude manoeuvres are not required in normal operation (Agrawal, 1986). Figure 4-30 is a typical structure of a biased momentum wheel control system.

The biased momentum wheel system exploits the gyroscopic stiffness to produce a resistance against disturbance. The principle of conservation of angular momentum vector renders the satellite to withstand environmental torques in a passive manner. When the wheel speed is changed, it causes the satellite to react in such a way as to conserve the total angular momentum of the satellite-wheel system . If the situation is as depicted in Figure 4-30, where the wheel axis is on the principal axis direction, the relation can be written as Equation (4-6).

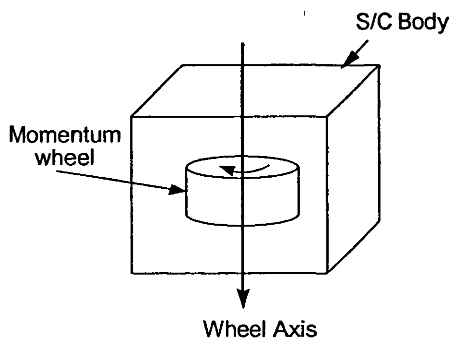

Figure 4-30 Biased momentum wheel control system

$$I_w \Delta\Omega = I_s \Delta\omega \tag{4-28}$$

, where I_w is the moment of inertia of the wheel rotor, $\Delta\Omega$ is the speed change of the wheel rotation, I_s is the moment of inertia of the whole satellite along the wheel axis, and $\Delta\omega$ is the spacecraft rotation rate change. The above equation also corresponds to the torque generated by the wheel if it is referred to Δt. As a matter of fact, this is a fundamental principle of a reaction wheel control system.

In essence all of the operations stated in Chapter 2 can be performed by single axis control as long as the wheel axis alignment is perfect and the solar panels are mounted to obtain the maximum Sun angle for a given local Sun time. However, we must take a certain degree of risk in selecting the orbit parameters and sacrifice the controllability of other two axes.

A 3-axis reaction wheel control system that uses at least 3 independently located wheels takes advantage of the momentum exchange technique described in Equation (4-6). The simplest way of building such a system is to use 3 orthogonal wheels as the *X*, *Y*, and *Z* wheels in Figure 4-31. The torque associated with a specific wheel controls the rotation motion of the satellite about that axis. It is dependent on the property of the eigen axes of the spacecraft body.

To increase the reliability of the control system, the arrangement method of the wheel axes can vary. One of the most commonly used arrangement is to add a fourth wheel to the 3 orthogonal wheel system in such a way that the redundant wheel has the same direction cosine vectors to all of the other 3 wheels. In some cases 4 wheels are placed with pyramidal orientations. (JAEA, 1992) The vector combination of torque in the 4-wheel system enables us to generate a desired torque even if a failure occurs in any one of the four wheels. Therefore, the reliability is increased twofold for any arbitrary axis.

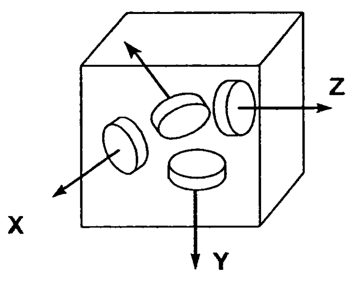

Figure 4-31 Skewed reaction wheel system

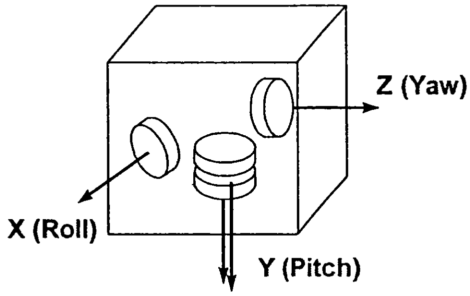

Figure 4-32 Three-axis reaction wheel system of KITSAT-3

The configuration of the reaction wheel system of KITSAT-3 is designed with a different approach. The operation scenario of the spacecraft is quite complicated. Although it is basically a 3-axis stabilisation system, the spinning control requirement for the space science experiment requires high pitch rate configuration. The formation of the wheel system is presented in Figure 4-32. The fourth redundant wheel is placed along the existing pitch axis wheel.

This special arrangement has the following advantages. Since all the wheels are oriented normally with respect to the spacecraft body axes, the mechanical design and machining process is quite simple. Compared to the skewed wheel system where the computational load is higher for coordinate transformations, the configuration in Figure 4-32 requires fewer calculations. Simultaneously operating two pitch wheels increases the torque and the momentum storage capacity twofold, which is useful for fast large angle manoeuvres and high-speed rotation control.

As mentioned previously a single pitch axis momentum wheel system may be applicable for the KISAT-3 mission. Therefore, increasing the reliability of the pitch axis by adding a parallel wheel is more attractive. However, failures either in the roll or the yaw axis may cause a problem since the mechanical system design did not consider the eigen axes alignments with the wheel axes. Thus, a nutation motion occurs since the instantaneous rotation axis is not aligned with a principal axis.

4.2.2 Hardware Descriptions

The reaction wheels, type DR01, manufactured by Teldix in Germany, were specially developed as low cost reaction wheels with integrated wheel drive electronics for use in small satellites. The wheels of this type were first delivered for the TUBSAT series of satellites for the Technical University of Berlin. The wheel is a ball bearing reaction wheel. It provides an angular momentum storage capacity of 0.1 Nms and a reaction torque of 4.7 mNm at 4000 rpm.

The wheel consists of four main subassemblies; flywheel mass, housing, motor with ball bearings and electronics. These are completely independent from each other and can be manufactured, measured, tested and exchanged separately. During the acceptance tests prior to the wheel delivery, a defect in the motor had been found and it was replaced with a spare part quite easily.

Figure 4-33 shows a cross-sectional view of the reaction wheel with the following main parts and subassemblies (Teldix, 1995).

Table 4-14 Reaction wheel subassemblies

1	Top housing	2	Bottom housing
3	Rotating mass	4	Motor support
5	Damping ring	6	Glass feedthrough
7	PCB & fixation screw	8	Rotating mass fixation screw
9	DC Motor fixation screw	10	DC motor

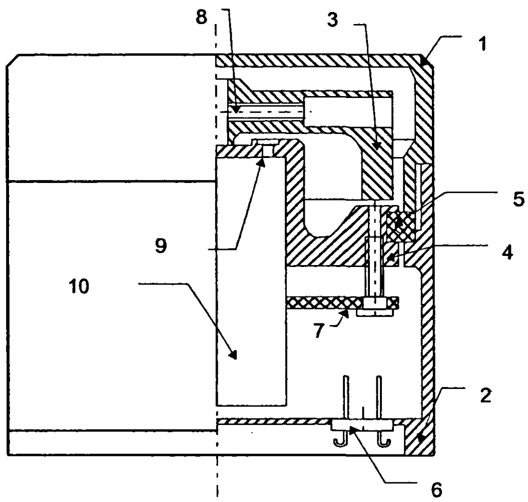

Figure 4-33 Cross-sectional view of the reaction wheel

The housing supports a damping ring (5) and the motor support (4), which carries the DC motor (10) with flywheel mass (3). The wheel is driven by a brushless DC motor. The motor support also holds up the PCB (7). The complete wheel is protected by an airtight housing, which is sealed by bonding.

The housing consists of a bottom housing (2) and a top housing (1). The bottom housing of the wheel forms the mechanical interface with the satellite's structure. The mechanical interface is defined by four feet that are relatively strong and stiff to achieve a high vibration load capability. The glass feedthrough (6) represents the electrical interface. The housing is sealed and not vacuumed.

The flywheel mass is essentially one piece of steel alloy. It is screwed to the shaft of the DC motor. The wheel and the motor were mounted and balanced as an assembly. Correction of the static and dynamic imbalances was carried out by adding balancing screws to the rim in two separate planes. The effects of the imbalance will be handled in Chapter 7.

The motor of the wheel can be subdivided into three subassemblies; motor rotor, stator, and commutation sensors. The motor is a brushless DC motor. It consists of a stator and a permanent magnet rotor. Commutation is performed electronically, using Hall sensors responding to the permanent magnets of the rotor. The stator winding forms three phases which are electrically 120° apart. The electronic commutation triggered by the Hall sensors avoids the possibility of life restrictions caused by wear, since physical contact is removed completely. The sensors feature simple design, low power dissipation and high reliability. The principal motor characteristics are summarised in Table 4-15. The system specifications of the reaction wheel are listed in Table 4-16.

Table 4-15 Motor characteristics

Number of phases	3
Armature resistance	8.4 Ω
Motor input voltage	12 V
Speed	Max : 5000 rpm, Nominal : 4000 rpm
Motor scale factor	20.2 mNm/A

Table 4-16 Reaction wheel specifications

Angular momentum at nominal speed	0.1 Nms
Nominal speed	4000 rpm
Operational speed range	± 4000 rpm
Speed limit	< 5000 rpm
Reaction torque @4000 rpm	4.7 mNm
Dimensions :	
Diameter	ϕ 80 mm
Height	70 mm
Mass	< 1.0 kg
Power consumption :	
Steady state @ Nominal speed	< 1.5W
Maximum torque @ Nominal speed	< 4.0W
Power interface :	
Supply voltage	12V ± 5%
Input current	< 1.5 A (max)
Signal interface	Digital speed command
Environmental conditions :	
Operating temperature	- 15°C ~ + 55°C
Storage temperature	- 25°C ~ + 65°C
Life time	5 Years (Design) 2 Years (Orbit)
Random vibration :	
30 Hz ~ 100 Hz	+6dB/oct
100 Hz ~ 800 Hz	0.03g^2/Hz
800 Hz ~ 2000 Hz	-3dB/oct
RMS Acceleration	7.3 g
Sinusoidal vibration : (Acceptance level)	
8 ~ 100 Hz	1.25 g
100 ~ 2000 Hz	0.8 g

The reaction wheels have passed a series of tests including sine and random vibration tests, post vibration tests and temperature tests which are all followed by performance tests. The stability of the wheel speed fulfilled the requirement of ± 1 rpm at 2000 rpm.

4.2.3 Electrical Interface

The glass feedthrough in Figure 4-33 provides the electrical interface with the satellite command and data handling system. Wires from the wheel are connected to the MTC4 by means of a separable D-type connector. Four lines are assigned for electrical interface per wheel. Two of them are for the while power interface, + 12V and ground, the other two are for serial communications.

Table 4-17 Electrical interface

Power supply	12V ± 5% (1 A max.), Ground
Serial interface :	
Baudrate	4800 bps
Protocol	Asynchronous 8 bits, No parity, 1 stop bit
Level	TTL (5V)

There are two modes of serial commanding. One is for speed command and the other is for speed reading. The reaction wheel system has a hand-shaking-type communication protocol; we transmit a byte and wait for receipt of an acknowledgement byte. If the received data is valid, we can proceed to the next step. Table 4-18 is the sequence of commands. One bit corresponds to 0.212 rpm in both sequences.

Table 4-18 Reaction wheel command sequence

Speed command sequence		Speed reading sequence	
Tx	FFh	Tx	0Ah
Rx	00h	Rx	Higher byte
Tx	Higher byte	Tx	0Bh
Rx	Higher byte	Rx	Lower byte
Tx	FEh		
Rx	01h		
Tx	Lower byte		
Rx	Lower byte		
Tx	14h		
Rx	ECh		

4.2.4 Mechanical Outline

The reaction wheel system is mechanically combined together with the gyro system. The whole system is named as *RCU* (Rate Control Unit) since it is able to measure and control the rotation rate of the satellite. The system has the same configuration as described in Figure 4-32. Three wheels are located in order to have orthogonal arrangements. The whole unit is mounted on a module box to facilitate easy access for mechanical assembly. A spare wheel and a gyro are positioned parallel to the *Y*-axis.

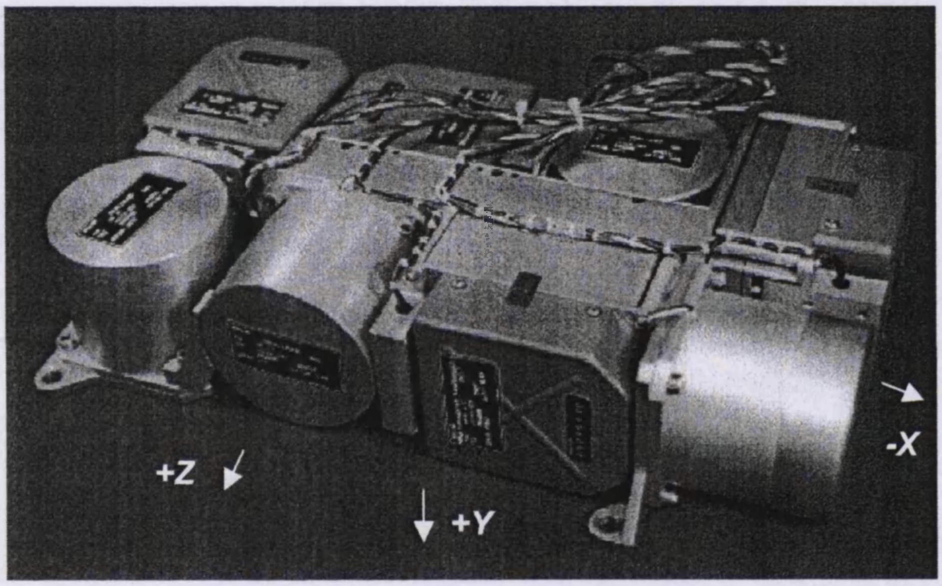

Figure 4-34 Photograph of RCU assembly

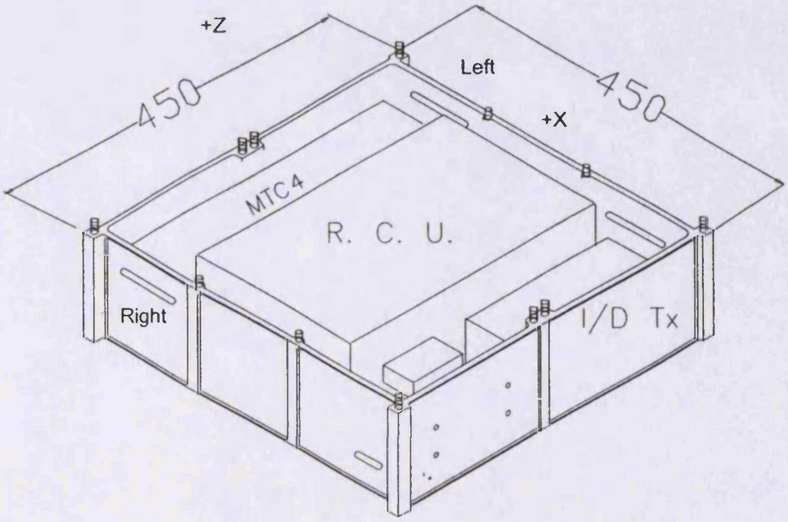

Figure 4-35 RCU module box mechanical shape

Figure 4-35 is the mechanical drawing of the RCU box located in the middle of the satellite. The RCU is mounted on the bottom of the module box using five M8 bolts with washers. The fixation holes can be seen in Figure 4-34. Since the RCU is relatively heavy, it is placed on the centre of the box, whilst MTC4 is located next to the unit for power and communication interfaces. The connectors of the MTC4 named as "Right" and "Left" are for external interfaces with other satellite subsystems.

The wheels and gyros in the RCU are named according to their axial designations as shown in Figure 4-36. The arrows in the figure indicate the mechanical orientations of the top housings. They are different from their actual directions. The sensing axes of the gyros are opposite to the arrows shown. Therefore, special care should be taken not to confuse the orientation system of the RCU. Comparing Figure 4-34, Figure 4-35, and Figure 4-36 gives the following axial reference table. Table 4-19 shows the reactions of the wheels when positive commands or readout requests are sent to the components. We should note that the x and y axes are negative oriented with respect to the satellite body frame.

The electrical interface consists of two 25 pin male D-type connectors. Each connector is dedicated to 2 wheels and 2 gyros. These connectors correspond to independent female connectors on MTC4. The grouping schemes and the definition of axes are shown in Figure 4-36.

Table 4-19 RCU orientation table

Component Name	Reaction to Positive Command / Reading
XW	Negative
YW	Negative
ZW	Positive
XG	Positive
YG	Positive
ZG	Negative

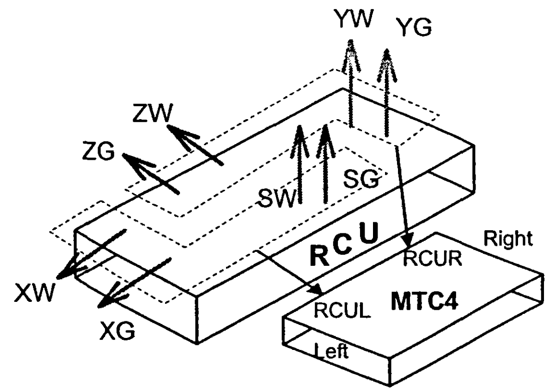

Figure 4-36 RCU component names and interfaces

4.2.5 Reaction Wheel Modelling

Conventional DC motors are highly efficient and their characteristics make them suitable for using as servomotors. However, their main drawback is that they require a commutator and brushes that are subject to wear and require maintenance. When the functions of a commutator and brushes were implemented by semiconductor switches, near maintenance-free motors were realised. Therefore, this type of a motor has great advantages for space applications where maintenance of the components is virtually impossible.

The armature windings are part of the stator and the rotor is composed of one or more magnets. Three-phase DC brushless motors are generally used in many applications, including the reaction wheels of KITSAT-3. When a three-phase brushless motor is driven by a three-phase bridge circuit, the efficiency, which is the ratio of the mechanical output power to the electrical input power is the highest (Kenjo & Nagamori, 1984).

The armature windings consist of three separate parts with Y or Δ-connections. We need to identify the position of the rotor to generate appropriate control signals to drive the current in the armature winding on time. Hall sensors are generally used for position detection nowadays. The motor drive logic sequentially turns on the power transistors connected to the windings to provide current paths. The stator's magnetic field creates adequate torque for the permanent magnet to rotate. The sequence determines the direction of rotation in bipolar motors and it is the key idea that could remove mechanical brushes.

The wheels and the gyros have been delivered as a unit as shown in Figure 4-34. Each sub-component of the RCU originally had its own connector for individual test.

Post-delivery tests were required since complete performance tests of the wheel were not performed in order to reduce the manufacturing cost. The configuration needs to be reformed as depicted in Figure 4-36 after completion of the tests.

The pre-integration test was performed with a test box shown in Figure 4-37. The test box can supply power lines for one wheel or gyro at a time. It also has to provide a data the conversion function to establish a communication between the components of RCU and a PC. The level converter circuit transforms the RS232 type signal into TTL level or vice versa. Therefore, the PC can give commands and collect experimental data from the sub-components. It then archives data on its memory system for further analysis.

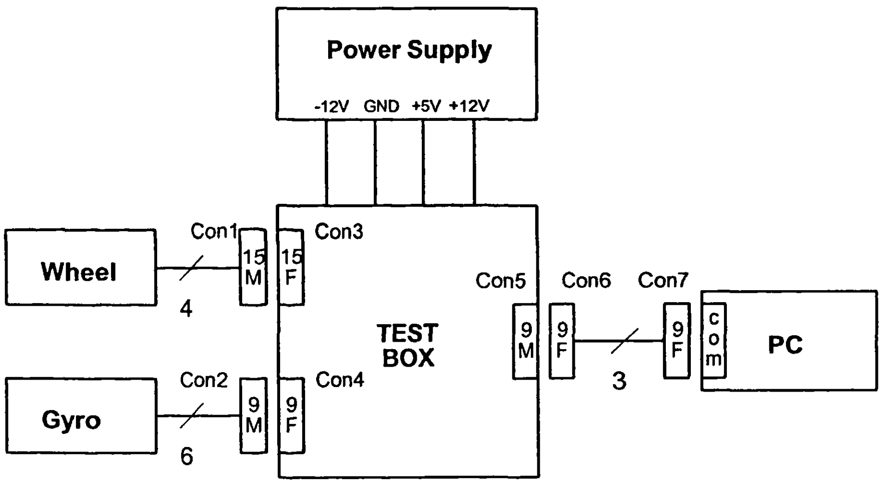

Figure 4-37 Test box set-up

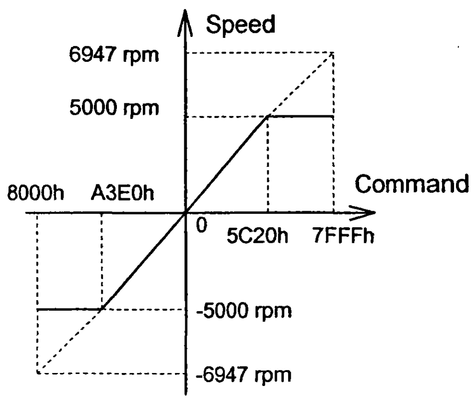

Figure 4-38 Command versus speed relation of the wheel

Figure 4-38 shows the command versus speed relation. The absolute maximum speed is limited by 5000 rpm. Any speed commands exceeding this limit will be handled with saturation logic. A speed command consists of a 2-byte code and it has hand-shaking communication protocol as explained in Table 4-18. Figure 4-38 shows that 5C20h corresponds to the positive maximum speed of 5000 rpm. The negative speed can be expressed with a 2's complement numbering method, where the most significant bit represents the sign of the number (Nagle *et al.*, 1975)

The first test was for the acceleration characteristics. Step input responses have been monitored by sending commands when the wheel is in stationary status. Speed commands of 1000, 2000, 3000, 4000, and 5000 rpm were executed and the resulting data are displayed in Figure 4-39. The plot is the result of actual speed readings of the wheel. The time step corresponds to 1/18.2 seconds, which is the fundamental frequency of the internal PC interrupt clock. (*i.e.* One hundred steps corresponds to 5.5 seconds.)

The starting time of the commands are manually synchronised to exhibit the acceleration characteristics of different target speeds. The figure shows that the slope is almost identical, regardless of the final target speed. It also reveals that the velocity readings at low speed have large uncertainties due to the limited number of position sensors. The problem at low speed looks more serious when we plot the torque data.

The moment of inertia of the wheel rotor, I_w, can be obtained from Table 4-16. The angular momentum storage capacity of wheel, H_w, is given as 0.1 N·m·sec when it is operated with 4000 rpm. Therefore, the Equation (4-29) gives the value of wheel moment of inertia, $I_w = 2.4 \times 10^{-4}\, kg \cdot m^2$.

$$H_w = I_w \times 2\pi \times 4000 \text{ rpm} / 60 \text{ sec} = 0.1 \text{ N} \cdot \text{m} \cdot \text{sec} \tag{4-29}$$

The torque graph in Figure 4-40 is calculated using Equation (4-30) and the speed measurement data in Figure 4-39. Changes between two consequent readings need to be calculated.

$$T_w = I_w \frac{\Delta\Omega}{\Delta t} \tag{4-30}$$

Figure 4-41 and Figure 4-42 are obtained when the zero speed command was sent while the wheel was rotating at 5000 rpm. The deceleration torque has a flat profile over a wide range of speeds. The calculated torque of an accelerating case in Figure 4-40 has a peak near 1000 rpm and decreases with an increase in speed.

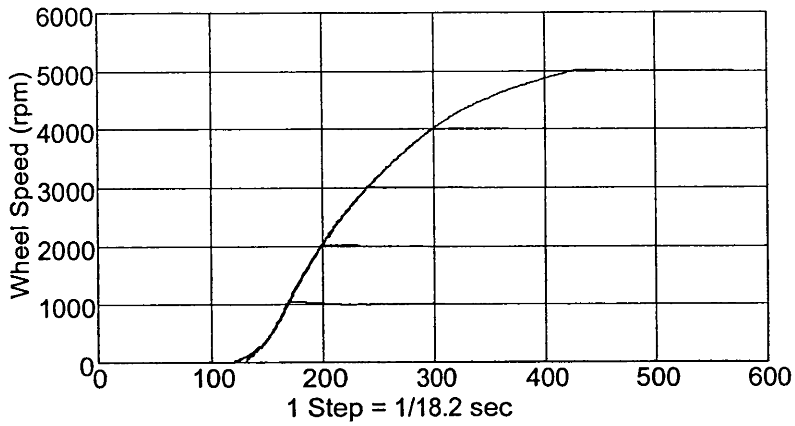

Figure 4-39 Step input response measurement of reaction wheel

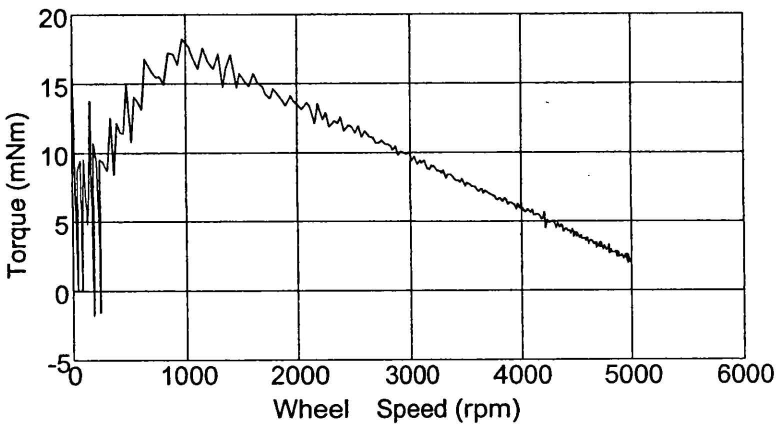

Figure 4-40 Acceleration torque

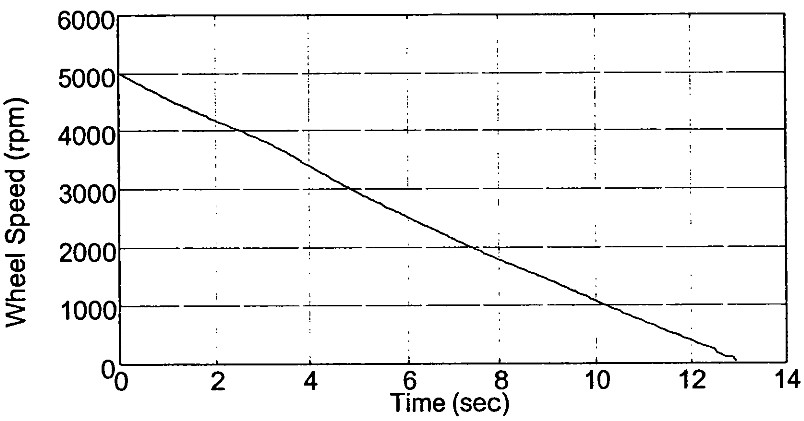

Figure 4-41 Decelerated wheel speed measurement

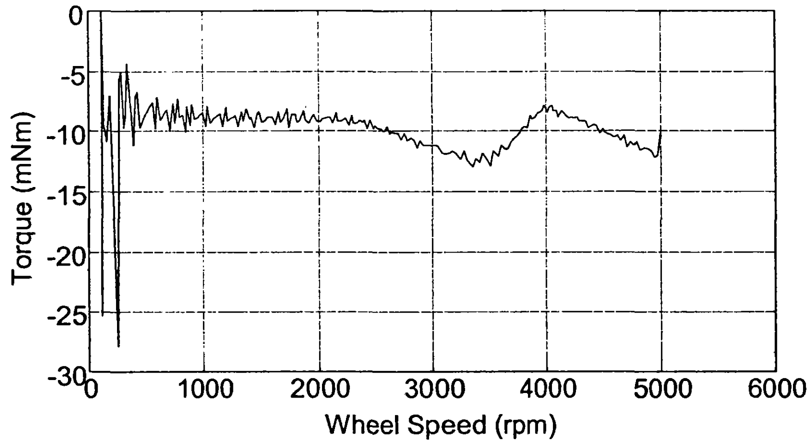

Figure 4-42 Deceleration torque

The low speed torque characteristic is totally different from an ordinary brushless DC motor, which has constant down slope over the whole operation range. It can be attributed to the fact that the wheel is designed for small satellites where high power is a critical problem. In view of the fact that that the torque is proportional to current, which implies consumed power, we can take advantage by limiting the torque at low speed. Problems incorporating this phenomenon will be discussed with the large angle manoeuvring control law.

For analytic purposes, it is essential to establish a mathematical model for the motor. The circuit diagram of a separately excited DC motor, where the magnetic flux, ϕ, is independent of the armature current, is shown in Figure 4-43 (Kuo, 1987). A brushless DC motor falls into this category, where R_a is the armature resistance, L_a is the coil inductance, and e_b is the back-emf voltage produced by the motor due to the duality as a generator.

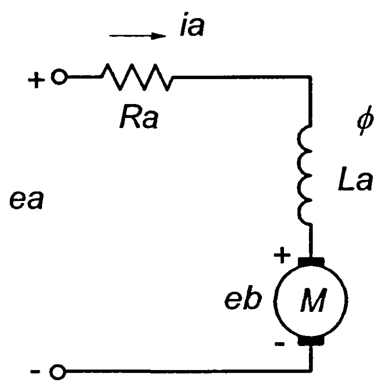

Figure 4-43 Model of a permanent magnet DC motor

The torque developed by the motor, T_w, is proportional to the constant magnetic flux and the armature current i_a. Then, the motor scale factor K_i can be defined as the parameter that represents the torque constant with respect to the current.

$$T_w(t) = K_i i_z(t) \tag{4-31}$$

The closed loop circuit system in Figure 4-43 gives rise to the following mathematical model in Equation (4-32).

$$e_a(t) = L_a \frac{di_a(t)}{dt} + R_a i_a(t) + e_b(t) \tag{4-32}$$

The voltage e_b and the rotation speed of a motor can be related by a back-emf constant K_b. Considering the viscous friction coefficient B_m, and the external load T_L, we can have a complete set of equation representing the dynamics of a motor as in Equation (4-33)

$$\begin{aligned} e_b(t) &= K_b \Omega(t) \\ T_w(t) &= I_w \frac{\Omega(t)}{dt} + B_m \Omega(t) + T_L(t) \end{aligned} \tag{4-33}$$

Therefore, the complete motor system can be summarised with a system block diagram in Figure 4-44. This diagram is used for the parameter estimations. The results are listed in Table 4-20 and are slightly different from the nominal values in Table 4-15

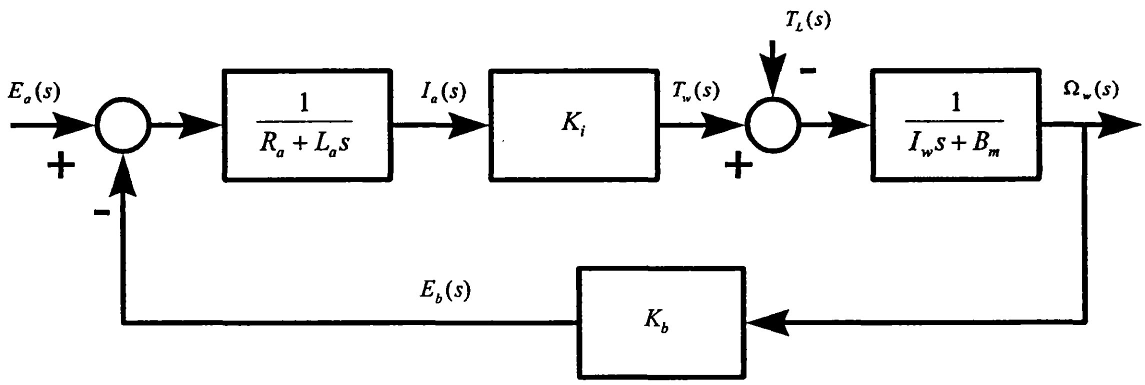

Figure 4-44 Block diagram of a DC motor system

Although functionally the torque scale factor K_i and the back-emf constant K_b are two separate parameters, for a given motor, their values are closely related. If they are expressed in SI units, the values are identical. The estimated K_i is slightly different from the specification given in Table 4-15. However, R_a coincides with the given specification. The viscous fraction coefficient B_m is set to be 0, since it is hard to measure and it has small effect in macro characteristics. The external load, T_L, is zero for a reaction wheel.

Based upon these estimated parameters, a simulation has been performed for a step input to drive the wheel with 5000 rpm. Figure 4-45 shows how well the model meets the actual measurement result.

Table 4-20 Estimated motor parameters

Parameters	Value
Ki	16.5 mN·m/A
Kb	16.5 mN·m/A
L	10 H
Ra	8.4 Ω
Bm	0 N/(m/sec)

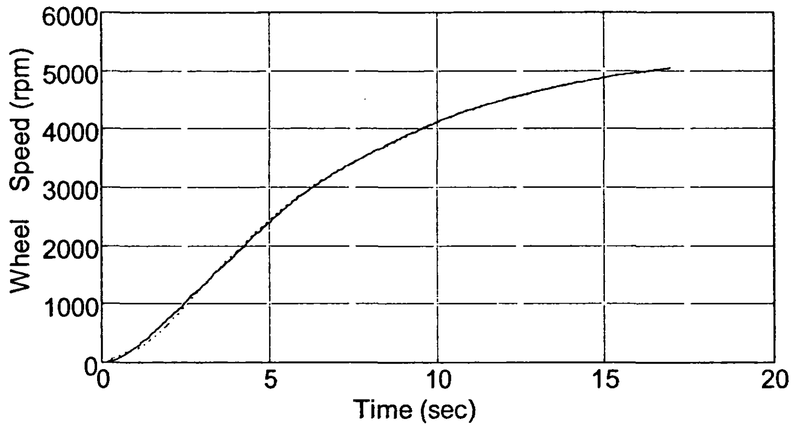

Figure 4-45 Measured and modelled speed history

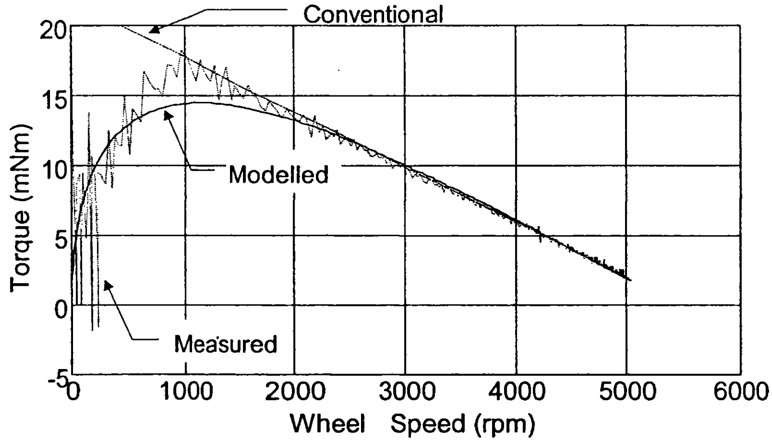

Figure 4-46 Measured and modelled torque characteristics

The solid curve in Figure 4-45 is the simulation result, where the speed limit of 5000 rpm is not considered. An unusually large value of L_a doesn't directly represent a physical inductance. It can be attributed to a software control algorithm to prevent over power consumption at low speed. By intentionally restricting the acceleration rate, we can limit the power consumption, which is a critical issue in small satellites.

Figure 4-46 shows the actual torque measurement and that of the simulated torque model developed based on Table 4-20. The straight line is a typical characteristic of an ordinary DC motor. The results indicate that near-zero speed control has large uncertainties. Using a small number of position sensors may cause this problem. If the motor is running very slowly, the position sensor cannot distinguish small position changes. It may result in a misinterpretation as a halt status, which will invoke excessive control input.

One of the most serious problems that the reaction wheel has is that only speed commanding is available. Torque commands are generally required as the control input for the attitude control. However, the simple and low cost design natures of the reaction wheel did not include the torque commanding capability. Therefore, exercising the torque control by using the speed command became an essential issue in developing the control algorithm.

Noise components in the position sensing and time delay effect due to the zero order holder make it impractical to use a hardware differentiator in torque control loop. In fact, the torque measurement is not a direct one. It is calculated value from the speed measurement. Therefore, differentiation will cause problems if it is used in torque control. A simple algorithm should be devised to cope with these problems.

If we define the desired torque at time $t = t_o + \Delta t$ as $T_c(t_o + \Delta t)$, and define the wheel speed at time $t = t_o$ as $\omega(t_o)$, then the wheel speed of $\omega(t_o + \Delta t)$ will bring up an approximated torque $T_c(t_o + \Delta t)$ at time $t = t_o + \Delta t$ as

$$\omega(t_o + \Delta t) = \omega(t_o) + \frac{T_c(t_o + \Delta t)}{K} \Delta t \tag{4-34}$$

Therefore, by sending a speed command of $\omega(t_o + \Delta t)$ to the reaction wheel, a desired torque $T_c(t_o + \Delta t)$ will be generated if the current wheel speed $\omega(t_o)$ is within the available torque boundary shown in Figure 4-46. The constant K is basically identical to the moment of inertia of the wheel, I_w. Since the wheel command is in hexadecimal numbers based on rpm unit with a minimum control bit of 0.212 rpm, a unit conversion is required to improve the calculation speed of the controller. The following relation is used for K.

$$K = I_w \frac{2\pi}{60} \times 0.212 = 5.3 \times 10^{-6} \text{ Nmsec / rpm} \tag{4-35}$$

The above value has inherently some error. Experimental results showed that actually $K = 5.0 \times 10^{-6}$ was more satisfying. The rest of the tests were carried out based on this empirical value.

As a starting point, the performance of sinusoidal torque tracking has been measured. Figure 4-47 is the result showing that the actual torque follows the commanded one. A peculiar phenomenon can be observed near zero speed. It can be clearly noted if we look at Figure 4-48 simultaneously. This figure is the speed history of the wheel during the torque control test. The speed itself is reasonably well behaved compared to the torque control case, which has numerical differentiation. As the wheel speed approaches zero, the uncertainty of the speed measurement increases. For this reason we should avoid operating the wheel near this point.

Another odd characteristic is that the decelerating rate is steeper than expected. When negative torque is commanded, the magnitude of the actual output is larger than the desired value. Discrepancies in the commanded and actual torque while decelerating can be seen clearly in Figure 4-47. This can be attributed to the different control algorithms applied for acceleration and deceleration. This problem was also attacked by an experimental method. $K = 7.5 \times 10^{-6}$ was found to be a more adequate value to resolve the problem. The following series of tests was performed with these two empirically found parameters.

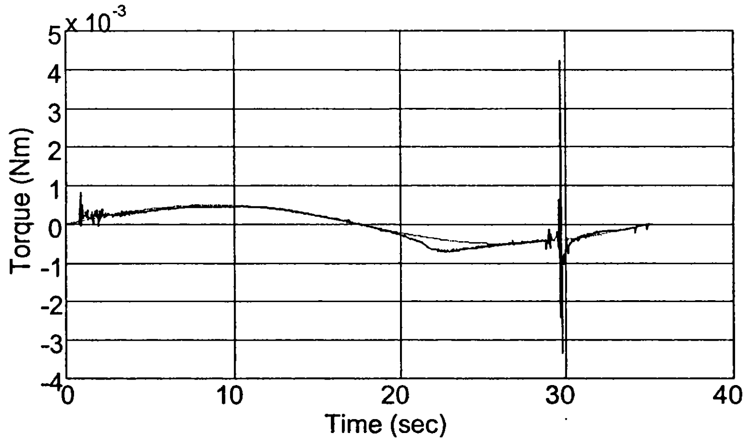

Figure 4-47 Sine torque tracking

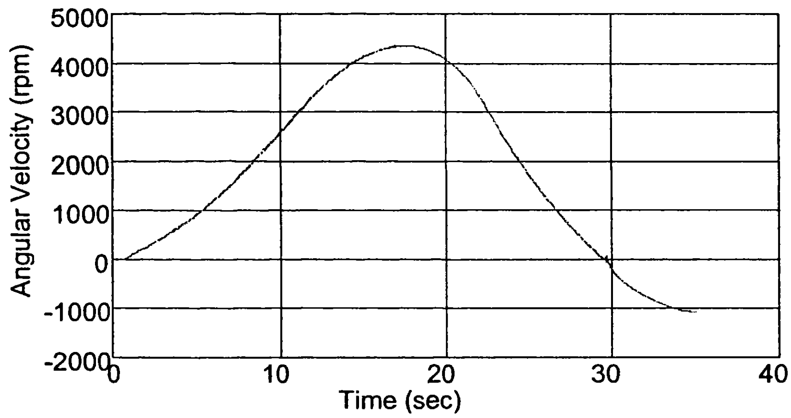

Figure 4-48 Command and actual wheel speed

The test results discussed so far tell us that operating the wheel near 2000 rpm will be the most attractive condition. The speed accuracy, torque generation capacity, torque level consistency and linearity are quite satisfying at this nominal speed. Further torque control tests were carried out when the initial wheel speeds were 2000 rpm.

Figure 4-49 and Figure 4-50 are the results of another torque control experiment. When the wheel was running at 2000 rpm, sinusoidal and square wave torques were commanded as the reference inputs, respectively. The frequencies of the reference input signals were taken relatively faster to avoid the situation when the wheel is rotating too far from the nominal rate. If the commanded torque is small, the wheel model can be simplified as a zero order holder with 2 Hz sampling frequency.

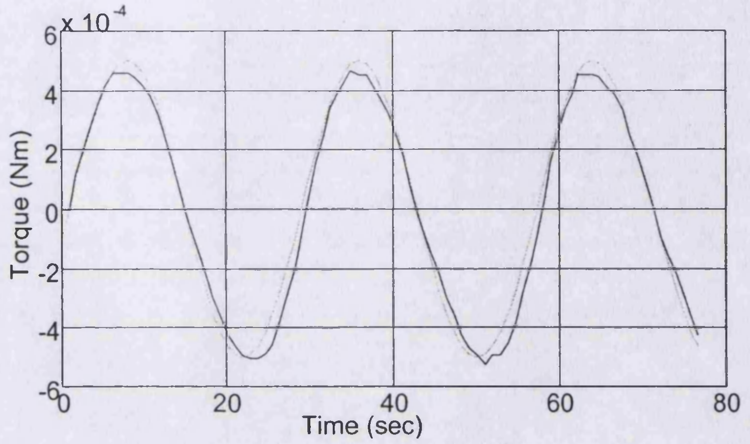

Figure 4-49 Fast sine torque tracking

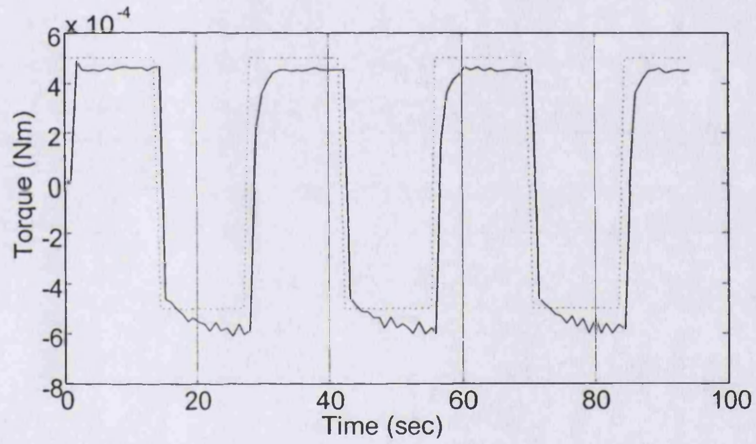

Figure 4-50 Fast square torque tracking

Chapter 5. Attitude Control System II : Sensors & Data Handling System

5.1 Fibre Optic Gyro

5.1.1 Introduction

To perform full three-axis control of a spacecraft, it is essential to have inertial sensors. Sun sensor, Earth Horizon Sensor (EHS), and magnetometer, are not adequate enough, especially when large angle manoeuvring is required. Faster sensor update rate is also desired to cope with fast control bandwidth.

Gyros can provide an attractive solution. A conventional mechanical mass spinning gyro utilises the principle of angular momentum conservation. State of the art modern micro-machining technology makes it possible to manufacture a gyro the size of a coin (Muller, 1995). However, this is only at an experimental stage. Generally, mechanical gyros are massive and consume high power; this obviously contradicts the mission concept of KITSAT-3. High failure rate during the launch is another problem. A spinning mass inherently generates unwanted angular momentum that makes the attitude control system more complicated.

Alternatively, laser gyros operate on the principles of general relativity (Siouris, 1993). Subsequently, they do not involve mechanically moving parts, which eliminates most of the previously mentioned disadvantages of mechanical gyros. There are two types of laser gyro, the ring laser gyro (RLG) and the fibre optic gyro (FOG). They are based on almost identical principles. Although RLGs have superior performance compared to FOGs, relatively high power consumption and high cost outweigh their advantages.

Table 5-1 Advantageous features of fibre optic gyro

• Instantaneous operational readiness after switch-on
• High reliability
• Absence of wear (No bearing or lubrication problems)
• Insensitive to vibration and shock
• High transmission bandwidth

5.1.2 Principles

The initial effort that gave impetus to the development of the laser gyro was performed by G. Sagnac. He used the *Sagnac Interferometer*, in which a beam splitter divided an incident beam so that one component beam traversed the perimeter of a rectangle in a clockwise direction and the other in a counter clockwise direction prior to recombination (Siouris, 1993). Two beams propagating in opposite direction around a closed path result in a shift in optical path when the system rotates normal to its path. Hence, the combined interference pattern shows a fringe shift proportional to the rotation rate. The early experiment by Michelson and Gale in 1925 demonstrated the feasibility of its practical implementation (Tipler, 1997).

If we consider an ideal circular interferometer, where the light is constrained to travel along the circumference as in Figure 5-1, light from the source is split by the beam splitter. Two beams travelling in opposite directions recombine at the same beam splitter after one rotation. For a stationary interferometer with a single loop the time to travel the complete path is

$$t = \frac{2\pi R}{c} \tag{5-1}$$

, where R is the radius of the circular path and c is the speed of light.

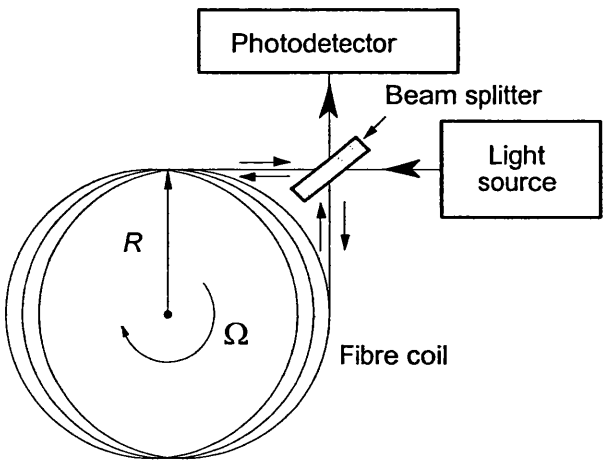

Figure 5-1 Principle of a fibre optic gyro

However, when the optical system in Figure 5-1 rotates about the axis perpendicular to the path, it experiences a relativistic phenomenon; the speed of light is independent of the speed of the light source. If we assume a constant rotation rate Ω during the time of interest, the time t_1 that takes for the light travelling in the clockwise direction can be calculated from

$$ct_1 = 2\pi R + R\Omega t_1 \tag{5-2}$$

Similarly, for the light in the other direction, the time t_2 is

$$ct_2 = 2\pi R - R\Omega t_2 \tag{5-3}$$

Therefore, the time difference Δt is given as

$$\Delta t = t_1 - t_2 = 2\pi R\left(\frac{1}{c - R\Omega} - \frac{1}{c + R\Omega}\right) = \frac{4\pi R^2\Omega}{c^2 - R^2\Omega^2} \tag{5-4}$$

Approximating Equation (5-4) with binomial expansion for $\frac{R\Omega}{c}$ describes the *Sagnac Effect* as shown in Equation (5-5). The expansion is valid for most navigational purposes where the rotation rate is small compared to the speed of light.

$$\Delta t \cong \frac{4\pi R^2\Omega}{c^2} \tag{5-5}$$

Here the optical path difference ΔL is found as

$$\Delta L = c\Delta t = \frac{4\pi R^2\Omega}{c} \tag{5-6}$$

Equation (5-6) implies that a rotation perpendicular to the plane of the optical path induces a path difference for the beams travelling in opposite directions. As a result the recombined light at the beam splitter produces an interference pattern, which varies as a function of the rotation rate of the optic system.

Let us consider an optical fibre with N turns and radius R as in depicted in Figure 5-1. The path difference ΔL_N is simply given as

$$\Delta L_N = N\Delta L = \frac{4\pi R^2 N\Omega}{c} \tag{5-7}$$

The phase difference $\Delta\phi$, hence, can be obtained as

$$\Delta\phi = 2\pi \frac{\Delta L_N}{\lambda} = \frac{8\pi^2 R^2 \Omega N}{\lambda c} \tag{5-8}$$

This produces a change in the intensity of the fringe pattern at the detector. Measuring the outputs of the photo-detector gives rise to the phase difference, thus the rotation rate can be measured.

The fibre optic gyro used in KITSAT-3, MFK 4-1, has a coupler instead of a beam splitter. A laser diode is used as the light source. To increase the accuracy, a second coupler, a polariser, a phase modulator and a depolariser are provided (Teldix, 1995). A change of the interference pattern causes a variation in the intensity that is sensed by the detector. An amplifier converts the detector signal to an equivalent voltage output. From this signal an analogue to digital converter (ADC) obtains sample values at the frequency synchronous to the phase modulation. These digital signal values are fed to a signal processor that analyses the frequency spectrum of the received signal to calculate the actual angular data.

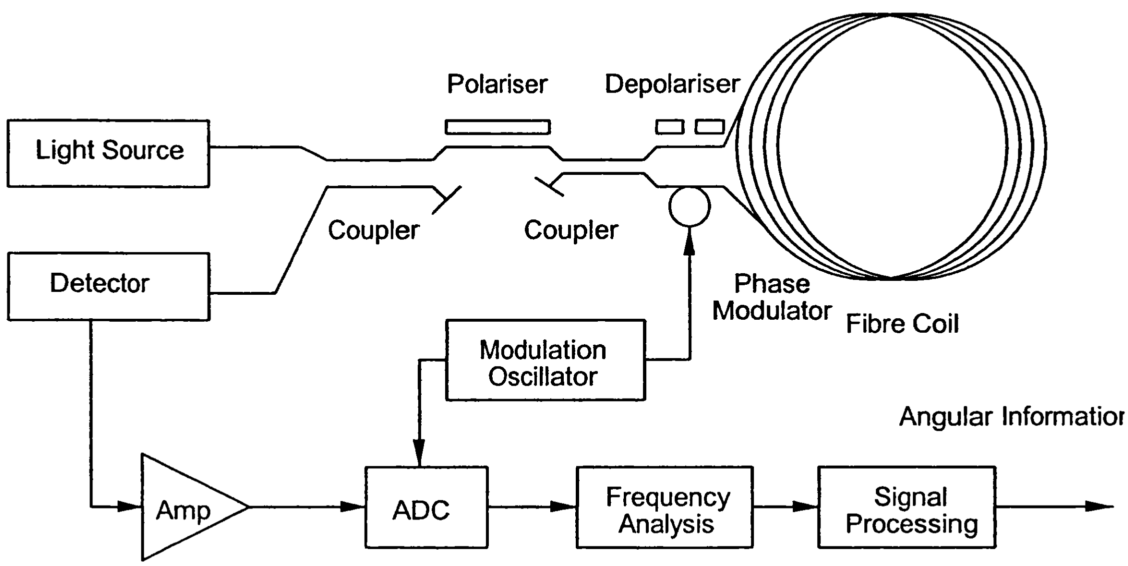

Figure 5-2 Optical and signal detection concept of FOG

5.1.3 Specifications of the FOG

The followings are specifications of the FOG, MFK 4-1.

Table 5-2 Specifications of MFK 4-1

Parameters	Values
Scale factor	2^{-12} deg / LSB
Dynamic range	±200 deg / sec
Dimension	109 mm × 73 mm × 85 mm
Weight	< 670 g
NER (Noise Equivalent Rotation rate)	< 30 deg / h / √Hz
Random Drift	< 3 deg / √h (1 σ)
Bias Uncertainty	<10 deg / h (1 σ)
Scale factor error	< ± 2000 PPM
Operation temperature	-30°C ~ +70°C
Power supply	±12 or ±15V, +5V
Power consumption	< 3W

5.1.4 Interface

The FOG of the type MFK 4-1 has a SUB-D 44-pin high-density connector electrical interface. It has 16-bit parallel data lines, other control and status signals and power lines. However, due to its complexity in harnessing, especially for 4 gyros on board, a parallel to serial adapter has been used to reduce the number of lines. TTL level (0~5V) serial data communication handles command and telemetry data in a transparent manner. As a result, there are only 6 required lines for the gyro.

Table 5-3 Communication protocol

Type	Asynchronous
Baud rate	4800 bps
Format	1 start bit, 8 data bits, 1 stop bit
Parity	No parity

Table 5-4 Pin assignment for FOG interface

Pin	Description
1	+15 or +12 V
2	-15 or -12 V
3	+5V
4	Ground
5	Rx data
6	Tx data

There are two basic commands for the adapter.

- A6h : Echoes an acknowledge → Relay the following 2 bytes to the gyro directly → Send the reaction 2 bytes from the gyro to user
- A7h : Echoes an acknowledge → Make gyro reset → Send A5A5h

In case of A6h, the adapter passes the immediately following 2 bytes to the main gyro unit and sends back the result from the gyro to the user. Therefore, the 2-byte commands in Table 5-5 can be sent via the serial link between the gyro and the adapter.

Table 5-5 Gyro commands

Command	Function
01xxh	Read out angle increment
02xxh	Read out sensor status
0300h	Read out sensor temperature
0500h	Sensor identification
0501h	Calibration identification
0502h	Software version
08xxh	Software reset
5555h	Test (Echo AAAAh)
AAAAh	Test (Echo 5555h)
Other	No reaction

The temperature read-out can be converted into a physical value in Celsius as

$$T = 0.045 \times (\text{Read out value}) - 55.8 \pm 5^{\circ} C \tag{5-9}$$

This is approximately 8 degrees higher than the ambient temperature due to the internally generated thermal effect.

The angle increment measured by the gyro is accumulated in the internal data storage. It can be read out upon the request of the user with the 01xxh command as listed in Table 5-5, where one bit corresponds 2^{-12} deg. The data is in 16-bit fixed-point 2's complement binary format. Once the read-out command is processed, the accumulator is reset. Therefore, the angular displacement $\Delta\theta$ during a read out period can be calculated from the read out value.

$$\Delta\theta = 2^{-12} \times (\text{Read out value}) \tag{5-10}$$

When the gyro is used as a rate sensor, the angular velocity components, $\Delta\omega$, normal to the fibre coil plane can be calculated with the read out frequency, f_o.

$$\Delta\omega = \Delta\theta \times f_o \tag{5-11}$$

Internally, the update rate of the accumulator is approximately 1.33 kHz. Since the size of the accumulator is limited $\pm\ 2^{-12} \times (2^{15} - 1)$ deg $= \pm\ 8$ deg, it must be read out at a frequency that will avoid an overflow. The read out frequency, f_o, is determined according to the range of rotation rate to be measured. For example, if f_o is faster than 25 Hz, it can detect an angular rate of ±200 deg / sec without an overflow error.

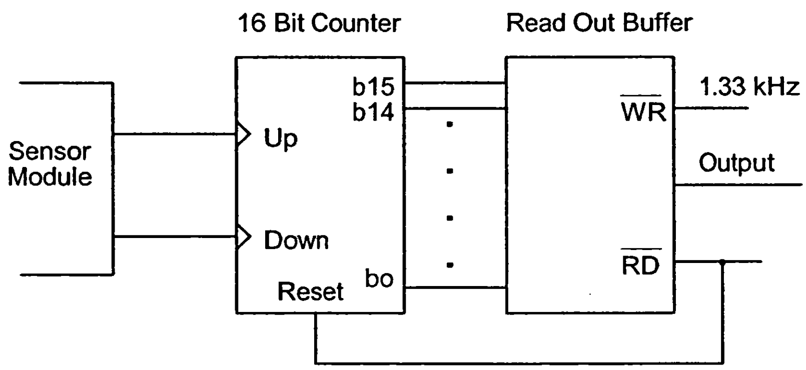

Figure 5-3 Angle increment accumulator of FOG

5.1.5 Test and Calibration of FOG

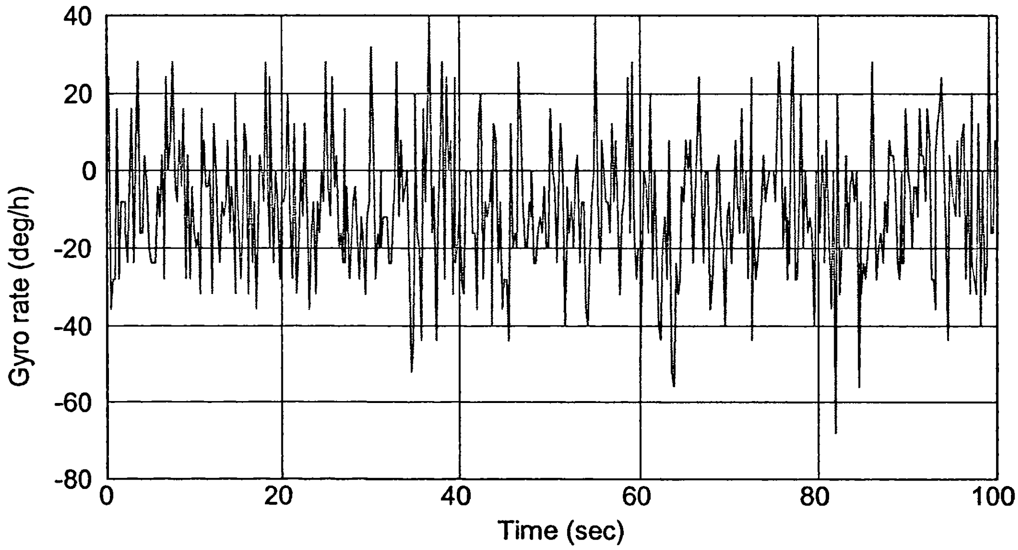

Figure 5-4 Gyro output data measurement

Figure 5-4 demonstrates a typical output pattern of an MFK 4-1 fibre optic gyro. Equation (5-11) is used to convert the actual gyro readout to physical data. The readout frequency is set as 4.55 Hz. Since the interfacing PC's internally generated interrupt rate is fixed to 18.2 Hz, it is convenient to use a frequency divided with an integer multiple. The data in Figure 5-4 are collected at Taejon, Korea (N 36.37°, E 127.5°) with a stationary condition in room temperature. It is possible to measure the rotation rate of the Earth E when a gyro is placed at latitude δ.

$$E = \cos(\delta) \times -15^\circ / \mathrm{h} \tag{5-12}$$

For example, E is -8.895° / h for Taejon. For more accurate calculation, the concept of sidereal day has to be applied (Wertz, 1978).

To analysis the data in Figure 5-4, we need to use statistical methods. The noisy component can be effectively eliminated by averaging the data. The mean value $\bar{x}$ and the variance σ^2 are defined for individual measuring values x_i as follows (Bendat & Piersol, 1991).

$$\bar{x} = \frac{1}{N}\sum_{i=1}^{N} x_i \tag{5-13}$$

$$\sigma^2 = \frac{1}{N-1}\sum_{i=1}^{N}(x_i - \bar{x})^2 \tag{5-14}$$

, where N is the number of data.

The mean value of gyro data in Figure 5-4 if applying equation (5-13) is $\mu = -9.38° / \mathrm{h}$, which differs by only -0.48°/h with the theoretical value calculated from Equation (5-12). The standard deviation of the data in Figure 5-4 represents the sensor specific noise. Equation (5-14) gives $\sigma_{4.55} = 17.71° / \mathrm{h}$, which is measured at the readout rate 4.55 Hz. We need to convert this measured variance into generalised form. As mentioned in the previous section, the internal update rate of the gyro is 1.33 kHz. The internal accumulator and the signal processing unit act as if it is a low pass filter. According to the external readout rate, the accumulator samples the mean of the data from the sensor module.

Let us assume σ_o^2 is the variance when the gyro is read with its maximum update rate, 1.33 kHz. Thus, the number of data accumulated in an interval is 1. We can have N data samples to be accumulated for slower read-out rates f. The output variance in case of N data samples can be calculated by using the variance of sampling distribution equation derived by Bendat & Piersol (1991).

$$\sigma_f^2 = E\left[(\bar{x} - \mu)^2\right] = \frac{\sigma_o^2}{N} \tag{5-15}$$

, where μ is the mean value of the original random data, $\bar{x}$ is the mean of the N sampled data and $E[\cdot]$ is expectation operator used in statistics. Reminding that $N = \dfrac{1333}{f}$, the standard deviation σ_f, for read out frequency f, can be calculated from the measured value $\sigma_{4.55}$.

$$\sigma_f = \frac{\sigma_o}{\sqrt{1333/f}} = \frac{\sigma_{4.55}}{\sqrt{455/f}} \tag{5-16}$$

For example, the NER value in Table 5-2 for the read-out rate 1 Hz is 30° / h. Therefore, the gyro noise measured in Figure 5-4 can be compared with the specification after a conversion. Using equation (5-16) results in $\sigma_1 = 8.4° / \mathrm{h}$, which satisfies the NER value of 30 deg / h / √Hz in Table 5-2.

The calibration of the FOGs has been performed for temperature and bias compensations to meet the specifications in Table 5-2. The result was written in an EEPROM inside the gyro signal processing unit. The performance of the sensor was checked before and after vibration tests as a part of the acceptance tests.

A thermal chamber with an internal rotation table is required for the thermal test. The rotation table is placed on a rigid monolith which is buried underground with 10 m depth. The laboratory floor and the monolith are separated to achieve vibration-free environment induced by human movements during the tests. A slip ring system is used to provide electrical connection from the rotation table to the outside computer system. The rotation rate of the turntable was controlled from -200°/sec to 200°/sec with 10°/sec intervals for scale factor measurements, where the accuracy of the table rotation is controlled within 1/10 of the Earth's rotation rate.

The temperature test comprises measurements with respect to bias and scale factor stability. For the measurements, a temperature cycle from maximum to minimum and back to maximum temperature is carried out. The temperature cycle is as follows.

80°C → 70°C → 55°C → 42°C → 27°C → 15°C → -1°C → -15°C → -30°C → -15°C
-1°C → 15°C → 27°C → 42°C → 55°C → 70°C → 80°C

A sufficient settling time, 1 ~ 2 hours, must be provided after a temperature change. A 30 minutes test is performed at each temperature with 1 second sampling rate. Therefore, the number of data is 1800 for each temperature.

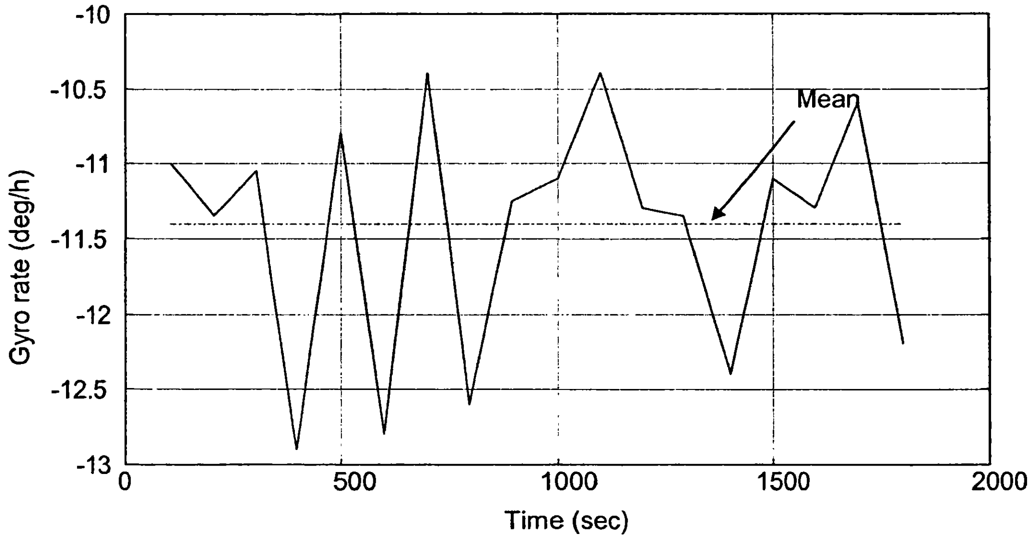

Figure 5-5 Mean value of gyro output

In order to remove the uncertainty due to noise, the mean value for 100 data has to be calculated. Thus, 18 mean values represent the gyro behaviour at a specific temperature. Figure 5-5 shows the mean values of gyro output calculated by Equation (5-13) for each 100 samples. It should be noted that all the measurements for the calibrations are made at Heidelberg Germany whose latitude is N 49.25°. Thus, the constant gyro bias due to the Earth's rotation is $-11.36°/\mathrm{h}$, which is different from the value measured at Taejon Korea.

The mean value indicated with a horizontal line in Figure 5-5 is -11.4°/h, which is an excellent performance considering the specifications of the gyro. The above measurement is made at room temperature. Therefore, the mean value yields the bias at that temperature. The sigma value (standard deviation) of the data in Figure 5-5 is 0.8°/h, which corresponds to the bias drift and uncertainty at that temperature. We can extend the experiment over the previously explained temperature range.

Figure 5-6 shows the results for a complete cycle of the temperature test. Each point in the figure represents the mean value of 18 sampled values at a specific temperature. It should be noted that the temperature in the figure is measured by the temperature sensor inside the gyro, which is 8°C higher than the ambient temperature. After analysing the data, the error between the mean value in Figure 5-6 and the actual rotation rate of the Earth was stored in the EEPROM to compensate temperature variation. The gyro was not so sensitive to temperature change.

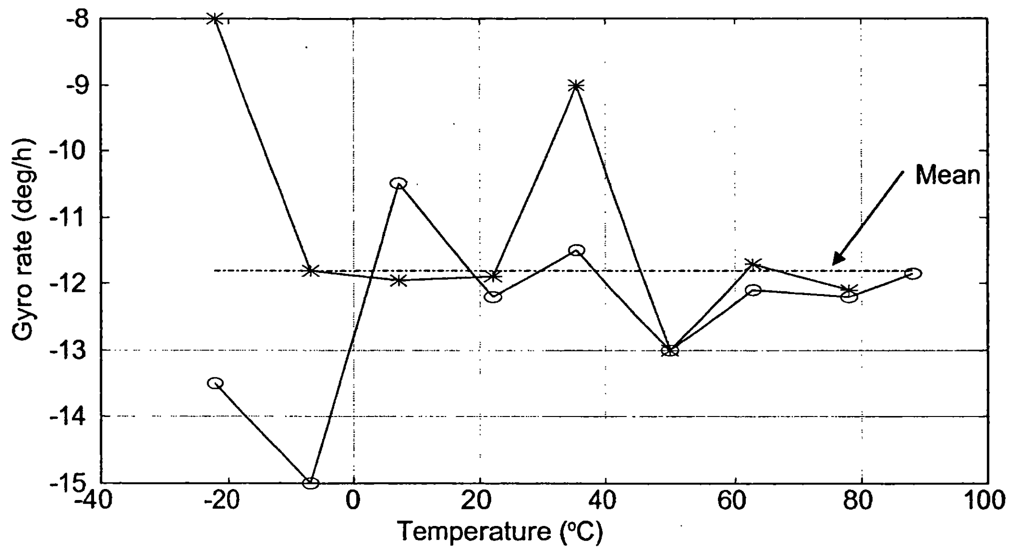

Figure 5-6 Mean value of gyro output

Bias repeatability is defined as the 1σ value of mean bias value. It is 1.47°/h for Figure 5-6, which is within the specification $\sigma < 6°/\mathrm{h}$. Bias or mean bias value over the whole temperature range is defined as the mean value in Figure 5-6 minus the apparent Earth rotation rate. It is also possible to plot the sigma values over the whole temperature range. The mean value in Figure 5-7 indicates the bias drift of the gyro in the operational temperature range.

As mentioned previously, the rotation table is controlled from -200°/sec to 200°/sec with 10°/sec interval for scale factor error assessment. 10 measurements are made at one-second intervals. The scale factor error, ΔSF, is defined as

$$\Delta SF = \frac{\Omega_{act} - \Omega_{nom}}{\Omega_{max}} \tag{5-17}$$

, where Ω_{act} is the mean of 10 sampled data, Ω_{nom} is the precisely controlled rotation rate of the table and Ω_{max} is the maximum detectable rate of the gyro, 200°/sec. In all, 41 measurements are made for each temperature range. The slope of a straight line, calculated from a least squares data fitting algorithm for the rate versus scale factor error curve, represents the mean scale factor error. This error value is registered and analysed after finishing the complete temperature cycle. The mean value of the means of scale factor error over the whole temperature range should satisfy the specification in Table 5-2, ± 2000 PPM.

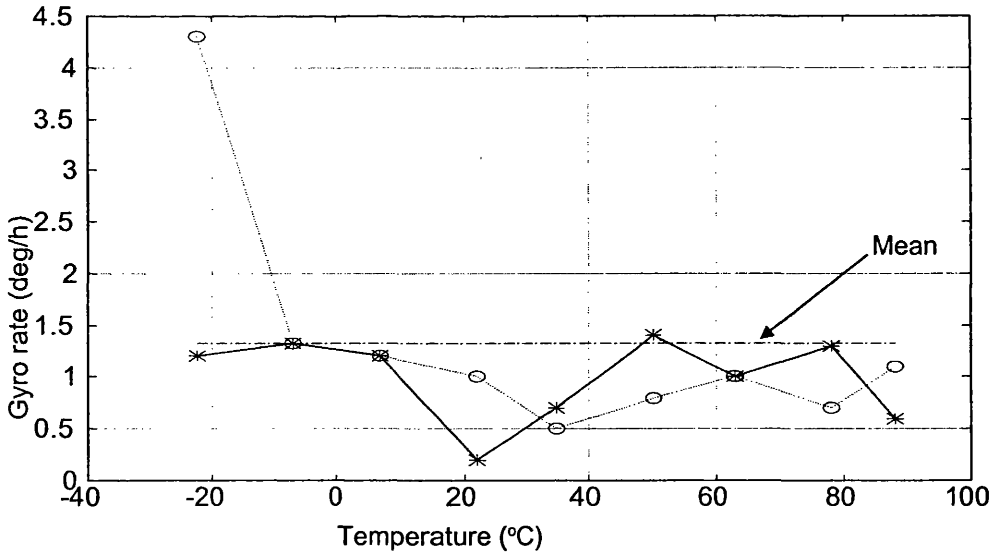

Figure 5-7 Temperature variation of gyro outputs

All the necessary information in calibrating the gyros is stored in the signal processing unit of each gyro. Once it is done, gyros are ready for environmental tests. Random and sine vibration tests were performed to guarantee launch survival. Thermal tests for the temperature extremes, -15°C, 20°C, and 55°C, were performed to ensure the calibration validity. Measurement of the Earth rotation rate was performed after each environmental test was done in order to check for any damage caused during the tests.

5.1.6 Gyro Model

It is generally regarded that mechanical gyro outputs have Gaussian distribution (Grewal & Andrews, 1993). A large portion of control algorithms used in aerospace adopt this statistical characteristic for filtering the noise component. Therefore, having a dynamic model of the gyro is very important to build a sensor data processing system. The histogram in Figure 5-8 is the result from 2 hours of continuous gyro measurement with the same stationary condition exercised for Figure 5-4. The mean and the standard deviation are $\mu = -8.894° / \mathrm{h}$, and $\sigma_{4.55} = 17.97° / \mathrm{h}$, respectively. The mean is virtually the same as the theoretical value obtained by Equation (5-12). The extended measurement time did not show up any severe drift, as expected from the sensor specifications.

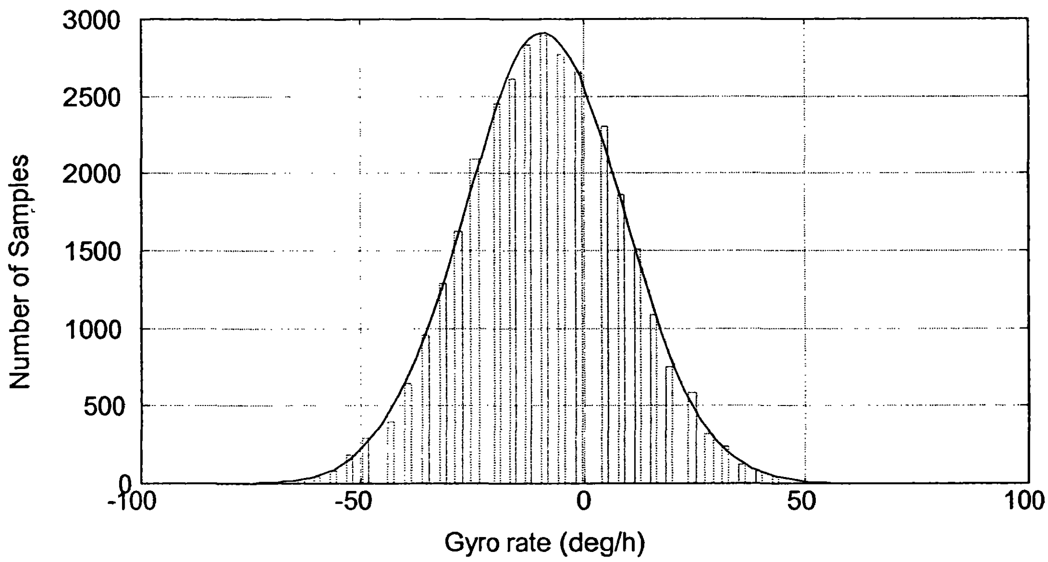

Figure 5-8 Gyro data distribution

The histogram suggests a mathematical model for the gyro output. We can start with a model based on a Gaussian probability density function (PDF) in Equation (5-18).

$$p(x) = \frac{1}{\sigma\sqrt{2\pi}} e^{\frac{-(x-\mu)^2}{2\sigma^2}} \tag{5-18}$$

, where μ and σ are defined in Equation (5-14) and (5-15).

We need to consider a multiplication factor to the PDF for taking into account the quantisation level and the size of the samples. There are $N = 32773$ samples for the measurement in Figure 5-8. The minimum data bit in Equation (5-10) is 2^{-12} deg. Therefore, the multiplication factor becomes $k = 2^{-12}\ \mathrm{deg} \times 3600\ \mathrm{sec/h} \times 4.55\ Hz$. The solid line in Figure 5-8 is plotted instantly from Equation (5-19). The result shows that the noise nature of a fibre optic gyro is in fact Gaussian.

$$\frac{kN}{\sigma\sqrt{2\pi}} e^{\frac{-(x-\mu)^2}{2\sigma^2}} \tag{5-19}$$

The measurement error of a fibre optic gyro has similar characteristics as a mechanical gyro except the mass and gyroscopic coupling related problems. Kim (1998) suggested a gyro measurement dynamic equation as

$$\vec{\omega}_m = (I_{3\times3} + \delta S)\vec{\omega} + \vec{\boldsymbol{b}} + \vec{\boldsymbol{A}} + \vec{\boldsymbol{n}}_w \tag{5-20}$$

, where $I_{3\times3}$ is 3 by 3 identity matrix, δS is scale factor error, $\vec{\omega}$ is the true angular velocity vector, $\vec{\boldsymbol{b}}$ is a drift error vector, $\vec{\boldsymbol{A}}$ is a gyro misalignment vector, and $\vec{\boldsymbol{n}}_w$ is a Gaussian noise vector which has the statistical property described in Equation (5-19).

The specifications of FOG in Table 5-2 indicate that the bias error and NER are dominant in the gyro measurement in the KITSAT-3 case. Therefore, Equation (5-20) can be simplified as

$$\vec{\omega}_m \approx \vec{\omega} + \vec{\boldsymbol{b}} + \vec{\boldsymbol{n}}_w \tag{5-21}$$

According to Siouris (1993), the drift error vector has the following dynamics:

$$\frac{d}{dt}\vec{\boldsymbol{b}} = \vec{\boldsymbol{n}}_{Rw} \tag{5-22}$$

The shaping equation implies that the bias is a constant with an additive noise whose derivative is white Gaussian. The noise vector $\vec{n}_{Rw}$ is referred as a random walk since it causes a bounded random change of the bias. Other factors neglected in approximating Equation (5-21) can be interpreted as the bias error.

5.2 ADCS Network Controller MTC4

5.2.1 RCU Interface Protocol

MTC4 has two redundant data links, M0 and M1. Each link has four serial communications ports, RTx1~4, and they are assigned to specific subsystems in the integrated configuration as defined in Table 5-6. RTx2 can be used for the data link to PC for bench tests.

MTC4 has the standard KITSAT-3 packet data format shown in Table 5-7. The frame always starts with a starting byte, ST (5Ah). We need to add a stuffing byte after 5Ah if it is used for a purpose other than ST. The source address and the destination address, SA and DA, should be set properly according to the link assignment.

Table 5-6 MTC4 serial link assignments

Link	Subsystem	Address (M0, M1)
RTx1	RCU	42h, 4Ah
RTx2	TUBSS (PC1)	43h, 4Bh
RTx3	OBC1 (PC2)	44h, 4Ch
RTx4	STS	45h, 4Dh

Table 5-7 OBC (or PC) → MTC → RCU command packet format

ST	DL	DA	SA	Data Field			
5Ah	Data Length	42h, 4Ah	44h, 4Ch 43h, 4Bh	MN	Data	.....	.....

MN (Module Name) designates the software function module in MTC4 to be accessed. The definitions are summarised in Table 5-8. The first 8 modules are associated with an individual wheel or gyro in RCU. The rest of the numbers are special functions required for group accessing. The group communication modules are requested for accessing the modules in RCU as a group to improve the efficiency in packet communication by minimising the header portion.

Table 5-8 MTC4 software module number definitions

Module Number (MN)	Description
00h	Reaction wheel - 1 (SW)
10h	Reaction wheel - 2 (ZW)
20h	Reaction wheel - 3 (XW)
30h	Reaction wheel - 4 (YW)
40h	Gyro – 1 (SG)
50h	Gyro – 2 (ZG)
60h	Gyro – 3 (XG)
70h	Gyro – 4 (YG)
80h	Gyro measurement enable frame (Option)
90h	Gyro measurement readout (Option)
A0h	Reaction wheel speed control in group
B0h	Reaction wheel speed readout in group
C0h	Gyro data readout in group
D0h	Gyro reset in group

MTC4 returns an acknowledgement packet back to the source address specified in the SA field in Table 5-7. The acknowledgement packet format is shown in Table 5-9, where the first byte in the data field is MN+1 for debugging purposes.

Table 5-9 RCU → MTC → OBC (or PC) acknowledgement packet format

ST	DL	DA	SA	Data Field			
5Ah	Data Length	44h, 4Ch 43h, 4Bh	42h, 4Ah	MN+1	Data	.....	.....

We should note that two byte checksum data are to be attached at the end of the all RCU data accessing packets.

- **Module Number 00h~30h (Wheel Access)**

Each wheel can be accessed separately with this function. Wheel speed reading and commanding need to be implemented in this module. Wheel speed in 2-byte hexadecimal format can be calculated from the 2's complement of rpm value $\times 0.212$. Speed commanding can be sent according to the format in Table 5-10, where the PC umbilical line interface is assumed. The MSB is the Higher Byte, and LSB is the Lower Byte of the wheel speed data. DL is 08h to include the omitted checksum bytes.

Table 5-10 Wheel speed control command format

ST	DL	DA	SA	Data Field			
5Ah	08h	42h	43h	00h~30h	AAh	MSB	LSB

The acknowledgement packet in Table 5-11 swaps DA with SA, and MN is incremented by +1. AAh, MSB, LSB are added in the data field for echo.

Table 5-11 Wheel speed control command acknowledgement format

ST	DL	DA	SA	Data Field			
5Ah	08h	43h	42h	01h ~ 31h	AAh	MSB	LSB

The speed read-out packet has the same structure as the commanding case except ABh is used as the identifier. The meaning of the MSB and the LSB are also the same as in the previous case.

Table 5-12 Wheel speed read command format

ST	DL	DA	SA	Data Field			
5Ah	08h	42h	43h	00h ~ 30h	ABh	0Ah	0Bh

Table 5-13 Wheel speed read command Acknowledgement format

ST	DL	DA	SA	Data Field			
5Ah	08h	43h	42h	01h ~ 31h	ABh	MSB	LSB

We should note that the reaction wheels and gyros do not follow the standard MTC4 packet format since the manufacturing order was made before the MTC protocol was fixed. Therefore, MTC4 had to be designed to interface with RCU and other systems by appropriately converting the packet format. The actual communication protocols for wheels and gyros are discussed in 4.2 and 5.1.4.

- **Module Number 40h~70h (Gyro Access)**

Each gyro is individually accessed by MTC4. There are basically two groups in the sub-functions, reset and other command. A reset command performs a hardware reset via the parallel to serial data converter located between MTC4 and gyro.

Table 5-14 Gyro reset command format

ST	DL	DA	SA	Data Field	
5Ah	06h	42h	43h	40h ~ 70h	A7h

Table 5-15 Gyro reset command acknowledgement format

ST	DL	DA	SA	Data Field			
5Ah	08h	43h	42h	41h ~ 71h	A7h	A5h	A5h

After receiving a reset command packet in Table 5-14, MTC4 acknowledges the success of the command by sending a packet in Table 5-15. In case the gyro does not respond, CCh and CCh are included at the end of the packet.

When A6h is used as the first byte in the data field, the parallel to serial converter transparently delivers commands to the gyro. CD1 and CD2 in Table 5-16 are examples of the commanding MSB and LSB listed in Table 5-17.

Table 5-16 Gyro command packet format

ST	DL	DA	SA	Data Field			
5Ah	08h	43h	42h	40h ~ 70h	A6h	CD1	CD2

Table 5-17 Gyro command set

CD1:CD2	Function	Acknowledge
01xxh	Read out angle increment	$(RD1 \times 256 + RD2) / 4096$ deg
02xxh	Read out Sensor Status	Warning if RD1 or RD2 is not 0
0300h	Read out Sensor Temperature	$(RD1 \times 256 + RD2) \times 0.045 - 55.8$
0500h	Sensor Identification	$(RD1 \times 256 + RD2) + 4000$
0501h	Calibration Identification	(int) RD2. (int) RD1
0502h	Software Version	(char) RD2. (char) RD1
08xxh	Software Reset	RD1==5Ah, RD2==5Ah if Success
5555h	Test (Echo AAAAh)	RD1==AAh, RD2==AAh if Success
AAAAh	Test (Echo 5555h)	RD1==55h, RD2==55h if Success
Other	No reaction	N/A

Table 5-18 Gyro command acknowledge format

ST	DL	DA	SA	Data Field			
5Ah	08h	43h	42h	41h ~ 71h	A6h	RD1	RD2

The acknowledgement packet format has a common structure for all the sub-functions of gyro in Table 5-18. The meanings of RD1 and RD2 are defined in Table 5-17, where the mathematical expressions are in standard C language format.

- **Module Number 80h (Automatic Gyro Measurement Enable)**

This function is designed as an option. Gyro angle data are automatically updated by MTC4 with a bandwidth of 2Hz in this function. MTC4 periodically sends and receives data from the gyros by using internally generated interrupt signals. Each gyro, including the redundant one, SG, has its own automatic read-out enabling flag in the memory of MTC4, which automatically generates the required set of commands and selects the appropriate multiplexing address. The requested data are archived in the ring buffer memory implemented in MTC4. Upon the request of OBC the whole data are to be read out.

The automatic readout enable statuses of the gyros need to be sent according to the format in Table 5-19 with the expected acknowledgement form in Table 5-20.

Table 5-19 Gyro automatic read enable format

ST	DL	DA	SA	Data Field	
5Ah	06h	42h	43h	80h	GS

Table 5-20 Gyro automatic read enable acknowledge format

ST	DL	DA	SA	Data Field	
5Ah	06h	43h	42h	81h	GS

The GS byte indicates the enabled status. According to the naming sequence in Table 5-8, the auto read enable flag is set. The flag has an 8-bit memory indicating the enable status of each gyro. The map is made in the sequence of: (SG,ZG,XG,YG, SG,ZG,XG,YG). By setting a specific bit as 1 for enabling and by resetting it for disabling, we can represent the status with two 4-bit data. For example when all the gyros are enabled the GS flag is FFh, and if the YG is the only enabled unit then GS is 88h. We should note that this enable flag is only for the auto read function. Therefore, previously defined manual accesses for MN = 40h ~ 70h are still available regardless of the GS setting as long as the powers are supplied.

- **Module Number 90h (Automatic Gyro Measurement Readout)**

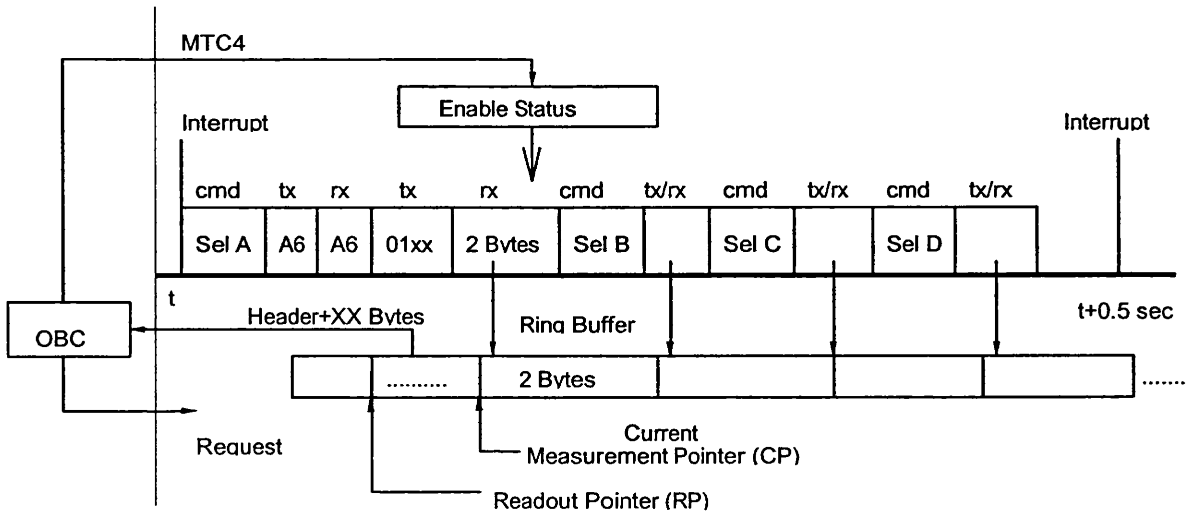

Figure 5-9 Gyro read out sequence

The periodically read gyro data are stored in the ring buffer of MTC4, according to the sequence shown in Figure 5-9 every 0.5 seconds. If the enable status is on, MTC4 gives a 01xxh command to the gyro in order to attain the angle increment and it archives received data into the internal buffer. If the flag reads "off", accessing of the gyro for that axis will be skipped and the buffer memory address will be increased. This means that every interrupt will spend 4-axis × 2 Bytes = 8 Bytes of memory, regardless of the enabling status.

In Figure 5-9, CP (Current Measurement Pointer) points to the lastly accessed buffer address and RP (Readout Pointer) indicates the end of the readout buffer address. There are 256 bytes of memory in total, which is sufficient for 8 seconds of 4-axis gyro data. If the data is not accessed for more than 8 seconds, overwriting of data is inevitable.

The automatic readout function does not actually start until the RUN command packet is received, shown in Table 5-21. When the RS byte is FFh, the automatic readout function starts and stores data in memory. Auto run stops if RS is 00h.

Table 5-21 Gyro automatic read RUN / STOP format

ST	DL	DA	SA	Data Field		
5Ah	07h	42h	43h	90h	AAh	RS

Table 5-22 Gyro automatic read RUN / STOP acknowledgement format

ST	DL	DA	SA	Data Field				
5Ah	09h	43h	42h	91h	RC	CP	RP	GS

The meanings of the CP, RP, and GS in the acknowledgement packet in Table 5-22 are already defined in Figure 5-9 and Table 5-20. GS is included in the packet to identify the enabled gyro units. The function MN=90h should be operated prior to MN=80h to obtain correct results. RC (Ring Counter) equals the number of unread data units (8 Byte), which implies that if RC is over 20h the buffer has been overwritten. We can have up to 10 units (80 bytes) of data in the ring buffer as a single packet. The readout command for the automatically saved data is demonstrated in Table 5-23. The actually retrieved gyro data are located at the end of the data field in Table 5-24.

Table 5-23 Automatically saved gyro data requesting format

ST	DL	DA	SA	Data Field	
5Ah	06h	42h	43h	90h	A9h

Table 5-24 Automatically saved gyro data retrieved format

ST	DL	DA	SA	Data Field					
5Ah	DL	43h	42h	91h	RC	CP	RP	GS	Data

- **Module Number A0h (Reaction Wheel Speed Control in Group)**

This function is designed to improve the communication link efficiency with the wheels. On receiving a packet, MTC4 will automatically generate all the required data and control signals for accessing the wheels that are defined in BM of Table 5-25. It indicates the bit map of the selected modules for accessing and it has the same structure as the GS flag in Table 5-20, with the same sequence defined in Table 5-8. The acknowledgement packet in Table 5-26 has a tag FFh at the end and the status pointers, S, Z, X and Y.

Table 5-25 Packet for reaction wheel speed control in group

ST	DL	DA	SA	Data Field									
5Ah	0Eh	42h	43h	A0h	BM	HS	LS	HZ	LZ	HX	LX	HY	LY

Table 5-26 Acknowledgement packet for reaction wheel speed control in group

ST	DL	DA	SA	Data Field													
5Ah	12h	43h	42h	A1h	0S	HS	LS	1Z	HZ	LZ	2X	HX	LX	3Y	HY	LY	FFh

The higher 4 bits of the status pointers correspond to the name of the wheels, as indicated with the numbers, 0, 1, 2, and 3. The lower 4 bits are status bits for checking the source of faults such as timeout or checksum errors as defined in Table 5-36.

- **Module Number B0h (Reaction Wheel Speed Readout as Group)**

The data format of requesting wheel data as group is in Table 5-27, where the definition of BM is the same number as Table 5-25. The packet gives rise to an acknowledgement packet as shown in Table 5-28. The higher and lower bytes of the speed of the wheels are in the order of SW, ZW, XW, and YW.

Table 5-27 Packet for reaction wheel speed readout in group

ST	DL	DA	SA	Data Field	
5Ah	06h	42h	43h	B0h	BM

Table 5-28 Acknowledgement packet for reaction wheel speed readout in group

ST	DL	DA	SA	Data Field												
5Ah	10h	43h	42h	B1h	0S	HS	LS	1Z	HZ	LZ	2X	HX	LX	3Y	HY	LY

- **Module Number C0h (Gyro Readout as Group)**

The data format of requesting gyro data as group is in Table 5-29, where the definition of BM is the same structure as the GS flag in Table 5-20. The packet gives rise to an acknowledgement packet as shown in Table 5-30. The higher and lower bytes of the speed of the wheels are in the order of SG, ZG, XG, and YG.

Table 5-29 Packet for gyro data readout in group

ST	DL	DA	SA	Data Field	
5Ah	06h	42h	43h	C0h	BM

Table 5-30 Acknowledgement packet for gyro data readout in group

ST	DL	DA	SA	Data Field												
5Ah	10h	43h	42h	C1h	4S	HS	LS	5Z	HZ	LZ	6X	HX	LX	7Y	HY	LY

The higher 4 bits of the status pointers correspond to the name of the gyros as indicated with the numbers, 4, 5, 6, and 7. The lower 4 bits are the processing states.

- **Module Number D0h (Gyro Group Reset)**

The gyro group reset format is in Table 5-31, where the definition of BM is the same structure as the GS flag in Table 5-20. The packet gives rise to an acknowledgement packet as shown in Table 5-32. The higher and lower bytes of the gyros are in the order of SG, ZG, XG, and YG.

Table 5-31 Packet for gyro reset in group

ST	DL	DA	SA	Data Field	
5Ah	06h	42h	43h	D0h	BM

Table 5-32 Acknowledgement packet for gyro reset in group

ST	DL	DA	SA	Data Field												
5Ah	10h	43h	42h	D1h	4S	HS	LS	5Z	HZ	LZ	6X	HX	LX	7Y	HY	LY

- **Checksum**

A communication error detection scheme was proposed as a safety measure for the ground based hardware simulator when an RF link was used for communications between a PC and the satellite. A simple checksum calculation algorithm was used for fast data processing. Checksum bytes are attached at the end of a command and acknowledge packets of the RCU data as shown Table 5-33.

Table 5-33 RCU access packet format

ST	DL	DA	SA	MN	Data Field	Chksum1	Chksum2

Each checksum byte corresponds to different computation logic, which includes the data from MN to the end of the data field. The initial values for the calculations of Chksum1 and Chksum2 are all zero. If the current checksum pointer is named BYTE, then the following routines can be applied for each checksum.

$$\text{Chksum1} = \text{Cksum1} + \text{BYTE}$$
$$\text{Chksum2} = \text{Rotate Left}\ (\text{Cksum2} \oplus \text{BYTE})$$

, where $\oplus$ stands for an exclusive OR operator.

- **Error Management**

If one of the modules in RCU does not transmit an acknowledgement for a given time interval, MTC4 should generate a time out error and exit the waiting process to avoid an infinite loop. MTC4 acknowledges a success by sending a packet according to Table 5-33 if a checksum or timeout error does not occur. If an error occurs MTC4 sends an acknowledge packet indicating the source of its error as shown in Table 5-34. This function is very useful during the development phase where errors inevitably occur. It will also be used after launch for diagnoses of any interface problems that may occur.

Table 5-34 Check sum, time out acknowledge packet format

ST	DL	DA	SA	Data Field				Chksum
5Ah	08h	43h	42h	ER1	ER2	ER3	ER4	2 Bytes

ER1 is FFh if an error occurs. ER2 is FFh for a checksum error. A time out error will return a byte composed of the higher 4 bits of RCU module numbers, 0~7 in the order specified in Table 5-8, and lower 4 bits of the time-out state as defined in Table 5-36. ER3 is FFh if a checksum error occurs. The time-out error will return the state where it occurs as specified in Table 5-35. ER4 contains internal MTC4 timer information

Table 5-35 MTC4-RCU accessing state definition

ER3	Description
A6h	Gyro data communication
A7h	Gyro reset
AAh	RW speed control
ABh	RW speed read out

Table 5-36 MTC4-RCU processing state definition

State	Gyro data flag	Gyro reset flag	RW write flag	RW read flag
state0	Link select command 1(cmd41/105)(send dummy byte for delay)			
state1	Link select command 2(cmd42/106)(send dummy byte for delay)			
state2	Link select command 3(cmd43/107)(send dummy byte for delay)			
state3	tx [A6h]	tx [A7h]	tx [FFh]	tx [0Ah]
state4	rx [A6h]	rx [A7h]	rx [00h]	rx [HB]
state5	tx [cmd1]	rx [A5h]	tx [HB]	tx [0Bh]
state6	tx [cmd2]	rx [A5h]	rx [HB]	rx [LB]
state7	rx [d1]	N/A	tx [FEh]	N/A
state8	rx [d2]	N/A	rx [01h]	N/A
state9	N/A	N/A	tx [LB]	N/A
state10	N/A	N/A	rx [LB]	N/A
state11	N/A	N/A	tx [14h]	N/A
state12	N/A	N/A	rx [ECh]	N/A
state13	END	END	END	END

5.2.2 Hardware Configuration

All the MTCs in KITSAT-3 have similar architecture as shown in Figure 5-10. For the sake of redundancy the electrical data handling system is designed in dual redundancy with. M0 and M1 links. Two independent microprocessors are used as the controllers, which are implemented with slightly different technologies. They establish communication links with external subsystems using multiplexed channels provided by the DUARTs (Dual Universal Asynchronous Receivers and Transmitters).

The digital commands from each controller are multiplexed by the time slicing signal controllers to provide full redundant channels. The execution status of all commands and other digital statuses are monitored by the telemetry units and are fed back to the controllers. The Power Distribution Module (PDM) is also included as a part of MTC. The major difference of MTC4 from other MTCs is that it does not include an analogue telemetry processing unit. This is mainly due to the design simplicity required due to the limitation in size. Figure 4-33 depicts this constraint well. MTC4 is implemented with two separate PCBs, UP and DOWN. They are mounted on the RCU module box. Two PCBs are stacked as shown in Figure 5-11.

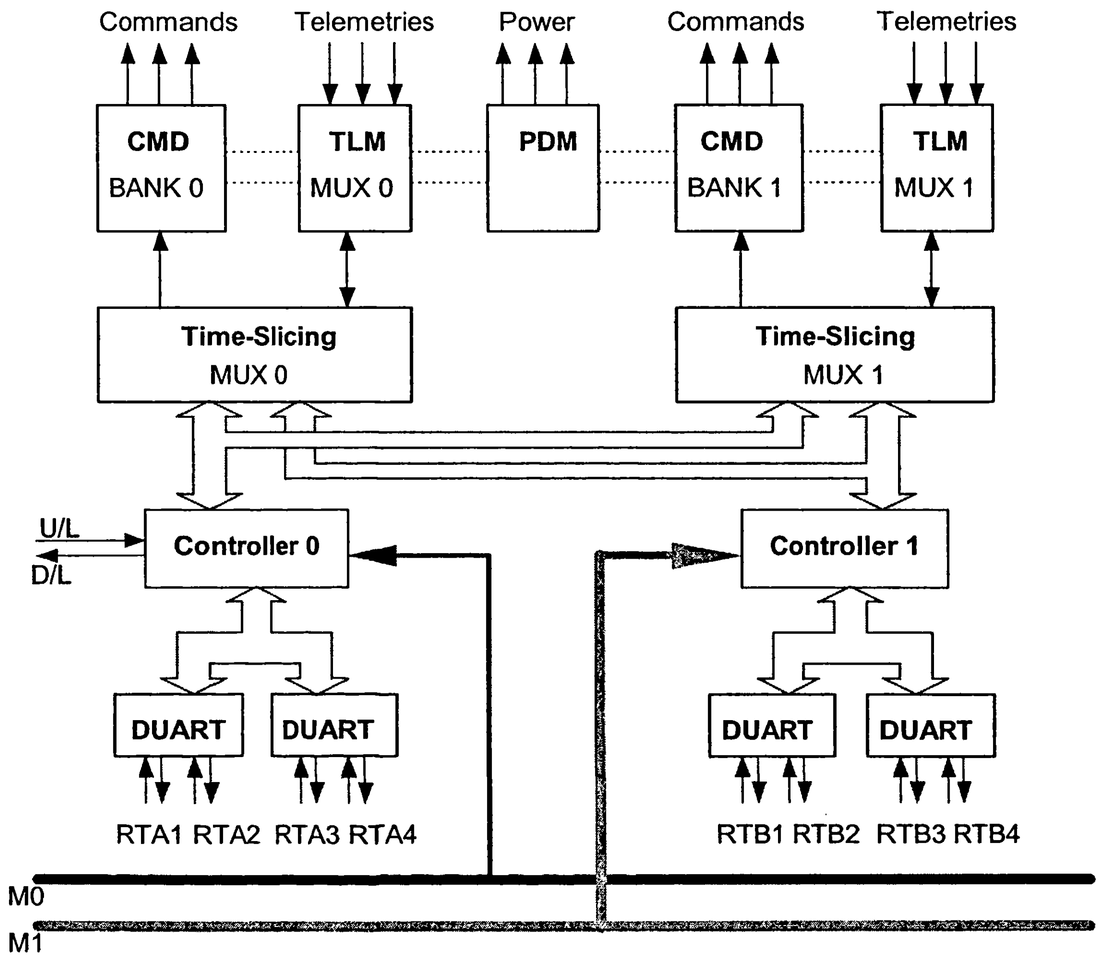

Figure 5-10 System architecture of MTC

Most of the parts in Figure 5-10 are implemented on the DOWN board except the command and telemetry banks. The powers of each RCU component are supplied by the bi-stable mechanical relays. Semiconductor switches are not employed due to the high in-rush and operation current requirements of the reaction wheels and the gyros. The 8 serial communication lines from each component are multiplexed and forwarded to the DUART located in the DOWN board. Two separate 25-pin connectors are assigned for the RCU. A failure at one point still guarantees the pitch control based on the single momentum wheel configuration.

MTC interfaces with external systems with two 37-pin connectors located on the edge of the UP board. Serial communications and power distributions to the star sensors are made at MTC4 too. A direct communication port is established with OBC1 to reduce time delay. Table 5-37 summaries the specifications of MTC4.

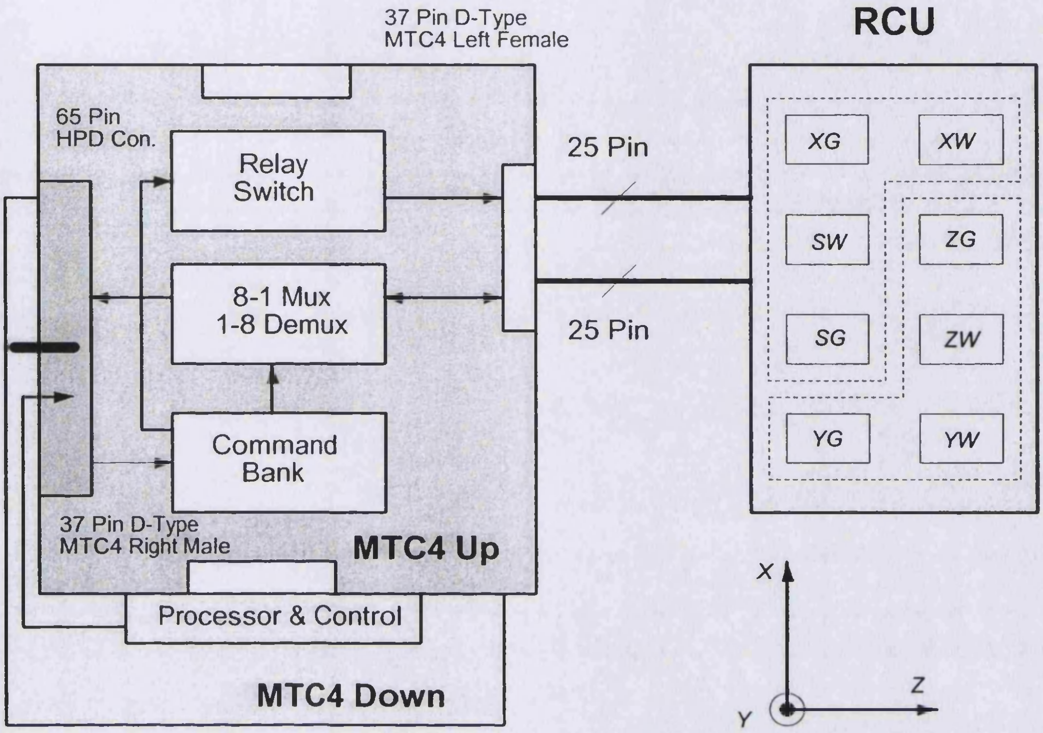

Figure 5-11 MTC4-RCU System Block Diagram

Table 5-37 Specifications of MTC4

Power consumption	0.5W (Nominal)
Mass	642g
Size	85 × 355 × 100 mm
Telecommands	32 (Digital)
Telemetry	50 digital channels

5.3 Other Sensors

5.3.1 Star sensors (STS & TUBSS)

It is widely accepted that star sensors are the most accurate inertial attitude measuring devices for space applications. Accuracy of a few arc-seconds is a common performance capability for these sensors (Wertz, 1978 and Sidi, 1997). However, star sensors are generally thought to be expensive, bulky, and consuming high power. Due to the development of very large-scale integrated circuits and CCD sensors, it has become possible to design and manufacture low cost small sensors.

The most attractive factor of a star sensor is that it can provide 3-axis attitude information with a single sensor. Multiple combinations of sun sensors, magnetometers and horizon sensors require for full 3-axis attitude information, which make the satellite system complex. Anther advantage of a star sensor is it that it has fewer restrictions in terms of operation conditions. This is a distinct advantage when we are planning a complex set of attitude operations such as is planned in the KITSAT-3 mission. However, we do need to ensure that sunlight does not encroach on the field of view of the sensor.

There are three major types of star sensors, V-slit star scanners, gimballed star trackers and fixed-head star trackers. The latter type is becoming popular due to its simplicity and the rapid development in CCD technology in recent years. The star sensors in KITSAT-3 fall into this category.

There are two star sensors in KITSAT-3. The first one is named as *STS* and is developed at SaTReC. The other is named as *TUBSS* and procured from Kaiser-Threde in Germany. This dual redundancy reflects the importance of the star sensor unit to the mission success. The sensors are positioned on the top of the spacecraft platform, as shown in Figure 1-5 and Figure 5-12.

The TUBSS is a back-up sensor for the STS in case of failure. The TUBSS has an accuracy of $0.02°(2\sigma)$ according to previous flight histories. The small size and mass is particularly suited to a micro-satellite like KITSAT-3.

Both sensors use star catalogues to ascertain the spacecraft attitude by identifying and comparing the coordinate of the star image with the on-board map. The star identification algorithm, optic system design, and image processing algorithm techniques are all crucial elements for this type of sensor. The low intensity nature of stars requires a low noise circuit design.

A thermoelectric cooler on STS reduces dark current noise and improves the performance. The cooler utilises the Peltier effect; a constant current flow between two metal plates separated by p-n type semi-conductors invokes heat absorption at the anode and heat dissipation at the cathode. The CCD sensor in STS has a built-in cooler. It is capable of cooling down the operation temperature to 40 °C below ambient. The dark current effect can be reduced up to 20 times by operation of the cooler.

Charges stored in the CCD cells are transferred to the output by clocking pulses. Analogue to digital conversion is required for further processing after a series of amplifications. High speed data conversion requirements, such as slew rate, settling time and conversion time, should be considered in selecting the A/D converter.

The digital processing part is implemented on a separate circuit board in order to prevent digital noise interference to the analogue circuits. The main DSP processor is 320C31 from TI. The digital part contains a ROM of 512Kbyte for program memory and the star catalogue. The data RAM of 512Kbyte is used for image processing.

The star sensors face dark space while the satellite is in normal operational mode, as discussed in Chapter 2. The sun-synchronous orbit characteristic thus helps to keep the star sensors cold not only for the normal operation period but also for the Earth imaging mode. The quaternion data from the sensor will be attached as ancillary data for image processing during downlink.

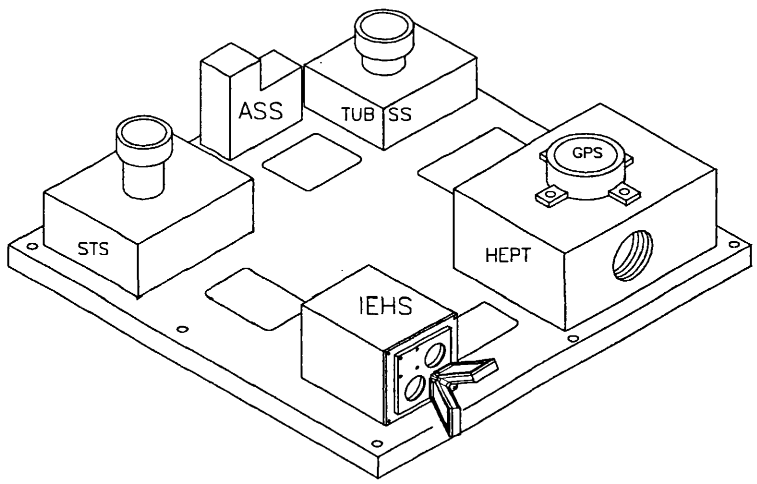

Figure 5-12 Attitude sensor positions on the sensor platform

Table 5-38 Specifications of STS

Power consumption	4~6 W
Mass	1.0 kg
Size	12.5 cm × 12.5 cm × 14.7 cm
Accuracy	1 arc min
Field of view (FOV)	30°× 23°
CCD	EEV CCD02-06 (288×385 pixels)
CPU	TMS320C31
CPU clock speed	22.1184 MHz
Effective brightness range	0 ~6 (Mv)
Maximum angular velocity measure	< 1°/sec (pitch rate)

Table 5-39 Specifications of TUBSS

Power consumption	4.2 ~ 5W
Mass	0.84 kg
Size	11.2 cm x 11.5 cm x 4.5 cm
Accuracy	0.02 (2σ)
Field of view (FOV)	31°x 21°
CCD	Thomson TH 7863
CPU	H8
Effective brightness range	-2 ~ +60 ~6 (Mv)

5.3.2 Infrared Earth Horizon Sensor (IEHS)

The horizon sensors in KITSAT-1, 2 were operated at visible wavelengths. The accuracy was relatively low due to large fluctuations of the atmospheric profile in the visible waveband. Thus, an infrared detection sensor was proposed to improve the accuracy. IEHS in KITSAT-3 detects far infrared (14-16μm) radiated from the Earth's CO_2 absorption region. The radiation flux changes sharply at the edge of the horizon (Wertz, 1978).

Two perpendicularly positioned linear sensors can provide information about the pitch and the roll axes when the satellite and/or the sensors is pointed toward the near centre of the Earth. Pyro-electric devices are used for the IR detection. Unlike conventional IR sensors, the sensor does not require cooling. Mechanical chopping of the IR radiation flux is required in order to attain adequate signals. After a series of filters and A/D conversion, the sensors generate a data set of 16 channels, which varies according to the pitch and roll attitude of the satellite.

Table 5-40 Specifications of IEHS

Power Consumption	1.1W
Mass	980g
Size	9.0 x 9.0 x 17.0 cm
Wave length range	14~16μm
Detectivity	$9 \times 10^6\, cm \cdot \sqrt{Hz} / W$
Accuracy	0.5°
Field of view	±2.64°

Figure 5-12 shows that IEHS has two gold plate mirrors and lenses for each sensor. The sensor will be used during the Earth imaging mode. Since it is proposed as an experimental payload, its success is not a critical issue for the operation of KITSAT-3. The main objective of the development is demonstrating a new technology in space.

5.3.3 Analogue Sun Sensor (ASS)

The analogue Sun sensor is fundamental for initial attitude acquisition and safe-hold operations of the satellite. Combination of the horizontal and the vertical sensors provides two-axis attitude information to identify the position of the Sun on the celestial sphere.

Each sensor has a silicon solar cell with a triangular shaped mask. Different Sun incident angles generate varying voltage signals after passing a slit. Based on ground calibrations, the angle and voltage relation data were collected and stored on-board as a table for accurate measurements.

Table 5-41 Specifications of the ASS

Power	0.1W
Mass	0.1 kg
Size	10.0 cm $\times$ 9.7 cm $\times$ 2.9 cm
Accuracy	0.5°
Field of view	±60°

5.3.4 Magnetometers (NMAG& SMAG)

There are two 3-axis magnetometers in KITSAT-3. The sensor part and the processing electronics of the navigational magnetometer (NMAG) are located in the SENSE module box. However, the sensor section of the scientific magnetometer (SMAG) is attached on the $+x$ deployable solar panel in order to minimise the magnetic field disturbance originated from the satellite body. The sensors are fluxgate type magnetometers where toroidal cores are used.

A magnetometer can be used as a coarse attitude sensor regardless of the orbital position and FOV for a low Earth orbiting satellite. It is used for magnetorquering to provide geomagnetic field information. The magnetic field telemetry data is also to be utilised on ground for analyses of the high energy particle detection experiment.

Table 5-42 Specifications of magnetometers

Power Consumption	0.3W
Mass	0.315 kg
Size	30 cm $\times$ 7 cm $\times$ 2 cm
Dynamic range	$\pm$ 60μT
Resolution	30 nT (NMAG), 5nT (SMAG)

5.3.5 Accelerometer (AXLM)

The objectives of the accelerometer experiment are the measurement of the shock resulting from the solar panel deployment, measurement of mechanical vibrations induced by reaction wheels and thermal shock, and testing innovative technology (micro-machining) in a space environment. This experiment was proposed as a payload. The output of this sensor is not intended to obtain attitude-related information.

The accelerometer utilises state of the art MEMS technology, which enables us to reduce the volume and mass of the sensor system both in a mechanical and an electrical sense. Testing this type of technology itself in space will be an interesting experience. Two types of micro-machined sensors are used. The specifications of the sensors are summarised in Table 5-43.

Table 5-43. Specifications of the ADXL50/05 accelerometer sensors

	ADXL50	ADXL05
Dynamic Range (Selectable)	-50 ~ +50 *g*	-5 ~ +5g
Sensitivity @ V_{pr}	~19 mV/g @25 °C, 15 *g*	~200 mV/g @25 °C
Noise Density (10Hz ~ 1KHz)	$6600\mu g/\sqrt{Hz}$	$500\mu g/\sqrt{Hz}$
Power	5V, 10mA	5V, 8mA
Temperature Range	-40 ~ 85 °C (AH type)	-40 ~ 85 °C (AH type)
Package	10 pin TO-100	10 pin TO-100
Weight	5 grams	5 grams

Chapter 6. System Analysis

6.1 Environmental Disturbance Modelling

The attitude motion of a spacecraft is disturbed by various kinds of environmental torques. Solar radiation, aerodynamic, magnetic field and gravity gradient are the major known sources of torque for low Earth orbiting satellites. The estimation and characterisation of the disturbance torques originating from these sources are important in designing the attitude control system. Sizing of the actuator system can be carried out based on the results of these analyses. The control system performance can also be investigated in terms of the reaction to these disturbances (Kim *et al.*, 1992).

6.1.1 Solar Pressure

The mean integrated solar energy flux at the Earth's position for the phase of the year *D* measured from the aphelion is given in Equation (6-1) (Wertz, 1978).

$$F_e = \frac{1358}{1.0004 + 0.0334 \cos D} \cong 1358 \quad W/m^2 \tag{6-1}$$

The mean momentum flux *P*, acting on a surface normal to the Sun's radiation, is given

$$P = \frac{F_e}{c} = 4.6 \times 10^{-6} kg/m \cdot \sec^2 \tag{6-2}$$

, where *c* is the speed of light.

We can categorise the types of solar pressures on satellite surface into three groups.

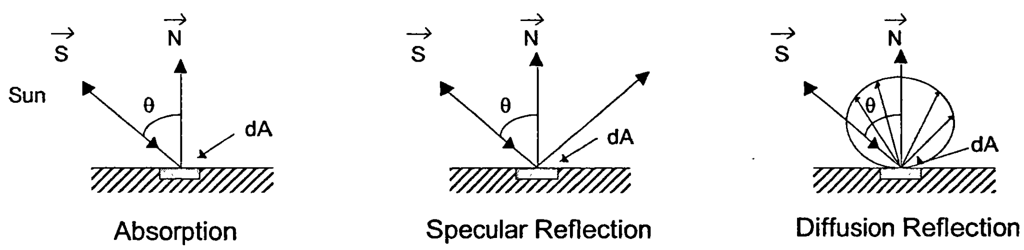

Figure 6-1 Three types of solar pressure

If we let P be the momentum flux on an elemental area dA with unit outward normal $\vec{N}$, the differential radiation forces are (Hughes, 1986)

$$\begin{aligned} d\vec{f}_{abs} &= -PC_a \cos\theta \vec{S}\, dA & (0 \le \theta \le 90^\circ) \\ d\vec{f}_{spc} &= -2PC_s \cos^2\theta \vec{N}\, dA & (0 \le \theta \le 90^\circ) \\ d\vec{f}_{dif} &= -PC_d(-\frac{2}{3}\cos\theta \vec{N} - \cos\theta \vec{S})\, dA & (0 \le \theta \le 90^\circ) \end{aligned} \tag{6-3}$$

, where $C_a + C_s + C_d = 1$. Then the total force is

$$\begin{aligned} \int d\vec{f}_{total} &= \int \left[d\vec{f}_{abs} + d\vec{f}_{spc} + d\vec{f}_{dif} \right] \\ &= -P\int \left[(1-C_s)\vec{S} + 2\left(C_s \cos\theta + \frac{1}{3}C_d)\vec{N} \right) \right] \cos\theta\, dA \end{aligned} \tag{6-4}$$

The highest pressure occurs when $\theta = 0$, $\vec{S} = \vec{N} = \vec{1}$, which is true for most of the time during the Sun tracking operation. According to conventional spacecraft applications, however, they are dependent on the surface property of a spacecraft. Let $C_s = 0.8$, $C_d = 0.2$,

$$\int d\vec{f}_{total} = -P\int \left[(1-C_s)\vec{N} + 2\left(C_s + \frac{1}{3}C_d \right)\vec{N} \right] dA = -8.95\times 10^{-6} \int dA\vec{N} \tag{6-5}$$

The solar pressure torque, then, can be obtained by the cross production of the moment arm and the force elements over the effective surface of the spacecraft as

$$\vec{T}_{solar} = \int \vec{r}_s \times d\vec{f}_{solar} \tag{6-6}$$

Considering the shape of the satellite and performing the surface integration, we can have the solar pressure disturbance torque model for the Sun tracking mode. The simplified mechanical model in Figure 6-2 can be used for this purpose. If we look at the Equation (6-6) closely, it reveals that the integration is just a simple problem involved with the centre of pressure and moment arm. In other words, finding the total force on the effective surface and multiplying the CG point offset, the distance between the centre of pressure and mass will give rise to the net torque. The offset values are $x_d = 0.1$, $y_d = 100$, and $z_d = -13.1$ mm for x, y, and z axes, respectively.

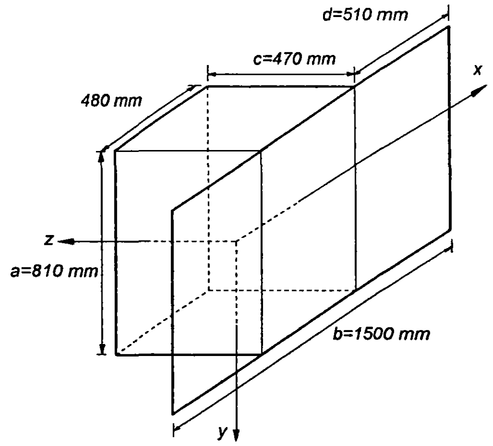

Figure 6-2 Simplified mechanical model

The integration of Equation (6-5) is defined over the whole area of the deployed solar panels. Therefore, the net solar torque for the Sun tracking mode is

$$\begin{aligned} \vec{T}_{solar} &= \int \vec{r}_s \times d\vec{f}_{solar} = 8.95\times10^{-6} A(x_d \vec{j} - y_d \vec{i}) \\ &= (-1.1\times10^{-6}\vec{i} + 1.1\times10^{-9}\vec{j})\,\mathrm{Nm} \end{aligned} \tag{6-7}$$

, where $\vec{i}$ and $\vec{j}$ are the unit direction vectors along the x and y axes, respectively.

The characteristic of the solar torque is that it is a constant during sunlit periods and it is zero during eclipse periods.

6.1.2 Aerodynamic drag

The aerodynamic drag force $d\vec{f}_a$ acting on an infinitesimal surface element dA, with outward normal $\vec{N}$ as shown in Figure 6-3, is given by

$$d\vec{f}_a = -\frac{1}{2} C_D \bar{\rho} V^2 \left(\vec{N}\cdot\vec{v}_o\right)\vec{v}_o dA \tag{6-8}$$

, where C_D is the drag coefficient of the satellite surface, $\vec{v}_o$ is the unit vector in the direction of the translational velocity, V, of the surface element relative to the incident air molecular stream and $\bar{\rho}$ is the mean atmospheric density.

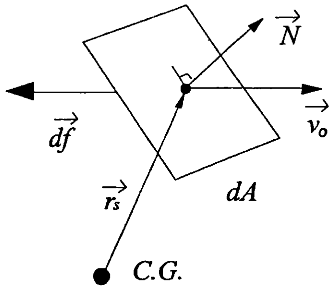

Figure 6-3 Aerodynamic pressure on a infinitesimal surface

The drag coefficient generally ranges between 2 ~ 4 for spacecraft surfaces (Larson & Wertz, 1992). Since neither a direct measurement nor a modelling of the coefficient is performed, a near-worst case value of 3 is selected for the following analysis. The magnitude of the orbital velocity can be found in Equation (2-9) as 7.49 km/sec. The atmospheric density is taken as $2.7 \times 10^{-13}\ \mathrm{kg/m^3}$, considering that the satellite has to survive the expected solar maximum around 2001.

The aerodynamic torque, $\vec{T}_{AD}$, in Equation (6-9) can be calculated by letting the angle between the orbit velocity vector and the surface normal vector of the deployed solar panels be θ as depicted in Figure 6-4.

$$\vec{T}_{AD} = \int_{\vec{N}\cdot\vec{v}_o>0} \vec{r}_a \times d\vec{f}_a = \frac{1}{2} C_D \bar{\rho} V^2 \cos\theta \int (\vec{v}_o \times \vec{r}_a) dA \tag{6-9}$$

The angle varies once per orbit period, *P*. Therefore, we can write the time varying form for θ as Equation (6-10), where the initial angle is defined when the satellite passes over its highest latitude region at the equinox.

$$\theta(t) = 2\pi / Pt = \omega_o t \tag{6-10}$$

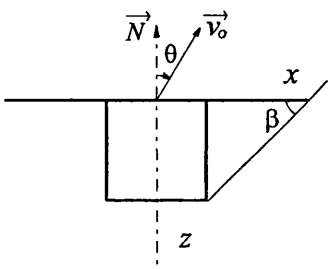

Figure 6-4 Satellite orientation for aerodynamic analysis

As discussed in the solar pressure torque estimation, Equation (6-9) can be simplified if we remember that $\vec{r}_a$ is the vector from the spacecraft centre of the mass to the surface element dA and the centre of mass offset plays an important role in the calculations too. Unlike the previous estimation of the solar pressure case, the reference attitude angle is no longer a constant. Therefore, the effective facets for analysis change with time. Hence, we need to proceed with the analysis on a case by case basis.

Case 1 : $\beta - \pi/2 < \theta \le \pi/2 - \beta$

Atmospheric molecular collisions occur only on the $-z$ axis solar panels. The angle β defined in Figure 6-4 is given as

$$\beta = \tan^{-1}\left(\frac{c}{d}\right) = 42.7^{o} \tag{6-11}$$

The net aerodynamic torque on the $-z$ axis solar panels is as follows.

$$\begin{aligned}\vec{T}_{AD1} &= \int \vec{r}_a \times d\vec{f}_a = 2.27\times10^{-5} A\cos\theta(x_d\vec{j} - y_d\vec{i}) \\ &= \vec{T}_{x1} + \vec{T}_{y1} = (-2.8\times10^{-6}\vec{i} + 2.8\times10^{-9}\vec{j})\ \cos\theta\,\mathrm{Nm}\end{aligned} \tag{6-12}$$

Case 2 : $\pi/2 - \beta < \theta \le \pi/2$

Neglecting the thickness of the solar panel, we have this second case. The torque calculation is more complicated since we need to consider two facets simultaneously, while one of them has a hidden area. Figure 6-5 shows the situation clearly. The deployed solar panels are under the same conditions as in Case 1, except that the collision angle is increased. The length of the shadowed area, l, in Figure 6-5 can be obtained from

$$l = c - d\tan(\beta - \alpha) \tag{6-13}$$

, where α is defined in Figure 6-5 as

$$\alpha = \theta + \beta - \pi/2 \tag{6-14}$$

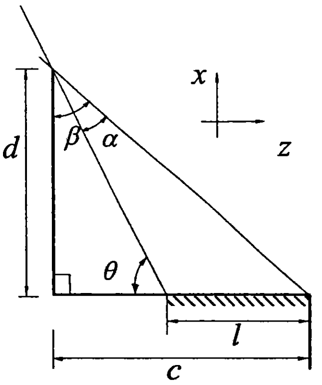

Figure 6-5 Geometry of aerodynamic torque for Case 2

Therefore, Equation (6-13) can be rewritten as

$$l = c - d\cot\theta \tag{6-15}$$

If we define the rectangular area of the $+x$ honeycomb panel as $B = ac$ and, using the relation in Equation (6-11), the shadowed effective area becomes

$$B' = \frac{c - d\cot\theta}{c}B = (1 - \cot\beta\cot\theta)B \tag{6-16}$$

The distance between the centre of mass and pressure along the z axis is

$$d_{z2} = c - \left(\frac{c}{2} + z_d\right) - \frac{l}{2} = \frac{d\cot\theta}{2} - z_d \tag{6-17}$$

Therefore, the torque for area B about the y axis is

$$\vec{T}_{y2B} = -d_{z2}B'\sin\theta\vec{j} \tag{6-18}$$

We should note that Equation (6-18) is a single variable function of θ and the torque from panel A, $\vec{T}_{2A}$, has to be add on it as (Refer Equation (6-12))

$$\vec{T}_{y2} = \vec{T}_{y2A} + \vec{T}_{y2B} = \left(2.8\times10^{-9}\cos\theta - d_{z2}B'\sin\theta\right)\vec{j} \tag{6-19}$$

The panel B also experiences torque about the z axis. The torque model follows a similar procedure as Equation (6-17) and there is no contribution from A for the z axis.

$$\vec{T}_{z2} = \vec{T}_{z2B} = -y_d B' \sin\theta \vec{k} \tag{6-20}$$

The torque about the x axis is the same form as $\vec{T}_{x1}$ in Equation (6-12) except the incident angle term.

$$\vec{T}_{x2} = -2.8 \times 10^{-6} \vec{i} \sin\theta \text{ Nm} \tag{6-21}$$

Case 3 : $\pi/2 < \theta \le \pi/2 + \beta$

This boundary starts where the air molecular collisions about to occur on -x side of the deployed solar panel. We have three separate facets to consider in this case. If we define the area of the +x honeycomb panel is $D = ad$ and the area of the +z honeycomb panel is $C = a(b - 2d)$, then the torque component about the y-axis is

$$\begin{aligned} \vec{T}_{y3} &= \vec{T}_{y3D} + \vec{T}_{y3B} + \vec{T}_{y3C} \\ &= \left(-D(b/2 - d/2 - x_d)\cos\theta + B\sin\theta z_d + C\cos\theta x_d\right)\vec{j} \end{aligned} \tag{6-22}$$

Following a similar procedure as in Case 2 gives rise to the torques for x and z axes.

$$\vec{T}_{x3} = \vec{T}_{x3D} + \vec{T}_{x3C} = -\left((D + C)y_d \cos\theta\right)\vec{i} \tag{6-23}$$

$$\vec{T}_{z3} = \vec{T}_{z3B} = -By_d \sin\theta \vec{k} \tag{6-24}$$

Case 4 : $\pi/2 + \beta < \theta \le \pi$

We have to consider four facets in this case and just add the torque term from the shadowed -x deployed solar panel to Case 3.

$$\vec{T}_{y4} = \vec{T}_{y3} + D(1 + \tan\beta \tan\theta) \times (b/2 + x_d - (d + c\tan\theta)/2)\cos\theta \vec{j} \tag{6-25}$$

$$\vec{T}_{x4} = \vec{T}_{x3} - Dy_d(1 + \tan\beta \tan\theta)\cos\theta \vec{i} \tag{6-26}$$

$$\vec{T}_{z4} = \vec{T}_{z3} \tag{6-27}$$

Case 5 : $\pi < \theta \le 3\pi/2 - \beta$

Case 5 has symmetric characteristics with respect to π if it is referred to Case 4. The *x*, *y* and *z* torques are in mirrored forms. The rest of the cases can be easily analysed utilising the symmetric property.

$$\vec{T}_{y5} = \vec{T}_{y4}(\pi - \theta) \tag{6-28}$$

$$\vec{T}_{x5} = \vec{T}_{x3} - Dy_d(1 - \tan\beta\tan\theta)\cos\theta\vec{i} \tag{6-29}$$

$$\vec{T}_{z5} = \vec{T}_{z3} \tag{6-30}$$

Case 6 : $3\pi/2 - \beta < \theta \le 3\pi/2$

$$\vec{T}_{y6} = \vec{T}_{y3}(\pi - \theta) \tag{6-31}$$

$$\vec{T}_{x6} = \vec{T}_{x3} \tag{6-32}$$

$$\vec{T}_{z6} = \vec{T}_{z3} \tag{6-33}$$

Case 7 : $3\pi/2 < \theta \le 2\pi - \beta$

$$\vec{T}_{y7} = \vec{T}_{y2A} + (d\cot\theta/2 + z_d)\times(1 + \tan\beta\cot\theta)B\sin\theta\vec{j} \tag{6-34}$$

$$\vec{T}_{x7} = \vec{T}_{x} \tag{6-35}$$

$$\vec{T}_{z7} = -(1 + \tan\beta\cot\theta)By_d\sin\theta\vec{k} \tag{6-36}$$

If we sum up all the torque components from Case 1 to Case 7, the effects of aerodynamic torque can be modelled. Figure 6-6 is the modelled torque over an orbit period when the satellite is in inertial point mode toward the Sun vector.

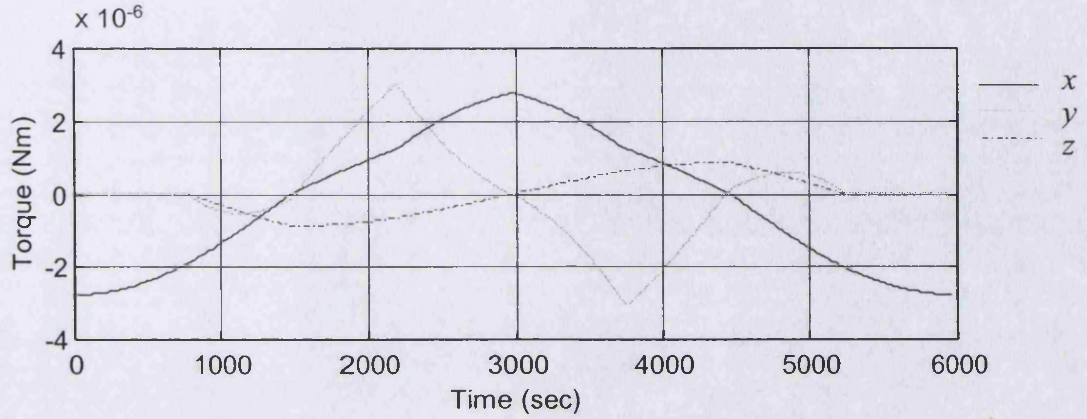

Figure 6-6 Aerodynamic torque model

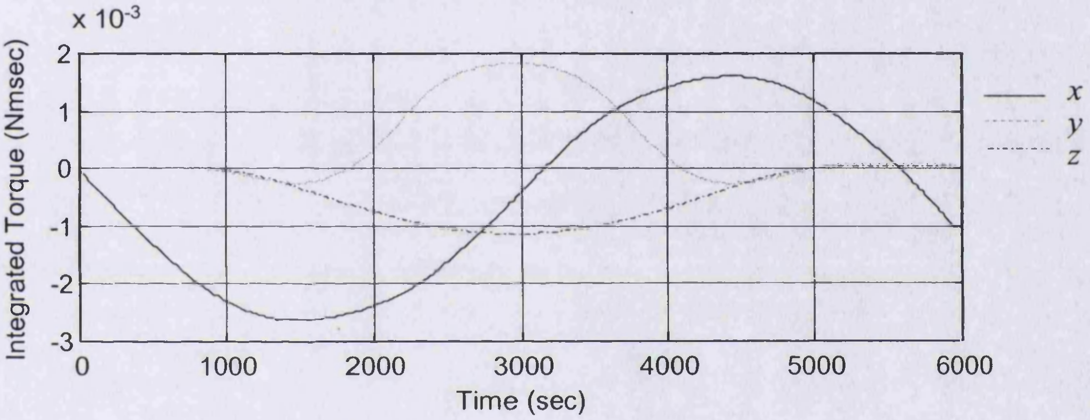

Figure 6-7 Integrated aerodynamic torque

Figure 6-6 shows that the aerodynamic torque is periodic with peaks of $\sim 3 \times 10^{-6}$ Nm for the x and y-axes, and z torque is relatively smaller than other torques. Since the accumulated torque over a certain period of time is very closely related with the reaction wheel control system, we need to study the secular characteristic of the disturbance torque. Figure 6-7 is the integrated aerodynamic torque model, where x-axis torque has a biased component. It may result in an in increment of wheel speed.

6.1.3 Gravity Gradient Torque

The orbital motion of a satellite is a result of the balancing of the gravitational and centrifugal forces at its centre of gravity. Small differences in the centrifugal force and gravitational field at the far edges of the satellite body invoke restoring torque to make the principal axes align with the gravitational field. The situation is well explained by the dumbbell model of a satellite in Figure 6-8.

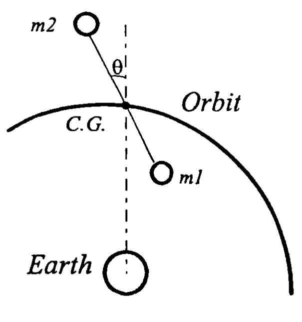

Figure 6-8 Gravity gradient dumbbell model

The gravity gradient torque to the satellite is given by (Kaplan, 1976)

$$\vec{T}_G = \frac{3\mu}{2a^3\sqrt{(1-e^2)^3}} \begin{bmatrix} (I_y - I_z)n_z n_y \\ (I_z - I_x)n_z n_x \\ (I_x - I_y)n_x n_y \end{bmatrix} \tag{6-37}$$

, where the scalar multiplying factors are from the orbital parameters defined in Chapter 2, n_x, n_y, and n_z are the unit components of the satellite position vector with respect to the principal axes of the spacecraft body, and I_x, I_y, and I_z are the principal moments of inertia. Since the spacecraft is in the Sun pointing mode for most of the time, the vector products in the above equation undergo periodic changes.

We need to find the principal axes of the satellite body in order to evaluate the effect of gravity gradient. The inertia tensor given in Section 2.4 and Equation (6-38) can be transformed into diagonal matrix, $\boldsymbol{I}_P$ as Equation (6-39), by finding the eigen axes.

$$\boldsymbol{I} = \begin{bmatrix} 7.10 & -0.043 & -0.017 \\ -0.043 & 5.84 & 0.017 \\ -0.017 & 0.017 & 8.16 \end{bmatrix} \tag{6-38}$$

The rotation matrix, $\boldsymbol{a}$, which transforms the principal axes into the body axes, is, in fact, the eigen vectors of Equation (6-38).

$$\boldsymbol{I}_P = \boldsymbol{a}^T \boldsymbol{I} \boldsymbol{a} \tag{6-39}$$

The eigen values of $\boldsymbol{I}$ are 7.1012, 5.8384, and 8.1604, which are the principal moments of inertia, I_x, I_y, and I_z. And the rotation matrix $\boldsymbol{a}$ is

$$\boldsymbol{a} = \begin{bmatrix} 0.9993 & 0.0340 & -0.0163 \\ -0.0338 & 0.9994 & 0.0076 \\ 0.0166 & -0.0071 & 0.9998 \end{bmatrix} \tag{6-40}$$

As pointed out in Chapter 3, a rotation matrix is a set of direction cosines. Equation (6-40) reveals that the offset of the *x*, *y*, and *z* principal axes with respect to the body axes are 2.16, 1.99 and 1.03 degrees, respectively. If we rewrite Equation (6-37) based on the calculated principal moments of inertia and the proposed orbital parameters, then

$$\vec{\boldsymbol{T}}_G = \begin{bmatrix} -7.76 n_z n_y \\ 3.45 n_z n_x \\ 4.22 n_x n_y \end{bmatrix} \times 10^{-6} \text{ Nm} \tag{6-41}$$

We can model the gravity gradient torque by defining the time varying terms of $n_{x,y,z}$. If there is no misalignment between the body and the principal axes, then

$$\boldsymbol{n}_o = \begin{bmatrix} n_{xo} \\ n_{yo} \\ n_{zo} \end{bmatrix} = \begin{bmatrix} \sin(\omega_o t - \pi/2) \\ 0 \\ -\cos(\omega_o t - \pi/2) \end{bmatrix} \tag{6-42}$$

, where $\pi/2$ is for phase synchronisation with the aerodynamic torque model.

To take into account of the seasonal variation of the reference pitch angle, $\pm 23.5°$, the rotation matrix $\boldsymbol{C}$ need to be considered, and then the resultant equation is

$$\boldsymbol{n} = \boldsymbol{a}^T \boldsymbol{C} \boldsymbol{n}_o \tag{6-43}$$

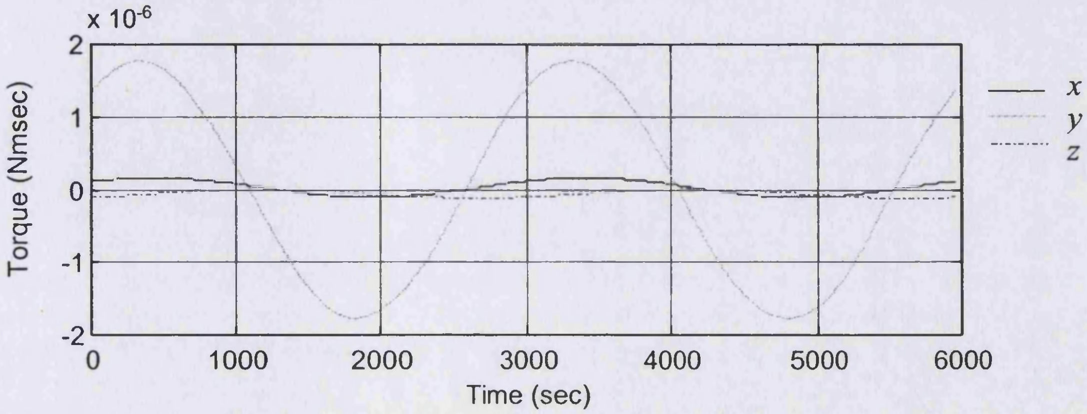

Figure 6-9 Gravity gradient torque model

Figure 6-9 is the simulation result of a gravity gradient model. It shows that the torque components are cyclic with a maximum value of $\sim 1.8 \times 10^{-6}$ Nm for the y-axis. Other torques are relatively small since the orbit has near 12:00 a.m. local Sun time. We should be aware that roll tilting is not considered here. If it were to be included, it would result in highly biased x axis torque.

6.1.4 Magnetic Disturbance

Magnetic torque is originated from the interaction between the spacecraft induced magnetism and the geomagnetic field as Equation (6-44).

$$\vec{T}_m = \vec{m} \times \vec{B} \tag{6-44}$$

, where $\vec{m}$ is the magnetic moment of satellite and $\vec{B}$ is the geomagnetic field.

When it is used in a controlled manner, it is the principle of a magnetorquer. However, unwanted residual magnetic moment and the current loops in the electrical system of a satellite generate disturbance torques. The magnetic characteristic is, unfortunately, very difficult to estimate or measure (NASA, 1969). Since an air core type magnetorquer is used in KITSAT-3, the largest magnetic disturbance comes from the permanent magnets in the IEHS chopping mechanism.

The location of the identical magnets, M_1 and M_2 are indicated in Figure 6-10.

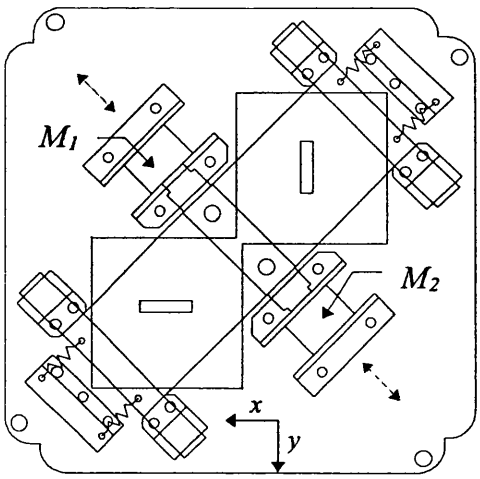

Figure 6-10 IEHS chopper mechanical structure

The magnetic field or the magnetic induction of the magnets is empirically measured at their surfaces as 2600 Gauss, which is equivalent to $0.26\ \mathrm{Wb/m^2}$. The magnets are cylindrical in shape with a diameter of 5 mm and length of 5 mm. The magnetic moment $\vec{m}$ of a cylindrical magnet can be obtained from the magnetic field model of the magnet. The magnetic field from a cylindrical magnet, for a point on the z axis, can be modelled as follows. If the magnet has a radius b and a length L and it is located on the centre of the xy plane with the top and bottom surfaces are along the z axis, then the magnetic field is, according to Cheng (1989),

$$\vec{B}_m = \frac{\mu_o M_o}{2}\left[\frac{z}{\sqrt{z^2+b^2}} - \frac{z-L}{\sqrt{z^2-b^2}}\right]\vec{k} \tag{6-45}$$

, where μ_o is the permeability of vacuum, $4\pi \times 10^{-7}\ \mathrm{N/A^2}$, M_o is the volume density of magnetic moment, $M_o\vec{k} = \vec{m}/(\pi b^2 L)$.

Since the measurement is made at the near surface of the magnet, $z \approx L$, and $2b = L$ in the interested permanent magnet, Equation (6-45) becomes

$$\vec{m} = \frac{2\pi b^2 LB}{\mu_o}\sqrt{\frac{5}{4}}\vec{k} = 2.27 \times 10^{-2}\vec{k}\ \mathrm{Am^2} \tag{6-46}$$

The torque generated by each magnet when it interacts with the geomagnetic field can be simply vector summed since they are independent. Thus the magnitude of the net magnetic moment, in this sense, is $4.54 \times 10^{-2}\ \mathrm{Am^2}$.

The result in Equation (6-46) corresponds to an approximated situation where the magnetic flux is proportional to the area covered, πb^2 and the dipole moment is also proportional to the moment arm. The factor 2 comes from the dipole nature of a magnet.

Considering the mechanical configuration in Figure 6-10, the actual magnetic moment vector is

$$\vec{m} = 1.61 \times 10^{-2}(-\vec{i} + \vec{j})\ \mathrm{Am^2} \tag{6-47}$$

We can analyse the effect of the residual magnetic moment by applying the geomagnetic field model discussed in Section 3.3. Cross product of Equation (6-47) and the geomagnetic field gives rise to the magnetic torque as described in Equation (6-44) and (6-48).

$$\vec{T}_m = \vec{m} \times \vec{B} = (m_y B_z - m_z B_y)\vec{i} - (m_x B_z - m_z B_x)\vec{j} + (m_x B_y - m_y B_x)\vec{k}$$
$$= m_y B_z \vec{i} - m_x B_z \vec{j} + (m_x B_y - m_y B_x)\vec{k} \quad (6\text{-}48)$$

Figure 6-11 is the simulated result over an orbit period.

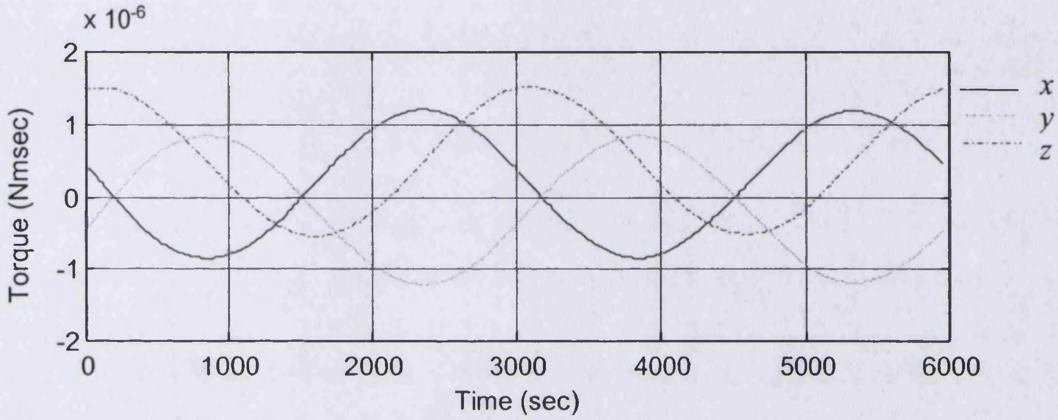

Figure 6-11 Residual magnetic torque model

6.1.5 *Integrated Environmental Torque Model*

We have discussed four major sources of space environmental disturbance torques. If the reference time of each torque model is synchronised in terms of the orbital position then the whole torque model can be built. Figure 6-12 is the result of the summing of all the torque models developed so far. Figure 6-13 shows cumulative torque behaviours over an orbit period.

The discontinuities of the *x* torque are from the discrete characteristic of the solar pressure torque. When the satellite goes into the umbra, whose portion is approximately 1/3 of the orbit, the solar torque disappears. Since it is the major term for the *x* axis, the effect is abrupt. Incidentally, all the environmental torques have similar order of importance. The peak magnitudes are around $10^{-6}\,\text{Nm}$. If they are combined together, the peak value is roughly $-4\times 10^{-6}\,\text{Nm}$. A large centre of mass offset along the *y* axis can be regarded as a culprit for the large *x* axis torque.

Since the long term behaviour of each torque term is more interesting, the cumulative torques are plotted to identify their characteristic in Figure 6-13. After an orbit period, the integrated torques are -4×10^{-3}, -1×10^{-3}, and 2.7×10^{-3} Nmsec for *x*, *y*, and *z* axes, respectively. The integrated torque implies a change of angular momentum of the spacecraft as can be seen from the Euler's equation in Section 3.1.

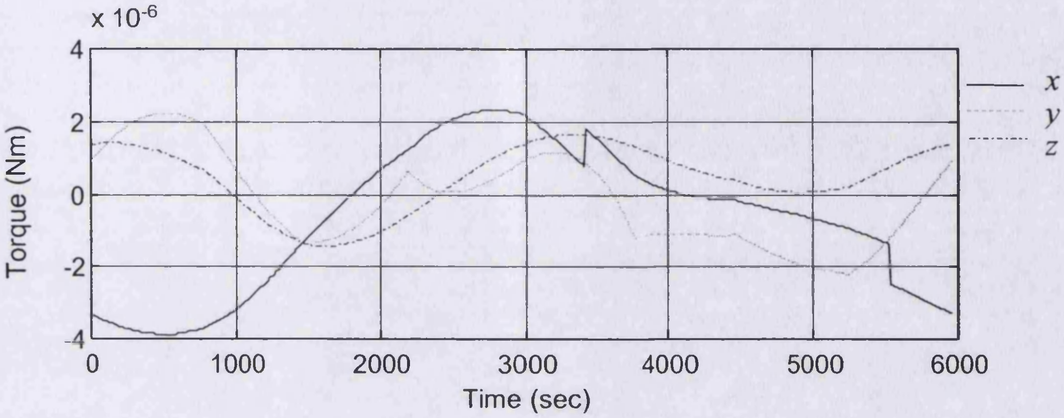

Figure 6-12 Combined environmental torque model

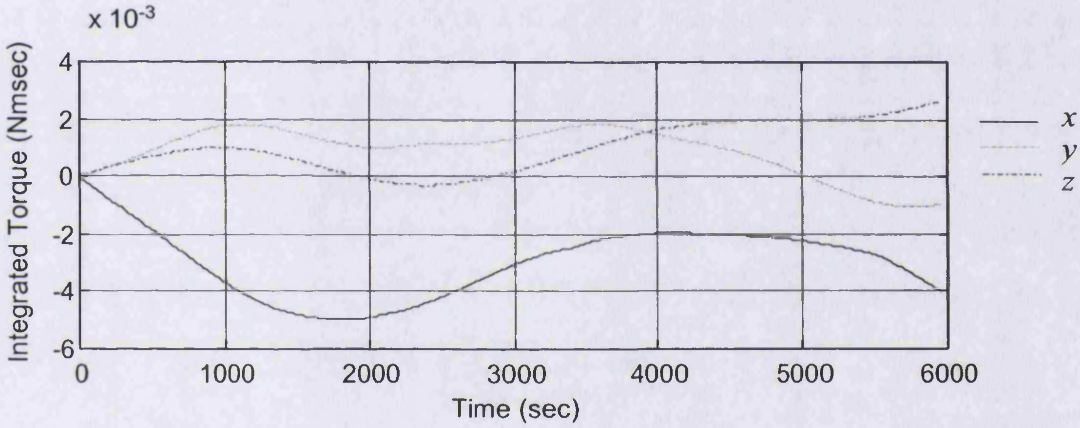

Figure 6-13 Cumulative environmental torque

We have assumed that the satellite has a stabilised attitude to the Sun for maximum power, which means that the orientation of the satellite is unchanged regardless of the angular momentum increment. Therefore, we have to provide a mechanism that can absorb the torque applied to the satellite. A reaction wheel can be used as a momentum storage device for this purpose. The angular momentum exchange technique stabilises the attitude of the satellite body in the presence of external disturbances.

Figure 6-13 suggests that after an orbit period, the reaction wheels of the satellite will gain angular momentum of the order of ~ mNmsec. We should note that the non-zero values of the cumulative torque would eventually result in a saturation of the wheel speed. Thus, we need to provide a way to dump the accumulated angular momentum of the wheel to keep the ADCS in operational condition. This procedure is called *momentum dumping* and the algorithm will be discussed in Chapter 7.

6.2 Evaluation of Effects of Mechanically Induced Noises

6.2.1 IEHS Chopper Vibration Noise

The mechanical chopper in the IEHS oscillates in the *xy* plane with 45° of oblique angle as shown in Figure 6-10. We need to develop a complex model to precisely describe the dynamics of the chopping mechanism. Instead of measuring or analysing the entire dynamic system, we can take advantage of the periodic nature of the chopper motion. For a rough order of magnitude evaluation, only the fundamental frequency is considered to obtain the position of the centre of the mass of the moving part as Equation (6-49).

$$\begin{aligned} x &= A\cos\omega t/\sqrt{2}+x_o \\ y &= -A\cos\omega t/\sqrt{2}+y_o \end{aligned} \tag{6-49}$$

, where A is the amplitude of the motion, 4 mm, ω is angular velocity from the oscillation frequency 20 Hz, x_o and y_o are the initial positions.

We can thus model the movement of the chopper as an oscillation of a point mass of 10 g, with an amplitude A. The difference between the centre of masses of the chopper and the rest of the spacecraft body is taken as 0.4, 0.4, 0.6 m along the x, y, and z axes.

We need to use the concept of reduced mass to develop the mathematical model of the satellite-chopper dynamics since the two body motion is physically connected with springs and we cannot regard the satellite main body as heavy enough to neglect the coupled effect. If we assign the mass of the chopper as m and the rest of the satellite as M, then the reduced mass μ is defined as

$$\mu = mM/(m+M) \tag{6-50}$$

The total dynamics of the system can be derived by calculating the torque from the chopper movement. We can assume that the satellite attitude motion is affected by the torque generated by the force and moment arm constructed from the difference between the centres of masses of the two systems. If we define the force as $\vec{f}=\mu\ddot{\vec{r}}$ then the torque is $\mu\ddot{\vec{r}}\times\vec{r}$. The angular momentum of the satellite main body about its mass centre $\vec{h}_B$ should react in such a way that the total angular momentum of the entire body is conserved. Therefore, neglecting other torques, the dynamic equation becomes

$$\dot{\vec{h}}_B + \mu\vec{r} \times \ddot{\vec{r}} = 0 \tag{6-51}$$

We can define $\vec{h}_B$ in the body-referenced frame of the satellite along the principal axes of the main body. Thus, the first term of the above equation does not contain the products of inertia and the components can be written using Euler's equation as

$$\begin{aligned}
\dot{h}_{Bx} &= I_x\dot{\omega}_x + (I_z - I_y)\omega_y\omega_z \\
\dot{h}_{By} &= I_y\dot{\omega}_y + (I_x - I_z)\omega_z\omega_x \\
\dot{h}_{Bz} &= I_z\dot{\omega}_z + (I_y - I_x)\omega_z\omega_x
\end{aligned} \tag{6-52}$$

Defining the components of the position vector, $\vec{r}$, of the mass centre of the chopper measured from the main satellite body as x, y, and z in the body fixed coordinate gives the components of the force $\vec{f}$ as follows.

$$\begin{aligned}
f_x &= \mu\left[\ddot{x} - 2\dot{y}\omega_z + 2\dot{z}\omega_y - y\dot{\omega}_z + z\dot{\omega}_y + y\omega_x\omega_y + z\omega_x\omega_z - x(\omega_y^2 + \omega_z^2)\right] \\
f_y &= \mu\left[\ddot{y} - 2\dot{z}\omega_x + 2\dot{x}\omega_z - z\dot{\omega}_x + x\dot{\omega}_z + z\omega_y\omega_z + x\omega_y\omega_x - y(\omega_z^2 + \omega_x^2)\right] \\
f_z &= \mu\left[\ddot{z} - 2\dot{x}\omega_y + 2\dot{y}\omega_x - x\dot{\omega}_y + y\dot{\omega}_x + x\omega_z\omega_x + y\omega_z\omega_y - z(\omega_x^2 + \omega_y^2)\right]
\end{aligned} \tag{6-53}$$

Substituting Equation (6-52) and (6-53) into (6-51) results in the total system dynamic equation in (6-54).

$$\begin{aligned}
&\left[I_x + \mu(y^2 + z^2)\right]\dot{\omega}_x + \left[I_z - I_y + \mu(y^2 - z^2)\right]\omega_y\omega_z \\
&+ \mu\left[-xy\dot{\omega}_y - xz\dot{\omega}_z + (2y\dot{y} + 2z\dot{z})\omega_x + yz(\omega_z^2 - \omega_y^2) - 2\dot{x}y\omega_y - 2\dot{x}z\omega_z - xz\omega_x\omega_y + xy\omega_x\omega_z + y\ddot{z} - z\ddot{y}\right] = 0 \\
&\left[I_y + \mu(z^2 + x^2)\right]\dot{\omega}_y + \left[I_x - I_z + \mu(z^2 - x^2)\right]\omega_z\omega_x \\
&+ \mu\left[-yz\dot{\omega}_z - yx\dot{\omega}_x + (2z\dot{z} + 2x\dot{x})\omega_y + zx(\omega_x^2 + \omega_z^2) - 2\dot{y}z\omega_z - 2\dot{y}x\omega_x - yx\omega_y\omega_z + yz\omega_y\omega_x + z\ddot{x} - x\ddot{z}\right] = 0 \\
&\left[I_z + \mu(x^2 + y^2)\right]\dot{\omega}_z + \left[I_y - I_x + \mu(x^2 - y^2)\right]\omega_x\omega_y \\
&+ \mu\left[-zx\dot{\omega}_x - zy\dot{\omega}_y + (2x\dot{x} + 2y\dot{y})\omega_z + xy(\omega_y^2 - \omega_x^2) - 2\dot{z}x\omega_x - 2\dot{z}y\omega_y - zy\omega_z\omega_x + zx\omega_z\omega_y + x\ddot{y} - y\ddot{x}\right] = 0
\end{aligned} \tag{6-54}$$

Analytically solving the above equation is impossible except for some special cases. Numerical simulation is more favoured for the study of the behaviour of the satellite attitude in the presence of the chopper motion. Since the oscillation frequency is as fast as 20 Hz, we need a very small time step to simulate the dynamics. A maximum time step of 0.005 second is allowed in the calculation. Therefore, a relatively short-term trend for 2 seconds has been simulated, in order to avoid extremely time consuming calculations. The main concern of this analysis is to evaluate the amplitude of the jittering motion rather than examine microscopic behaviour. We have used initial conditions in Table 6-1 for the dynamic simulation. Active attitude control is not applied in the analysis to observe the pure vibration effect.

Table 6-1 Initial conditions for the chopper dynamic simulation

Axis	x	y	z
Satellite Body Rate (rad/sec)	0	0	0
Wheel Speed (rpm)	0	0	0
Angle Offset (deg)	0	0	0

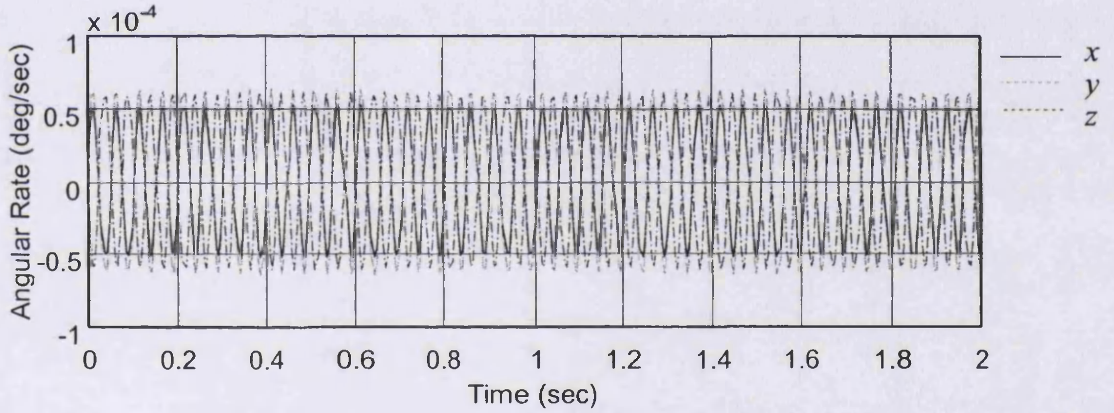

Figure 6-14 Satellite angular velocity change due to the chopper motion

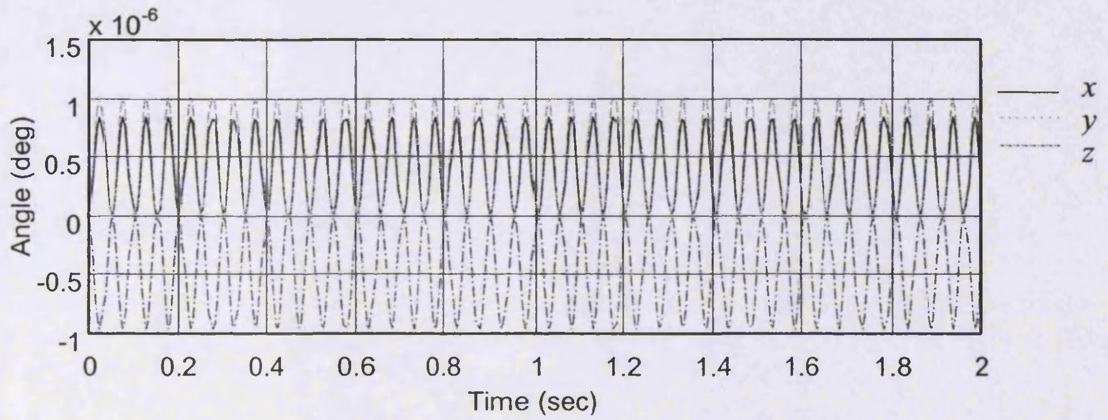

Figure 6-15 Satellite angle propagation due to the chopper motion

Figure 6-14 shows the history of the satellite angular velocity referred to its body frame. Figure 6-15 is the result of the integration of Figure 6-14. The figure shows that the pointing error caused by the chopper motion is bounded within 1.0×10^{-6} deg for the uncontrolled operation, which is 800 time smaller than the mid frequency vibration amplitude requirement at 20 Hz.

The attitude stability requirement is 0.016 deg/sec as described in Chapter 2. Figure 6-14 shows that the effect of the chopper vibration is about 6.0×10^{-5} deg/sec, which is also approximately 270 times smaller than the mid frequency stability requirement. The attitude error budget is discussed in conjunction with reaction wheel noise in the following section as well as Chapter 8.

6.2.2 Reaction Wheel Noise Effect Analysis

Reaction and momentum wheels are not ideal rotating devices. They generate various kinds of mechanical noise and the result will be micro vibration of the satellite attitude as discussed in the chopper noise case. The sources of motor noise can be categorised as flywheel imbalance, bearing disturbance, motor disturbance, motor drive disturbance and the effect of structural dynamics. The flywheel imbalance is considered the largest noise source (Bailke, 1997).

We can subdivide the flywheel imbalance into static and dynamic imbalance. The former comes from the offset of the wheel rotation axis to the real mass centre. The latter is from the fact that the rotation axis cannot be the same as the principal axis in reality. They can be modelled with two planar disks and two point masses that representing the imbalance as shown in Figure 6-16. We can assume that two homogeneous disks represent the ideal situation where the balance is perfectly matched. Small point masses located on the rims of disks, m_1 and m_2, can be regarded as effective imbalance sources. The angles α and β are measured from an arbitrary reference axis x to m_1 and m_2.

Static imbalance implies the moment applied to the wheel when it is in stationary condition. In other words, when α and β have 180° difference, the wheel can be thought to be statically balanced. We can define the effective static imbalance mass M_s to reflect the vector sums of the moments by the imbalance masses m_1 and m_2.

$$M_s = \sqrt{(m_1 \cos\alpha + m_2 \cos\beta)^2 + (m_1 \sin\alpha + m_2 \sin\beta)^2} \tag{6-55}$$

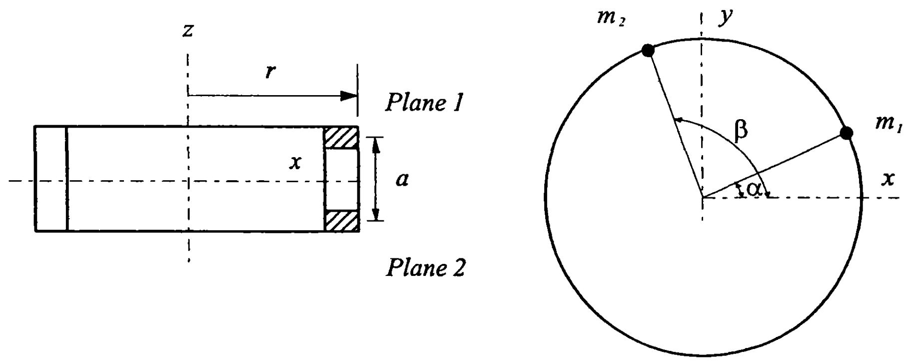

Figure 6-16 Flywheel imbalance model

The effective static imbalance U_s, then can be obtained from

$$U_s = rM_s \tag{6-56}$$

, where r is the radius of the disk. It has the same effect as putting a point mass M_s on the rim of the disk. The direction of the moment vector U_s is parallel to the disk planes.

Whereas the dynamic imbalance is related to the torque from the separation of the two planes. The torque, or the moment of force, T due to the imbalance is a function of the rotation rate ω and the imbalance mass m. The centrifugal force is given as $\vec{F} = m\vec{r}\omega^2$ and the resultant torque is $\vec{T}_{wd} = \frac{1}{2}\vec{a} \times \vec{F}$, where $\vec{a}$ is the position vector of m_1 and m_2 measured along the z axis in Figure 6-16. Similar to the static imbalance case, we can define the effective dynamic imbalance mass M_d to represent the vector difference of the moments by the imbalance masses m_1 and m_2.

$$M_d = \sqrt{(m_1 \cos\alpha - m_2 \cos\beta)^2 + (m_1 \sin\alpha - m_2 \sin\beta)^2} \tag{6-57}$$

The effective dynamic imbalance U_d for a unit angular velocity ω can be obtained.

$$U_d = \frac{1}{2} a \times r \times M_d \tag{6-58}$$

Table 6-2 is the actual measurements and calculation results for a reaction wheel in the worst case.

Table 6-2 Mass imbalance

m_1	α	m_2	β	M_s	M_d	U_s	U_d
0.028 g	215 °	0.028 g	65 °	0.015 g	0.054 g	0.22 gcm	1.6 gcm^2

The effects of the static and dynamic imbalances can be estimated based on the results in Table 6-2. If the wheel is rotating with a speed of 4000 rpm, the static force $F_{ws} = U_s\omega^2$ and the dynamic torque $T_{wd} = U_d\omega^2$ are 0.394 N and 0.0276 Nm, respectively.

Precise analysis of the imbalance effect needs an extremely complex dynamic model with very small simulation time steps for high frequency interpretation. Utilising the fact that the wheel mechanical noise has a striking resemblance to the IEHS chopper dynamics case allows us to simplify the model.

The dynamic imbalance analysis is straightforward since it is expressed in terms of torque. The noise torque of a specific axis can be considered as a rotation of a torque vector perpendicular to the axis, where the toque rotation is synchronised with the wheel rotation as depicted in Figure 6-17. The disturbance torque can be mathematically modelled with coupled sinusoidal functions as

$$T_{wd} = A\sin(\Omega_1 t + \phi_1) + B\sin(\Omega_2 t + \phi_2) \qquad (6\text{-}59)$$

, where, the amplitudes, A and B, are the dynamic imbalance torque, 0.0276 Nm as discussed previously. Ω and ϕ are the rotation speed and the phase of the torques by the perpendicular pair of wheels.

For instance the dynamic imbalance torque about x axis is a superposition of the torque generated by y and z wheels. A and B are taken as 0.0276 Nm, Ω is 4000 rpm, and ϕ is in phase for the worst case analysis.

If we simplify the spacecraft attitude dynamics as $I\omega' = T$, the attitude rate change due to the disturbance torque T can be written as $\omega = \frac{1}{I}\int T dt$ in terms of the moment of inertia I of the axis of interest. Therefore, a sinusoidal type torque $T = A\sin(\Omega t + \phi)$ will result in $\omega = \frac{A}{I\Omega}\cos(\Omega t + \phi)$. Applying the pitch principal moment of inertia 5.84 kgm^2 to this equation gives a maximum attitude rate disturbance of 1.3×10^{-3} deg / sec.

The static imbalance force generates torque proportional to the moment arm length formed by the mass centre of the wheel and the satellite body. 20 cm is taken as the maximum distance. Following the similar procedure as the dynamic imbalance case we can get the rate disturbance level of 3.7×10^{-3} deg / sec.

The worst case torque occurs when the dynamic and the static torque are in phase as well as the coupled torque. Adding directly the dynamic and static effects gives a worst case peak-to-peak rate disturbance level of 5.0×10^{-3} deg / sec. However, the torque components cannot be all in-phase from their definitions. It is more reasonable to use an RMS calculation, which results in 3.9×10^{-3} deg / sec. The actual level of disturbance will be far less then this estimate since out of phase components will diminish the effect.

Another source of wheels disturbance is the motor control error. The wheels are controlled within the accuracy of 1 rpm of the commanded speed when they are operated over 1000 rpm. The error acts like a torque noise. The ratio of the moments of the inertia of the satellite body and wheel is directly related with this noise effect. The quantisation error of the speed command, 0.212 rpm, has a similar outcome to the control error.

As discussed in Section 8.1.2 operating the chopper under the wheel noise environment complies the mid frequency rate stability requirement. The result indicates that the mass imbalance effects are the dominant factors as mechanically induced noise.

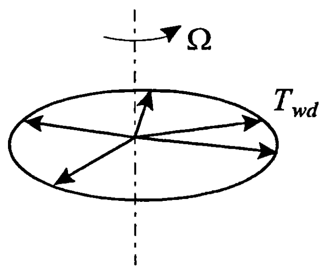

Figure 6-17 Flywheel dynamic imbalance torque

Chapter 7. Control System Design

7.1 Magnetorquering Algorithm

7.1.1 Momentum Dumping

While the spacecraft maintains its attitude in maximum Sun tracking mode, the angular momentum of the reaction wheels, especially in the x axis, builds up due to the environmental torques, as simulated in Figure (6-12) and Figure (6-13). After one of the wheels reaches its maximum momentum storage capacity, the satellite is no longer able to control its attitude by means of momentum exchange. Thus, occasional momentum dumping is necessary, utilising external torque. Magnetorquers can be used to generate a controlled disturbance torque that invokes counter torque by the wheels.

The magnetic torque vector should be controlled such that it reduces the speed of the wheels. However, the controllability of the magnetorquers is severely limited by the ambient geomagnetic field condition. Consulting Equation (6-48), we find that the controlled magnetic torque is allowed only on the plane perpendicular to the geomagnetic field vector. It is also clear that the parallel component of the magnetic moment to the geomagnetic field has a null effect on the resultant magnetic torque. Hence there is no reason to consume power to generate current flow in the magnetorquer coil. Generating the magnetic moment vector to be perpendicular to the surrounding geomagnetic field line thus becomes the basic control law.

We need to define the desired control torque to develop the control algorithm further. A simple weighting rule has been proposed according to the errors between the target and the observed wheel speeds, $\Delta\Omega$ (Kim *et al.*, 1995).

$$\vec{T}_{dc} = -K_w \Delta\vec{\Omega} \tag{7-1}$$

, where K_w is a constant gain, which includes the moment of inertia of the wheel.

The next step is to obtain the desired magnetic moment vector $\vec{m}$ in the sense of power effectiveness. The inverse of Equation (6-44) can be attained by multiplying geomagnetic field vector on the right and using vector identity for triple multiplication.

$$\vec{T}_{dc} \times \vec{B} = (\vec{m} \times \vec{B}) \times \vec{B} = \vec{B}(\vec{m} \cdot \vec{B}) - \vec{m}(\vec{B} \cdot \vec{B}) \tag{7-2}$$

Remembering that $\vec{m}$ should be perpendicular to $\vec{B}$ for maximum power efficiency, it becomes

$$\vec{T}_{dc} \times \vec{B} = -\vec{m}\left\|\vec{B}\right\|^2 \tag{7-3}$$

Combining Equation (7-1) and (7-3) gives rise to the following control law.

$$\vec{m} = K_m(\Delta\vec{\Omega} \times \vec{B}) \tag{7-4}$$

, where K_m is a positive real variable control gain which includes K_w and the norm of the magnetic field vector.

We need to create actual command data for the magnetorquer control packet discussed in Chapter 4. The direction cosines of $\vec{m}$, m_{xo}, m_{yo}, and m_{zo} can be obtained by decomposing Equation (7-4) as

$$\vec{m}_o = \begin{bmatrix} m_{xo} \\ m_{yo} \\ m_{zo} \end{bmatrix} = \frac{1}{K}\begin{bmatrix} B_z\Delta\Omega_y - B_y\Delta\Omega_z \\ B_x\Delta\Omega_z - B_z\Delta\Omega_x \\ B_y\Delta\Omega_x - B_x\Delta\Omega_y \end{bmatrix} \tag{7-5}$$

, where K is a scaling factor for unit vector constraint. By sensing the geomagnetic field and the wheel speed errors, we can calculate the controlled magnetic moment. It should be noted that K is positive real for momentum unloading and it is applicable for bi-directional wheel speeds.

For practical applications, we should consider the unbalanced magnetic moments of each axis as summarised in Table 7-1. The largest possible magnetic momentum vector must be calculated first within the limits defined in Table 7-1. The constraint confines the availability of the magnetic moment. The problem then becomes finding the norm of the vector $\vec{G}$ when it intersects the boundary surface as

$$\begin{aligned} &\vec{G} = \left\|\vec{G}\right\|(m_{xo}\vec{i} + m_{yo}\vec{j} + m_{zo}\vec{k}) \\ &|x| \le a,\ |y| \le b, c_2 < z < c_1, \end{aligned} \tag{7-6}$$

, where the constants a, b, c_1 and c_2 are the maximum magnetic moments of 10.1, 6.21, 10.1 and –11.88 Am^2, respectively. The solution can be easily obtained from the following logic with an exception, if $m_{zo} < 0$, $c = c_2$ else $c = c_1$.

Table 7-1 Magnetic torquer implementation results

Axis	±x, +z	-z	±y
Magnetic moment (Am^2)	10.10	11.88	6.21

$$\text{Case 1}: |m_{xo}|b < |m_{yo}|a, \text{ and } |m_{zo}|b < |m_{yo}|c$$

$$m_y = sign(m_{yo})b, m_x = \frac{m_{xo}}{m_{yo}}b, m_z = \frac{m_{zo}}{m_{yo}}b \tag{7-7}$$

$$\text{Case 2}: |m_{yo}|a < |m_{xo}|b, \text{ and } |m_{zo}|a < |m_{xo}|c$$

$$m_x = sign(m_{xo})a, m_y = \frac{m_{yo}}{m_{xo}}a, m_z = \frac{m_{zo}}{m_{xo}}a \tag{7-8}$$

$$\text{Case 3}: |m_{xo}|c < |m_{zo}|a, \text{ and } |m_{yo}|c < |m_{zo}|b$$

$$m_z = sign(m_{zo})c, m_y = \frac{m_{yo}}{m_{zo}}c, m_x = \frac{m_{xo}}{m_{zo}}c \tag{7-9}$$

The 8-bit control logic spans n = 256 level quantisation space. However, the hardware design deliberately imposed a saturation region in order to guarantee linearity, as mentioned in Chapter 4. The actual maximum control input is, therefore, limited to 240 levels. The signs of the input values determines which one of the two magnetorquers, MTQR1 or 2, should be used. The following procedures can be applied for control law:

1. Measure $\vec{B}$ and $\Delta\vec{\Omega}$, then calculate $\vec{m}_o$
2. Calculate m_x, m_y, and m_z
3. $L_x = 240m_x/10.1$
4. $L_y = 240m_y/6.21$
5. $L_z = 240m_z/10.1$ (if $m_z > 0$) or $240m_z/11.88$ (if $m_z < 0$)
6. Use MTQR1 if L >0 or MTQR2 if L <0

During normal operation, MTQR1 and 2 are assigned for positive and negative magnetic moment control respectively. If one of the two modules fails, we have to use the polarity changing function to meet the bi-directional control requirement. This will reduce the lifetime of the relay since switching is guaranteed only 100,000 times.

Figure 7-1 demonstrates the momentum dumping capability of the KITSAT-3 based on these rules. A sampling time of twenty seconds is used for the magnetometer and it is assumed that the same control output is maintained for two seconds. Nominal speeds Ω_0 of x, y, and z wheels of -2000, -2000 and 2000 rpm are used. The speed increments after 15 orbits were estimated based on the analysis in Figure 6-13, as –2400, -600 and +1600 rpm.

We need to implement control logic to avoid excessive control effort close to the desired target point. The cost function J that explains the level of acceptance is defined as the error angular momentum of the wheel. A value of 0.01 Nmsec is selected in the simulation. Moreover, hysteresis logic is utilised to prevent chattering. After Momentum dumping is disabled, re-enabling occurs when the cost function crosses 0.012 Nmsec.

$$J = I_w \left\| (\vec{\Omega} - \vec{\Omega}_0) \right\| \tag{7-10}$$

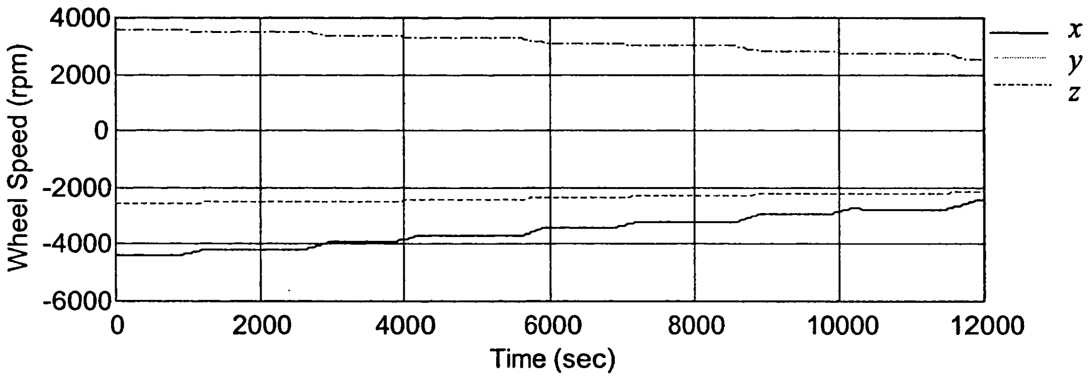

Figure 7-1 Wheel speed change

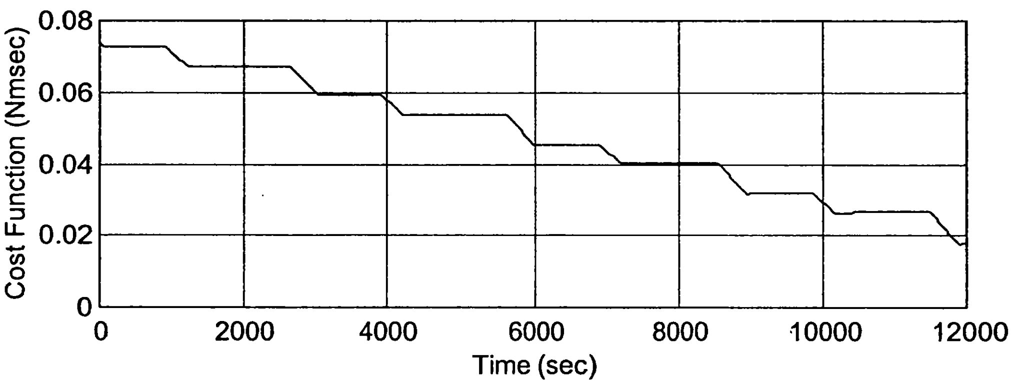

Figure 7-2 Momentum dumping cost function

For effective usage of power, the magnetic moment vectors must be controlled carefully. The x axis is likely to be controlled most since the x disturbance torque is the dominant one, as shown in Figure 6-13. When the geomagnetic field component B_x is near zero, the magnetic dipole component m_x of the magnetorquer must be close to zero too. Therefore, the resultant undesired torques along the transverse axes become relatively small compared to the desired axial torque.

Magnetic field components with respect to the satellite body fixed frame in the Sun tracking mode vary with half of the orbit period, as discussed in Section 3.3. Magnetic moment must be controlled when the geomagnetic field is near perpendicular to the axis for which the momentum is to be dumped. This algorithm eliminates possibilities of momentum change in unwanted directions. Such opportunities are available four times per orbit period as shown in Figure 7-3.

We need to quantitatively define the term, near perpendicular, in mathematical form for logic implementation. This can be achieved by calculating the control efficiency in terms of desired and undesired torque. If we use a 1-2-3 coordinate system with the second axis parallel to the error angular momentum vector, then the former can be written by consulting Equation (6-48) as

$$|T_{ds}| = |-m_1 B_3 + m_3 B_1| = \sqrt{(m_1^2 + m_3^2)(B_1^2 + B_3^2)} \tag{7-11}$$

, where B is the magnetic field vector in the 123 frame. The fact that $\vec{m}$ should be perpendicular to $\vec{B}$ is assumed in the above calculation. Conversely the latter is

$$|T_{un}| = |-m_3 B_2 \vec{i} + m_1 B_2 \vec{k}| = B_2 \sqrt{(m_1^2 + m_3^2)} \tag{7-12}$$

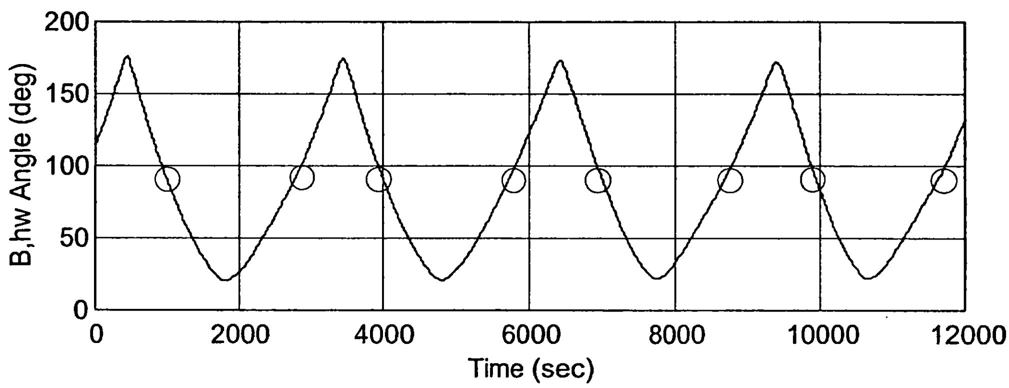

Figure 7-3 Angle between the magnetic field and wheel angular momentum

Therefore the efficiency E is

$$E = \frac{|T_{ds}| - |T_{un}|}{|T_{ds}|} = 1 - \frac{B_2}{\sqrt{B_1^2 + B_3^2}} = 1 - \frac{1}{\tan\Phi} \tag{7-13}$$

, where Φ is the angle between the error angular momentum vector and the geomagnetic field vector. We should note that this calculation could be easily performed about the satellite body referenced frame as follows: (It is shown in Figure 7-3.)

$$\cos\Phi = \frac{\Delta\vec{\Omega} \cdot \vec{B}}{|\Delta\vec{\Omega}||\vec{B}|} \tag{7-14}$$

Previous figures result from dead band switches with hysteresis characteristics. They are employed to avoid unnecessary control efforts when the power-torque efficiency is too low. The enabling logic will be turned on when the angle reaches 80 degrees, which corresponds to 82% efficiency, and it turns off if it falls below 60 degrees.

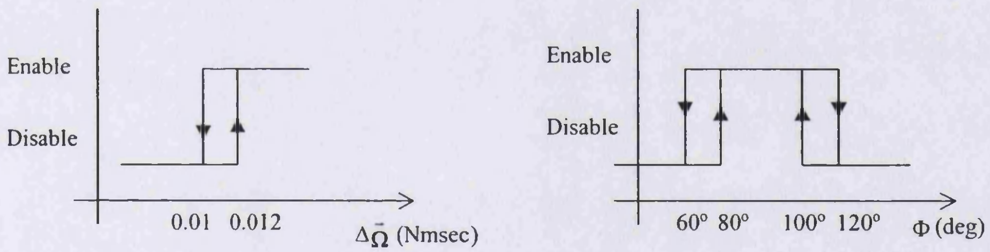

Figure 7-4 Momentum dumping enabling logic

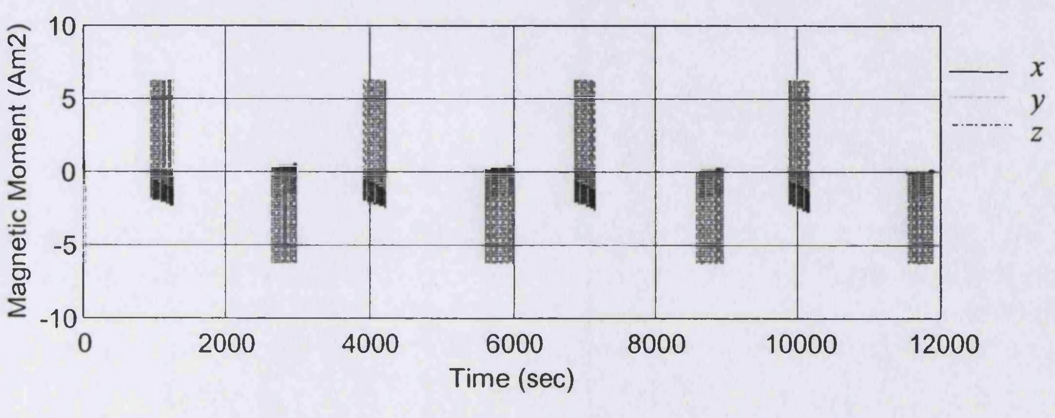

Figure 7-5 Magnetic moment control history

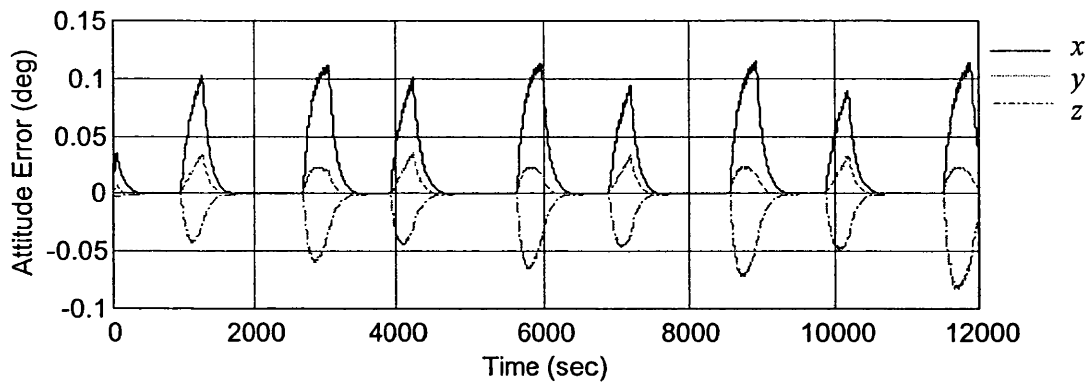

Figure 7-6 Attitude angle error during momentum dumping

The flat parts in Figure 7-1 and Figure 7-2 result from the logic described in Figure 7-4. It shows that only a small portion of the orbit is utilised for the sake of efficiency. However, the performance is good enough to dump the momentum acquired for one day within two-orbit period with 10% duty cycle of the magnetorquer operation. The total on time for the magnetorquer firing is 277 sec. If we average the power consumption over an orbit period, it is merely 0.23W, which imposes few problems in the power budget. Figure 7-6 is the resultant Sun pointing angle error due to the disturbance caused by magnetorquering. The maximum error around 0.12° will not affect the solar power generation greatly.

7.1.2 Initial Detumbling

The fourth stage of the PSLV ejects KITSAT-3 by the stored force in a spring mechanism. The centre of gravity offset of the satellite will result in lateral spin about the x axis with nominal rate of 2.1°/sec. If we include all the uncertainties, the maximum spin rate can reach 7 °/sec (Antrix, 1998). The initial angular momentum is too large for the reaction wheel systems to absorb completely. We need to reduce it within an acceptable boundary before sending a command to turn on the wheels.

This initial attitude detumbling is slightly different from momentum dumping process. The main interest is just reducing the rotation speed of the satellite body. Therefore, the control logic is even simpler than the previous one. Magnetometer data is used for the rate control instead of the gyro data, since the FOG module cannot be turned on due to the power restriction while the solar panels are stowed. Sun sensor data is used to avoid an emergency situation where the solar power is not available.

It is analysed that the cross product law in Equation (7-4) is optimal for controlling the angular momentum vector. The major difference for the initial detumbling mode is that direct rate measurement is not possible. Therefore, we need to develop a method to estimate the satellite angular rate by means of magnetometer measurement only. Referring to Equation (3-9), the time derivative of the magnetic field vector can be expressed as follows.

$$\dot{\vec{B}}_{ib} = \dot{\vec{B}}_b + \vec{\omega} \times \vec{B}_b \tag{7-15}$$

, where the subscript *ib* implies the inertial vector expressed in the satellite body frame and *b* is for measurement with respect to the satellite body axes.

If the rotation rate of the satellite $\vec{\omega}$ is large enough then the term $\dot{\vec{B}}_{ib}$ can be ignored. (The validity of this assumption will be discussed shortly.) Thus the above equation can be approximated as

$$\dot{\vec{B}}_b \approx \vec{B}_b \times \vec{\omega} \tag{7-16}$$

The right side of Equation (7-16) corresponds to that of Equation (7-4) in exactly the same manner except the direction, where $\vec{\omega}$ represents the rate error in this case. The control law, therefore, becomes

$$\vec{m} = K_m (\Delta\vec{\omega} \times \vec{B}) \approx -K_m \dot{\vec{B}}_b \tag{7-17}$$

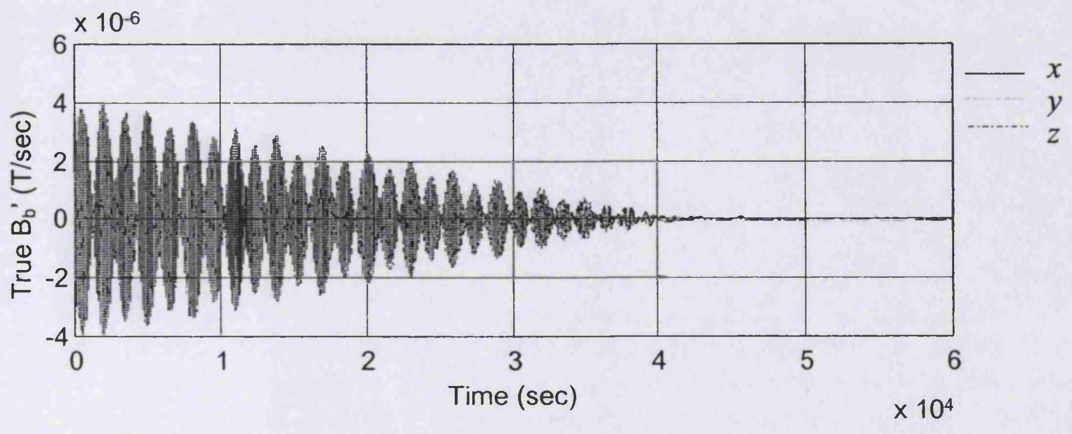

Figure 7-7 True magnetic field derivatives, $\dot{\vec{B}}_b$

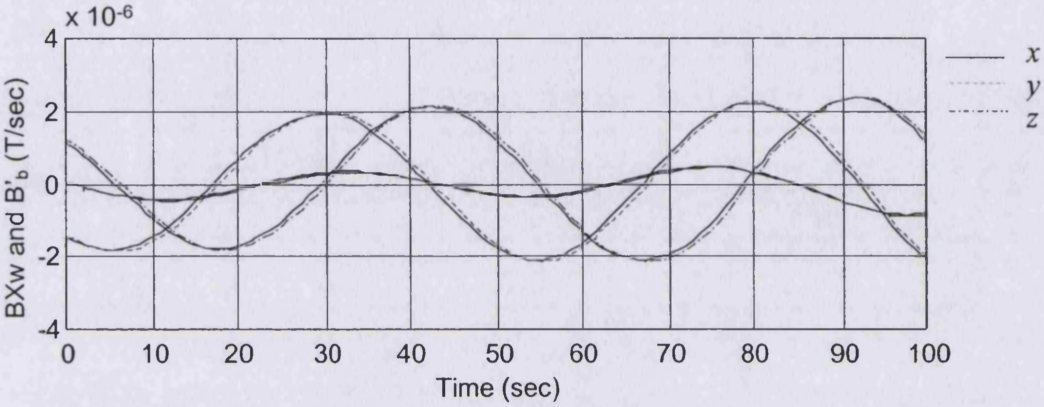

Figure 7-8 Estimated $\vec{B}_b \times \vec{\omega}$

Figure 7-7 shows the true value of $\dot{\vec{B}}_b$ generated by computer-aided simulation with initial separation angular velocities of –0.12, 0.02, and 0.03 rad/sec about the x, y, and z axis, respectively. The validity of the approximation can be checked by comparison with Equation (7-16), as shown in Figure 7-8

We need to prove the stability of the control law in Equation (7-17) before applying it. Wisniewsky (1996) showed that the system is stable by neglecting the $\dot{\vec{B}}_{ib}$ term. However, we can extend his work including this ignored term. We can assess the effect of the term by defining a criterion function as the rotational energy E that we would like to reduce.

$$E = \frac{1}{2}\vec{\omega} \cdot \vec{h} \tag{7-18}$$

The derivative of energy can be obtained by rearranging Equation (3-17) and (3-18) as

$$\begin{aligned} \dot{E} &= \frac{1}{2}(\dot{\vec{\omega}} \cdot \vec{h} + \vec{\omega} \cdot \dot{\vec{h}}) = \vec{\omega} \cdot \dot{\vec{h}} \\ &= \vec{\omega} \cdot (-\vec{\omega} \times I\vec{\omega} + \vec{T}) = \vec{\omega} \cdot \vec{T} \end{aligned} \tag{7-19}$$

If we use the approximated control law in Equation (7-17), then (7-19) becomes

$$\dot{E} = \vec{\omega} \cdot \vec{T} = -K_m \vec{\omega} \cdot (\dot{\vec{B}}_b \times \vec{B}_b) \tag{7-20}$$

Further development is possible if we use Equation (7-15) and (7-21).

$$\vec{\omega} \cdot (\dot{\vec{B}}_b \times \vec{B}_b) = \dot{\vec{B}}_b \cdot (\vec{B}_b \times \vec{\omega}) \tag{7-21}$$

$$\dot{E} = -K_m \dot{\vec{B}}_b \cdot (\dot{\vec{B}}_b - \dot{\vec{B}}_{ib}) = -K_m \left(\left\| \dot{\vec{B}}_b \right\|^2 - \dot{\vec{B}}_b \cdot \dot{\vec{B}}_{ib} \right) \tag{7-22}$$

To ascertain $\dot{E} < 0$, the following condition has to be satisfied.

$$\left\| \dot{\vec{B}}_b \right\|^2 - \dot{\vec{B}}_b \cdot \dot{\vec{B}}_{ib} = \left\| \dot{\vec{B}}_b - \dot{\vec{B}}_{ib}/2 \right\|^2 - \left\| \dot{\vec{B}}_{ib} \right\|^2 /4 > 0 \tag{7-23}$$

Using the fact $\left\| \dot{\vec{B}}_{ib} \right\|^2 = \left\| C_{bi} \dot{\vec{B}}_i \right\|^2 = \left\| \dot{\vec{B}}_i \right\|^2 \approx \text{constant} < 6 \times 10^{-15}$, we can define a sufficient condition for the energy dissipation control excluding a trivial solution at $\vec{B}_b = \vec{0}$ as

$$\dot{E} < 0 \text{ if } \left\| \dot{\vec{B}}_b \right\|^2 > 6 \times 10^{-15} \tag{7-24}$$

The result suggests that the detumbling control should be deactivated if the measured $\left\| \dot{\vec{B}}_b \right\|^2$ is smaller than the predefined constant value. Similar to the momentum dumping case, Schmitt trigger logic in Figure 7-9 can be applied in addition to Equation (7-17). The square of the norm of the magnetic field derivative is preferred to the norm itself since it reduces the extra computation required for the square root function. As described in Chapter 5, the resolution of the navigation magnetometer is 30 nT. A single bit difference corresponds to 9×10^{-16} in the criterion function. This implies that the triggerring occurs if the measured magnetic field diferrential is around 6~8 bits.

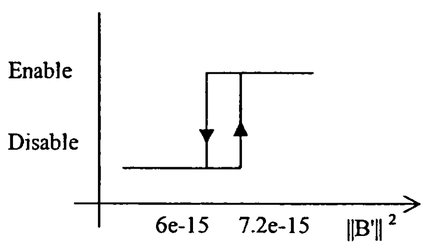

Figure 7-9 Detumbling control enabling logic

The detumbling control cannot be performed continuously due to the power limitation during the initial phase where the solar arrays are in the stowed position. Moreover, the magnetorquering interferes with magnetometer readout data. Two seconds of control action is allocated for every 20-second period in on-board software; this corresponds to 10% of the duty cycle. The following simulations are based on these realistic assumptions to assess the control capability.

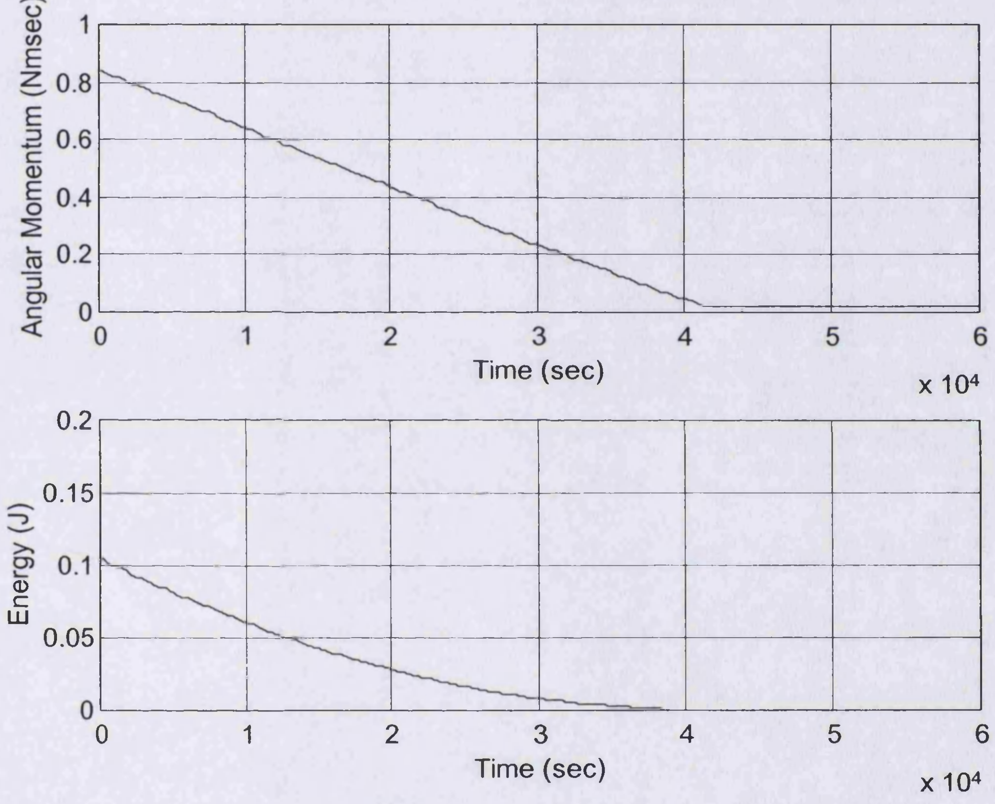

Figure 7-10 Angular momentum and energy reduction

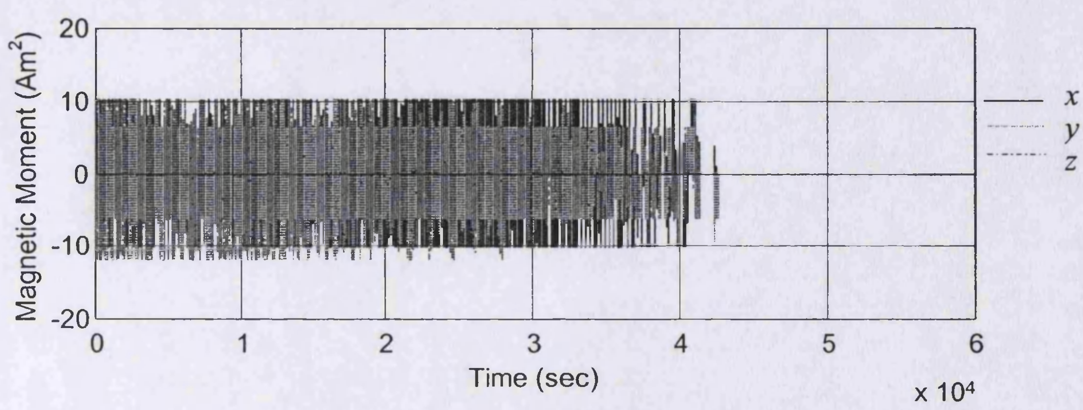

Figure 7-11 Magnetic moment control history

Figure 7-10 confirms that not only the rotational energy, but also the angular momentum, decreases by the proposed control law. Considering the momentum storage capacity of a reaction wheel, 0.1 Nmsec, it shows that the reaction wheel system is able to absorb the entire residual angular momentum after approximately seven-orbit period. We can also postulate that the satellite will be aligned with the local geomagnetic field from Figure 7-7 just like a compass. As previously mentioned, the 10% of operation duty cycle is applied.

The magnetic moment control logic developed in Equation (7-7) ~ (7-9) is applicable for the detumbling case too. A series of simulations showed that the enabling logic did not make a significant impact on the energy dissipation, although it ensures monotonic energy decrease, since the boundary given in Equation (7-24) is so small.

However, a practical importance of the logic arises from the power system's point of view. Figure 7-11 reveals that the control enabling logic in Figure 7-9 activated on the interval starting from 40000 sec. Unnecessary control effort, that can be characterised as a chattering, near the equilibrium point was removed by the logic. It cost 1.42W orbit average power for the magnetorquering.

7.2 HEPT Operation

The HEPT operation mode was originally intended to be initiated with pitch axis rotation control as described in Chapter 2. However, the result of analysis showed that there was no noticeable advantage in terms of the probability of observing highly confined energetic particles. This is mainly due to the fact that the geomagnetic field vector lies close to the orbital plane.

To enhance the observation rate, rotation about the roll axis instead of the pitch axis is an intuitive solution. Unfortunately, the roll axis has intermediate moment of inertia as shown in the inertia tensor in Equation (6-38), which implies that the motion is naturally unstable (Kaplan, 1976). Therefore, we need to find another way to increase the number of samples by aligning the geomagnetic field to be perpendicular to the $+z$ axis.

Keeping in mind that the pitch axis is the primary operation axis, we can suggest a free tumbling motion induced by the pitch rotation only. Free motion implies that no active control is involved. Figure 7-12 is the simulation result of the nutation angle about the pitch axis when the reaction wheels are at their nominal speeds, as indicated in Figure 7-1. It is assumed that the y wheel is commanded to a new speed of +2000 rpm from –2000 rpm at time 0, and the motor model in Chapter 4 is used.

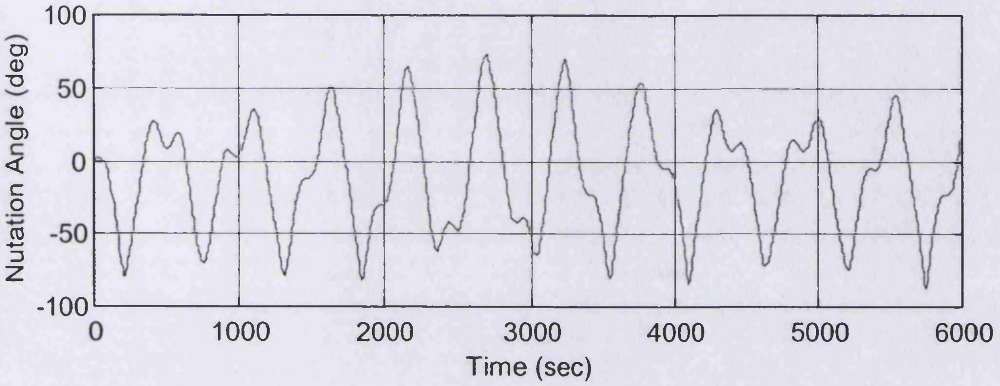

Figure 7-12 Nutation angle in free tumbling motion

The nutation angle can be easily obtained from the direction cosine matrix calculated from the integrated quaternions. Defining the nutation angle as the angle between the orbit normal axis and the y axis of the satellite body, then it is simply derived from the element of the direction cosine matrix $\boldsymbol{R}(2,2)$ in Equation (3-48)

$$N = \pi / 2 - \cos^{-1}(2q_1q_2 - 2q_3q_4) \tag{7-25}$$

The simulation is performed with zero initial error condition. The result in Figure 7-12 shows that the attitude motion is loosely bounded. This is due to the angular momentum stored in other wheels. The attitude wobbles but it is stable in a global sense. The nutation effect is advantageous in that it enhances the likelihood of encountering perpendicular magnetic field as shown in Figure 7-13.

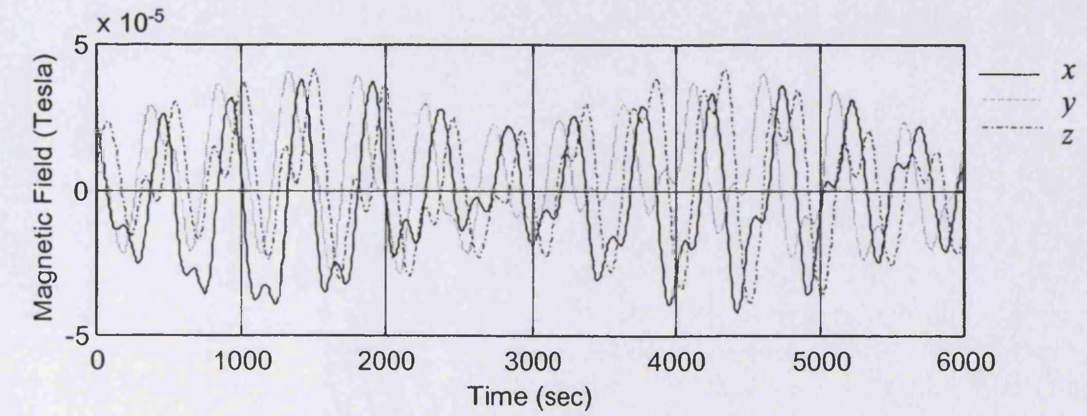

Figure 7-13 Magnetic field variation during free rotation

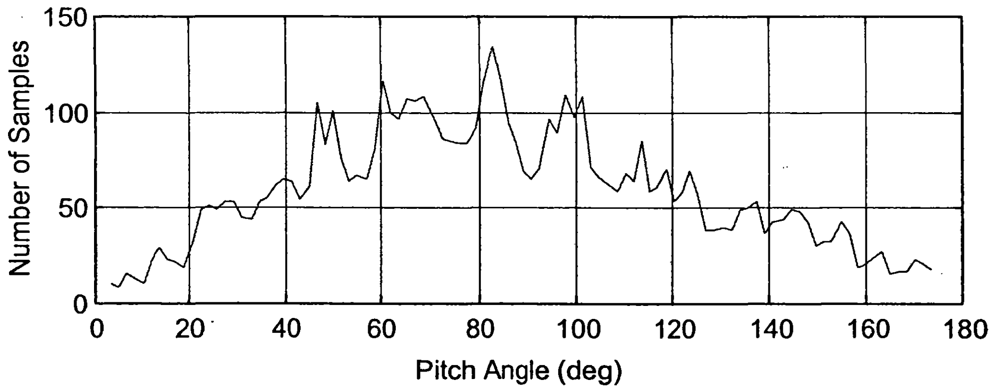

Figure 7-14 Pitch angle distribution change due to nutation

It was pointed out in the mission analysis in Chapter 2 that there is no distinguishable difference in terms of the number of samples of the pitch angle near 90° in the flat spin case. The modified distribution in Figure 7-14 shows that the probability has been increased almost two-fold compared to Figure 2-6.

Another important factor that we should keep in mind is the solar power reduction due to the change of the Sun vector. The cosine of the angle between the Sun vector and the –z axis is proportional to the solar power generation. If the angle is less than 90° then there is no power from the solar panels.

The Sun angle is also directly obtainable from ***R***(3,1) of the rotation matrix in Equation (3-48), upon the assumption that the initial Sun angle is 0.

$$S = \cos^{-1}(q_1^2 + q_2^2 - q_3^2 - q_4^2) \tag{7-26}$$

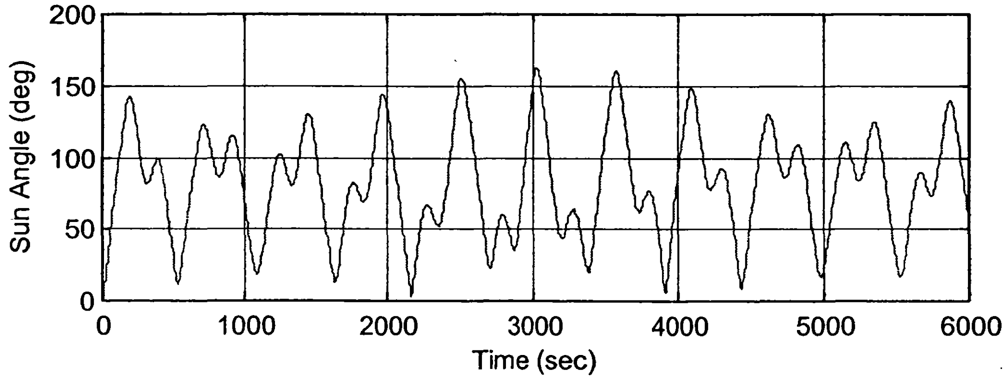

Figure 7-15 Sun vector change due to nutation

Considering eclipse regions, the Sun angle plot in Figure 7-15 gives an orbit average solar power of 30.8W, which is merely half of the required average power for minimum bus maintenance and HEPT operation. The battery system should provide energy to the rest of the satellite, approximately 45 Whr. Comparing with the designed discharging energy level during eclipse, 27 Whr, the required level is too high. The DoD (Depth of Discharge) is 20% after an orbit period if it is fully charged initially.

If we take other spinning approach *i.e.* z spin, the incoming solar power level can be escalated. However, through a series of decision-making processes, it is concluded that the operation is too risky. Sun pointing attitude is preferred as the normal HEPT operation orientation in this context. Spinning operation is excluded for this reason.

The analysis results are, however, useful for safe-hold mode assessment. The main difference is the required power level. Switching off the payload system and the gyros will give large margins for the power budget. A minimum subset of hardware will be utilised during this operation mode.

7.3 Large Angle Manoeuvres

7.3.1 Single Axis Manoeuvre

KITSAT-3 should change its attitude from Sun tracking to Earth pointing prior to imaging actions being performed. According to the mission analysis in Chapter 2, large angle manoeuvring is required about the pitch and the roll axis. Considering the seasonal variation and orbital drift of the reference angles, simultaneous manoeuvring of 90^o and 25^o along the pitch and the roll axes is taken as the baseline for the performance analysis.

Controlling the satellite attitude needs a way to quantitatively express the error. The control law uses the calculated error to generate appropriate control torque to reduce the error. Generally, the satellite attitude control algorithm has the following PD (Proportional and Derivative) logic as its basic rule.

$$\boldsymbol{T} = -\boldsymbol{K} f(\theta) - \boldsymbol{D} g(\dot{\theta}) \tag{7-27}$$

, where $\boldsymbol{K}$ and $\boldsymbol{D}$ are positive control gain matrices for position and rate representation.

The control law generates torque opposite to the angle and angular velocity errors. The velocity term is included for damping purpose. Reducing the rate and position error at the same time is the fundamental policy in attitude control (Wertz, 1978).

There are three common ways in describing the angular error, Euler angles, direction cosines and error quaternions (Sidi, 1997). The first one is simple and easy to understand but it has critical problems when being applied for large angle manoeuvres, where non-linearity cannot be neglected and singular point can be encountered. The second method is free from these problems but extensive computation load is put on the onboard computer system. The third way has the same advantages as the second case and it needs a simple set of arithmetic calculations only.

An arbitrary vector $\boldsymbol{a}$ in the reference frame can be expressed with respect to the measured orientation and the desiring commanded frame using the rotation matrices as

$$\begin{aligned} \boldsymbol{a}_m &= \boldsymbol{A}_m \boldsymbol{a} \\ \boldsymbol{a}_c &= \boldsymbol{A}_c \boldsymbol{a} \end{aligned} \tag{7-28}$$

Therefore, the attitude error matrix $\boldsymbol{A}_e$ can be defined as the rotation matrix that relates $\boldsymbol{a}_c$ to $\boldsymbol{a}_m$.

$$\boldsymbol{a}_c = \boldsymbol{A}_c \boldsymbol{A}_m^{-1} \boldsymbol{a}_m = \boldsymbol{A}_e \boldsymbol{a}_m \tag{7-29}$$

If the commanded and measured attitude coincide, the error matrix becomes an identity matrix. By examining the elements of the error matrix, we can obtain attitude error information. The error direction cosine matrix can be written in terms of the error quaternion q_{ei} , using the mathematical properties discussed in 3.2.3. From the definition of $\boldsymbol{A}_e$ in Equation (7-29), the error quaternions become

$$\boldsymbol{q}_e = \boldsymbol{q}_m^{-1} \boldsymbol{q}_c \tag{7-30}$$

Comparing Equation (7-30) with (3-38) and inserting (3-39) gives

$$\begin{bmatrix} q_{e1} \\ q_{e2} \\ q_{e3} \\ q_{e4} \end{bmatrix} = \begin{bmatrix} q_{c4} & q_{c3} & -q_{c2} & q_{c1} \\ -q_{c3} & q_{c4} & q_{c1} & q_{c2} \\ q_{c2} & -q_{c1} & q_{c4} & q_{c3} \\ -q_{c1} & -q_{c2} & -q_{c3} & q_{c4} \end{bmatrix} \begin{bmatrix} -q_{m1} \\ -q_{m2} \\ -q_{m3} \\ q_{m4} \end{bmatrix} \tag{7-31}$$

Rearranging Equation (7-31) results in simplified form of q_{ei} as

$$-\begin{bmatrix} q_{e1} \\ q_{e2} \\ q_{e3} \\ q_{e4} \end{bmatrix} = \begin{bmatrix} q_{c4} & q_{c3} & -q_{c2} & -q_{c1} \\ -q_{c3} & q_{c4} & q_{c1} & -q_{c2} \\ q_{c2} & -q_{c1} & q_{c4} & -q_{c3} \\ -q_{c1} & -q_{c2} & -q_{c3} & -q_{c4} \end{bmatrix} \begin{bmatrix} q_{m1} \\ q_{m2} \\ q_{m3} \\ q_{m4} \end{bmatrix} \tag{7-32}$$

It should be noted that if there is no error, *i.e.* $q_{mi} = q_{ci}$, then the error quaternions are $\begin{bmatrix}0 & 0 & 0 & 1\end{bmatrix}^T$. It is a great advantage that only 16 multiplications and 12 additions are required for the calculation. If the commanded attitude is the reference frame itself, then the relation, $q_{mi}^{-1} = q_{ei}$, and it simplifies the matrix computation. To design the control parameters and assess the capacity of the attitude control system, the simplified situation is quite useful.

Since the rotation along the Euler axis provides the shortest angular path between two orientations, it is an optimal manoeuvre. Finding the axis is a key issue of the controller design. If the control torque has the same direction as the Euler axis then the satellite manoeuvres in an optimal way.

Referring to the definitions of the quaternions in Equation (3-31) and (3-35), the elements of error quaternions can be used to describe the Euler axis.

$$e_i = q_{ei} / \sin\frac{\phi}{2} \tag{7-33}$$

The sine function in Equation (7-33) is common for all e_i. Thus, q_{ei} becomes a part of the proportional torque. We can construct a control law based on this reasoning. Equation (7-27) can be revised as

$$\boldsymbol{T} = -\boldsymbol{K}\boldsymbol{q}_e - \boldsymbol{D}\boldsymbol{\omega} \tag{7-34}$$

, where the sign inversion of the error quaternions are made to positive proportional gain. This is in accordance with the definition of the error direction in Equation (7-29).

Wie & Barba (1985) proposed other similar control laws based on the previous reasoning. Although there are some differences, the proposed algorithms have basically similar characteristics. For instance, the performance can be improved if the sign of the q_{e4} term is included when the angle is over 180°. The relation, $\boldsymbol{T} = -\boldsymbol{K}sign(q_4)\boldsymbol{q}_e - \boldsymbol{D}\boldsymbol{\omega}$, is an example of the modified control algorithm. Wie and Barba also rigorously proved the global stability of the control law using Lyapunov functions. The control law is also robust against inertia parameter uncertainty.

The attitude dynamic equation can be written with respect to the Euler axis upon small angular rate assumption. Neglecting the gyroscopic term in Equation (3-23) and remembering that $\vec{\omega} = \dot{\phi}\vec{e}$ for Euler axis rotation gives

$$(\ddot{\phi} + d\dot{\phi} + k\sin\phi/2)\boldsymbol{Ie} = 0 \tag{7-35}$$

, where the constant gain matrices should satisfy $\boldsymbol{K} = k\boldsymbol{I}$ and $\boldsymbol{D} = d\boldsymbol{I}$.

The constant gains, *k* and *d*, can then be assigned by analysing the second order non-linear differential equation containing a sine function. A conventional method is to find the critical damping parameters where there is no overshoot, which implies that there is no wasted control effort. However, we cannot use well-established linear second order system theory since the system includes sine term.

The adaptation of the linear system theory is possible if we consider relatively small angles $\phi < \pi/4$. Linearisation of Equation (7-35) about the rotation axis results in

$$\ddot{\phi} + d\dot{\phi} + k\phi/2 = 0 \tag{7-36}$$

We need to determine the settling time t_s of the feedback control system first, which is defined as the time required for a step response to decrease and stay within 5% of its final value. For the small angle case it becomes (Kuo, 1987)

$$t_s\omega_n\zeta \cong 3 \tag{7-37}$$

, where ω_n is the natural frequency and ζ is the damping ration satisfying

$$\begin{aligned} d &= 2\omega_n\zeta \\ k &= 2\omega_n^2 \end{aligned} \tag{7-38}$$

The selection of the approximated constant on the right side of Equation (7-37) affects convergence rate characteristics and peak torque. As the maximum rotation angle increases, we need to apply a modified value. Wie *et al.* (1989) used 4 and 8 for angles under $\pi/2$ and π respectively.

The system characteristics can be assessed by simulating the dynamic equation. A series of observations using various sets of parameters revealed that there is no fundamental difference except that the peak control torque dramatically changes. This is a common problem for constant gain control; we can use variable control gain schemes to resolve this. For example, a control algorithm based on a genetic algorithm was proposed by Kim *et al.* (1995). However, practical engineering analysis showed that it required extremely high computation capacity for the on-board microprocessor.

A simple torque limiting logic turned out to be very useful in many aspects. The test results of reaction wheel in Chapter 4 showed that there exists a wide range of operation speeds for 5 mNm of control torque. This statement holds for both the positive and the negative torque cases. A range of operation speeds of 1000 ~ 4000 rpm guarantees the torque envelope. Limiting the torque, however, does not give any unwanted effect for the Euler axis rotation since it is still proportional to the error angle.

If we select the settling time as 50 seconds then $\zeta = 1$ for critical damping constraint and $\omega_n = 0.06$ rad/sec. This corresponds to the constant control gains of $k = 0.0072$ and $d = 0.12$. A fast settling time is obtainable without exceeding the available torque range by limiting the control torque. This approach also improves convergence characteristics when the error gets smaller.

The dynamic equation in (7-36) is based on rest-to-rest manoeuvre where the initial and final angular velocities are zero. However, in KITSAT-3 case, it is a rest-to-constant rotation manoeuvre since the pitch rate should be synchronised with the negative orbital rate ω_0 for Earth scanning motion. A modified control law can be fabricated to take into account this requirement as

$$\ddot{\phi} + d(\dot{\phi} - \omega_0) + k\sin[(\phi - \omega_0 t)/2] = 0 \qquad (7\text{-}39)$$

The performance of the proposed control law is demonstrated in Figure 7-16. A time varying reference angle is assumed as $\phi_0 = \omega_0 t$.

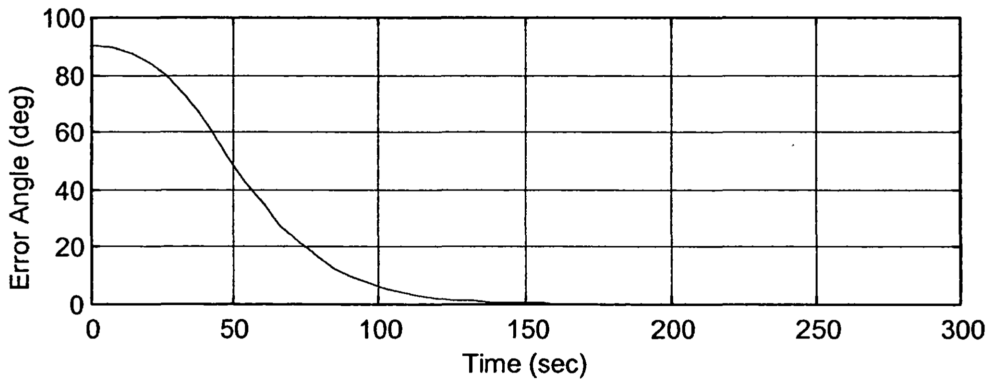

Figure 7-16 1-axis large angle manoeuvre about the Euler axis

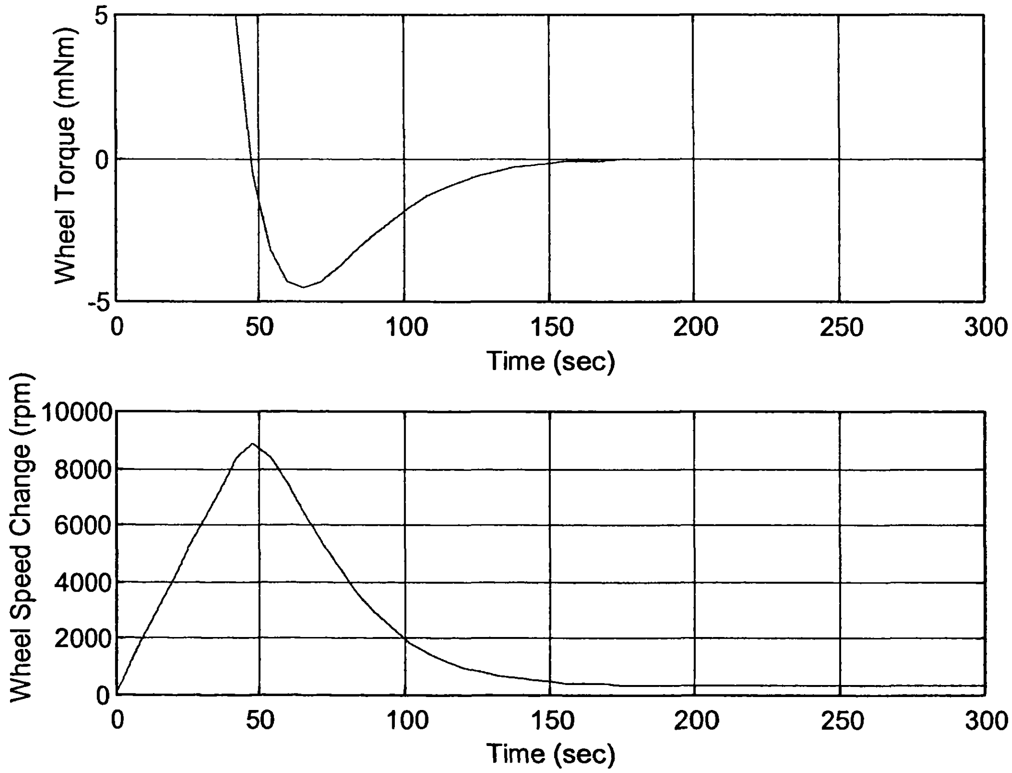

Figure 7-17 1-axis reaction wheel torque and speed change history

The initial error angle and velocity are assumed to be $\pi/2$ and 0, respectively. After 150 seconds the actual angle tracks within 0.5 degrees of error bound of the constantly rotating reference angle. We can observe that over-damping is not occurring as expected. This is due to the fact that the error angle rapidly becomes small enough to justify the linearisation.

Figure 7-17 shows the generated reaction torque and the resultant wheel speed change for a normalised moment of inertia of 8 kgm^2. When the error angle is over 60^o, the saturation logic is activated to limit the torque within 5 mNm. As the error becomes smaller, the torque follows the given control law. The final steady state wheel speed is slightly higher than its initial speed. This can be attributed to non-zero target pitch rate.

However, the control law has a problem in practical applications due to the excessive wheel speed change. Remembering that the maximum speed of DR01 type wheel in KITSAT-3 is 5000 rpm, there must exist a measure that can limit the wheel speed. Limiting the rotation rate of the spacecraft can equivalently do it. Applying a restriction to the position feedback simply performs the role. Figure 7-18 shows the control logic in Matlab simulink® block diagram. Two saturation blocks limit the torque and speed of the wheel for small satellite control.

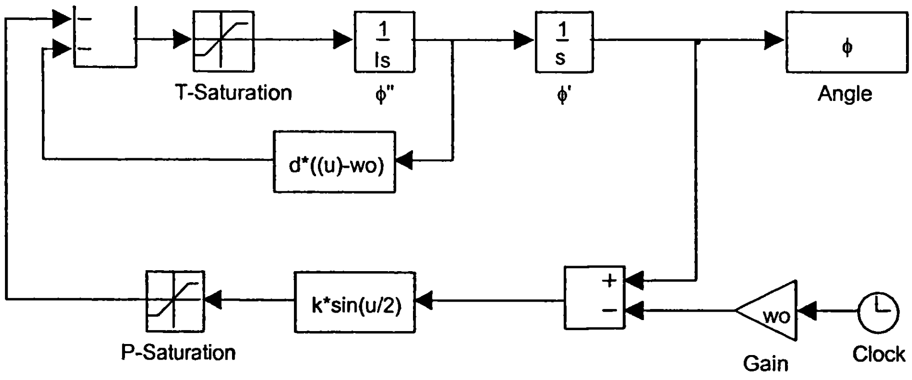

Figure 7-18 Large angle manoeuvre control block diagram

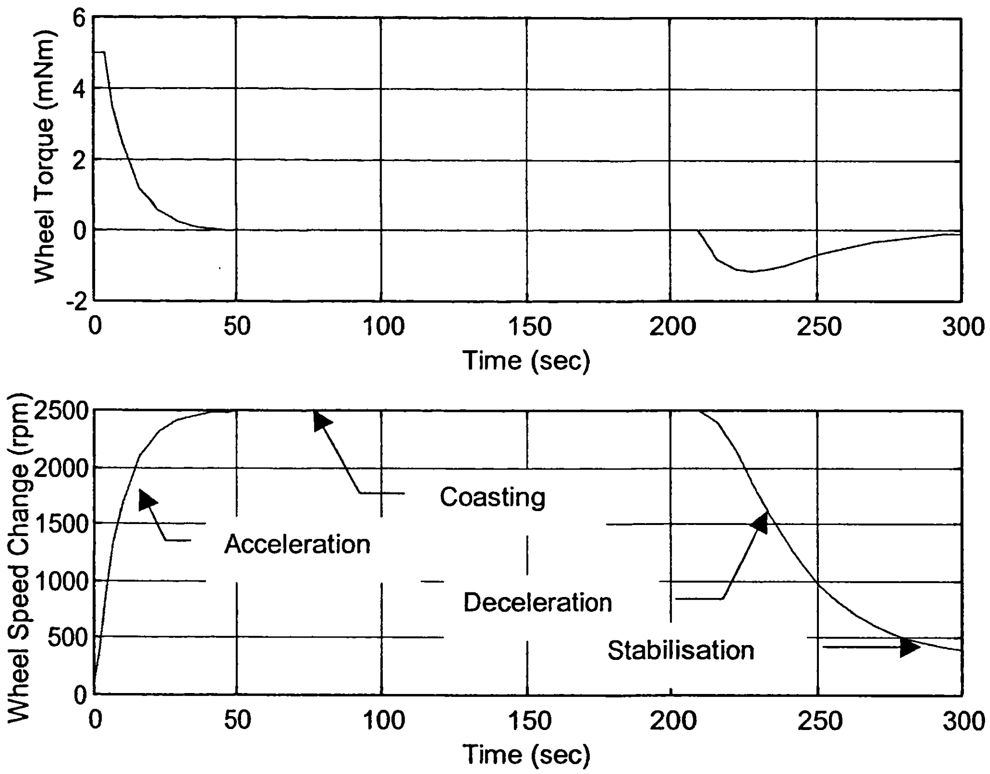

Figure 7-19 Saturated proportional feedback control

The control law in Equation (7-39) can be modified to adopt the previously discussed small satellite limitations using saturation blocks shown in Figure 7-18. The effects of the position feedback saturation are clearly shown in Figure 7-19. The control process can be divided into four phases. During the acceleration phase the wheel generates torque according to the PD control law with torque saturation. When the rotation rate of the satellite reaches a predefined value, the position feedback saturation forces the wheel to rotate at a constant speed. Therefore, the control torque is almost zero during this coasting phase. If the error angle becomes smaller, the rate feedback component takes over the positional one, which triggers the deceleration phase. The control torque is well within the saturation.

We should note that two simple saturation blocks effectively resolve all the practically imposed problems. The boundary of the position feedback, P_{ks}, can be determined from the maximum designed satellite body rate ω_m.

$$P_{ks} = (\omega_m + \omega_o)Id \tag{7-40}$$

The maximum allowed wheel speed change $\Delta\Omega_m$ is thus obtainable using the momentum exchange principle in Equation (7-41).

$$\omega_m I = \Delta\Omega_m I_w \tag{7-41}$$

The wheel speed limitation effect due to the saturation logic was clearly shown in Figure 7-19. The settling time is inevitably delayed due to the torque limit. Comparing Figure 7-17 and Figure 7-19 reveals the extended control time. However, the control torque or equivalently required power is dramatically reduced.

7.3.2 Three-axis Manoeuvre

The control law in the previous section is derived on the Euler angle rotation assumption. However, there are a few reasons why in practice the rotation cannot be performed about the perfect Euler axis. One of the main reasons is the uncertainty of the inertia tensor, especially the cross product terms that have quite a large error as discussed in Chapter 2. In deciding the proportional gain matrix, we need to take account to some degree of potential errors. Wie *et al.* (1989) showed that the control law in equation (7-35) is robust against the inertia tensor uncertainty. Therefore, taking the eigen values of the inertia tensor still ascertains the stability.

The induced error by doing this will result in near Euler axis rotation. We cannot accurately decompose the desired torque. The gain matrix $\boldsymbol{K}$ and $\boldsymbol{D}$ are then

$$\boldsymbol{K} = k\boldsymbol{I} = Diag(0.051, 0.042, 0.059)$$
$$\boldsymbol{D} = d\boldsymbol{I} = Diag(0.85, 0.70, 0.9792) \qquad (7\text{-}42)$$

, where *Diag()* represents diagonal matrix.

The initial error quaternions are set based on the roll, pitch and yaw error of 25°, 90°, and 8°, respectively, for the control system evaluation.

$$\boldsymbol{q}_{ei} = [0.1045 \quad 0.6993 \quad -0.1045 \quad 0.6993]^{\mathrm{T}} \qquad (7\text{-}43)$$

Basically, the control law is the same as the one-axis case. All we need do is properly separate the control torque components into three-axis wheels, where magnitude scaling process similar to Equation (7-7) ~ (7-9) is required. The resultant saturated torque will be in the same direction as the original. Only the magnitude will be changed. Therefore, the Euler axis manoeuvre is still valid even though the saturation logic is applied. The rate feedback will result in deviation from the Euler axis, unlike for the one-axis case. Another major difference from the previous case is that we cannot precisely limit the wheel speed by the pre-assigned P-saturation value due to the gyroscopic effect. The initial and final wheel speeds are not conserved as well if they are biased.

Since the y axis requires the highest control effort, the saturation limit design process can be performed by taking it as the reference axis. Allowing 2500 rpm as the maximum wheel speed change, the value of P_{ks} becomes 6.8 mNm, which corresponds to 0.613 deg/sec of satellite body rate.

Figure 7-20 is the simulation result of the rest-to-constant rotation manoeuvre using the control law. It shows 3-axis control is performed simultaneously.

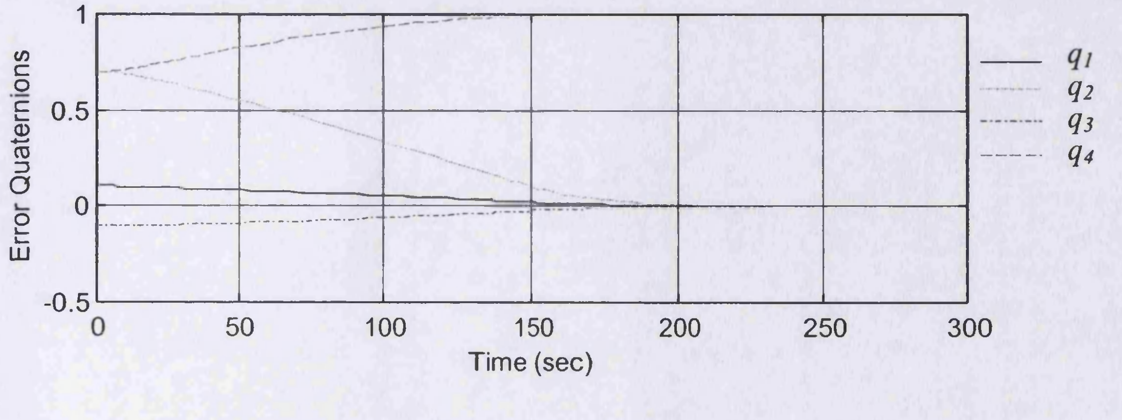

Figure 7-20 Error quaternions control history

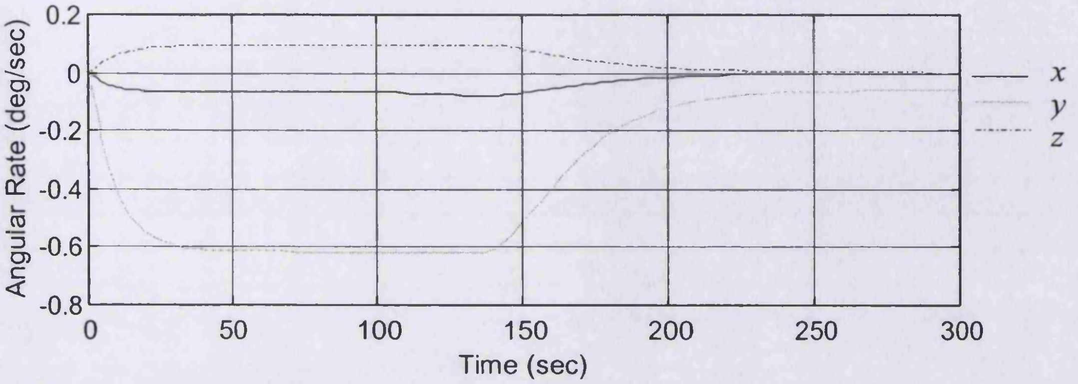

Figure 7-21 Satellite body rates during large angle manoeuvre

The error quaternion history indicates that the target angle is being tracked by the satellite as intended. The satellite body rate in Figure 7-21 verifies that the pre-assigned maximum rate is well observed. The final pitch rate is also synchronised with the orbit period. The wheel speed and control torque histories in Figure 7-22 support the validity of the control algorithm. The maximum speed change is confined within the limit of 2500 rpm while the control torque is also less than 5 mNm.

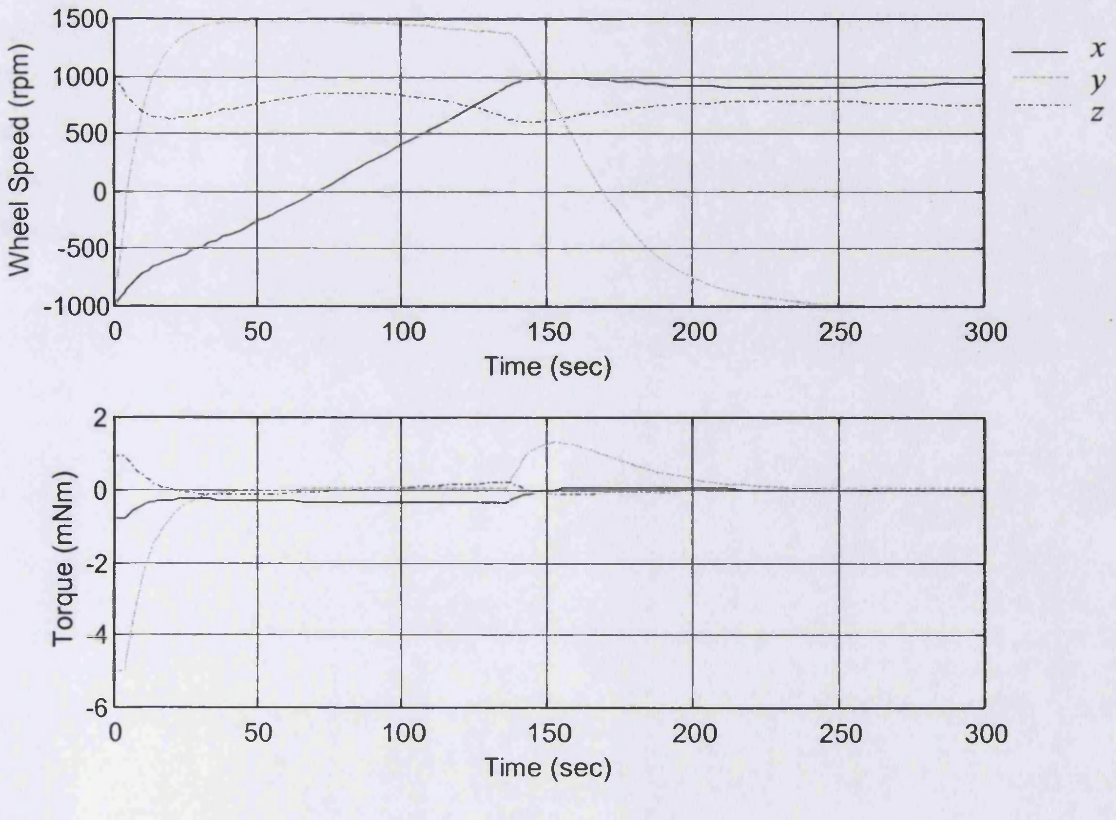

Figure 7-22 Wheel speed and control torque during large angle manoeuvre

The initial rotation speeds of the reaction wheels are assumed to be –1000, -1000 and 1000 rpm for x, y and z axis, respectively. If the nominal speed is too low, near zero speed operation is likely to occur after or during the manoeuvre. Conversely, if it is too high, gyroscopic effect becomes the dominant factor in the attitude dynamics, which results in unnecessary power usage for wheel speed change.

The principle of angular momentum conservation requires speed changes in non-rotating axes wheels. Zero crossings of these wheels are unavoidable. However, we would like to keep the change as small as possible. Moreover, high rotation speed needs high steady state power too. In this context, the nominal operating wheel speeds can be determined.

The performance of the large angle control law can be assessed in terms of how closely the Euler angle rotation is maintained. It can be done by plotting the error quaternion history with respect to one of the components. The level of straightness indicates the closeness to the Euler axis manoeuvre. Figure 7-23 shows the relative ratio of the error quaternions. It is self-evident that the q_{e1}-q_{e1} plot is a perfect straight line. It is almost straight for q_{e1}-q_{e3} too. However, there exist some deviations for q_{e1}-q_{e2} since it has the largest rotation angle.

There are a few reasons why the rotation is not a perfect Euler axis rotation. Firstly, constantly changing target attitude makes the line curved. Secondly, gyroscopic torque affects the calculated control torque for the high speed wheel and satellite body rotation case. Lastly, the uncertainty of the inertia tensor or the principal axes results in inappropriate control torque decomposition. Among them the second source can be removed by applying a modified control law.

$$\boldsymbol{T} = -\boldsymbol{K}\boldsymbol{q}_e - \boldsymbol{D}\omega - \vec{\omega} \times (\vec{\boldsymbol{h}}_s + \vec{\boldsymbol{h}}_w) \qquad (7\text{-}44)$$

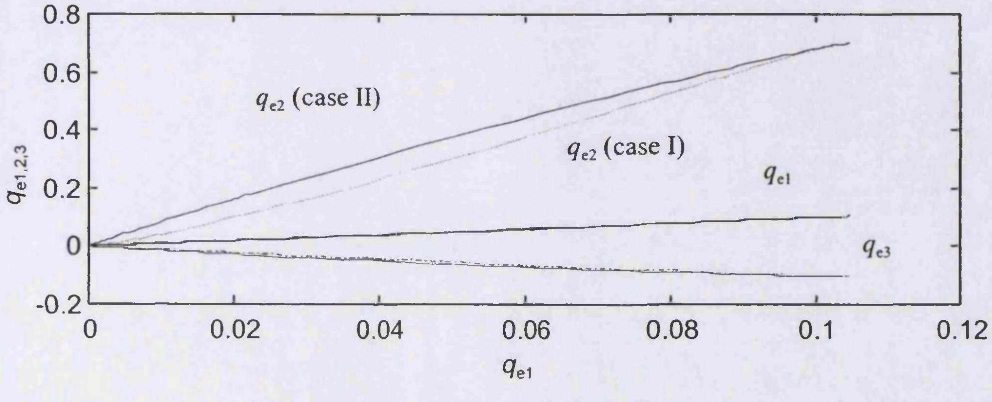

Figure 7-23 q_{e1} versus $q_{e1,2,3}$ plot

The effect of cancelling the gyroscopic torque can be seen from case II of q_{e2}. The parameters for this cancelling torque are directly available from the gyro and wheel speed measurement. Considering the computational burden, Equation (7-34) is favoured.

7.4 Fine Attitude Control

7.4.1 Kalman Filtering

Since there is some noise present in every real world dynamic process and all observations are subject to noise, we need to develop a noise filtering mechanism to achieve high accuracy estimation. In 1960 Kalman showed that a linear observer is optimum for a linear process if the noise has a Gaussian probability distribution. The Gaussian noise characteristics of the attitude sensors strongly suggest using this method.

The mathematical derivation relating to the Kalman filter algorithm is a complex series of matrix manipulations. Instead of describing details of the algorithm, a discrete-time case can be summarised as follows: (Friedland, 1996).

Steps 1 and 6 provide intuitive interpretations of the algorithm. The first is simply the equation of the dynamic process, where Φ_n is the state transition matrix, and Γ_n is the control distribution matrix for the control input u_n. We can interpret $\tilde{x}_n$ as the optimum state estimate immediately before the nth observation, i.e. an *a priori* state estimate. Likewise, $\hat{x}_n$ is the optimum state estimate immediately after the nth observation, *i.e.* an *a posteriori* state estimate.

Table 7-2 Flowchart of discrete-time Kalman filter

Step	Perform	Equation
1	Propagate state	$\tilde{x}_{n+1} = \Phi_n \hat{x}_n + \Gamma_n u_n$
2	Predict observation	$\tilde{y}_{n+1} = H_{n+1}\tilde{x}_{n+1}$
3	Propagate covariance	$\tilde{P}_{n+1} = \Phi_n \hat{P}_n \Phi_n^T + Q_n$
4	Compute gain	$K_{n+1} = \tilde{P}_{n+1} H_{n+1}^T (H_{n+1}\tilde{P}_{n+1}H_{n+1}^T + R_{n+1})^{-1}$
5	Read observation	$y_{n+1} = H_{n+1}x_{n+1} + v_{n+1}$
6	Update state estimation	$\hat{x}_{n+1} = \tilde{x}_n + K_{n+1}(y_{n+1} - \tilde{y}_{n+1})$
7	Update covariance	$\hat{P}_{n+1} = (I - K_{n+1}H_{n+1})\tilde{P}_{n+1}$

With these interpretations Step 6 tells us how the new observation is used to obtain an *a posteriori* estimate from the *a priori* estimate. Step 1 predicts how that estimate propagates in time to give the *a priori* estimate of the state just before the (n+1)st observation.

The measurement sensitivity matrix $\boldsymbol{H}_n$ relates the true state $\boldsymbol{x}_n$ to real measurement with noise $\boldsymbol{v}_n$. The noise has a mean of $E[\boldsymbol{v}_n] = \boldsymbol{0}$ and the covariance matrix $E[\boldsymbol{v}_n \boldsymbol{v}_n^T] = \boldsymbol{R}_n$. The true system dynamics is $\boldsymbol{x}_{n+1} = \Phi_n \boldsymbol{x}_n + \Gamma_n \boldsymbol{u}_n + \boldsymbol{w}_n$ where $\boldsymbol{w}_n$ is a zero mean random system noise with the covariance matrix $E[\boldsymbol{w}_n \boldsymbol{w}_n^T] = \boldsymbol{Q}_n$.

The goal of the Kalman filter algorithm is to minimise the estimation covariance matrix $\widetilde{\boldsymbol{P}}_n$. Since $\hat{\boldsymbol{P}}_n$ is mathematically always smaller than $\widetilde{\boldsymbol{P}}_n$, then as the observation progresses the estimated error becomes zero too. Step 7 shows how the covariance matrix is updated over a time interval in which no observations are made, and Step 3 explains how the covariance matrix is updated as a result of an observation.

Determining the system dynamics is the key issue of constructing the filtering algorithm. For a continuous-time linear process, the dynamic model can be written in terms of the state vector $\boldsymbol{x}$ as

$$\dot{\boldsymbol{x}} = \boldsymbol{A}\boldsymbol{x} + \boldsymbol{B}\boldsymbol{u} \tag{7-45}$$

The discrete-time dynamic equation is obtainable from the following relation.

$$\begin{aligned} \boldsymbol{x}_{n+1} &= \Phi \boldsymbol{x}_n + \Gamma \boldsymbol{u}_n \\ \boldsymbol{x}_n &\equiv \boldsymbol{x}(nT) \\ \Phi &\equiv e^{AT} \\ \Gamma &\equiv \int_0^T e^{A\lambda} \boldsymbol{B} d\lambda \end{aligned} \tag{7-46}$$

, where T is the sampling interval of the discrete system.

The central part of the algorithm is how we properly define the state vector and the state transition matrix Φ. Other procedures are straightforward and well established from the wide range of previous works in modern control engineering.

The pointing error is the most important factor that we would like to minimise by means of the control action. Therefore, the state vector should contain the pointing error terms. Since the control algorithm is basically PD control, the angular rate of the satellite body also plays an important role in the system design. The gyro readout error, particularly the biased one, needs to be estimated by the observer too. We can define the state vector as

$$x = [q_{e1} \quad q_{e2} \quad q_{e3} \quad \Delta b_x \quad \Delta b_y \quad \Delta b_z]^T \tag{7-47}$$

, where the error quaternions and gyro bias errors are used as the six elements of the state vector.

The uncontrolled system dynamics in continuous-time can be written as

$$\frac{d}{dt}x = Ax + w \tag{7-48}$$

If the error angle is small, the error quaternions can be approximated in terms of the roll, pitch and yaw errors as $2[q_{e1} \quad q_{e2} \quad q_{e3}]^T \approx [\Delta\phi \quad \Delta\theta \quad \Delta\varphi]^T$. We can then take into account the gyro bias and complete the state equation as:

$$\frac{d}{dt}\begin{bmatrix} q_{e1} \\ q_{e2} \\ q_{e3} \\ \Delta b_x \\ \Delta b_y \\ \Delta b_z \end{bmatrix} = \begin{bmatrix} 0 & 0 & 0 & -0.5 & 0 & 0 \\ 0 & 0 & 0 & 0 & -0.5 & 0 \\ 0 & 0 & 0 & 0 & 0 & -0.5 \\ 0 & 0 & 0 & 0 & 0 & 0 \\ 0 & 0 & 0 & 0 & 0 & 0 \\ 0 & 0 & 0 & 0 & 0 & 0 \end{bmatrix} \begin{bmatrix} q_{e1} \\ q_{e2} \\ q_{e3} \\ \Delta b_x \\ \Delta b_y \\ \Delta b_z \end{bmatrix} + \begin{bmatrix} n_{wx}/2 \\ n_{wy}/2 \\ n_{wz}/2 \\ n_{Rwx} \\ n_{Rwy} \\ n_{Rwz} \end{bmatrix} \tag{7-49}$$

, where n_w and n_{Rw} are the gyro measurement noise and random walk vector respectively, as defined in Section 5.1.

Defining the error quaternions as the state vectors has advantages in terms of computational requirements. However, we should consider a pseudo-pitch bias for the Earth pointing mode. The y gyro gives a rate offset even if there is no bias component. This approach is much simpler since only the final estimation result need be adjusted.

When transforming the continuous-time equation into discrete-time, one requires a calculating matrix exponential function as given in Equation (7-46). It is attainable by a numerical method using a Taylor series (Chen, 1984) as

$$e^{At} = \sum_{k=0}^{\infty} \frac{1}{k!} t^k A^k \tag{7-50}$$

If we apply the system dynamics only for the fine Earth pointing attitude control mode, we can consider the state transition matrix as constant, $\Phi_n \approx \Phi$. Equation (7-49) and (7-50) give the discrete-time state transition matrix.

$$\Phi = \begin{bmatrix} 1 & 0 & 0 & -0.25 & 0 & 0 \\ 0 & 1 & 0 & 0 & -0.25 & 0 \\ 0 & 0 & 1 & 0 & 0 & -0.25 \\ 0 & 0 & 0 & 1 & 0 & 0 \\ 0 & 0 & 0 & 0 & 1 & 0 \\ 0 & 0 & 0 & 0 & 0 & 1 \end{bmatrix} \tag{7-51}$$

The $\boldsymbol{H}_n$, $\boldsymbol{R}_n$, and $\boldsymbol{Q}_n$ can be regarded as a constant matrix for the fine control mode. Since the star sensors generate quaternion output directly with an accuracy of $1'$ (1σ) and using the relation $\boldsymbol{R}_n = \frac{1}{T}\int_{nT}^{n(T+1)} \boldsymbol{R}(t)dt$, $\boldsymbol{Q}_n = T\int_{nT}^{n(T+1)} \boldsymbol{Q}(t)dt$ (Grewal & Andrews, 1993)

$$\begin{aligned} \boldsymbol{H} &= \left[I_{3\times3} \mid O_{3\times3} \right] \\ \boldsymbol{R} &= 4.231\times10^{-8} I_{3\times3} \\ \boldsymbol{Q} &= 1\times10^{-9} \begin{bmatrix} 1.674\times I_{3\times3} & O_{3\times3} \\ O_{3\times3} & 0.026\times I_{3\times3} \end{bmatrix} \end{aligned} \tag{7-52}$$

, where the worst case of gyro bias of 10°/h and random walk of 3°/√h are assumed. (Actual measurement results are far better than these values from the specifications.)

The control distribution matrix Γ_n is a constant too and it can be approximated for the time gap T and a control torque $\boldsymbol{u}_n$ as

$$\Gamma = \frac{T^2}{4} \begin{bmatrix} 1/I_x & 0 & 0 \\ 0 & 1/I_y & 0 \\ 0 & 0 & 1/I_z \end{bmatrix} \tag{7-53}$$

Thus, we have all the information required to construct the Kalman filter.

7.4.2 *Performance Evaluation*

Generally, the Kalman filter is used to compensate gyro drift errors when direct angular measurement is not available. The update rates of conventional star sensors are around the order of second. The rate data from the gyro must be integrated to obtain the predicted angle according to Equation (3-33). If high accuracy sensor data are provided, the Kalman filter processes the measurement data to estimate the state vector.

The sampling rate of the star sensor is the same as that of the gyro in the KITSAT-3 case. The Kalman filter update rate is therefore synchronised with the gyro readout sequence, which is quite different from the traditional approach. Figure 7-24 and Figure 7-25 are the simulation results of applying the Kalman filter for an ideal nadir-pointing situation. The sensor noise and biases are assumed as in Equation (7-52).

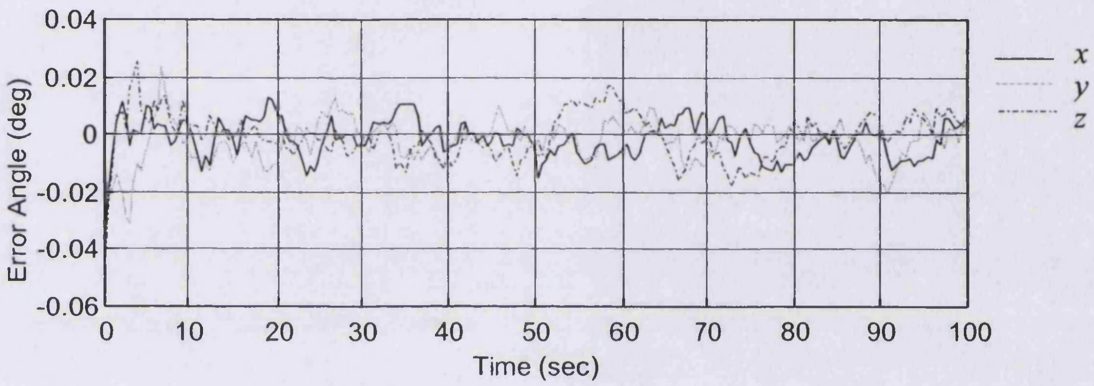

Figure 7-24 Error angle estimation

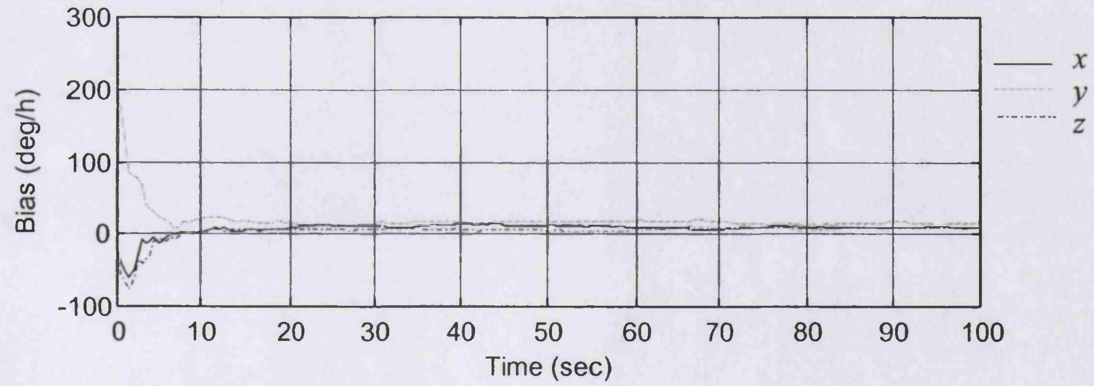

Figure 7-25 Gyro bias estimation

The performance of the error angle estimate is directly connected with the measurement accuracy of the star sensor 1′ (1σ) since the measurement and estimation data update rates are the same. However, it takes time to properly estimate the gyro bias. Within 10 seconds, which is equivalent to 20 angular measurements, the filter estimates the gyro drift very well, even though measurement noise and random walk exist. As shown in Figure 7-25, the y axis has the slowest convergence characteristics. This is due to the pitch rate bias $-\omega_o$.

The main purpose of using the Kalman filter is to compensate the bias of the gyro. The simulated large angle manoeuvring performance in Figure 7-20 showed that after 300 seconds the residual angular error is negligible. However, the reference attitude calculated from the gyro data contains errors due to bias. A maximum 10°/hour of bias results in 0.83 degree of error after 300 seconds. A new reference angle needs to be provided by high accuracy sensor for stabilisation.

The initial conditions of the fine control simulation are 0.5°, 1° and 0.8° for the error angles and 0.2, -1.11 and 0.1 mrad/sec for the rate, respectively for roll, pitch and yaw axis. The estimated error angles and the gyro biases are used for compensating the sensor measurements in the simulation. The state estimate for the error angle has an excellent convergence characteristic due to use of the high accuracy star sensors.

The gyro drift estimation result was almost the same as the ideal case in Figure 7-25, which contains ~3°/hour of estimation error. It reflects the random walk error. Since the simulation interval is just 100 seconds, a rather slowly varying random characteristic was difficult to estimate. A linear second order system tends to have a steady state error for rate control (Kuo, 1987).

The initial wheel speeds are taken from the final value of the large angle manoeuvre in Figure 7-22. The wheel speeds remain almost constant. Even though the gyro measurements bear a significant level of noise, the true rates have smooth curves due to the integration part of the satellite dynamics as shown in Figure 7-27. The rate control accuracy satisfies the attitude stability requirements of the imaging mode in Table 2-6.

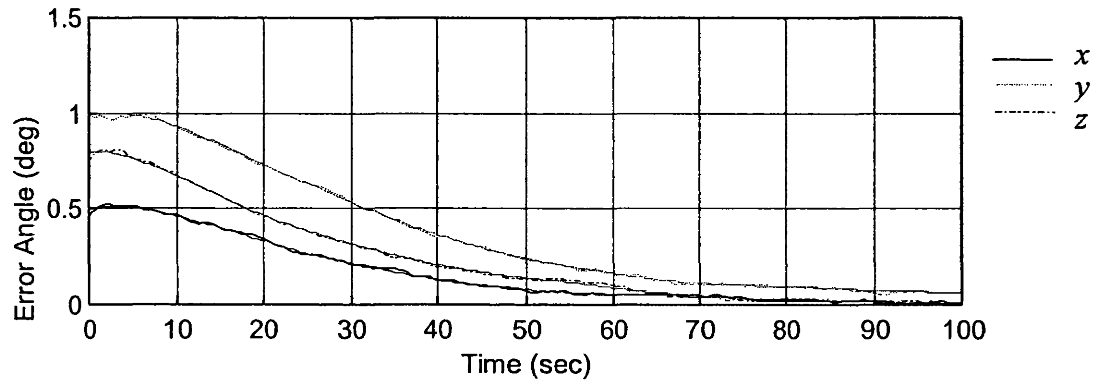

Figure 7-26 Fine angle control with Kalman filter

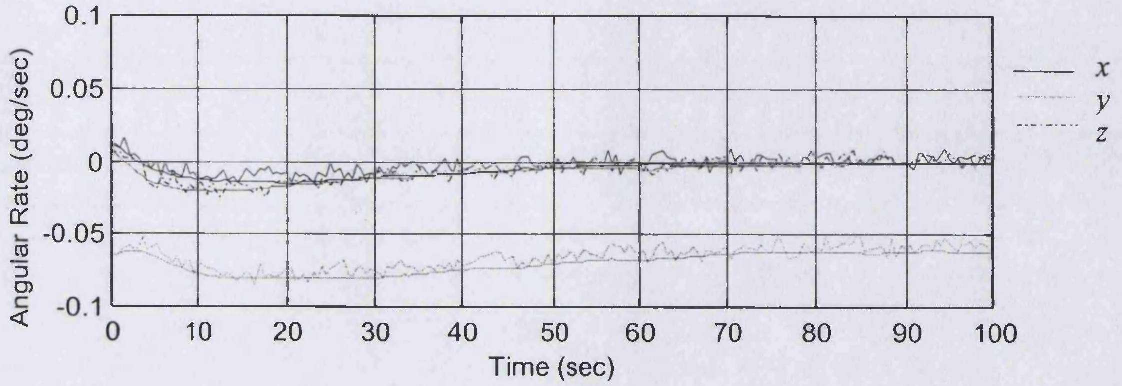

Figure 7-27 Rate control with Kalman filter

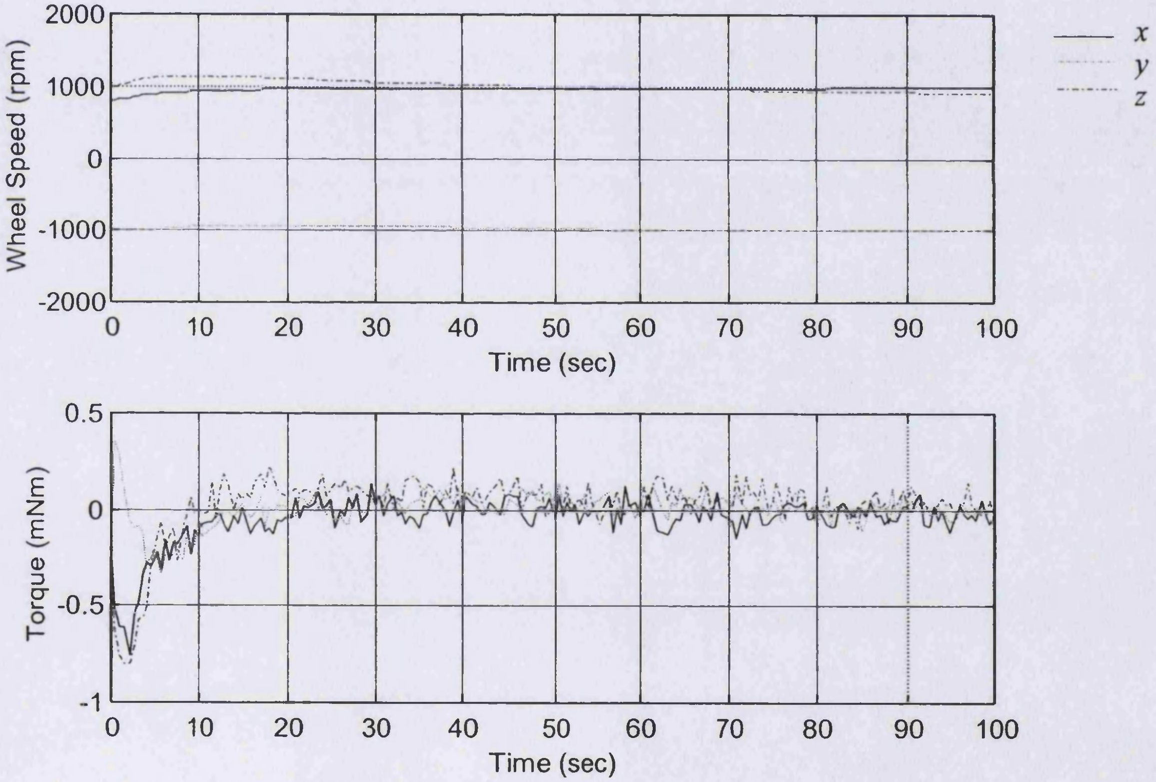

Figure 7-28 Wheel speed and torque for fine control

The generated control torque is within the wheel specification; 2 Hz of control frequency is also used. Speed quantisation and 0.5 second of zero-order-holder are considered for the wheel control logic.

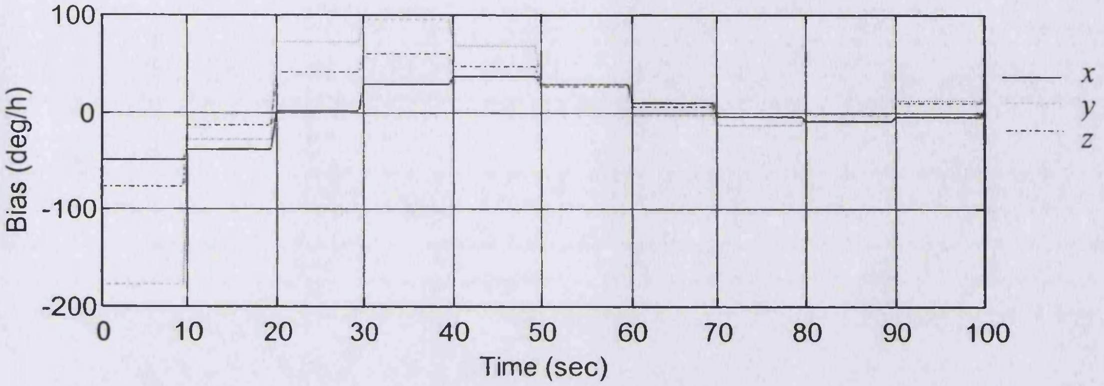

Figure 7-29 Gyro bias estimation (Under sampled case)

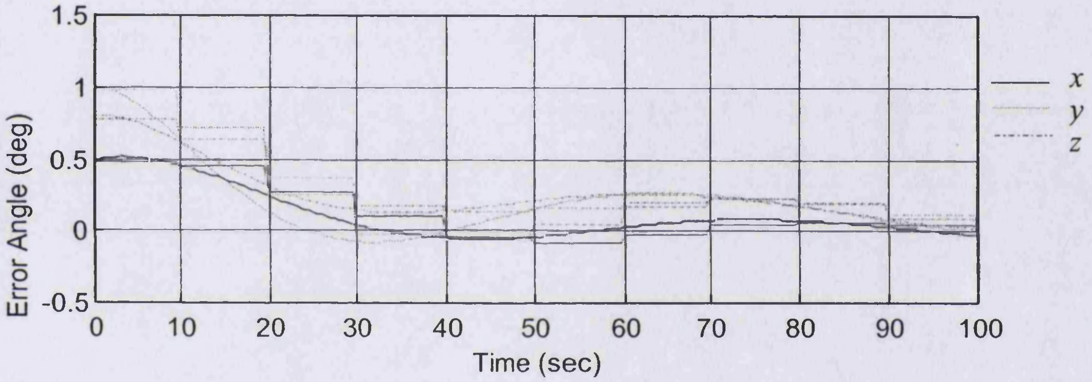

Figure 7-30 Controlled & estimated error angle (Under sampled case)

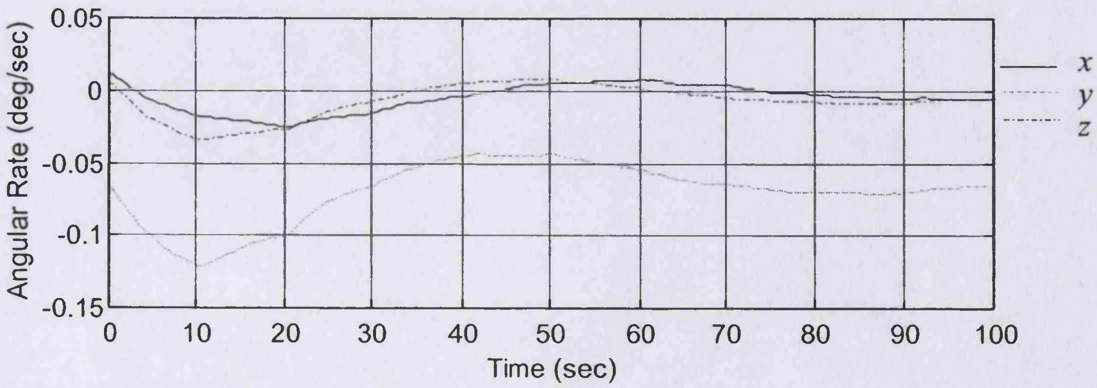

Figure 7-31 Controlled rate (Under sampled case)

We have assumed that the gyro update rate is the same as that of the star sensor. However, this situation is not always possible. The star sensors are only able to generate attitude data two times a second in stable conditions. If the satellite rotates too fast, the sensor cannot give attitude information. If the initial attitude knowledge is not available, it takes more than 10 seconds for initialisation. False stars created by cosmic rays or obstruction by the moon will hamper the sensor from correct star identifications.

Therefore, we need to consider dual rates of gyro measurements and the Kalman filter update. Figure 7-29 ~ Figure 7-31 are the simulation results of applying the Kalman filter every 10 seconds, *i.e.* there are 20 gyro updates. The lowered filtering rate results in the loss of accuracy and it slowed convergence speed of the estimate. Controlling with the estimated values during the early stage turned out to be inefficient. Angular overshoot occurs due to the erroneous estimation. Comparing Figure 7-30 with Figure 7-26 tells us that the pointing error is increased by around 0.2 degree. It is desirable to use the estimated values as control input after an ample amount of observations are made.

We can summarise that approximately 5 minutes of manoeuvring and 2 minutes of stabilisation time are required to change the attitude from the Sun pointing to the Earth imaging mode. The performance of the fine stabilisation depends on how often the star sensor gives accurate attitude data. Since the gyros have large bias uncertainties, long absence of revised star sensor data will result in large errors both in pointing and rate.

We should consider one more point regarding the behaviour of the system under disturbance. If we apply the disturbance model developed in Chapter 6 to the control system model, we can assess the capability of the controller. Figure 7-32 shows the pointing error under disturbance conditions. The steady state pitch error is due to gyro bias estimation error as mentioned before. Detailed discussion for error budgeting and system margin consideration will be summarised in Chapter 8 with actual in-flight results.

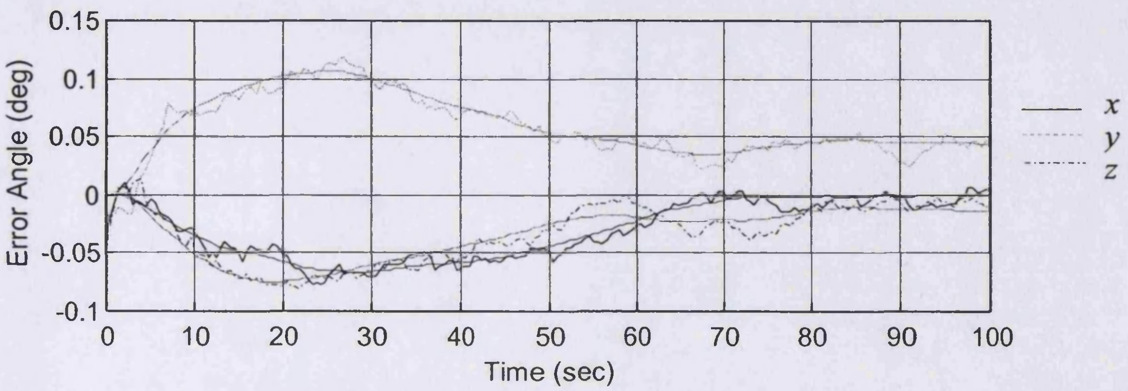

Figure 7-32 Fine control under disturbance

Chapter 8. System Margin & Flight Results

8.1 Control System Margin

8.1.1 Control System Stability Margin

Closed-loop stability is the major concern in any feedback control system design. If the system is linear and time-invariant, many stability criteria are available. If the system is non-linear, such stability criteria do not apply. Lyapunov's method is generally used for the non-linear system stability analysis. Wie (1989) rigorously had proven that the basic form of the quaternion feedback control scheme is globally stable. The stability can be guaranteed if the damping gain d is a positive scalar.

However, the degree of stability cannot be evaluated through the mathematical proof using Lyapunov's stability criterion. It only guarantees the general trend of the system's behaviour toward the stable point. Moreover, we need to consider the effect of the non-linear function for the saturation logic. Analysis of the control system margin is not feasible in this case. However, if we closely examine the nature of the non-linearity in the control loop, we can assess the stability of the control system.

The non-linear parts in the proposed control algorithm are sine and saturation functions. These functions have sector characteristics, *i.e.*, they can be contained between two tangents drawn through the origin. In another word, we can define a linear function with finite slope that passes through the origin and it is always larger than the original non-linear function. It can be simply expressed as Equation (8-1).

$$\begin{aligned} &\sin\frac{\theta}{2} \le \frac{\theta}{2} \\ &sat(x)_{x>a} \le x \end{aligned} \tag{8-1}$$

Linearising a non-linear function in these cases implies that we sacrifice any information about the non-linear characteristic other than the fact that it is a sector type. Because of this declaration of ignorance, we can hope to get conservative results in general. Behaviour of a linearised system may be different from the original non-linear system. But the system will not incur instability since the assumption is conservative.

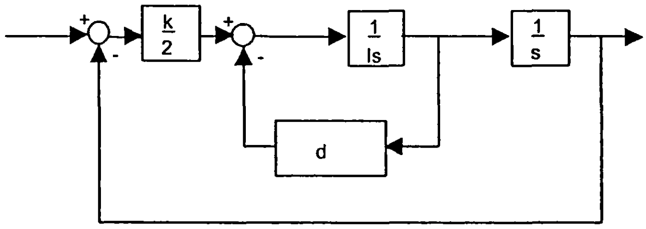

Figure 8-1 Conservatively linearised control loop

The linearised control loop is shown in Figure 8-1. We can notice that the control torque for non-linear system is always smaller than the conservatively linearised system.

It is now possible to utilise generally used stability analysis techniques developed for linear systems. The transfer function of the system described in Figure 8-1 can be obtained by applying well-known signal flow graphic technique (Kuo, 1987). The forward path gain is give as $\frac{K}{2Is^2}$ and the sum of the individual loop gain is $-\frac{d}{Is}-\frac{K}{2Is^2}$. Therefore, the transfer function $H(s)$ becomes

$$H(s)=\frac{K}{2Is^2+2ds+K} \tag{8-2}$$

Hence, the characteristic equation of Equation (8-2) is $2Is^2+2ds+K$. It is evident that the equation has no right-hand pole if d is a positive scalar. It also coincides with the result from Wie (1989), where non-linear analysis approach was made.

We need to study the effects of varying each parameter on the system stability since the system has multiple parameters, K and d. If we fix d first as 0.12, then the root locus of the characteristic equation gives the result shown in Figure 8-2. It is clear that all the roots are located on the left-hand side of the s-plane. It implies that the system is stable for all values of feedback gain K.

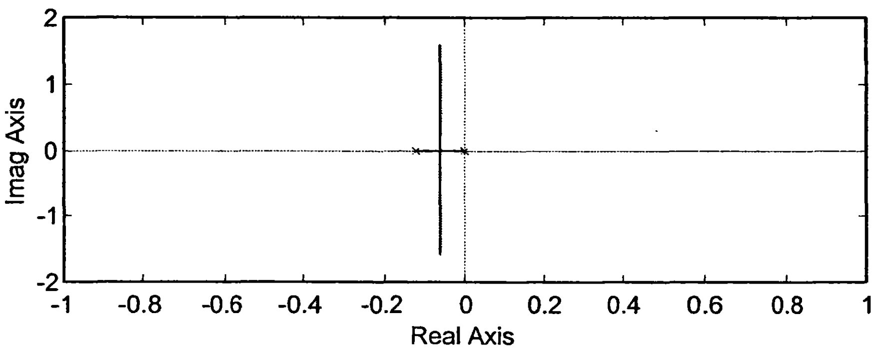

Figure 8-2 Root locus diagram of the linearised system with fixed d

The result validates the basic assumption for the linearisation. The system is, mathematically, stable regardless of the choice of K. Therefore, we can conclude that the original non-linear system is also stable for the same position gain K with more stability margin. To give a quantitative way of measuring the relative stability of the proposed control system, a quantity called gain margin can be defined. The gain margin is a measure of the closeness of the gain crossover point to the gain at the frequency of the phase crossover point. The gain margin is the amount of gain in decibels that can be allowed to increase in the loop before the closed-loop system reaches instability.

In practice, we have to first determined the stability of the system as shown in Figure 8-2. Then the magnitude of the gain margin needs to be evaluated. Once the stability or instability condition is ascertained, the magnitude of the gain margin simply denotes the margin of stability. It is convenient to assess the gain margin graphically from the Bode plot or the Nichols chart as shown in Figure 8-3 and Figure 8-4. The result shows that there is no phase crossover point, *i.e.* the gain margin is infinite. This means that the value of the loop gain can be increased to infinity before instability occurs.

The gain margin is merely one of the many ways of representing the relative stability of a feedback control system. A system with a large gain margin should be relatively more stable than one that has a smaller margin. Unfortunately, the gain margin alone does not sufficiently indicate the relative stability of all system.

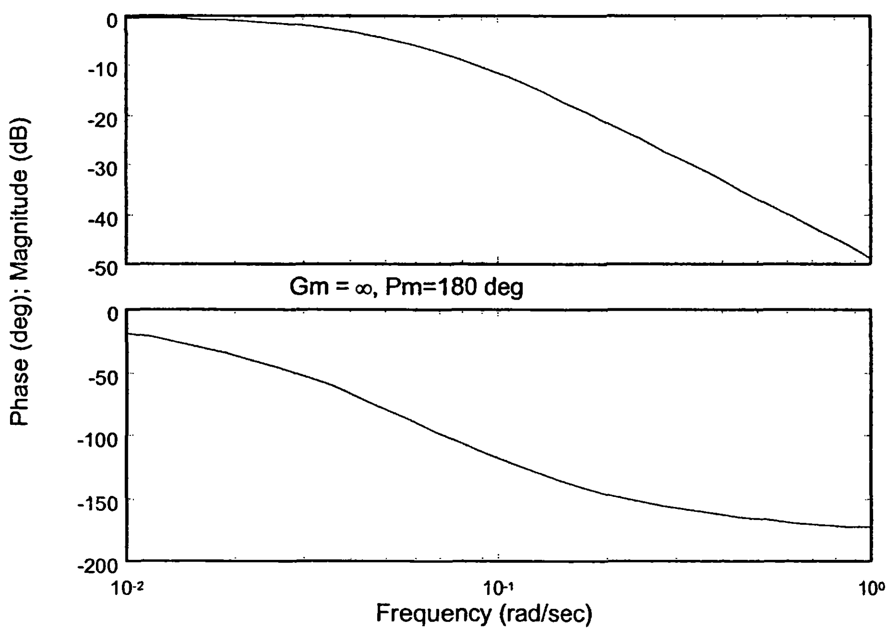

Figure 8-3 Bode plot of H(s) with fixed d

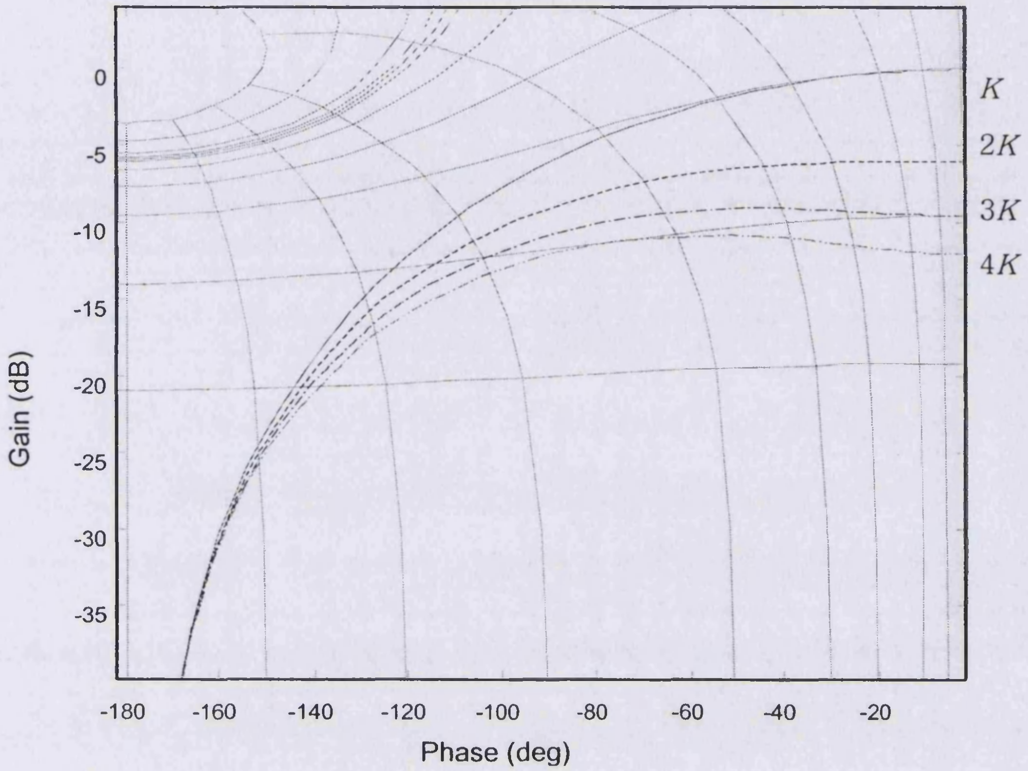

Figure 8-4 Nichols chart of H(s)

In order to strengthen the representation of relative stability of a feedback control system, the phase margin is defined as the angle in degrees between the phase crossover point and the phase angle at the frequency of the gain crossover point, which is supplementary to gain margin. In contrast to the gain margin, which gives a measure of the effect of the loop gain on the stability of the closed-loop system, the phase margin indicates the effect on stability due to changes of the system parameters that theoretically alter the phase only. The phase margin of the proposed control system is 180 degrees. It implies that the system has robustness against the parameter changes other than the gain. The control system $H(s)$ is, therefore, stable with infinity gain margin and large phase margin.

We can also change the viewpoint by fixing K and then examining the effects of varying d. The root locus plot of the system with varying d is given is Figure 8-5. It has similar characteristic as Figure 8-2. The trajectories are on the left-hand side of the s-plane except the two poles on the imaginary axis. It also means that the system is stable for all positive damping gain d. This again confirms that the assumption made for linearisation is valid.

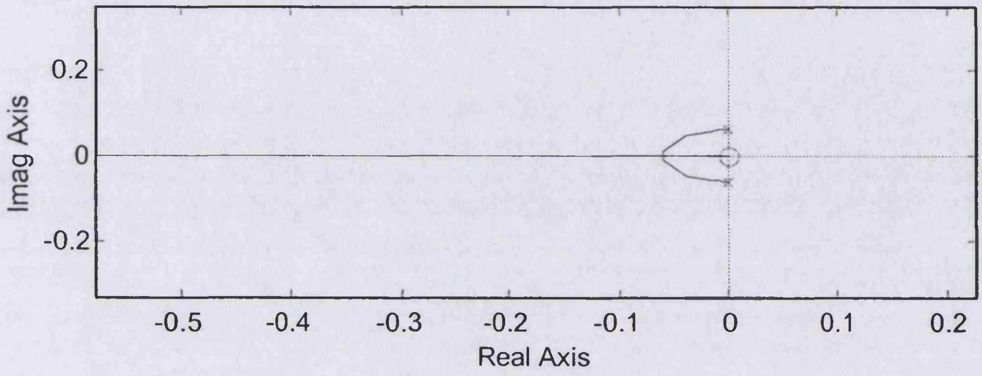

Figure 8-5 Root locus diagram of the linearised system with fixed K

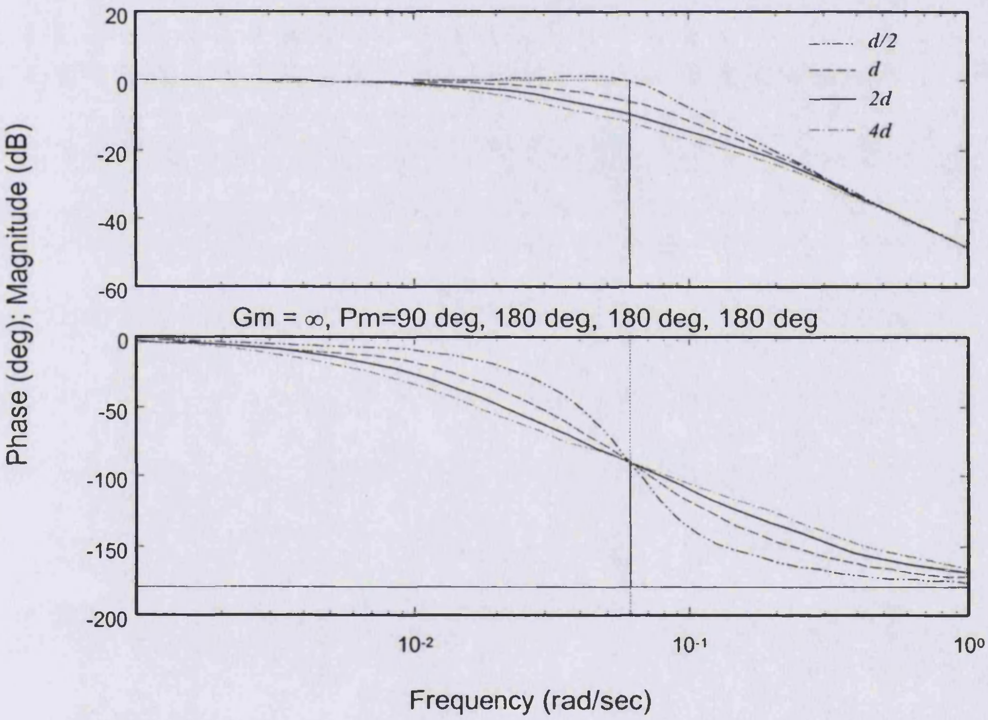

Figure 8-6 Bode plot of H(s) with fixed K

The Bode plot shown in Figure 8-6 is for different damping gains, $d/2$, d, $2d$, and $4d$. As expected from Figure 8-5, the system is globally stable for various values of d and it has infinite gain margin. The phase margin improves as the damping gain increases. However, the phase margin does not have significance in such a situation. We can conclude that the proposed control system is stable and has a certain degree of robustness.

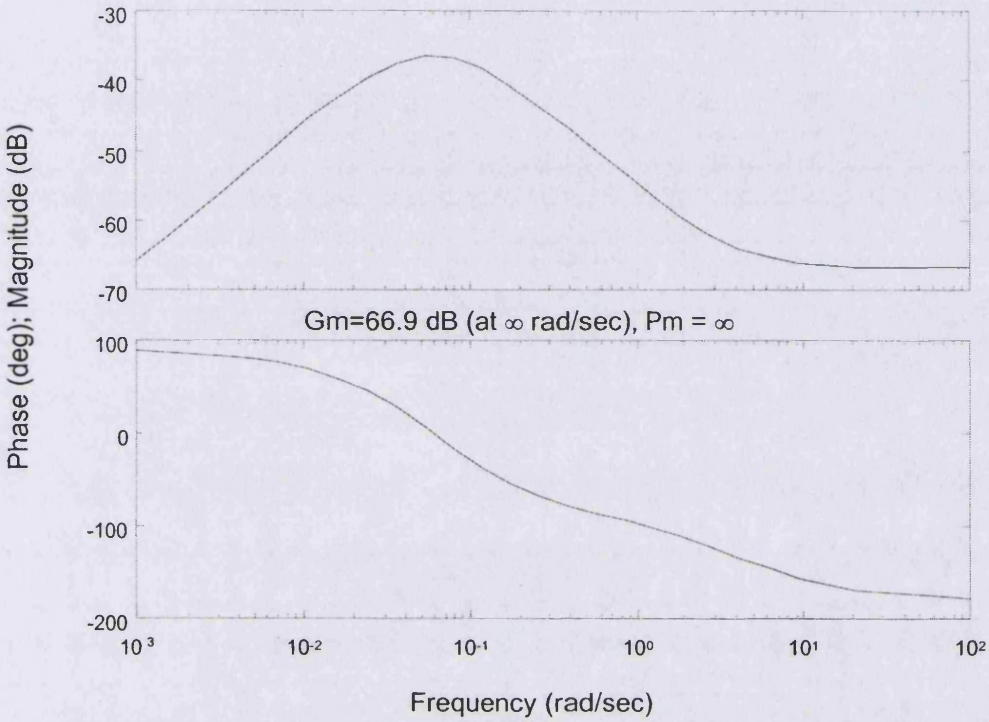

Figure 8-7 Bode plot of discrete control system

The stability for the discrete sample and hold system needs to be examined. The digital control nature of KITSAT-3 requires analysis in the point of discrete control. The system has large gain margin of 66.9 dB for the control frequency of 2Hz as shown in Figure 8-7. The stability margin decreases as the sampling frequency increases. It is a natural phenomenon in for a discrete control scheme.

8.1.2 Hardware Performance Margin

The mission analysis results in Chapter 2 require cross-examination with the hardware capability of the satellite. The cross track pointing accuracy error budget can be allocated as shown in Figure 8-8. The cross tracking pointing accuracy is the major concern. Along track and yaw pointing errors are less significant for pushbroom type imaging sensor. Considering 0.2 deg of mechanical mounting margin and 0.02 deg of other unknown errors such as thermal distortion, we can meet 7.16 km of cross track pointing error requirement. The attitude hardware and software have to satisfy 0.45 deg of roll accuracy. The analysis includes various margins on component, subsystem, element and system levels. The following analysis for error budgeting and margin allocation is a common practice in aerospace engineering. It is based on the methodology used by TRW Inc. (Lee, 1998).

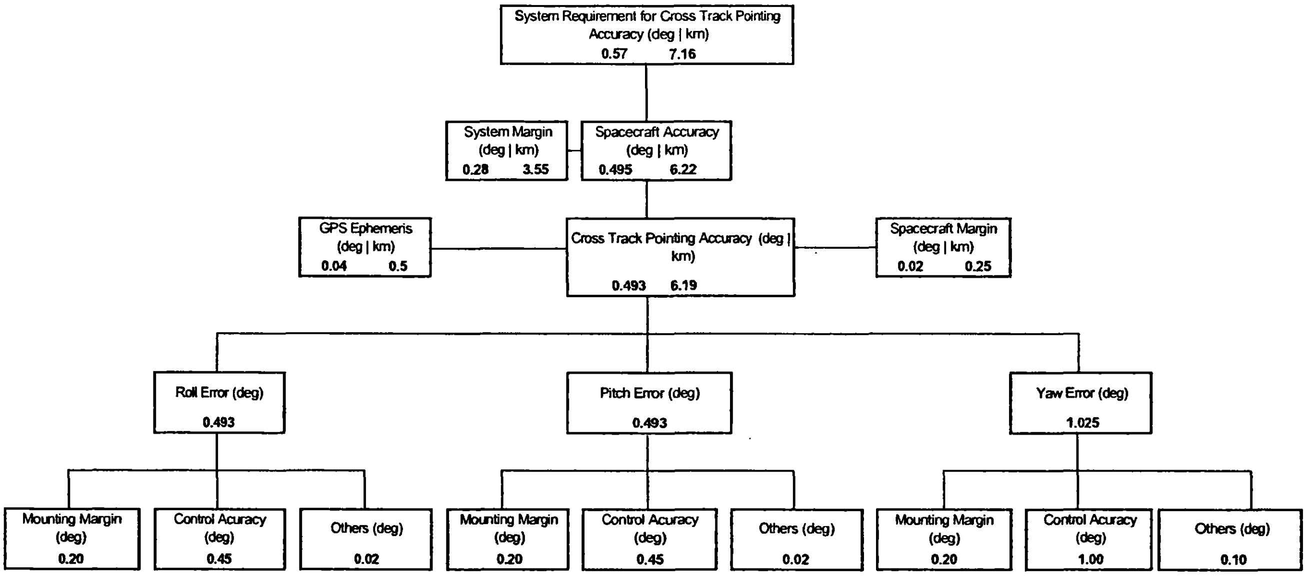

Figure 8-8 Cross track pointing error margin

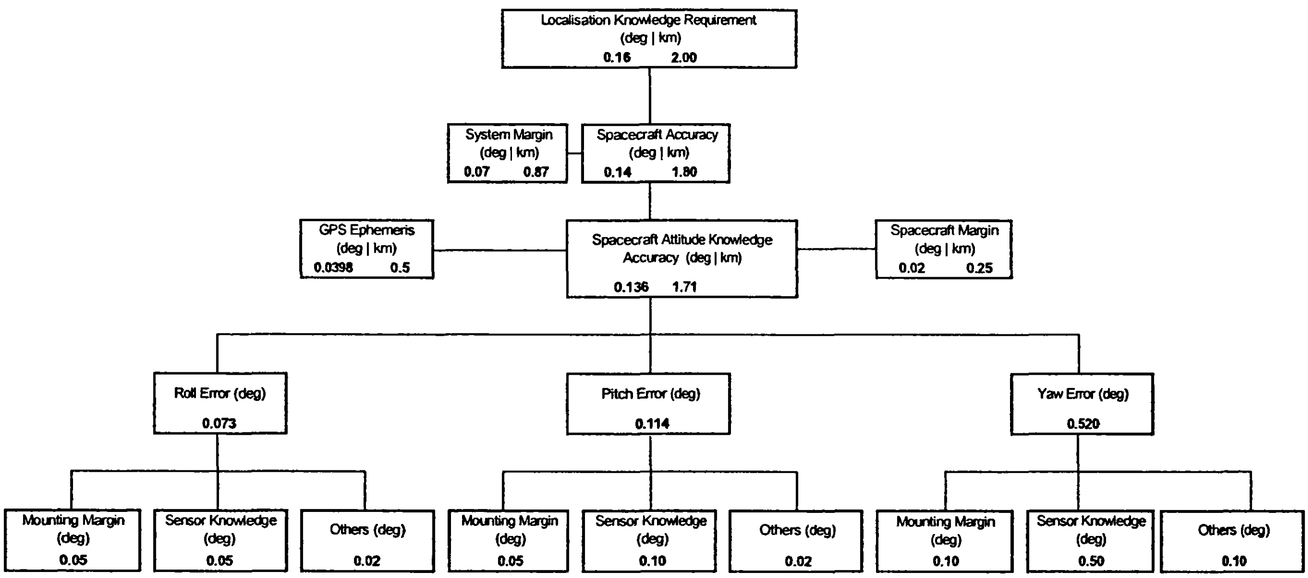

Figure 8-9 Localisation error margin

More stringent requirements come from the localisation error analysis as shown in Figure 8-9. Localisation means the level of ground positioning accuracy using only the satellite telemetry data here. Utilisation of Ground Control Point (GCP) is not considered in this analysis. This analysis is useful for the images when we are not allowed to take ground reference points.

The components of 3-axis error contribute to the whole system error, which is different from pointing accuracy budget. Since yaw error has the smallest contribution, we can allocate a loose requirement to this axis. Pitch attitude knowledge error allocated a bigger margin than the roll error because the optical axis of the star sensor is parallel with the pitch axis. We can achieve 1.4 km of localisation accuracy when the system meets the requirement is Figure 8-9. With 1 arc min of the star sensor accuracy, we have margin in component level as well as the spacecraft element and system level margins. GPS accuracy needs to be better than 500 m in this analysis.

If GCPs are available for ground image processing, the quality of image is dependant on the performance of the gyro. It is anticipated to produce Class III-1:100,0000 quality image map at the later stage of the mission development, which was not a driving requirement during initial mission analysis phase. The limiting RMS error for this class of image map is 75 m in horizontal (X) or vertical (Y) direction (PE & RS, 1990). Gyro bias error is the main factor that contributes to the system error.

Table 8-1 shows the coordinate accuracy requirements for class I maps according to the scales, where the term 'well-defined points' pertains to features that can be sharply identified as discrete points. The accuracy is relaxed 2 times for Class II, and 3 times for Class III.

Table 8-1 Coordinate Accuracy Requirement for Well-defined Points

Planimetric (*X* or *Y*) coordinate accuracy - Limiting RMS error (m)	TYPICAL MAP SCALE (Class I Map)
1.25	1:5,000
2.5	1:10,000
6.25	1:25,000
12.5	1:50,000
25	1:100,000

Figure 8-10 shows the error allocation for low frequency length alteration and middle frequency distortion for the production of class III image map, scale 1:100,000. We regarded only the low frequency and he middle frequency components in interpreting the requirements in Table 8-1 considering the nature of image quality degradation. The mounting uncertainty error and the other biased systematic errors are neglected assuming that image processing can compensate the systematic error using GCP. Since the FOG has 3 deg/hour of bias drift, it complies the requirement in Figure 8-10.

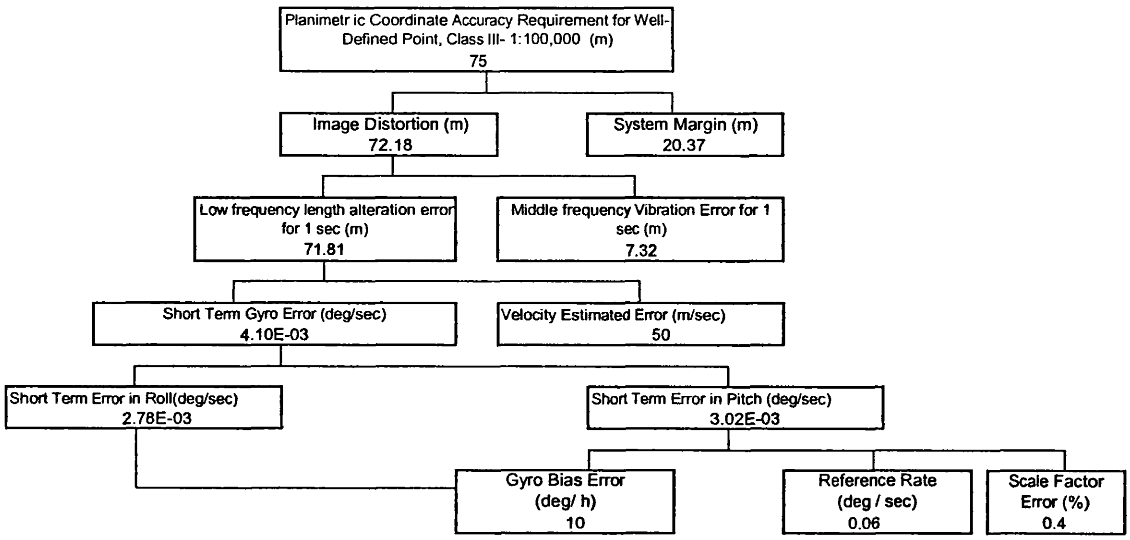

Figure 8-10 Length alteration error margin

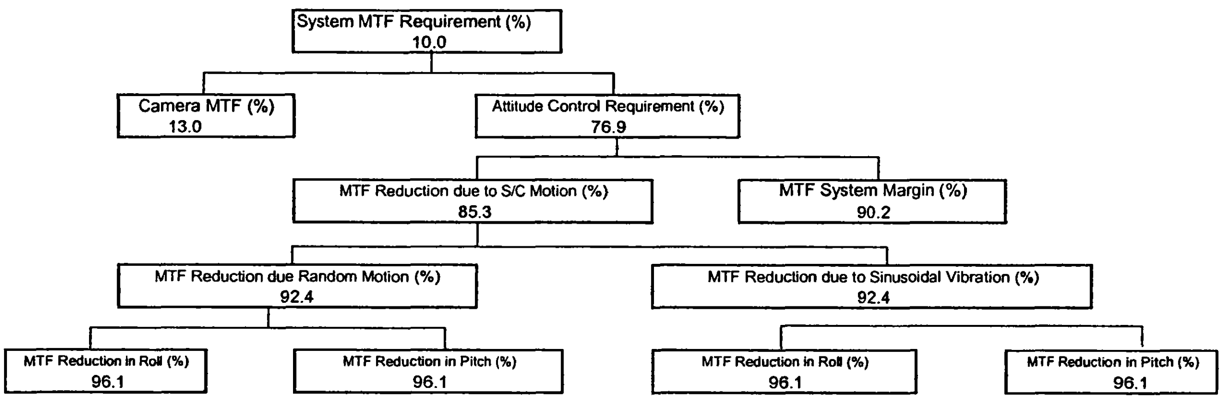

Figure 8-11 System MTF requirement allocation

High frequency vibration affects the system MTF and the quality of the image product as discussed in Chapter 2. Each vibration source can be decomposed as shown in Figure 8-11. It is not practically possible to model or measure these high frequency components. However, it can be inferred from the middle frequency vibration case, where the requirement is tighter, that high frequency requirement can be met since the amplitude of vibration is smaller.

Moving parts of the hardware components also need error budgeting in the line of image quality. Figure 8-12 shows that wheel and chopper vibration effects are in acceptable range, where the comparison is made for the normalised frequency 1 Hz.

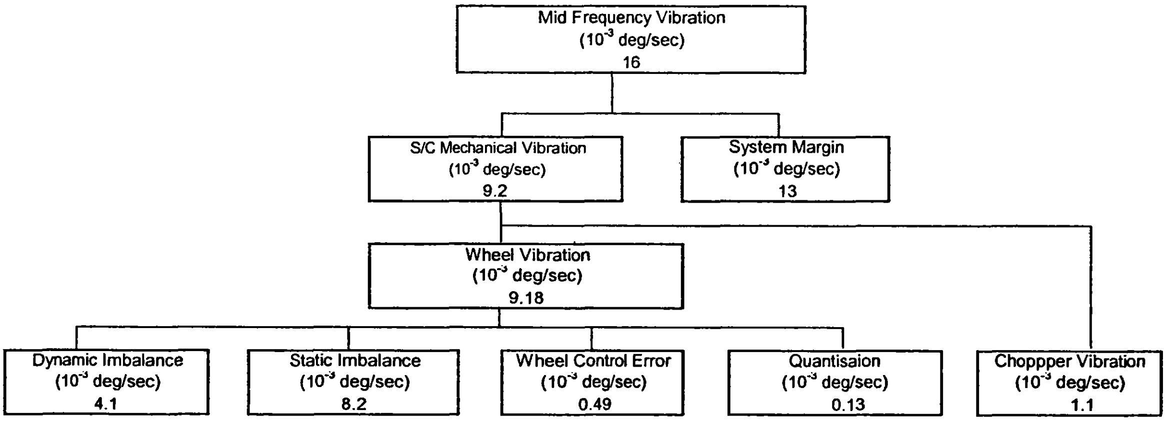

Figure 8-12 Mechanical vibration error allocation

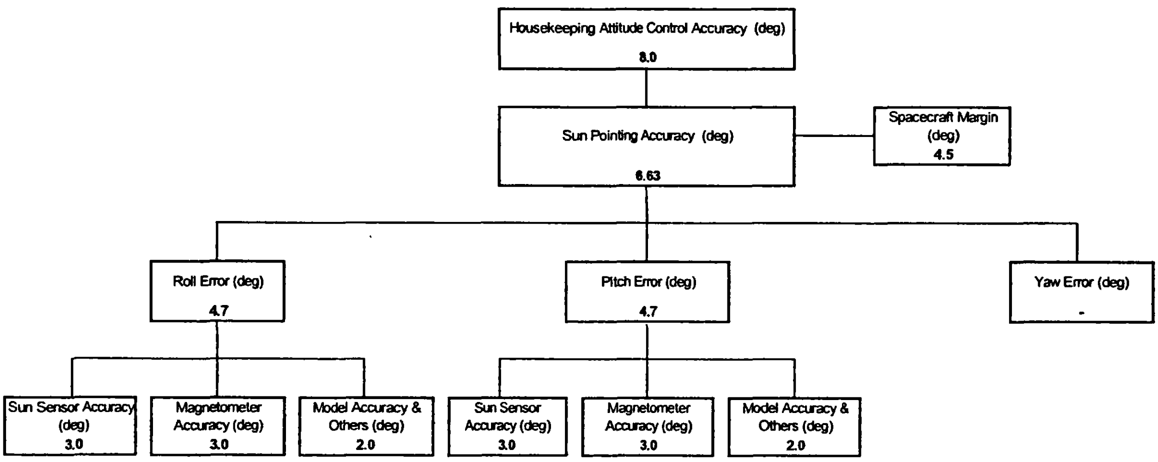

Figure 8-13 Pointing error allocation for housekeeping operation

We can summarise the compliance of the hardware specifications with respect to the system requirements and margins as follows. The reaction wheel system is quiet enough not to cause middle frequency image distortion due to its mass imbalance. The RMS system margin is sufficiently large even after including chopper vibration effect as shown in Figure 8-12. A large system margin is allocated to account for other potential error such as motor bearing disturbance. Components margins are used in terms of maximum values to indicate non-statistical figures.

It is not straightforward for wheel capacity, wheel torquer, and magnetorquer capacity margin analysis. The figures given in Table 8-2 are basically from the limit numbers that were imposed on control algorithm. For instance, the torque is limited as 5 mNm in Section 7.3.2, which implies an expandable margin compared to its hardware capacity. The momentum storage and torque capacities have enough margins to absorb worst case environmental disturbance torque as discussed in Chapter 6 and Table 8-2.

The star sensor has different accuracies for on-axis and off-axis measurements. Over 2 and 3 arc minutes of margins are allocated for the star sensor. It also has 0.02° of system level margin. The star sensor has the highest accuracy demand and the smallest absolute accuracy margin among the ADCS hardware. Even if the localisation requirement was not raised during the mission definition period, the star sensor accuracy determines the quality of image information in terms of pinpointing its absolute coordinate.

Table 8-2 Hardware component margins

Component	Related Parameter	Margin		Remark
		System (RMS)	Component (Max)	
Vibration	Dynamic imbalance	0.013° / sec	3.43 gcm^2	Figure 8-12,
	Static imbalance		0.28 gcm	Section 6.2
	Control error		1 rpm	(Bialke, 1997)
	Quantisation error		0.29 rpm	
	Chopper vibration		$1^{\circ}\times10^{-3}$ /sec	
Wheel capacity	Torque	-	~ 10 mNm	Section 7.3.2
	Momentum storage	-	~ 0.05 Nms	Section 6.1
Magnetorquer	Magnetic Dipole	-	~ 50 % duty / 6 Am^2	Section 7.1 (Steyn, 2001)
Star sensor	On-axis accuracy	0.02°	0.034°	Figure 8-9,
	Off-axis accuracy		0.052°	(Renner, 1993)
Sun sensor	Accuracy	4.5°	2.5°	Figure 8-13, (Rhee,
Magnetometer	Accuracy		~ 1000 nT	1996), (Lee, 1994)
EHS	Accuracy	-		Experimental
Gyro	Bias	20.4 m	7° / hour	Figure 8-10,
	Scale factor error		0.2 %	(Renner, 1994)
GPS	Position accuracy	-	250 m	Figure 8-9, Figure
	Velocity accuracy	-	30 m/sec	8-10, (Lee, 2000)
Control law	Gain margin	66.9 dB		Figure 8-7,
(2Hz)	Phase margin	Inf.		(Kuo, 1987)

As discussed in Chapter2, the Sun tracking mode is a baseline operation for housekeeping. Eight degrees of pointing accuracy is required for coarse solar power acquisition. Figure 8-13 shows the pointing error allocation, where we have large margins compared to imaging operation. Sun sensor has 2.5° of component margin, if it is compared with the calibrated 0.5° accuracy (Rhee *et al,* 1996). Magnetometer accuracy has over 1000nT of component margin for 1° accuracy attitude determination (Wertz, 1978). The on-board 10th order IGRF model accuracy also meets the requirement since the 7th order model has better than 0.1° RMS accuracy. In-flight experience from KITSAT-1 and 2 showed that the magnetometer was very reliable and met the accuracy specification (Lee, 1994).

Gyro drift and scale factor accuracy contribute the quality of the processed image product in terms of length alteration. It has large component and system margins. Mechanical vibration also results in length alteration. However, it can be absorbed into the system margin. TUBSAT A and B that had the same type of gyro demonstrated feasibility of using FOG in space (Renner, 1994).

GPS position and velocity accuracy can be considered to have 250m and 30m/sec margin. The margin can be verified by the in-flight results and other missions that have similar type of GPS receivers (Lee, 2000).

The analysis data including Chapter 6, 7 and Table 8-2 confirm us that in the worst case environment condition the satellite attitude control system has margin to accomplish the mission requirements. The level of redundancy implemented in the satellite also improves the reliability of mission success.

8.2 Flight Results

8.2.1 Orbit Parameters

The pre-launch orbit parameters used in the target launch turned out to be different from the actual post-launch parameters, as shown in Table 8-3. Major differences are in altitude, eccentricity and the local sun time. The first two parameters have effects on the satellite imager and its products although ground processing can compensate this. However, the last parameter affects operational aspects of the attitude control system. The satellite must tilt along the roll axis in order to obtain maximum solar power during normal operation. This results in a higher disturbance torque for the attitude control system. The roll axis is affected most by the gravity gradient torque.

Figure 8-14 is 3-dimensional graphical representation of the in-flight GPS measurement result at June 19th 1999, which was the first GPS telemetry data from the satellite. The data were generated on-board in real-time. The function of the GPS receiver and its software were partially verified through this data. However, the absolute accuracy cannot be evaluated since there is no other way for fine orbit determination that is more accurate than the publically available observation data from NORAD.

The two line element (TLE) data from NORAD is very useful for tracking the satellite on the ground. However, the accuracy is relatively low. When using the SGP4 as the propagation algorithm, the accuracy is around ~2km within 2 days after the reference epoch. Therefore, it is not possble to evaluate the absolute GPS accuracy in full. The result in Figure 8-14 shows that the difference between the measurement and the model is within 2 km. Inherently the SGP4 model has the best performance along the range direction. Utilising this characteristic, we can assess the performance of the GPS receiver on KITSAT-3.

Table 8-3 Orbit characteristics

Parameters	Target (Pre-launch)	Actual (Post-launch)
Altitude (Nominal)	720 km	733.2 km
Inclination	98.27 deg	98.383 deg
Eccentricity	0 deg	0.0016 deg
Local sun time	12:00	12:25

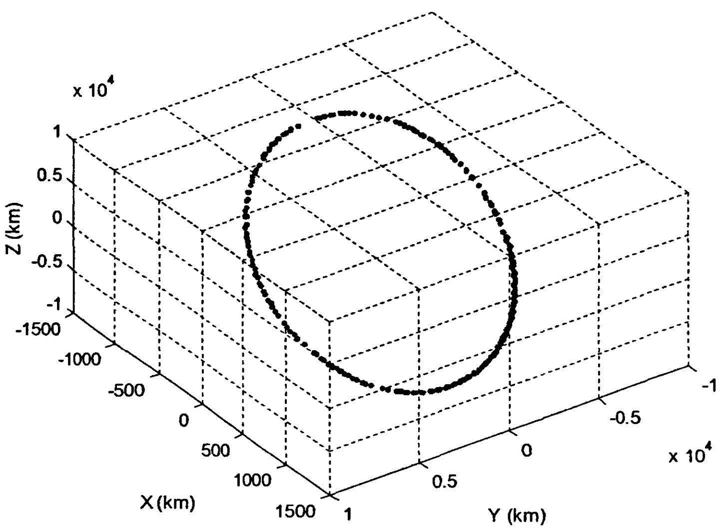

Figure 8-14 In-flight GPS data

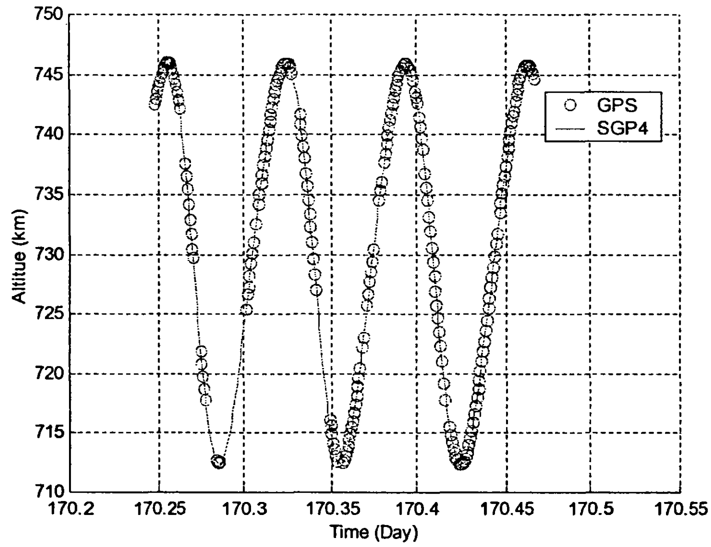

Figure 8-15 Measured altitude vs. SGP4 model

The comparison result for the range direction in Figure 8-15 shows that the maximum error is less than 250 m. Although the accuracy cannot be fully verified due to the lack of accurate reference observation data, it can be demonstrated that the GPS can be used as the input of the orbit propagator in case the orbit parameter information is not released. The missing data points in Figure 8-15 are due to the software performance limit before the tune-up of the internal calculation parameters.

8.2.2 Attitude Stabilisation

KITSAT-3 was launched on May 26th, 1999 at the Shar launch base in India. Figure 8-16 shows launcher site integration on the fourth stage with other satellites, IRS-P4 and DLR-TUBSAT. KITSAT-3 is on the left corner below the Indian remote sensing satellite, IRS-P4, which is the primary passenger. The initial spin rate was about 2°/sec, which is close to the minimum value from the pre-launch analysis. After 3 days of initial commissioning and basic health checking, de-spinning command was sent from the mission control centre in Korea. Due to the power limitation, the gyro units were not switched on at this stage. Only the magnetometer data were used for the de-spinning process. The detumbling control law was applied to reduce the satellite body spin rate to the manageable level for the reaction wheels. Figure 8-17 and Figure 8-18 show the telemetry data from the navigational magnetometer and analogue sensor.

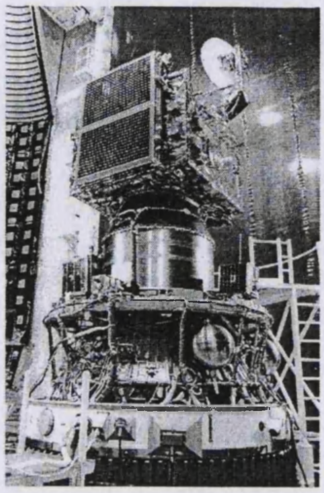

Figure 8-16 Launcher integration

The telemetry data in Figure 8-17 is displayed for one day. Since the initial spin rate was somewhat lower than the expected worst case, 7°/sec, the angular momentum reached the critical level for attitude capture by reaction wheels within 12 hours.

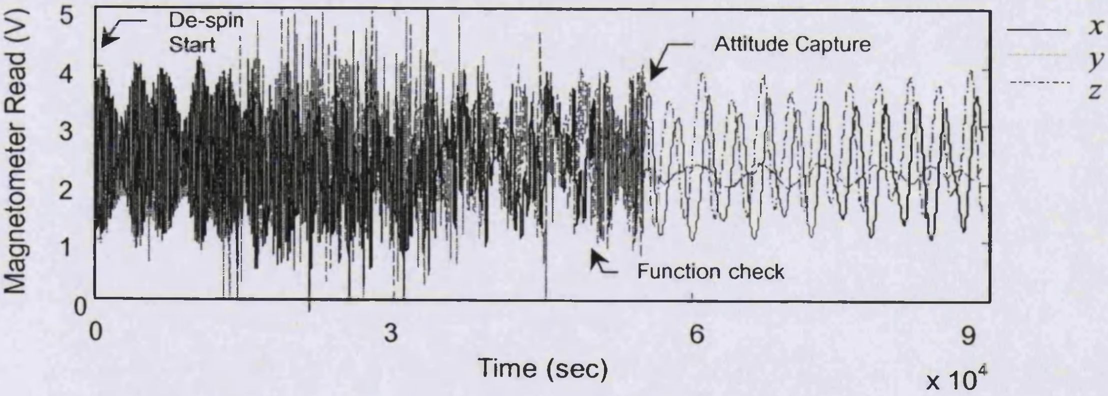

Figure 8-17 Magnetometer data telemetry

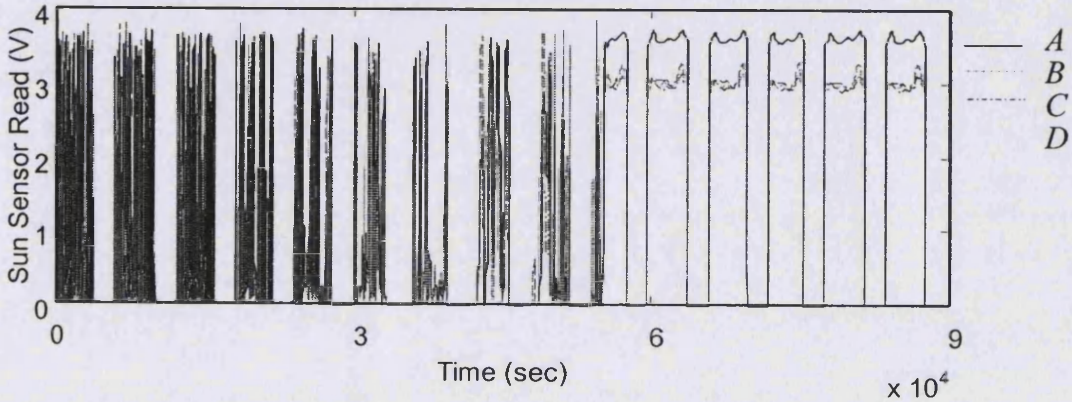

Figure 8-18 Sun sensor data telemetry

The attitude capturing process was carried out in two phases. The functioning status of the reaction wheels and gyros was checked at the first stage by switching on the powers and monitoring telemetries. To validate the software algorithm, the attitude capture process was terminated a few seconds after the initiation command. Proper functioning of the hardware and software was verified by analysing the telemetry on the ground. Gaining confidence in the performance of the control system, the capturing command was re-issued at the following orbit.

The telemetry from the fibre optic gyro is plotted in Figure 8-19. The data is displayed after the initial function check. It shows that the rotational motion of the satellite body is dramatically stabilised using the reaction wheel control. Figure 8-20 shows the controlled quaternion history. The quaternions are expressed with respect to the Earth centred inertial frame. The –z axis of the satellite is commanded to track the Sun. For the convenience of clear understanding, the Euler angle between the reference and the satellite body frame is plotted in Figure 8-21.

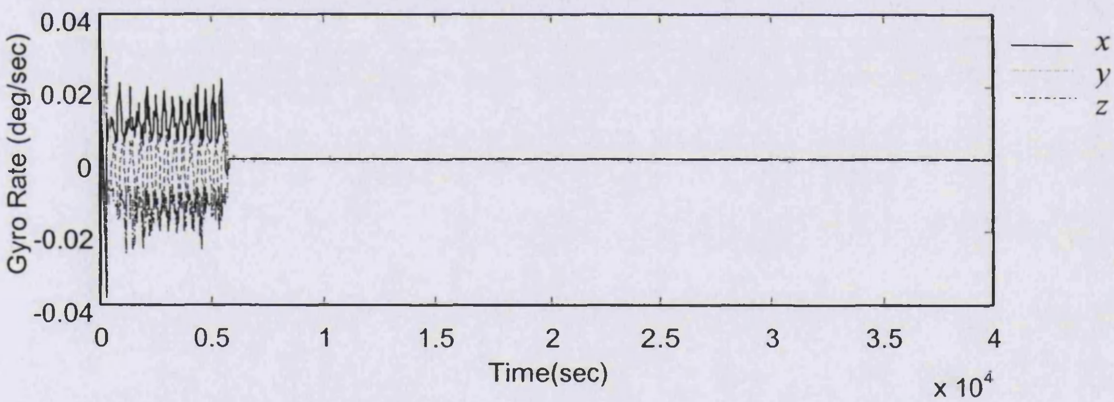

Figure 8-19 Gyro data telemetry

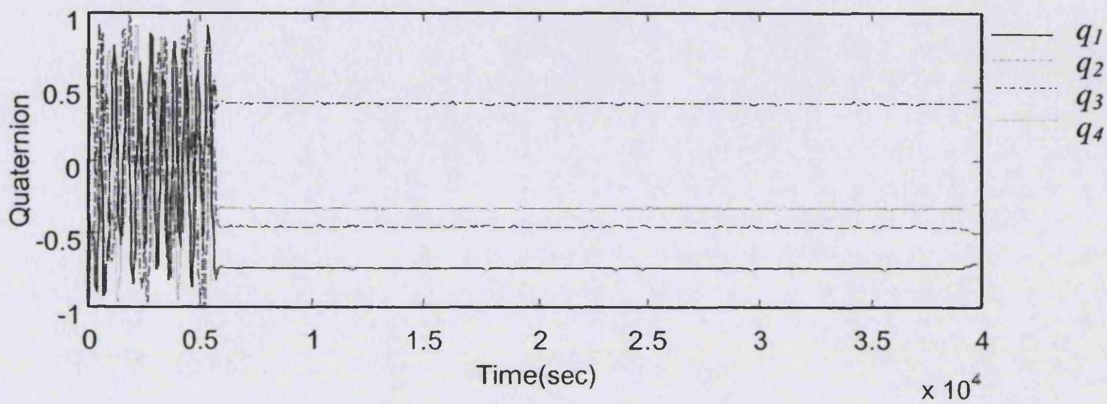

Figure 8-20 Quaternion telemetry

The Euler angle represents the inertial pointing accuracy and stability in terms of angle, which is more familiar for human perception. Figure 8-22 shows the Euler angle difference between the desired and actual angles. The graph indicates that the overall pointing accuracy is within the pointing requirement of 0.5°. Statistically, the pointing error falls in the range ±0.4° (2σ).

The error becomes high when the satellite enters the Sun light region. The sudden output in the Sun sensor reading, as shown in Figure 8-18, results in the abrupt change in the control reference.

The star sensor experiment in KITSAT-3 was successful for eclipse side operation, as shown in the star image of Sextant in Figure 8-23. The output satisfied 1 arc minute of performance requirement after verifying the result with ground processing. However, the problem in the baffle design of the star sensor resulted in limitations in the dayside sensor performance. The fine control mode with star sensor was only applicable during the night side, where the pointing accuracy was within 0.2°.

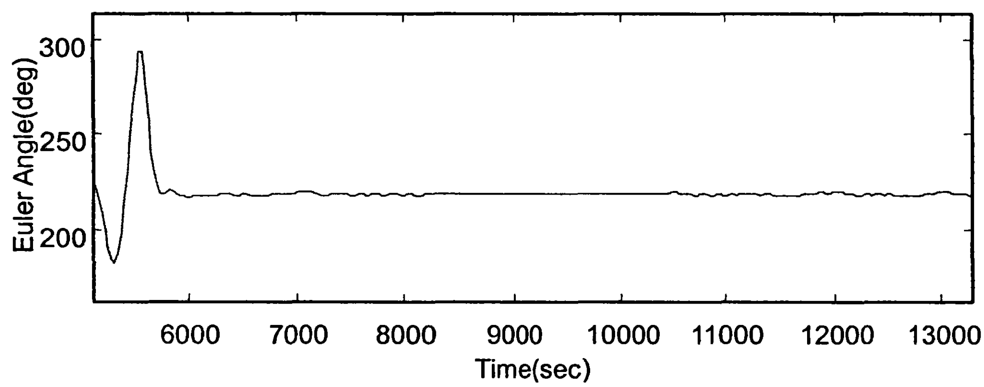

Figure 8-21 Controlled Euler angle

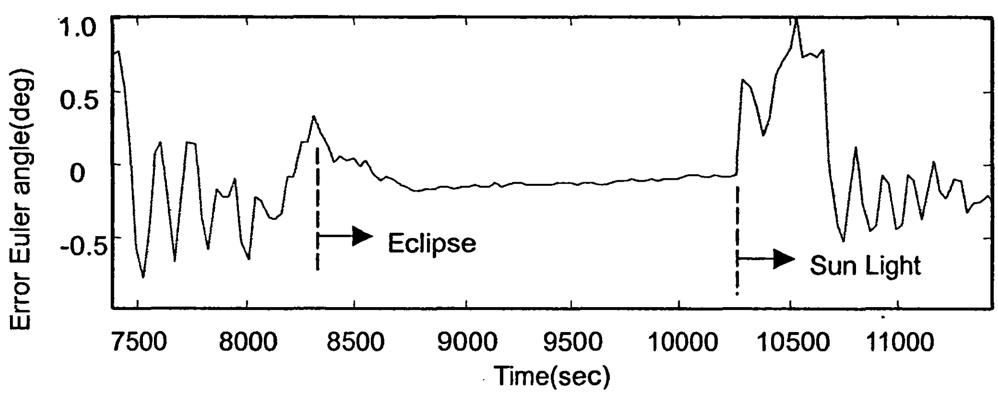

Figure 8-22 Euler angle control error

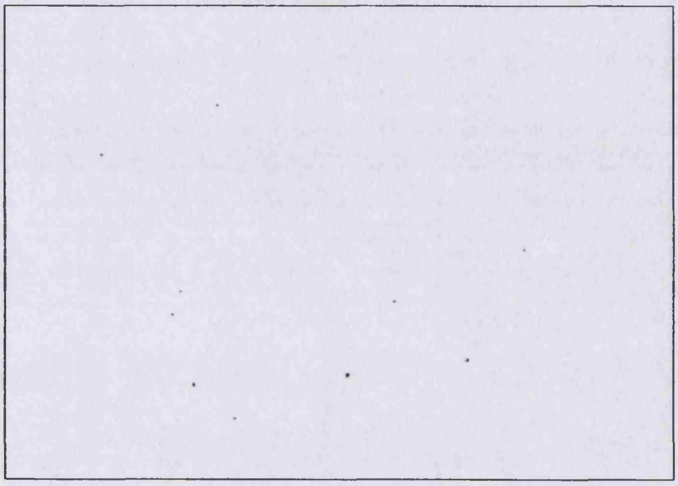

Figure 8-23 Star sensor image

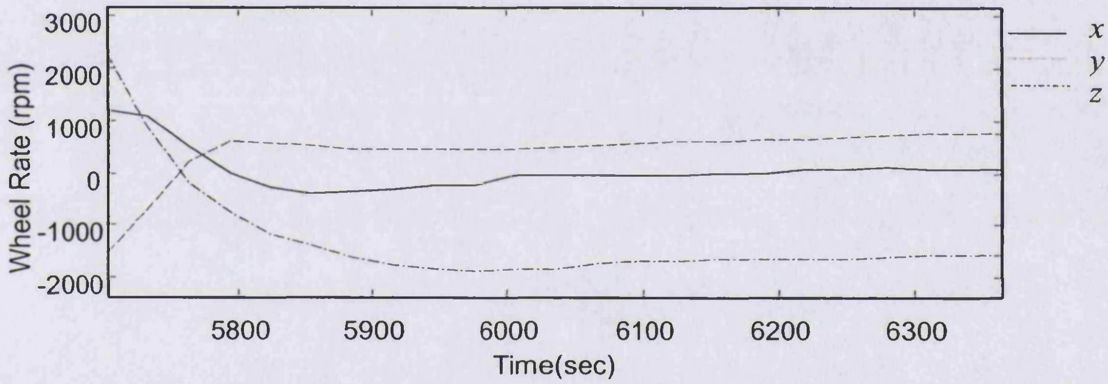

Figure 8-24 Reaction wheel speed telemetry

The reaction wheel speed telemetry in Figure 8-24 verifies the design of the inertial control system. The biased initial speeds are due to the wheel speed change during the initial check up of the reaction wheels. The actual result shows that the speeds of the reaction wheels were controlled properly to absorb the residual angular momentum of the satellite rotation. The gyro data in Figure 8-19 explains that the angular momentum is completely transferred from the main satellite body to the wheels.

After the attitude is stabilised the gyro output in Figure 8-25 guarantees that the rate control of the satellite body is also adequately performed. Except for the peaks at the boundary of the eclipse region, the stability was maintained within 1.0×10^{-4} deg/sec range. It is well in the boundary of the stability budget.

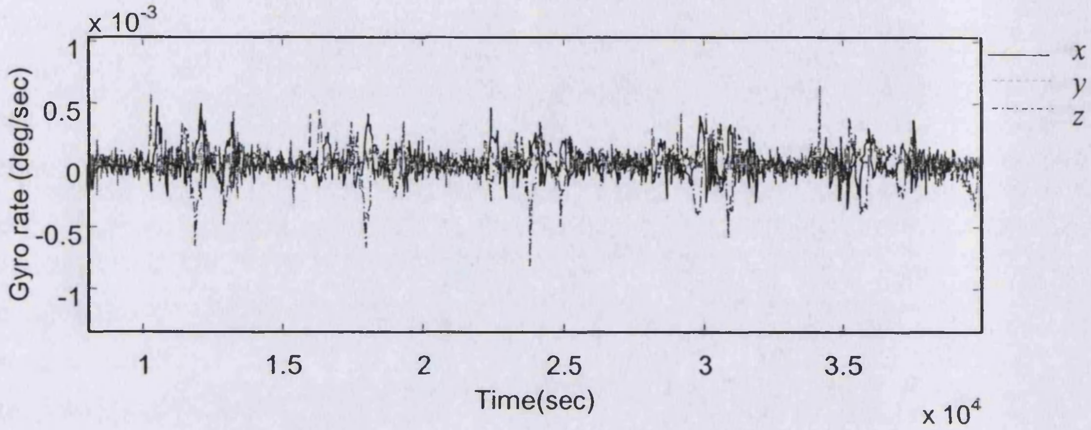

Figure 8-25 Rate control history

8.2.3 *Environmental Torque*

Figure 8-26 shows telemetry and modelled values of the reaction wheel speed changes when the momentum dumping is disabled. The data explains the effect of environmental disturbance. As discussed in Chapter 6, the environmental disturbances such as solar pressure, gravity gradient, aerodynamic drag and magnetic field cause the satellite to rotate depending on the orbital position and the satellite orientation.

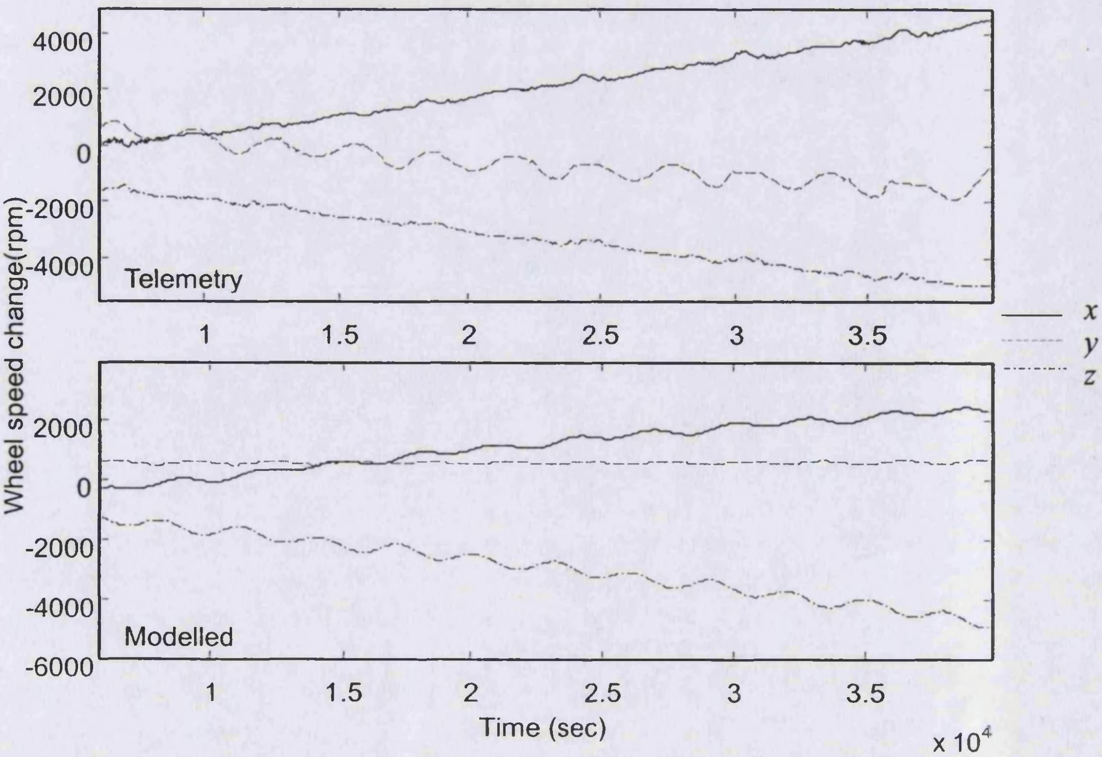

Figure 8-26 Wheel speed build up due to environmental disturbance

The general tendency of in-orbit momentum build-up agrees with the simulated case. The amount of increased momentum about the z axis is matched quite well. However, there are some discrepancies about the x and y axis. The error can be attributed to many difference sources. The surface characteristics of the satellite such as drag coefficient and light scattering coefficients assumed in Chapter 6 contain certain degree of errors. The space environment model for upper atmosphere also has a large uncertainty.

The un-modelled residual magnetic dipole moment can be regarded as the largest error source. The value has time-varying characteristics since magnetic induction from the internal electric circuits has a large effect. Even though this part of the disturbance source is practically very difficult to model, the results in Figure 8-26 explain the order of magnitude of the un-modelled residual magnetic dipole moment. It can be said through a series of simulations that the value is around the standard uncompensated magnetic dipole moment in small satellite, 0.1 Am^2 (Larson and Wertz, 1992). This kind of information is valuable for future mission design. Care should be taken to minimize this effect in the harness design. Twisted pair power and return lines may reduce the magnetic disturbance effect.

Figure 8-26 also suggests that the momentum of the reaction wheel system should be managed properly. The wheel speed saturates within 10 hours without magnetorquering. Figure 8-27 displays the effect of momentum dumping. The telemetry is obtained when the nominal wheel speed was set at ±1000 rpm. The data over a 24-hour period confirmed the proper operation of the magnetorquer hardware and software developed in this paper. Periodic peaks occur when the satellite escapes the eclipse region. Sudden changes in the reference input cause short-term attitude jittering.

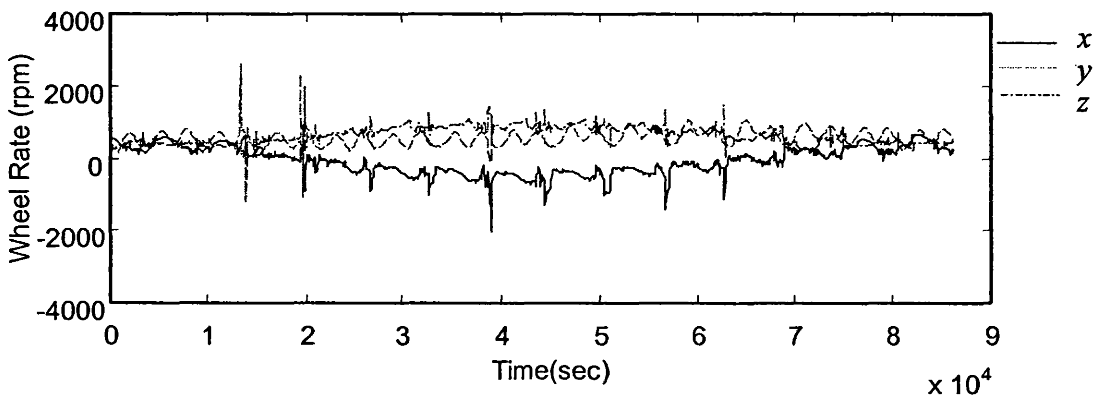

Figure 8-27 Momentum management history

8.2.4 Imaging Performance

The availability of KITSAT-3 image products makes it possible to locate major buildings and to measure and evaluate ground features larger than 13.5 meters. The satellite imagery permits the recognition of airports, ports and harbours, coasts, railroad yards, factories, roads, urban areas, ships, icebergs, volcanic eruptions, terrain and so on. Figure 8-28 shows multi-spectral (red, green and near infrared) pseudo-colour images of some areas taken from KITSAT-3. Multi-spectral images enable land classification such as vegetation field, bare land, river, etc. Periodical imaging of the same area allows the detection of land usage change.

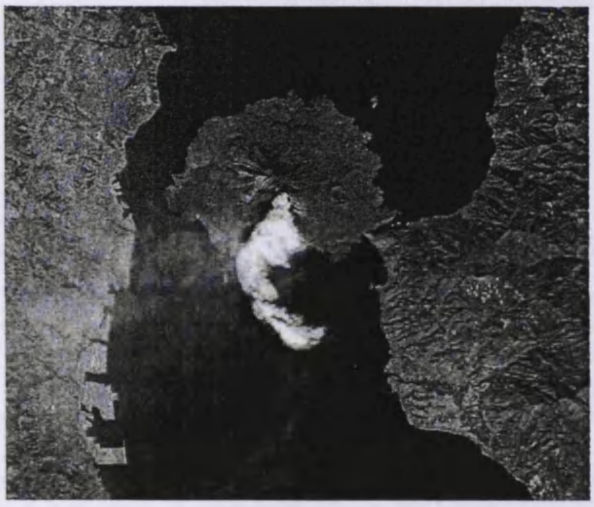

(a) Volcanic Eruption (Sakurajima Mt., Japan)

(b) Construction (New Seoul Airport, Korea)

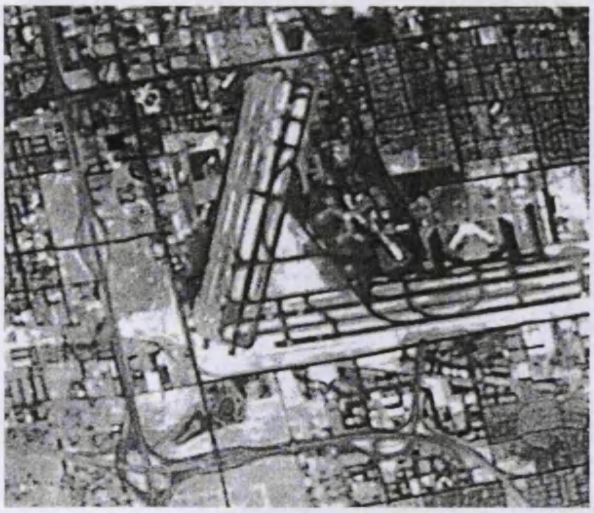

(c) Airport (Las Vegas, U.S.)

(d) Ports (Oakland Naval Base, U.S.)

Figure 8-28 Multi-spectral images over different areas

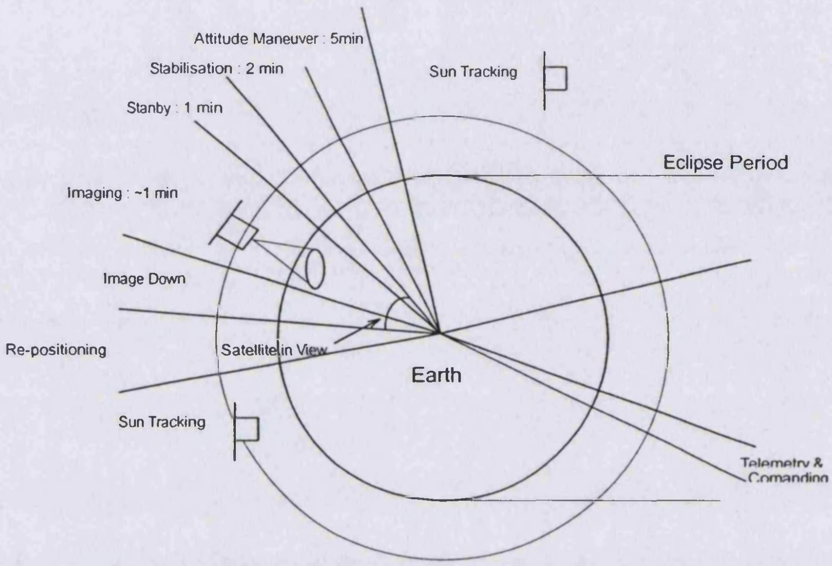

Figure 8-29 Earth imaging operation time lines

Figure 8-29 shows the operation time lines for the Earth imaging mode. Prior to the image scanning, 5 and 2 minutes of manoeuvring and stabilisation time respectively are allocated. Since the maximum length of the scanned strip is 465 km, approximately one minute is available for imaging. After completing the imaging, a part of the image data can be downloaded to the ground. Once the satellite is out of view from the ground station, the attitude should be repositioned to the Sun tracking mode.

The body tilting capability, which shortens the revisit period and provides off-nadir imaging, can enhance mission operations. Figure 8-30 depicts the imaging flexibility utilizing the attitude control system. A large portion of areas around the flight path can be imaged with the tilting command. The effects of GSD reduction and the accessible field-of-regards according to the tilt angle are indicated in the figure.

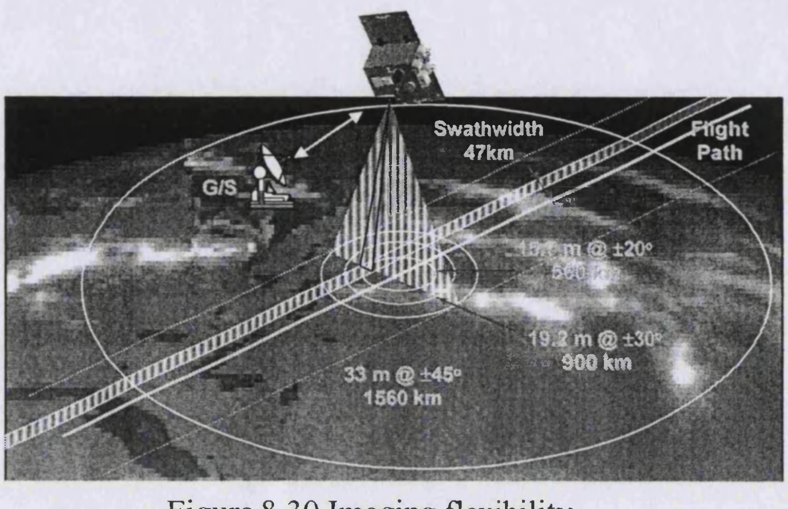

Figure 8-30 Imaging flexibility

The stability of the attitude can be indirectly compared with higher resolution satellites. Fusion of KITSAT-3 multi-spectral image with KOMPSAT-1 panchromatic image that has 6.6m GSD in Figure 8-31 reflects that the cost-effective ADCS design of a low cost microsatellite can be compatible with the performance of standard space qualified design.

Figure 8-31 Fusion with higher resolution image

Chapter 9. Conclusions

This dissertation is based on the development results of the KITSAT-3 micro-satellite programme that was carried out from 1994 to 1999. It covers mission characterisation, mission analysis, designs and tests of attitude sensors and actuators, modelling of hardwares, assessments of system performance, control system design, and flight results.

Attitude control system requirements were derived from the payload operations in this thesis. The multi-spectral Earth observation camera imposed the most stringent attitude pointing and stability requirements as 0.5° and $0.016\ ^{\circ}/\mathrm{sec}$, respectively. The causes and effects of attitude knowledge and control errors were analysed. The in-orbit operation concept of the satellite was proposed from the attitude point of view.

General theory of attitude dynamics was summarised as a baseline for developing control theory. The dynamic equations were modified for the biased reaction wheel system of the satellite. An attitude control system with three orthogonal wheels and a redundant pitch wheel was proposed to maximise the efficiency of the pitch control.

Hardware design of the magnetorquer with 3-axis magnetic moment control capability was explained in detail. Test results showed that it could drive vector torque with an excellent linearity. Data handling system architecture and the communications protocol were also suggested based on actual implementation results. The system was proven to be capable of handling all the data from the ADCS subsystems.

Modelling of the hardwares including magnetorquer, reaction wheel, and fibre optic gyro were done based upon actual implementations and experiments. Combining the models with the attitude dynamics of the satellite, the performance of the ADCS was evaluated. Space environmental torques such as solar, aerodynamic, gravity gradient and magnetic torques were modelled and analysed. The mechanical and electro-magnetical effects of the vibrating chopper in the horizon sensor were assessed.

Initial phase detumbling control law was proposed with a stability analysis. Schmidt trigger logic was applied to avoid instability and enhance the efficiency. Momentum unloading algorithm showed that it could desaturate the wheel against the environmental torques. Quaternion feedback control law for large angle manoeuvre was modified to meet the torque and momentum capacity limitations of the small, low cost reaction wheels. Kalman filtering theory was applied to show the compliance of the fine control requirements. Notwithstanding the low cost approach, the in-flight results showed that high accuracy control is achievable and micro-sized satellites have prospecting future.

Bibliography

Agrawal, B. N., (1986), *Design of Geosynchronous Spacecraft*, Prentice-Hall, New Jersey.

Alexander, S. T., (1986), *Adaptive Signal Processing: Theory and Applications*, Springer-Verlag, New York.

Antrix Corporation Ltd., (1998), *PSLV-C2 Preliminary Mission Analysis Document on KITSAT-3*, Bangalore, India.

Arianespace, (1992), *Launch System/Spacecraft Interface Control File KITSAT-A*, DCI 10/388 10.

Barbour, N., Madden, P., and Socha, M., (1996), *A Micromechanical Gyro Package with GPS under Development for Small Pointing Satellites*, Proc. of the 10th Annual AIAA/USU Conference on Small Satellites, Utah State University.

Bate, R. R., Muller, D. D., and White, J . E., (1971), *Fundamentals of Astrodynamics*, Dover Pub. Inc., New York.

Battin, R. H., (1987), *An Introduction to the Mathematics and Methods of Astrodynamics,* AAIA Education Series, New York.

Bendat, J. S., and Piersol, A. G., (1991), *Random Data : Analysis and Measurement Procedures* 2nd ed., John Wiley & Sons, Singapore.

Bialke, B., (1997), *A Compilation of Reaction Wheel Induced Spacecraft Disturbances*, 20th AAS GNC Conference, AAS 97-038, Breckenridge, U.S.A.

Bonometti, R. J., (1993), *The Role of Small Satellites in the Emerging National Information Infrastructure and the Future Defense Global Grid*, Proc. of the 7th Annual AIAA/USU Conference on Small Satellites, Utah State University.

Boylestad, R., and Nashelsky, L., (1987), *Electronic Devices and Circuit Theory*, 4th ed., Prentice-Hall, New Jersey.

Bryson Jr., A. E., (1994), *Control of Spacecraft and Aircraft*, Princeton University Press, New Jersey.

Campana, S. B., ed. (1993), *Passive Electro-Optical Systems*, The Infrared & Electro-Optical Systems Handbook, Vol. 5, SPIE Optical Engineering Press, Washington.

Chang, D. H., (1992), *Magnetic Momentum Bias Attitude Control Design for the HETE Small Satellite*, Proc. of the 6th Annual AIAA/USU Conference on Small Satellites, Utah State University.

Chen, T.-S., (1984), *Linear System Theory and Design*, Holt-Saunders International Ed., Japan.

Cheng, D. K., (1989), *Field and Waves Electromagnetics*, Addison-Wesley Pub. Co., Reading.

Chetty, P. R. K., (1991), *Satellite Technology and Its Applications* 2nd ed, TAB Professional and Reference Books.

Choi, S. D., Kim, B. J., and Shin, Y-H, (1997), *An Introduction to the KITSAT Programs and the Activities at the SaTReC in Korea*, COSPAR Colloquium on Scientific Microsatellites, Tainan, Taiwan.

Dyne, S. J. C., Thunbridge, D. E. L., and Collins, P. P., (1993), *The Vibration Environment on A Satellite in Orbit*, IEE Colloquium on High Accuracy Platform Control in Space, London, 12/1.

Goldberg, D.E., (1989), *Genetic Algorithms in Search, Optimization, and Machine Learning*, Addison-Wesley Pub., Reading.

Goodwin, G. C., and Sin, K. S., (1984), *Adaptive Filtering Prediction and Control*, Prentice Hall Inc., N.J.

Grewal, M. S., and Andrews, A. P., (1993), *Kalman Filtering; Theory and Practice*, Prentice-Hall Inc., New Jersey.

Han, W., Yoo, S., and Kim, B. J., (1995), *Multi-Channel remote Sensing CCD Controller Design with Multiplexing Concept,* Korean Journal of the Astronomy and Space Sciences, **12-1**, 54-65.

Heidemann, H., (1994), *Attitude and Orbit Control System of ERS Satellites*, Dornier Post, **4**, 15.

Hodgart, M. S. and Wright, P. S., (1987), *Attitude Determination, Control and Stabilization of UoSAT-2*, The Journal of the Institution of Electronic and Radio Engineers, **57** (Supplement), S151.

Hodgart, M. S., (1982), *Attitude Control and Dynamics of UOSAT Angular Motion*, The Radio and Electronic Engineer, **52** , 379

Holst, G. C., (1996), *CCD Arrays, Cameras, and Displays*, JCD pub., Florida.

Hughes, P.C., (1986), *Spacecraft Attitude Dynamics*. John Wiley & Sons, New York.

Japan Aerospace Engineering Association, (1992), *Aerospace Engineering Handbook,* pp. 1017-1018, (In Japanese).

Joseph, G., (1996), *Imaging Sensors for Remote Sensing*, Remote Sensing Reviews, **13**, 257.

Kaplan, M.H., (1976), *Modern Spacecraft Dynamics and Control*, John Wiley & Sons, New York.

Kenjo, T. and Nagamori, S., (1984), *Permanent Magnet and Brushless DC Motors*, Sogo Electronics Pub. Co., Tokyo. (English Translated Version)

Kim, B. J., (1991), *Attitude Control of a Microsatellite,* M. Sc. Project Report, University College London.

Kim, B. J., (1992), *SOLID(Solar Oblatness, Irradiance and Diameter) Mission Analysis*, Project Report, University College London.

Kim, B. J., Lee, H., and Choi, S. D., (1995), *Three-axis Reaction Wheel Attitude Control System for KITSAT-3 Microsatellite,* IFAC International Conference on Intelligent Autonomous Control in Aerospace, Beijing.

Kim, B. J., and Lee, H. (1997), *Attitude Control System Tests Using Three-axis Air Bearing Hardware Simulator,* IFAC International Conference on Control of Small Satellite, Breckenridge, U.S.A.

Kim, B. J., and Lee, H. (1997), *Spacecraft Attitude Dynamics Analysis Using Three-axis Air Bearing,* Space Technology, Vol. 17, No. 1, pp. 45-50.

Kim, J. H., (1998), *Review on the ADCS of KOMPSAT Performance,* Project Report, Inha University.

Kim, S., Park, S., Sung, D. K., and Choi, S. D., (1995), *Mission Overview of Engineering Test Satellite, KITSAT-3,* Proc. of the 9th Annual AIAA/USU Conference on Small Satellites, Utah State University.

Königsmann, H. J., Wiegand, M., and Matthews, O., (1995), *The Magnetic Attitude Control of ABRIXAS,* Proc. of the 9th Annual AIAA/USU Conference on Small Satellites, Utah State University.

Kohno, T., Munakata, K., Nagata, K., Murakami, H., Nakamoto, A., Hasebe, N., Kikuchi, J., and Doke, T., (1990), *Intensity Maps of MeV Electrons and Protons Below the Radiation Belt,* Planet Space Sci., **38**, 483.

Kraus, J. D., (1984), *Electromagnetics* 3rd Ed., McGraw-Hill, New York.

Kuo, B. C., (1987), *Automatic Control Systems* 5th ed., Prentice-Hall Inc., New Jersey.

Kuramasu R., Inoue, K., Mine, M., Yamaguchi, Y., Tanamachi, T., Nakamura, D., and Iwamoto, Y., (1994), *Attitude Control Design for Advanced Earth Observing Satellite (ADEOS),* Information and Communication Engineers, 39 (In Japanese).

Larson, W. J., and Wertz J. R., (1992), *Space Mission Analysis and Design* 2nd ed., Kluwer Academic Pub.

Lee, J., and Chang, Y. K., (2000), *A study on GPS Data Tracking Method for KOMPSAT Spcecraft Orbit Control,* Proc. of the 14th Annual AIAA/USU Conference on Small Satellites, Utah State University.

Lee, H., (1991), *The Design of Construction of a Magnetic Test Facility,* M. Sc. Project Report, Dept. EE Eng., University of Surrey.

Lee, H., Kim, B. J., Yoo, S., and Han, W., (1995), *Prototype Development of the Star*

Sensor for the KITSAT-3, Korean Journal of the Astronomy and Space Sciences, **12-2**, 256-264 (In Korean).

Lee, H., Park, D., and Choi, S. D., (1994), *In-flight Calibration of Magnetometer by LMS Algorithm for the Korean Experimental Micro Satellite KITSAT-1&2*, IEEE/SAIEE Symposium on Small Satellites and Control Systems, University of Stellenbosch, South Africa, 9-1.

Lee, I. P., Sung, D. K. and Choi, S. D., (1993), *Experimental Multimission Microsatellites -KITSAT Series*, Proc. of the 7th Annual AIAA/USU Conference on Small Satellites, Utah State University.

Lee, S., (1998), *Mission Analysis of KOMSAT-1,* Workshop on satellite design, KAIST.

Light, D. L., (1990), *Characteristics of Remote Sensors for Mapping and Earth Science Applications*, Photogrammetric Engineering and Remote Sensing, **56-12**, 1613-1623.

Lin, C.-F., (1991), *Modern Navigation, Guidance, and Control Processing*, Prentice-Hall Inc., New Jersey.

Lin, C.-F., (1994), *Advanced Control Systems Design*, Prentice-Hall Inc., New Jersey.

Mitomi, Y., Yoshida, B., and Martinelli, V., (1995), *Brings Fiber Optic Gyroscopes to Market*, Photonics Spectra, July, 88-96.

Miah, M. A., (1991), *The ONR-602 Experiment and Investigation of Particle Precipitation Near the Equator*, J. Geomag. Geoelectr., **43**, 445.

Miah, M. A., Nagata, K., Kohno, T., Murakami, H., Nakamoto, A., Hasebe, N., Kikuchi, J., and Doke, T., (1992), *Spatial and Temporal Features of 0.64-35 MeV Protons in the Space Station Environment: EXOS-C Observation*, J. Geomag. Geoelectr., **44**, 591.

Muller, L., (1995), *Micro Electro-Mechanical systems (MEMS) Technology Integration into Micro-Spacecraft*, Proc. of the 9th Annual AIAA/USU Conference on Small Satellites, Utah State University.

Nagle, H. T., Carroll, B. D., and Irwin, J. D., (1975), *An Introduction to Computer Logic*, Prentice-Hall, New Jersey.

NASA, (1969), *Spacecraft Magnetic Torques*, NASA SP-8018.

Ninomiya, K., (1994), *Attitude Control of Scientific Satellites in Japan-A Technical Overview*, Transactions of the Japan Society of Mechanical Engineers, **60**, vol. 580, pp. 4008-4015. (In Japanese)

Park, S. D., Kim, S, Sung, D. K., & Choi, S. D., (1995), *Mission Analysis for Engineering Test Satellite, KITSAT-3*, Proc. of the 16th Asian Conference on Remote Sensing, Nakhon Ratchasima, Thailand, PS-6-1.

PE&RS (Photogrammetric Engineering & Remote Sensing), (1990), *Annual Report:*

ASPRS Accuracy Standards For Large-Scale Maps.

Press, W. H., Teukolsky, S. A., Vetterling, W. T., and Flannery, B. P., (1992), *Numerical Recipes in C* 2nd ed., Cambridge University Press.

Purcell, E. M., (1985), *Electricity and Magnetism* 2nd Ed., McGraw-Hill, New York.

Reitz, J. R., Milford, F. J., and Christy, R. W., (1979), *Foundation of Electromagnetic Theory* 3rd Ed., Addison-Wesley Pub. Co.

Renner, U., Lübke-Ossenbeck, B., and Butz, P., (1993), *TUBSAT, Low Cost Access to Space Technology*, Proc. of the 7th Annual AIAA/USU Conference on Small Satellites, Utah State University.

Renner, U., Lübke-Ossenbeck, B., and Butz, P., (1994), *TUBSAT-A,B,C*, 2nd International Symposium on Small Satellites Systems and Service, Biarritz, France.

Rhee, S., Lee, M., Lee, H., Lim, K. S., and Choi, S. D., (1996), *In-Orbit Error Analysis of Sun Sensor for KITSAT-2*, Korean Journal of the Astronomy and Space Sciences, **13-2**, 254-264.

Riley, W. F., and Sturges, L. D., (1993), *Dynamics*, John Wiley & Sons Inc., New York.

Sidi, M. J., (1997), *Spacecraft Dynamics and Control*, Cambridge Univ. Press.

Siouris, G. M., (1993), *Aerospace Avionics Systems : A Modern Synthesis*, Academic Press Inc., California.

Sweeting, M. N., (1994), *UoSAT Microsatellites & Minisatellites for Affordable Access to Space*, IEEE/SAIEE Symposium on Small Satellites and Control Systems, University of Stellenbosch, South Africa, 1-1.

Steyn, W. H., (1994), *Optimal Reaction Wheel Desaturation of a Nadir Pointing Satellite Using Magneto-Torquers*, IEEE/SAIEE Symposium on Small Satellites and Control Systems, University of Stellenbosch, South Africa, 5-1.

Steyn , W., H., and Hashida, Y., (2001), *In-Orbit An Attitude Performance of 3-Axis Stabilised SNAP-1 Nanosatellite*, Proc. of the 15th Annual AIAA/USU Conference on Small Satellites, Utah State University.

Takaki, S., (1994), *A Study on Particle Distribution Chage in Radaition Belts and Damage on Semi-Conductor Devices*, Ph.D Thesis, Tohu University, Japan (in Japanese).

Tascoine, T. F., (1988), *Introduction to the Space Environment*, Orbit Book Company, Florida.

Teldix, (1995), *Data Package RCU 1-0 for KITSAT-3 (Operation Manuals & Environment Test Results)*, Heidelberg.

Tipler, P. A., (1997), *Modern Physics*, Worth publishing Co.

Unwin, M., (1994), *Differential GPS Implementation on Microsatellites*, The 3rd.

International Conference on Differential Satellite Navigation Systems, London.

Wertz, J. R. ed., (1978), *Spacecraft Attitude Determination and Control*, Kluwer Academic Pub.

Wie, B. and Barba, P. M., (1985), *Quaternion Feedback for Spacecraft Large Angle Maneuvers*, Journal of Guidance, **8**, 360-365.

Wie, B., H. Weiss and Arapostathis, A., (1989), *Quaternion Feedback Regulator for Spacecraft Eigenaxis Rotations*, Journal of Guidance, **12**, 375-380.

Wisniewski, R., (1996), *Satellite Attitude Control Using Only Electromagnetic Actuation*, Ph.D. Thesis, Aalborg University, Denmark.

Acknowledgements

I would like to express my gratitude to all the people who helped me throughout writing this thesis. First of all, my sincere thanks to Prof. Soon Dal Choi for giving a chance to study in Britain. Without his pioneering spirits and financial supports for the study, my work would not be possible. I also endeavour to give credit to all the members of the KITSAT-3 team. I would like to give special acknowledgement to Mr. Hyunwoo Lee for working together from the very beginning of the project.

I wish to thank Prof. John Parkinson, Dr. Dave Linder, Alan Smith, and Prof. Len Culhane for guidance, assistance and advice during my study at UCL and MSSL. My warm thanks to my M.Sc. supervisor Mr. Tom Patrick for opening my eyes on mechanical aspects of spacecraft. I deeply appreciate the expert advice from Mr. Dave Hall and Jim Brown of Matra Marconi Space at the early stage of my study. I owe a debt to Mr. Wand of Teldix for arranging the tests carried out in Heidelberg.

Most of all, to my family for their support and understanding through the years of study. Especially, to my wife Seonhee who encouraged and gave me strength during the times of depression. I would like to dedicate this work to her.